Swansea University
Prifysgol Abertawe

Towards a Precision Measurement of the 1S-2S Transition in Antihydrogen

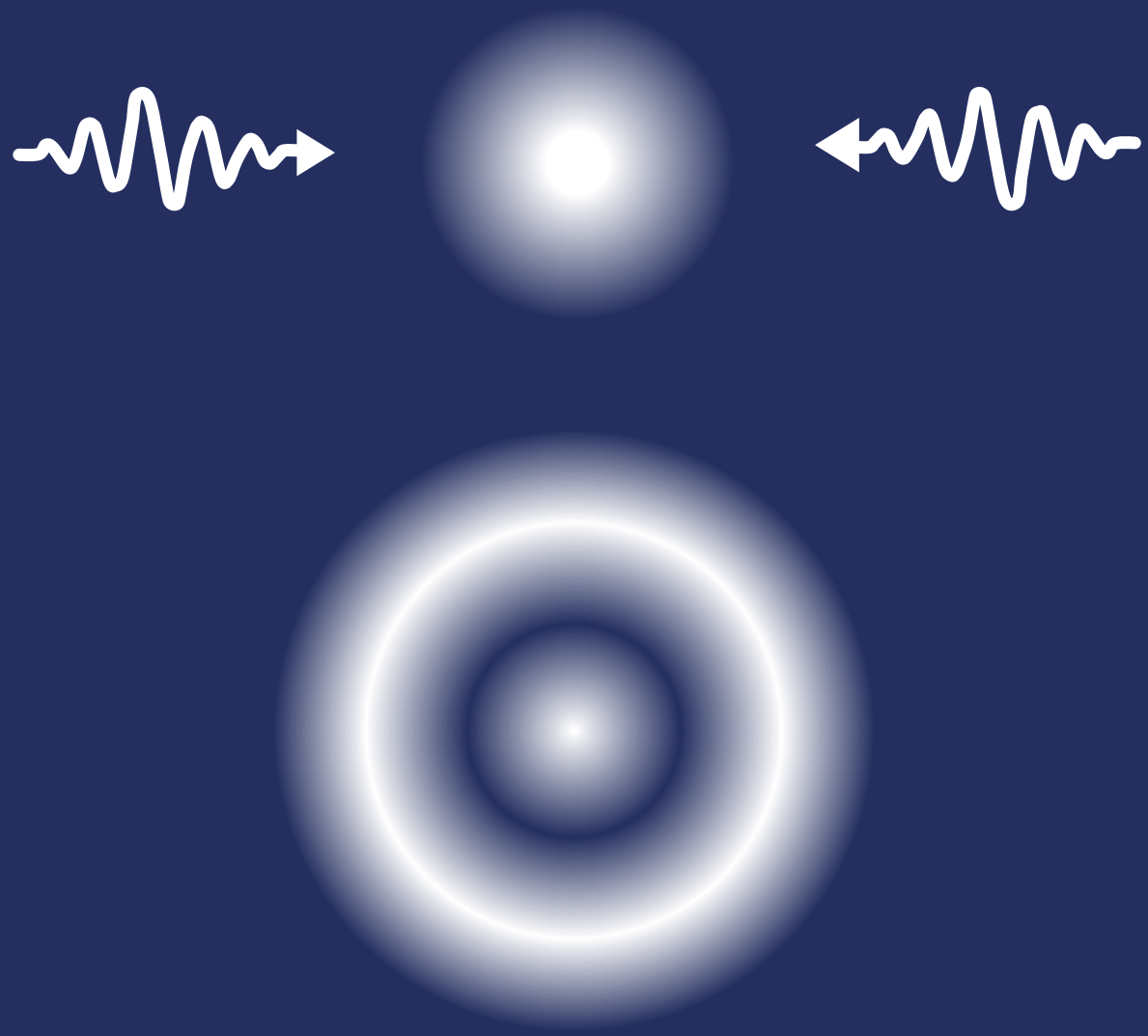

Edward Thorpe-Woods

Final version submitted to Swansea University in fulfillment of the requirements for the Degree of Doctor of Philosophy; January 2025

Abstract

Antihydrogen, the simplest pure antimatter atom, can be synthesised and confined for extended periods in the ALPHA experiment at CERN. According to the CPT invariance, antihydrogen is predicted to exhibit an energy spectrum identical to that of hydrogen. Consequently, a precise comparison of the spectra of both antihydrogen and hydrogen constitutes a direct test of CPT invariance. The narrow 1S-2S two-photon transition serves as the gold standard for precision measurements of hydrogen, where it has been measured with an exceptional 15 digits of precision. Equivalent measurements conducted with antihydrogen have so far been limited to 12 digits of precision – this thesis presents work which took place to improve this precision, through updated instrumentation and new methodologies.

The stability of the laser frequency was a key limitation in the precision of the previous 1S-2S measurements in antihydrogen. A major focus of this thesis is the development of a new frequency metrology suite to improve laser frequency stability, integrating a caesium fountain clock and a hydrogen maser. Preliminary measurements indicate that the upgraded metrology yields a significantly more stable laser system which can be used for extremely precise spectroscopy. This thesis also presents preliminary results of the 2023 experimental campaign to improve the precision of the 1S-2S transition in antihydrogen. This effort made use of the significantly improved laser frequency stability, and is also aided by other new techniques such as laser-cooling of antihydrogen and improved antihydrogen production. Although a full analysis of the experimental data is still ongoing, some preliminary approaches presented in this thesis suggest results that may substantially improve the precision of the 1S-2S antihydrogen transition frequency.

Declarations

This work has not previously been accepted in substance for any degree and is not being concurrently submitted in candidature for any degree.

Edward Thorpe-Woods, 8th of October 2024

This thesis is the result of my own investigations, except where otherwise stated. Other sources are acknowledged by footnotes giving explicit references. A bibliography is appended.

Edward Thorpe-Woods, 8th of October 2024

I hereby give consent for my thesis, if accepted, to be available for electronic sharing **after expiry of a bar on access approved by the Swansea University**

Edward Thorpe-Woods, 8th of October 2024

The University's ethical procedures have been followed and, where appropriate, that ethical approval has been granted.

Edward Thorpe-Woods, 8th of October 2024

Acknowledgements

Blimey. I can't quite believe I have written all of this.

Firstly, I wish to express my gratitude to my supervisor, Prof. Stefan Eriksson, for his guidance during my PhD. Thank you for all your constructive feedback – which made this thesis into the document it is, and for providing your extensive knowledge of physics throughout my PhD. I also wish to express my gratitude to Prof. Niels Madsen. You were probably the professor with whom I spent the most hours during my PhD, and your extensive experience with the ALPHA experiment was incredibly valuable. I am sure I will find it in my heart to forgive you for all those night shifts you put me on over the years. There are so many more senior staff of ALPHA who made this thesis possible – I would like to thank you all by name, but this thesis is already becoming to long.

I have also been extremely lucky to have worked alongside two extraordinarily talented postdoctoral researchers on much of the work presented in this thesis. I don't know how this thesis would have been possible without Dr. Janko Nauta's pragmatic ability to find the solution to almost any problem, and Dr. Alvaro Nunes' calm and thorough approach to ensuring everything functioned optimally. I honestly have learnt so much from you both, so thank you so much. I would also like to thank Dr. Steven Jones - I know you are a professor now but you are getting put in this paragraph anyway. You were the person who introduced me to the laser system, the concept of locking a cavity, and even Allan deviations. It was a pleasure working with you during the early stages of my PhD. There are so many other postdocs who were absolutely excellent, but I will also refrain from naming them all here - you know who you are, thank you for everything.

During my PhD journey, I was fortunate to form close friendships with fellow students. I know many of you are doctors now, but hey I am refusing to give you that title here. Andrew Christensen, we had such a laugh living together for almost all of our time at CERN - I can't really have pictured it without you. You are a great friend and an extraordinarily talented physicist. It has been a lot of fun trying to keep up with your scientific ability for four years. Danielle Hodgkinson, you have also been an excellent friend to me throughout my PhD. I miss grabbing a spontaneous beer somewhere in town, and having engaging discussions about physics (and the foibles of doing a PhD at ALPHA). Your ability to think deeply about any physics problem and make sure that you truly understand every detail properly is unparalleled, and something I really admire. Peter Granum - you are one of the most direct human beings I have ever met, but you're alright. It was so much fun working with you that first year, and I'm gonna miss having someone to drive me to skiing. Joos Schoonwater, you're continuing as

the PhD student in ALPHA's spectroscopy team since I left. The overlap we had was loads of fun, and they're lucky to have you. Maria Beatriz Gomes Goncalves, Jaspal Singh, Jack Jones, Partick Mullan, Asia Peska - its been so much fun sharing an office with all of you over the years, I'm gonna really miss the vibes. Also Beth Sweeney - it was a pleasure supervising your summer student project at CERN, you absolutely smashed it, I really hope you stick on and do a PhD one day.

My time in Geneva was also marked by making some great friends outside of work. Sam, James and Irish James, gonna really miss hanging out with you guys in Geneva (and sorry for being so busy with PhD work all the time). I am also lucky to have had such excellent friends with whom I lived. Living with Siara, Phillipp, Hannes, and Julia in the mouldy Saint-Genis house was such a delight. Rado, Elle, Clara, Anke, Naomi, Ime, Rami, and Giovanni, I'm really going to miss our time in Meyrin. I think the Meyrin shed is probably my favourite place I have ever lived (although the rat infestation somewhat detracted from this).

After completing my time at ALPHA, I have embarked upon a new adventure at ETH Zurich. However, there was considerable overlap with my postdoctoral work, alongside completing the writing of my PhD thesis. **I strongly advise against this approach for anyone.** However, again, I have been lucky to be surrounded by wonderful people. Irene, I'm happy that there was another person going through the struggles of the the final stages of a PhD - It was good to have someone who understood the pains. Marcus and Evans, it is truly daunting for me to help supervise such talented new PhD students. I'm looking forward to working with you over the coming two years, and I'm confident that you will both go far. And to Prof. Paolo Crivelli, thank you for taking me on in this next step - I'm already having so much fun working within the exotic atoms group.

Finally I'd like to thank some lovely people who weren't there with me in Geneva. Paige, you were the first person I told when I got offered this position, and you were really instrumental and encouraging me to take that daunting step of moving to CERN. Mum and Dad, you were the last people I told when I got offered this position – knowing full well that you would insist that I accept it. Well I did, and you were right of course, as always. Lastly, to all of my friends back in the UK, I have missed of you more than you can imagine whilst I've been away. And specifically to Liv, you have always been there for me regarding the non-Physics aspects of my life during these last four years.

It has been said that science is a noble pursuit. Maybe there is some truth in that, but my god, it can also be a tiring, infuriating, tedious, hilarious, exhilarating and humbling pursuit too. It would be great to be all nonchalant about this, but this PhD has truly been so much of my life over the past four years. So thank goodness that it is something that I didn't have to do on my own. Every single one of you, whether you were mentioned here or not, was incredible.

And you know what? So was I.

Contents

List of Figures

List of Tables

Acronyms

- **AD :** Antiproton Decelerator
- **AEGIS:** Antihydrogen Experiment: Gravity, Interferometry, Spectroscopy
- **ALPHA:** Antihydrogen Laser PHysics Apparatus
- **AOM:** Acousto-Optic Modulator
- **ASACUSA:** Atomic Spectroscopy And Collisions Using Slow Antiprotons
- **ATHENA:** AnTiHydrogEN Apparatus
- **ATRAP:** Antihydrogen trap
- **BASE:** Baryon-Antibaryon Symmetry Experiment
- **BBR:** Black Body Radiation
- **BDU:** Beat Note detection Unit
- **BEC:** Bose Einstein Condensate
- **BIPM:** Bureau International des Poids et Mesures
- **CERN:** European Organization for Nuclear Research (Conseil Européen pour la Recherche Nucléaire)
- **CGGTTS:** Common GNSS Generic Time Transfer Standard
- **CODATA:** Committee on Data of the International Science Council
- **CODE:** Center for Orbital Determination Europe
- **CPT:** Charge-Parity-Time (Symmetry)
- **CV:** Common View
- **DBR:** Distributed Bragg Reflector
- **DFS:** Distributed File System
- **DL:** Diode Laser

- **ECDL:** Extended Cavity Diode Laser
- **ECR:** Electron Cyclotron Resonance
- **EGM:** Earth Gravitational Model
- **ELENA:** Extra Low ENergy Antiprotons
- **EOM:** Electro-Optic Modulator
- **EVC:** EVaporative Cooling
- **FFT:** Fast Fourier Transform
- **FHG:** Fourth Harmonic Generation
- **FRD:** Fast Ramp Down (of magnetic trap (and not even that fast))
- **FSK:** Frequency Shift Key
- **FTP:** File Transfer Protocol
- **FWHM:** Full Width Half Maximum
- **GBAR:** Gravitational Behaviour of Antimatter at Rest
- **GCADE:** Gaussian Convolved Asymmetric Double Exponential
- **GIS:** Geographic Information System
- **GNSS:** Global Navigation Satellite System
- **GPS:** Global Positioning System
- **HD:** High Density
- **HFS:** Hyper Fine Structure
- **HV(A/B):** High Voltage electrode (A/B)
- **IGS:** International GNSS Service
- **ISOLDE:** Isotope mass Separator On-Line facility
- **ITRF:** International Terrestrial Reference Frame
- **LIBGA:** Laser Induced Background Gas Annihilations
- **LD:** Low Density
- **MASER:** Microwave Amplification by Stimulation Emission of Radiation.

- **MCP:** Multi Channel Plate
- **MJD:** Modified Julian Date
- **MOT:** Magneto-Optical Trap
- **MPQ:** Max Planck Institute of Quantum Optics
- **MVA:** Multi Variate Analysis
- **NPL:** National Physcial Laboratory
- **OM:** Optical Molasses
- **OP:** Optical Pumping
- **OXCO:** Oven Control Crystal Oscillator
- **PDH:** Pound-Drever-Hall (Technique)
- **PID:** Proportional–Integral–Derivative controller
- **PPP:** Precise Point Positioning
- **PLL:** Phase Locked Loop
- **PPS:** Pulse Per Second
- **PSD:** Position Sensitive Detector
- **PUMA:** antiProton Unstable Matter Annihilation
- **PXI:** PCI eXtensions for Instrumentation
- **QED:** Quantum Electro-Dynamics
- **QFT:** Quantum Field Theory
- **RF:** Radio Frequency
- **RINEX:** Receiver Independent Exchange Format
- **SDR:** Strong Drive Regime
- **SNR:** Signal-to-Noise Ratio
- **SHG:** Second Harmonic Generation
- **STEP:** Symmetry Tests in Experiments with Portable antiprotons
- **SVD:** Silicon Vertex Detector

- **SYRTE:** Sytèmes de Référence Temps Espace
- **TAI:** International Atomic Time (temps atomique international)
- **TEM:** Transverse electromagnetic modes
- **TOF:** Time of Flight
- **TPC:** Time Projection Chamber
- **ULE:** Ultra Low Expansion glass reference cavity
- **UTC:** Coordinated Universal Time
- **WEP:** Weak Equivalence Principal
- **WSL:** Windows Subsystem For Linux

It's still magic even if you know how it's done

– Terry Pratchett

CHAPTER 1

Introduction

> *Antimatter...terrible and horrible terminology*
>
> — **Denis Pelletier**

Antimatter, and more specifically antiparticles, have been a key feature of modern physics since Dirac formulated his theory of relativistic quantum mechanics and discovered the existence of negative energy solutions [1, 2]. They were later proven to be more than just a theoretical curiosity when Carl D. Anderson discovered unexpected particle tracks in his cloud chamber [3], which were produced by a particle with the electron mass but with the opposite (positive) charge. Dirac would go on to consider the existence of negatively charged antiprotons [2, 4], which were discovered experimentally years later by the Bevatron accelerator at Lawrence Berkeley National Laboratory in 1955 [5], along with the antineutron a year later [6]. Since then many other subatomic antiparticles have been discovered experimentally, and it is now known that every particle has an associated antiparticle, with an equal mass and spin, but opposite charge. Antiparticles can form bound states just like regular particles; these include matter-antimatter bound states such as positronium, hadronic bound states such as the antiproton, or even atoms made purely out of antimatter. Interest in creating the simplest pure antimatter atom, antihydrogen, emerged following the discovery of the positron and antiproton. The first confirmed detection of high-energy antihydrogen was achieved by the PS210 experiment in 1995 at CERN's Low Energy Anti-Proton Ring (LEAR) facility [7], closely followed by a Fermilab Experiment, E862 [8]. In 2002, the ATHENA and ATRAP experiments, based at CERN's Antiproton Decelerator (AD) facility, LEAR's successor, successfully produced low-energy antihydrogen for the first time [9, 10]. Today there are many experimental collaborations based in the AD facility which are dedicated to the study of antimatter and antihydrogen, which are outlined in section 1.2.

1.1 | Motivations for studying Antimatter

When antimatter was discovered in the early 20th century, it was believed that every physical process would remain unchanged under three separate transformations: C (charge conjugation, which switches all particles with their corresponding antiparticles), P (parity transformation, which inverts the sign of all spatial coordinates), and T (time reversal, which

inverts the sign of the time coordinate, effectively reversing time). While these symmetries had been tested in electromagnetic and the strong interactions, theorists pointed out in 1956 that they had not yet been verified in weak interactions [11]. In the same year, studies of beta decay in polarised cobalt-60 demonstrated that weak interactions violate both the P and C symmetry [12]. However, the decays did not violate a combined CP symmetry, and subsequently CP symmetry was instead considered to be the fundamental conserved symmetry in nature. Yet, soon after this unexpected experimental finding revealed that CP symmetry is also violated, with neutral kaons transforming to their antiparticles with a different probability than the reverse process [13].

The discovery of CP symmetry violations offered a possible route to resolving one of the outstanding problems in physics, that of baryon asymmetry. Following the big bang, once the universe had cooled enough such that it no longer had enough energy to produce particle-antiparticle pairs via pair production, those existing pairs would have annihilated to produce photons. To produce the universe we witness today – almost entirely composed of matter and devoid of any antimatter – there must have been some process that produced a dominance of matter over antimatter in the early universe. The baryon-to-photon ratio observed in the universe suggests that this matter dominance in the early universe was of the order of one part in ten billion [14]. The discovery of CP symmetry violations inspired Andrei Sakharov to propose a set of conditions that must be satisfied to produce matter and antimatter at different rates in the early universe [15], providing a potential mechanism to produce the predominance of matter. The three 'Sakharov Conditions' are:

- Baryon (B) number violation
- C and CP symmetry violation
- An expanding universe leading to processes out of thermal equilibrium.

At energies corresponding to the early universe, there are theoretical processes within the Standard Model of particle physics which satisfy each of the Sakharov conditions [16]. However, the amount of CP violation allowed within the standard model is insufficient to generate the matter-antimatter asymmetry observed within the present universe [16], and the baryon asymmetry remains an unresolved problem in physics. In the hopes to explain the observed matter-antimatter asymmetry, physics requires mechanisms beyond the standard model.

Although CP violations have been observed, to the best of our knowledge all physical phenomena are invariant under a combined CPT transformation. CPT symmetry is considered an exact and fundamental symmetry of nature, an essential component of the Standard Model, and currently no physical processes violating CPT have been observed. However, lessons from history suggest that we should avoid placing complete trust in any fundamental symmetry in nature, and it is essential scientific work to probe for CPT violating phenomena. CPT symmetry requires that antiparticles have the same mass, lifetime, spin, and a charge of the same magnitude but opposite sign. Additionally, pure antimatter bound states are

required to have the same energy eigenvalues as their pure matter counterparts [17]. If CPT symmetry holds, equivalent atoms and anti-atoms should exhibit the same energy spectrum. The spectrum of hydrogen, the simplest atom, has been studied in immense detail, and comparing these with equivalent spectra measured in antihydrogen constitutes a direct test of CPT symmetry.

1.2 | Antimatter Experiments

The production and study of antiprotons and antihydrogen is the goal of many of the experiments at the AD/ELENA facility at CERN, which is displayed schematically in figure 1.1.

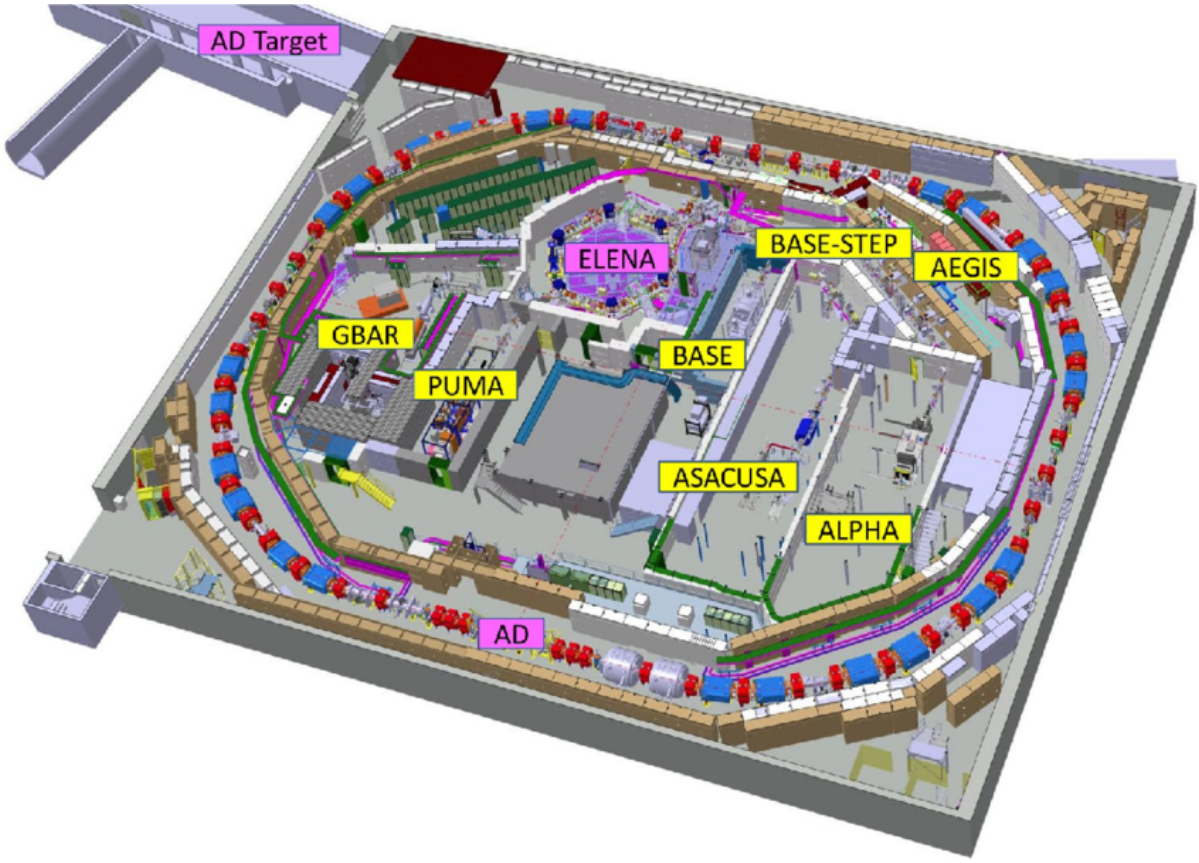

Fig. 1.1. A diagram of the AD/ELENA facility at the time of writing. The AD target, AD, and ELENA are labeled in purple, the individual AD experiments are labeled in yellow. At the time of writing AEGIS, ALPHA, ASACUSA, BASE and GBAR are established experiments, whereas BASE-STEP and PUMA are still in the commissioning phase. Figure taken from [18].

The Antiproton Decelerator (AD) is a storage ring particle accelerator that provides low-energy antiprotons for experiments based at the facility. Antiprotons are produced when a proton beam with an energy of 26 GeV from the CERN Proton Synchrotron (PS) strikes an iridium target. Antiprotons are formed through pair production and are magentically guided into the AD ring [19]. Within the AD antiprotons are decellerated in radiofrequency (RF) cavities and undergo many cycles of electron cooling and stochastic cooling, reducing their energy to 5.3 MeV. The antiproton bunch is then directed to a second smaller storage ring,

called ELENA (Extra Low ENergy Antiproton ring). The ELENA ring cools the antiprotons bunch even further, through techniques similar to the AD, resulting in 100 keV antiprotons [20].

The antiproton bunches from ELENA, having been significantly cooled, are then delivered to various experiments at the AD/ELENA facility. The AD/ELENA facility houses five established experiments: AEGIS, ALPHA, ASACUSA, BASE, and GBAR, along with two experiments that are currently being commissioned: BASE-STEP and PUMA. The BASE experiment (Baryon Antibaryon Symmetry Experiment), focuses on precision measurements of fundamental properties of the proton and antiproton; primarily their magnetic moment and the charge-to-mass ratio [21]. The BASE-STEP experiment (STEP: Symmetry Tests in Experiments with Portable antiprotons) aims to create a method for transporting trapped antiprotons, allowing BASE to perform its measurements in a stable magnetic environment away from the AD/ELENA facility [22]. Similarly, the PUMA experiment (antiProton Unstable Matter Annihilation) aims to transport antiprotons from the AD/ELENA facility to the ISOLDE facility at CERN for studies of exotic nuclear-physics phenomena [23]. ASACUSA (Atomic Spectroscopy and Collisions Using Slow Antiprotons) primarily engages in two spectroscopy studies: microwave spectroscopy of the hyperfine structure of antihydrogen [24], and laser spectroscopy of antiprotonic helium [24]. The AEGIS experiment (Antimatter Experiment: gravity, Interferometry, Spectroscopy) produces a pulsed beam of antihydrogen atoms, with the primary aim being to use this beam to make a direct measurement of the gravitational acceleration of antihydrogen atoms [25]. The GBAR experiment (Gravitational Behaviour of Antimatter at Rest) also primarily aims to measure the gravitational acceleration of antihydrogen; however, it aims to do this by first forming antihydrogen ions, which can be cooled to microkelvin temperatures using laser-cooling techniques [25].

Finally, there is ALPHA (Antihydrogen Laser Physics Apparatus), which studies magnetically trapped antihydrogen, and is the apparatus used for the key results of this thesis. The first successful magnetic trapping of antihydrogen in ALPHA was achieved in 2010 [26], closely followed by the ATRAP experiment (which now no longer operates) [27], providing the first opportunity to study antiatoms for extended periods of time [28]. With trapped antihydrogen, ALPHA has measured multiple antihydrogen spectra [29–31], demonstrated antihydrogen laser cooling [32], and observed the effects of the gravitational field of the Earth on the motion of antihydrogen [33].

1.3 | Outline of Thesis

This thesis focuses on a specific experiment conducted in ALPHA: 1S-2S spectroscopy. The narrow 1S-2S two-photon transition serves as the gold standard for precision spectroscopy of hydrogen, where its transition frequency has been measured with a fractional frequency uncertainty of 4.2×10^{-15} [34]. ALPHA has made measurements of the 1S-2S transition frequency in antihydrogen, first at the fractional frequency precision of 2×10^{-10} [29], and

then at an even better precision of 2×10^{-12} [35]. So far, the 1S-2S transition frequency measured in antihydrogen agrees with hydrogen, which is consistent with the CPT symmetry with relative precision 2×10^{-12}, but this uncertainty is dominated by the measurements of antihydrogen. This thesis presents the work conducted towards improving the precision of 1S-2S transition measurements of antihydrogen in ALPHA, through improved instrumentation and new methodologies.

Chapter 2 introduces the ALPHA experiment. This chapter provides an overview of how ALPHA functions, examines how antihydrogen is formed, and summarises its past experimental measurements.

Chapter 3 presents the theoretical aspects of the 1S-2S transition of antihydrogen within ALPHA. The expressions for determining the energy levels of and antihydrogen are discussed, along with the theoretical lineshapes and broadening mechanisms applicable to antihydrogen spectroscopy in ALPHA. Simulations of 1S-2S spectroscopy within ALPHA are also briefly discussed.

Chapter 4 the integration of an active hydrogen maser into the frequency metrology setup at ALPHA. This chapter summarises the maser's operation and the time-frequency transfer methods used to measure and correct its frequency error.

Chapter 5 presents the commissioning of a caesium fountain clock for frequency metrology at ALPHA. It discusses the methods used within the fountain, its hardware components, operational cycle, and evaluates its performance as a frequency reference.

Chapter 6 covers the 1S-2S laser system, reviewing its components and functionality. Much of this chapter is spent evaluating the frequency stability of the laser system following the metrology upgrades discussed in the previous two chapters.

Chapter 7 presents an overview of the experimental campaigns conducted in 2022 and 2023 to measure the 1S-2S spectrum. It outlines the conditions under which the experiments were conducted and presents the preliminary raw data that was measured.

Chapter 8 presents a preliminary analysis of the 2023 experimental data. A full, more comprehensive analysis of data is still ongoing at the time of writing. The chapter contains examples of techniques which can be used to determine the 1S-2S transition frequency from the experimental data, and makes some preliminary estimates of statistical and systematic uncertainties.

Finally, Chapter 9, provides a conclusion to the thesis, and presents the outlook for 1S-2S spectroscopy at ALPHA.

1.4 | Author Contributions

During my PhD studies, I have been an active member of the ALPHA collaboration and been based full time at the experiment at CERN. ALPHA has achieved numerous experimental successes during my time there, and whilst these achievements cannot be attributed to a single individual, I have contributed in some way to all of them. However, the focus of this thesis is

on improving the precision of 1S-2S antihydrogen spectroscopy, which is what I spent most of my time working on.

A significant part of my PhD research was focused on developing the new ALPHA metrology lab, which involved commissioning and integrating the active hydrogen maser and the caesium fountain clock, detailed in chapters 4 and 5. This was a group effort which took place under the guidance of Prof. Stefan Eriksson, which involved myself, Dr. Janko Nauta, Dr. Alvaro Nunes de Oliveira, and later in my PhD, Joos Schoonwater. The GNSS time-frequency transfer methods discussed in chapter 4 are well established methods; however, the scripts which implement them were developed by me (with the exception of the PPP FORTRAN code, which was developed at MIT). The evaluation of the caesium fountain, discussed in chapter 5, was also conducted by the group mentioned above, alongside the NPL team involved in the construction of the instrument, including Dr. Rich Hendricks, Dr. Josh Whale, Dr. Krzysztof Szymaniec and Andrew Wilson. Much of the analysis presented in chapter 5 is being collated into a manuscript publication, which was drafted by myself and Dr. Janko Nauta. The analysis which will be presented in that future publication may contain differences from what is presented here, as it will benefit from additional data - however the methods are unlikely to change significantly from those presented here. The automatic steering technique, presented at the end of chapter 5, was work undertaken by CERN summer student Beth Sweeny, which she conducted under my supervision.

A large part of my PhD involved also working with the 1S-2S laser system, integrating it with recent metrology upgrades. It's important to note that much of the 1S-2S laser system described in chapter 6 was originally developed by various ALPHA collaborators prior to my involvement, and many elements have remained unchanged since then. Any additional upgrades and preparations for the spectroscopy campaigns in 2022 and 2023 were carried out by me and the team mentioned above, along with Levi Oliveira de Araujo Azevedo. Although the laser and metrology work was crucial for the results presented in chapter 7, these achievements are the collective effort of nearly all ALPHA collaborators involved in those campaigns. A full analysis of these results is still ongoing within an ALPHA working group, of which I am a key member. The preliminary analysis which is presented in chapter 8, is the product of discussions within this working group. However, the execution of the analysis in Chapter 8 was work carried out by myself, unless otherwise stated. The physics-driven fits mentioned in chapter 3 and applied in chapter 8 are inspired by previous work by Prof. Francis Robicheaux and R. Andrew Gustafson [36], but the extension to account for AC Stark shift effects is my own work.

This thesis has been entirely written by myself, in my own words. However, I have edited in response to feedback and suggestions from others. Throughout the writing of this thesis, I have also made use of spell-checking widgets, Grammarly and Writefull, to look for errors in spelling, punctuation, grammar, and occasionally taking suggestions on phrasing.

CHAPTER 2

ALPHA

> *Experimental Physics is really ninety percent plumbing*
>
> — **J. Robert Oppenheimer**
> American Prometheus

The **A**ntihydrogen **L**aser **Ph**ysics **A**pparatus, or **ALPHA**, based within the AD/ELENA facility at CERN is an experimental setup for studying trapped antihydrogen. The first successful trapping of antihydrogen was achieved in 2010 by ALPHA [26], closely followed by ATRAP and ASACUSA experiments [27, 37], which provided the first opportunity to study anti-atoms for extended periods of time [28]. The ALPHA experimental setup, which has grown significantly since antihydrogen was first trapped, is composed of four distinct sections connected by one beamline; a schematic of the current ALPHA setup with the experimental sections labeled is displayed in figure 2.1 on the following page. The terminology 'upstream' and 'downstream' has been adopted throughout this thesis to refer to the direction of the antiproton beam entering the apparatus. The farthest upstream section is the catching trap (CT), which captures and cools antiprotons from AD in a Penning-Malmberg trap [38]. The farthest downstream section is the positron accumulator, where positrons from a source of ^{22}Na are accumulated and cooled. The two remaining sections are for conducting antihydrogen experiments: the ALPHA-2 experiment and the ALPHA-g experiment. Here, positrons and antiprotons are mixed together to form antihydrogen, which can be trapped in a magnetic minimum Ioffe-Pritchard trap for extended study. The ALPHA-2 experiment includes instrumentation for antihydrogen spectroscopy, while the ALPHA-g experiment is designed to study the effects of gravity on antihydrogen.

This chapter provides a comprehensive overview of the functioning of ALPHA, covering the methods used and hardware components which implement them. We begin by summarising the techniques used for trapping and controlling charged particle plasmas within the various sections of ALPHA and discuss the diagnostics used to measure them. Following this, we examine the experimental cycle developed for the formation, trapping and cooling of antihydrogen. We shall then cover the various hardware used for antihydrogen detection. Finally, we will conclude the chapter by reviewing some of the key experiments conducted on antihydrogen in ALPHA.

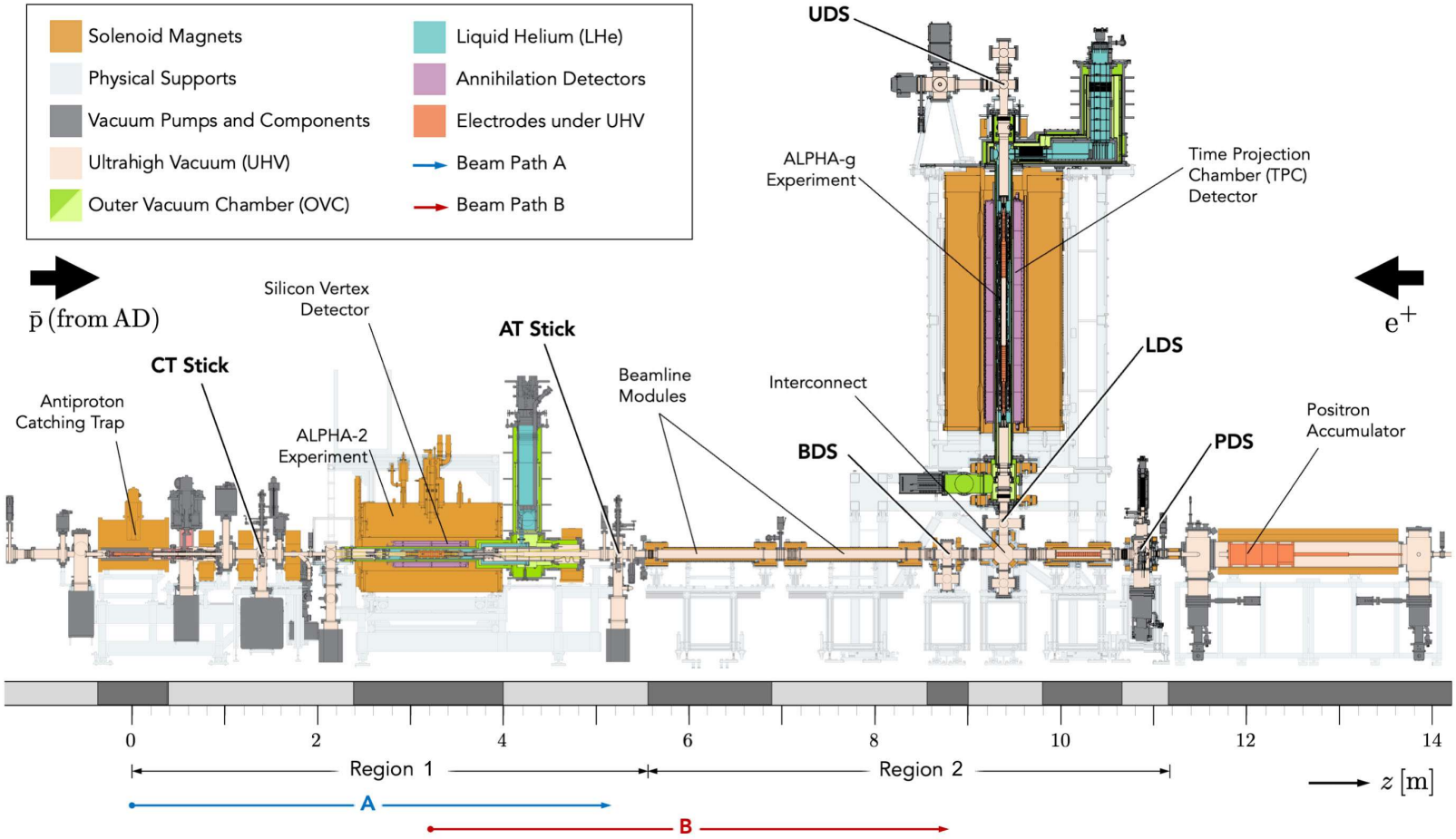

Fig. 2.1. Schematic displaying a cross sectional view of ALPHA. Many of the components which are referenced within this chapter are labeled.

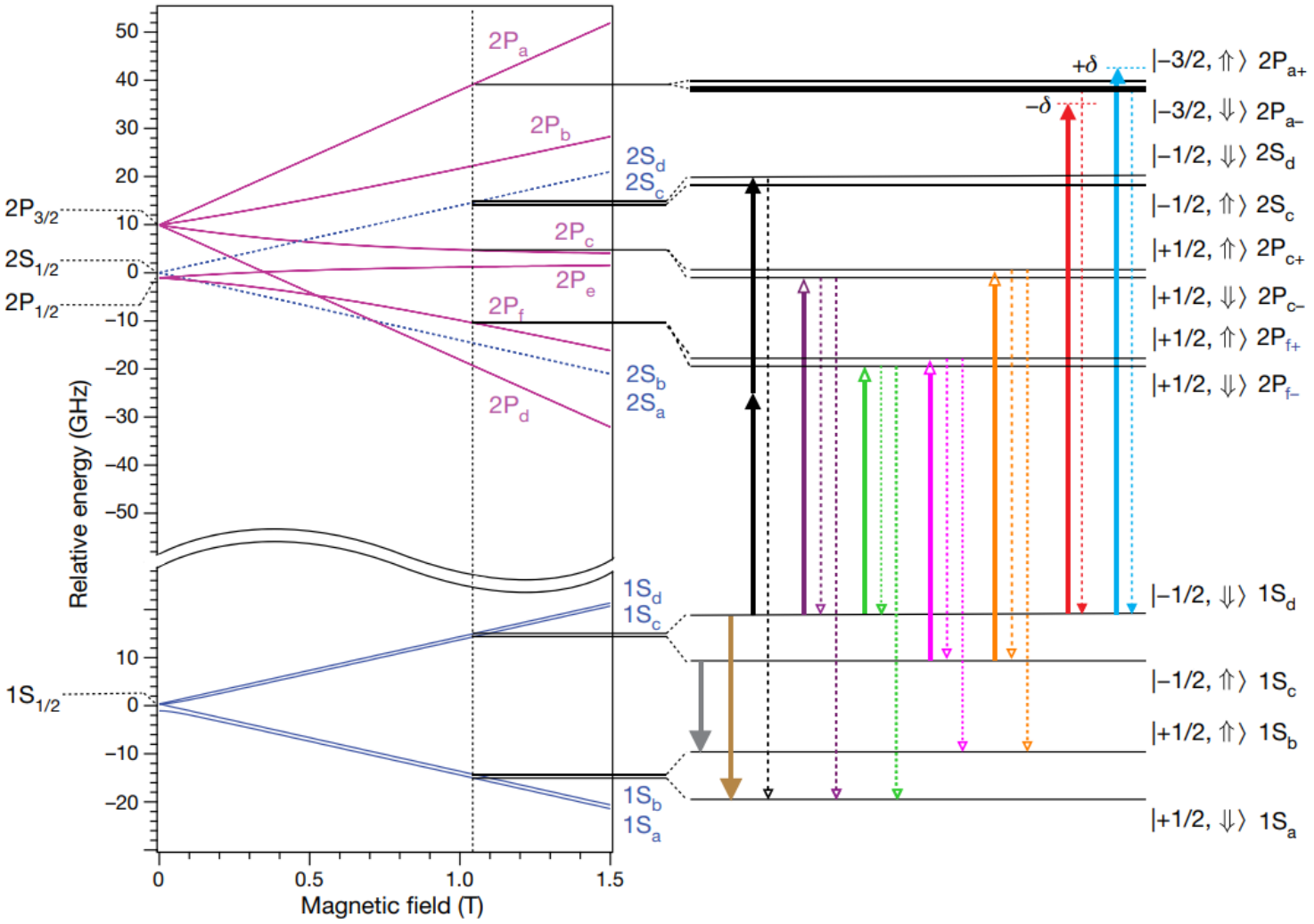

Fig. 2.2. Energy level diagram (up to $n = 2$) illustrating the transitions measured in the ALPHA experiment. The ket notation for each state displays the projection of the positron's total angular momentum, and the projection of the antiprotons spin (spin up ⇑, or down ⇓). Transitions measured in ALPHA have been displayed by solid arrows and the probable decays from those excited states are indicated as dotted arrows. Each state has been indicated with spectroscopic notation, with fine and hyperfine structure levels identified by a subscript letter and in the case of P states a further $+/-$ subscript. Figure taken from [39].

2.1 | Charged particles

The storage and manipulation of charged particles is integral to the process of forming trappable antihydrogen. In ALPHA four types of charge particles are used; positrons (e^+) and antiprotons ($\bar{p}$)–the constituent parts of antihydrogen, alongside electrons (e^-) and Beryllium ions (Be^+)–used to sympathetically cool the $\bar{p}$ and e^+ respectively. Penning-Malmberg traps [38][40] are used for the confinement and manipulation of charged particles within each of the four sections of ALPHA, each section containing a variant best designed for its specific use case.

2.1.1 Penning traps

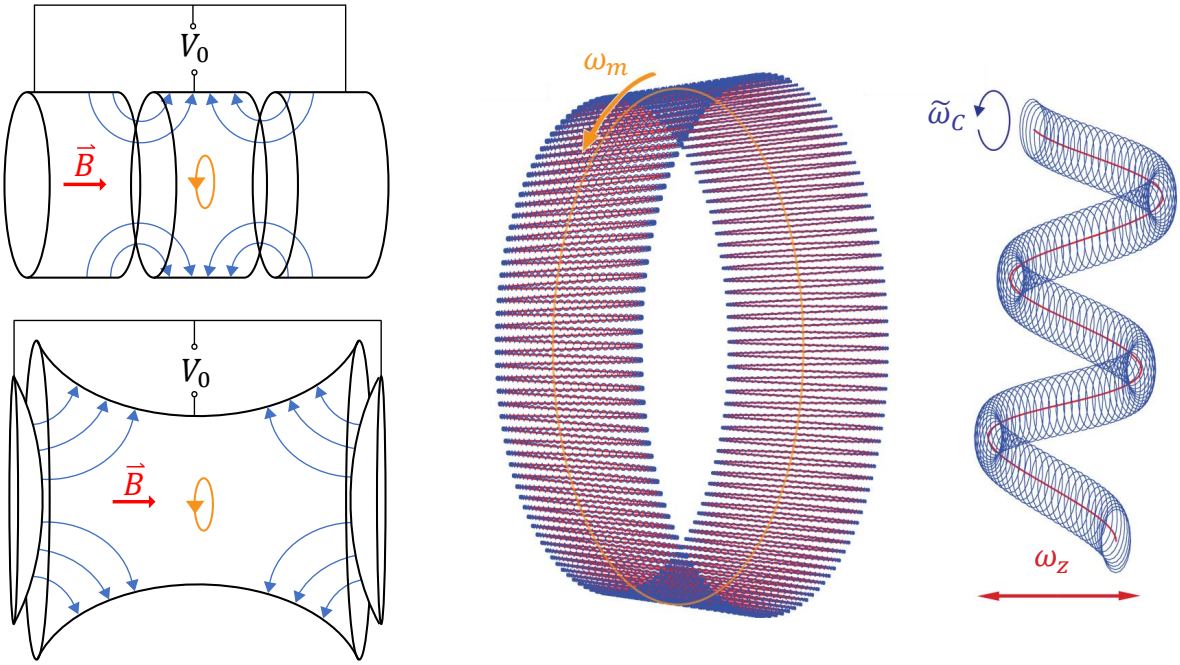

Fig. 2.3. The diagrams on the left display Penning trap electrodes in two configurations: the bottom left is a classic Penning trap formed from a hyperbolic electrode and two endcaps. The top left displays a Penning-Malmberg trap, the type used within ALPHA, formed of cylindrical electrodes. In both diagrams the central electrode is biased by V_0 relative to the end electrodes. For both diagrams electric field lines are displayed with blue arrows, the direction of the uniform magnetic field is displayed in red, and the magnetron motion in amber. The diagrams in the middle and on the right, modified from [41] provides visualisation of the motion a single trapped particle. The axial, magnetron, and cyclotron motions are displayed in red, amber and blue respectively.

Earnshaw's theorem states that it is impossible to achieve three dimensional confinement of charged particles by static electric fields alone. However, confinement is possible through the use of dynamic electric fields in Paul traps [42], or through the combination of static electric and magnetic fields in Penning traps [38]–the technique used within ALPHA. Penning traps confine charged particles axially using electric fields, and radially using a magnetic field. In the optimal

case, the potential due to the electric field is quadratic, $U(x,y,z) = \frac{qV_0}{4m}\left(2z^2 - x^2 - y^2\right)$, where z is the direction of the uniform magnetic field, q and m are the charge and mass of the trapped particle respectively, and V_0 is the maximum potential difference across the electrodes. Calculating the Lorentz force on a charged particle in this potential, and with a uniform magnetic field $\vec{B}$ pointing along z, it is possible to derive the equations of motion for the particle [43][44]

$$\begin{aligned} \ddot{x} + \omega_c \dot{y} - \left(\omega_z^2/2\right) x = 0, \\ \ddot{y} - \omega_c \dot{x} - \left(\omega_z^2/2\right) y = 0, \\ \ddot{z} + \omega_z^2 z = 0, \end{aligned} \tag{2.1}$$

where $\omega_c = eB/m$ and $\omega_z^2 = \frac{qV_0}{m}$. The decoupled third equation describes a sinusoidal oscillation of the particle in z. The first two equations can be solved by subtituting in the complex variable $u = x + iy$, resulting in

$$w(t) = Ae^{-i\tilde{\omega}_C t} + Be^{-i\omega_m t}, \tag{2.2}$$

where $\tilde{\omega}_c = \omega_c - \omega_m$ and $\omega_m = \frac{1}{2}\left(\omega_c - \sqrt{\omega_c^2 - 2\omega_z^2}\right)$. The motion of trapped charged particles within a Penning trap can therefore be described through the combination of three frequencies: the axial frequency ω_z of the sinusoidal axial frequency; the modified cyclotron frequency $\tilde{\omega}_C$; and magnetron frequency ω_m, which describes the slow cyclic motion perpendicular to z. The combination of these draw out an oscillating epitrochoid, and is displayed in the right hand side of figure 2.3. These equations of motions are not applicable to a trapped plasma, since they neglect the interactions between charged particles; instead the plasma fills the potential, and its motion is better viewed as a rigid body of constant density which rotates around the trap axis [45].

A classic Penning trap, displayed in the bottom left of figure 2.3, is formed from a hyperbolic ring electrode and two hyperbolic endcaps. When machined correctly, this Penning trap configuration can produce a nearly perfect quadratic potential over an extended volume. However, the classic setup provides only limited access for particle insertion and manipulation– as a result the traps used within ALPHA are cylindrical Penning-Malmberg traps [40], displayed in the top left of the figure 2.3. This trap configuration can be made out of multiple stacked electrodes, known as nested Penning traps, which can translate plasmas around the trap, divide a plasma into multiple plasmas, and confine two plasmas of opposite charges simultaneously– essential for antihydrogen production. The lack of endcap on the Penning-Malmberg trap also make laser interrogation and plasma diagnostics easier to implement. The disadvantage is that Penning-Malmberg traps do not naturally produce harmonic electric potentials. However, for a given cylindrical trap, electrode voltage combinations can be found which produce a potential that can be approximated as quadratic within a limited volume–discussed within section 3.11 of [41].

2.1.2 Rotating wall techniques

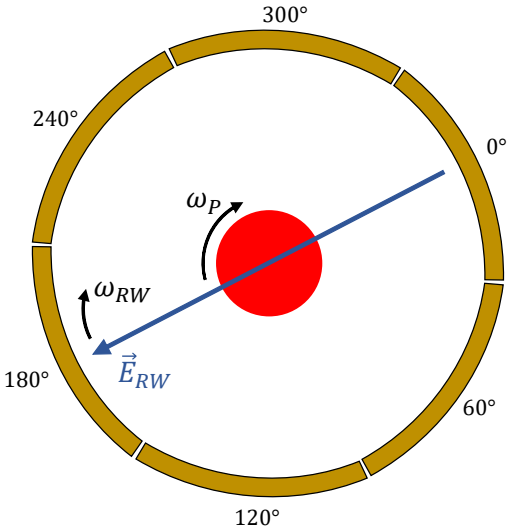

Fig. 2.4. Cross sectional view of a rotating wall 6-part segmented electrode. The respective phase difference for the time varying potential is labeled for each segment. The red indicates the trapped plasma, which rotates with angular frequency ω_P. The blue arrow indicated the electric field seen by the plasma due to the rotating wall, $\vec{E}_{RW}$, which rotates with angular frequency ω_{RW}.

The nested Penning trap configuration provides a means for controlling the distribution of a trapped plasma along the trap axis. To control the radial distribution, density and rotating frequency of a trapped plasma, rotating wall (RW) techniques can be used. The RW technique exposes the plasma to a rotating electric field $\vec{E}_{RW}$; it is implemented by a segmented electrode, in ALPHA a six part segmented electrode is used, as displayed in figure 2.4. The field $\vec{E}_{RW}$ is produced by introducing the time varying potential with a 60° phase difference between adjacent electrode segments: $V_{RW}(n,t) = A_{RW}\cos(n \cdot 60° - \omega_{RW} t)$, where n is the electrode segment, ω_{RW} is the angular frequency of $\vec{E}_{RW}$, and A_{RW} is the amplitude of the applied voltage. Given this setup, charged particles within the trap experience an electric field, $\vec{E}_{RW}$, which rotates at angular frequency ω_{RW}. When the electric field rotates at an angular frequency greater than the natural rotation of the plasma, $\omega_{RW} > \omega_p$, it spins up the plasma which compresses it radially. If the rotation frequency of the electric field is less than the plasma, it spins down the plasma which leads to radial expansion. The process of expansion and compression can be understood by balancing the torques of the plasma, discussed in [46].

The RW electrodes within ALPHA are typically operated in the strong-drive regime (SDR) [47], where the rotating wall frequency is near the natural rotation frequency of the plasma. In this regime the the plasma density increases or decreases (compressing or expanding the plasma) until the plasma rotation frequency is the same as that of the RW and the plasma density is linearly proportional to the RW frequency. The ALPHA collaboration developed a novel variation of the SDR technique called strong-drive regime evaporative cooling (SDR-EVC) [48]. This technique exposes a plasma to rotating walls in the SDR, whilst also evaporatively

cooling the plasma by slowly reducing the depth of the confining potential. The combined result of SDR-EVC is that by tuning the final well depth, one is able to reproducibly control the final number of charged particles in the plasma–regardless of the number of initial particles. The SDR-EVC method allows the plasma to be controlled and prepared reproducibly, leading to greater consistency in antihydrogen production.

A downside of RW techniques is that their application tends to increase the temperature of the plasma–an issue for antihydrogen production, as trapping efficiency decreases with constituent plasma temperatures. Positron plasmas have a high cyclotron frequency, ω_C, due to their low mass, which cools the plasma quickly ($\approx 4\,\mathrm{s}$) through the emission of cyclotron radiation. However, the relatively high mass of $\bar{p}$ (1.007 Au) means that the plasma cannot effectively cyclotron cool. To circumvent this the $\bar{p}$ plasma is mixed with cyclotron cooled electron (5.485×10^{-4} Au) plasma, the thermalisation of the two plasmas cools the antiprotons in a process known as sympathetic cooling.

2.1.3 The catching trap

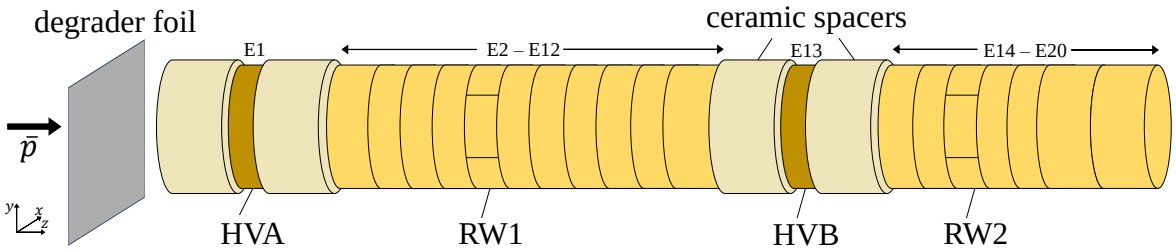

Fig. 2.5. Schematic of the catching trap (CT) degrader foil and electrode stack, with the direction of the incoming antiprotons displayed by the black arrow. High voltage electrodes, rotating wall electrodes, and ceramic spacers are labeled.

The catching trap is the furthest upstream section of the ALPHA experimental setup, which is visible on the far left of the schematic diagram of ALPHA in figure 2.1. It is responsible for the capture of high-energy antiprotons from the AD, and cooling them to temperatures that allow them to be delivered to the experimental sections of ALPHA for antihydrogen formation. The catching trap consists of twenty electrodes (E1-E20), displayed in figure 2.5, two of which are high voltage electrodes (HVA and HVB), and a further two of which are segmented RW wall electrodes (RW1 and RW2). The high voltage electrodes are electrically isolated from the rest of the stack using ceramic spacers, whereas the rest of the electrodes are electrically isolated from each other with ruby balls. A 3 T uniform magnetic field permeates through the trap, parallel to the trap axis, which is supplied by an external solenoid known as the Swansea magnet. The upstream inlet of the trap is covered with an aluminium degrader foil, which also separates the ALPHA beamline vacuum from the AD vacuum, and is displayed in figure 2.5.

Incoming 100 keV antiprotons are supplied every two minutes from the AD, and in the standard antihydrogen production sequence ALPHA catches every second bunch of antiprotons.

As the antiprotons pass through the degrader foil they slow down and the beam emittance and energy spread increases. The majority of the antiprotons pass through the foil and reach the Penning-Malmberg trap. A more detailed discussion into the functionality of the degrader foil can be found in [41]. An electron plasma is loaded into the catching trap before the arrival of the beam via an electron gun situated on the catching trap stick (sticks are discussed in 2.1.6); this electron plasma is made consistent shot-to-shot using SDR-EVC. HVB is energised to 5 kV in preparation of the oncoming beam. Upon the arrival of the antiproton beam a fast amplifier triggers the energising of HVA to 5 kV, closing the trap. Only the lowest energy portion of the oncoming beam can be confined by the high voltage electrodes; once trapped, the antiprotons sympathetically cool with the electron plasma. After some cooling time, the high voltage electrodes are de-energised; most of the antiproton plasma will have cooled enough to be confined by the standard electrodes, but some residual hot particles escape. The mixed plasma is then transferred to RW1, where it can be compressed through RW methods whilst electrons sympathetically cool the antiproton plasma during the compression. The electrons must be removed from the mixed plasma before transferring it to the experimental sections; to achieve this one side of the potential barrier is briefly lowered, allowing some of the lighter and faster moving electrons to escape–colloquially known as an e-kick. The typical antihydrogen production sequence contains two stages of RW compression, interspersed with an e-kick, followed by two successive e-kicks. The sequence produces a cooled and compressed pure antiproton plasma which can be transferred to the ALPHA experimental sections.

2.1.4 The positron accumulator

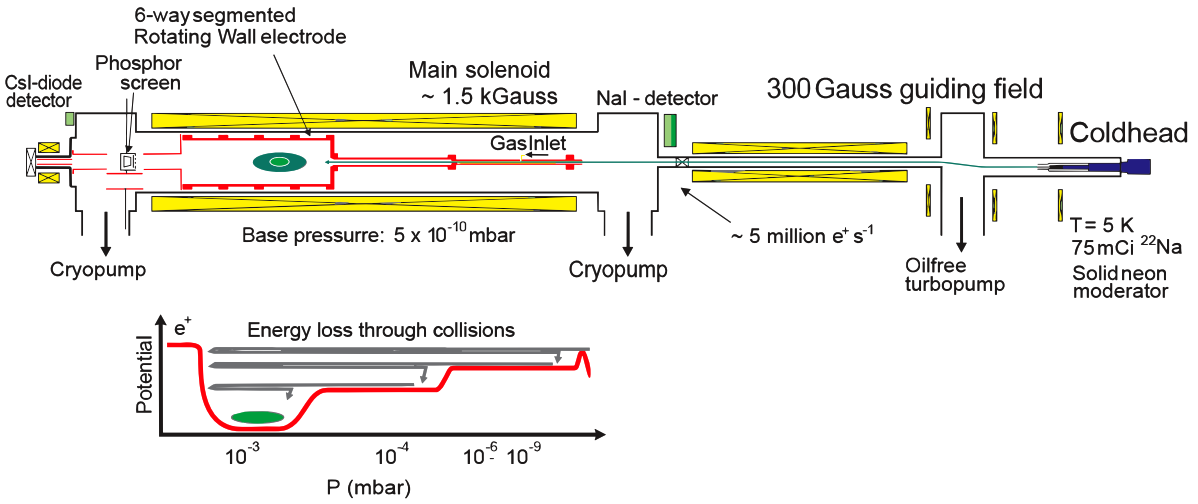

Fig. 2.6. Top: Schematic of the positron accumulator, taken from [49] and flipped to reflect upstream/downstream geometry. The ^{22}Na source and coldhead are displayed in blue, solenoids are displayed in yellow, and Penning trap electrodes in red. Bottom: Visualisation of buffer gas cooling. Positrons are cooled through their collisions with nitrogen molecules, cooling into the successive stages, eventually accumulating in the third stage where they are compressed by segmented RW electrodes.

ALPHA obtains the positrons required for antihydrogen production from a radioactive ^{22}Na source, which it produces via β^+ decay. The role of positron accumulator, the most downstream section of ALPHA which is displayed on the far right of figure 2.1, is to accumulate and cool these positrons for their delivery to the experimental sections of ALPHA. A more in depth description can be found in [50]. Positrons are emitted by the ^{22}Na source with a large spread of kinetic energies, all the way up to $\approx 545\,\text{keV}$. The emitted positrons are slowed down through the process of moderation: Collisions with a layer of solid neon (the moderator), which is condensed onto the surface of the ^{22}Na source, lower the emission energy of the positrons which make it through (with an efficiency of around 0.5%) to around 50 eV.

Positrons at these energies can be readily formed into a beam using 300 G guiding fields, which is directed into a Surko-type accumulator [51]–an elongated Penning trap with three distinct stages. Nitrogen buffer gas is emitted into the first stage of the accumulator, and is deferentially pumped such that the nitrogen pressure decreases with each successive stage. As positrons pass through the first stage of the accumulator, they cool through collisions with the buffer gas, allowing them to be captured. As they undergo further collisions, they cool into the second stage of the accumulator, and then eventually into the third. In the third stage the buffer gas is the lowest density and the positrons have a lifetime of around 100 s. Within the third stage a segmented rotating wall electrode is continuously operated, compressing the positron plasma which accumulates there; within 4 minutes 250 million positrons can accumulate in the third stage [49]. Following a standard accumulation time of one hundred seconds, the nitrogen gas is pumped out of the trap and the positrons are ready to be transferred to the experimental sections of ALPHA.

2.1.5 The atom trap

Once antiprotons and positrons have been prepared in the catching trap and positron accumulator, they are transferred to either the ALPHA-2 or ALPHA-g atom trap (AT). The ALPHA-2 atom trap is displayed in figure 2.7. The AT is a 34 electrode Penning-Malmberg trap, embedded within an Ioffe-Pritchard trap [52] for the confinement of neutral antihydrogen, all contained within a uniform 1 T magnetic field provided by an external solenoid known as the Carlsberg magnet. The Penning trap configuration within the atom trap is separated into three parts, for antiproton preparation, positron preparation and for antihydrogen synthesis and trapping. They are known colloquially as the recatching, positron and mixing traps respectively, and can be controlled independently.

The purpose of the recatching trap is to capture, compress, and cool the antiprotons that are transferred from the catching trap. This follows an identical procedure of RW compression, electron cooling, and e-kicks used for antiproton preparation in the catching trap, described in section 2.1.3. The positron trap is used to catch and compress positrons transferred from the positron accumulator. The recatching and positron traps have identical Penning trap configurations, mirrored in a radial plane intersecting the centre. Both are formed from seven

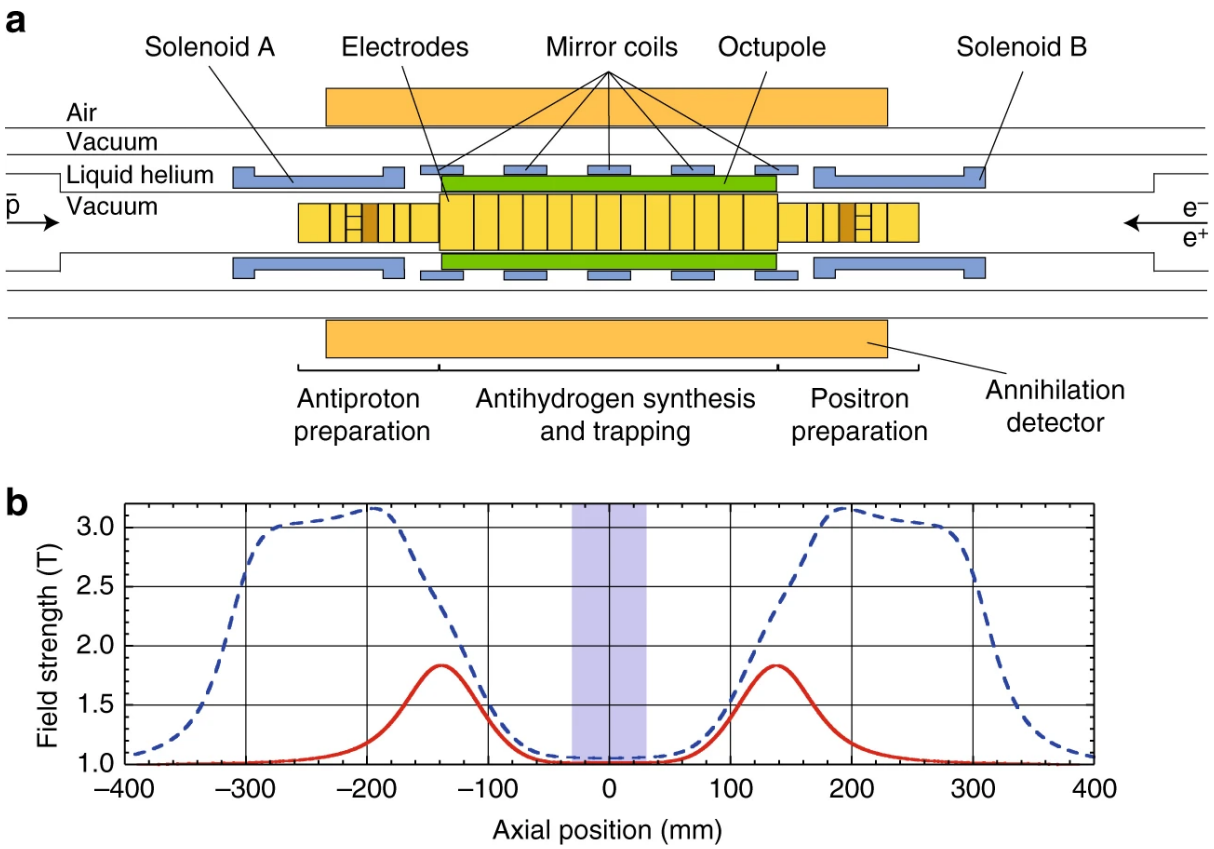

Fig. 2.7. **a)** Diagram of the Atom Trap (AT) electrode stack and magnet configuration. Antiprotons ($\bar{p}$ upstream (left); electrons and positrons (e^- & e^+) enter from downstream (right). **b)** The AT magnetic field on-axis strength as a function of axial position. The axial position maps directly to the diagram in (a). The red solid curve gives the magnetic field strength with only the mirror coils energised. The blue dashed curve gives the magnetic field with mirror coils and solenoid A and solenoid B are energised.

electrodes, one of which is a six-segment RW electrode, and are situated within the field of a solenoid (solenoid A and B) which raises the magnetic field to 3 T for improved cyclotron cooling. The mixing trap sits between the recatching and positron traps, and is the location where antihydrogen is formed through the process described in section 2.2.1. The electrodes that make up the mixing trap are thinner than the electrodes in the recatching and positron traps, which allows for a larger trapping volume for the neutral antihydrogen.

The mixing trap is embedded within an Ioffe-Pritchard trap [52], a magnetic minimum trap which can trap neutral particles using their magnetic moment, described in more detail in section 2.2.2. The trap is formed using a number of superconducting magnets: five "mirror" coils (Mirror A-E) which confine the antihydrogen on the axis and an octupole that confines the antihydrogen radially. The two outer mirror coils typically provide axial confinement, and the inner mirror coils can be used to change the shape of the magnetic confining potential along the trap axis. In an alternative setup, the mirror coils can slowly change the axial length of the trap whilst antihydrogen is confined, enabling adiabatic cooling, discussed in section 2.2.3. The magnetic trap, $\vec{B}(\rho, \varphi, z)$ can be modelled using the dimensions of the magnets and the applied currents using the Biot-Savart law (described in section 3.4.2 in [39]), and is also

continuously measured using Hall probes. To obtain a precise measurement of the magnetic field on the axis, an in situ technique called electron cyclotron resonance (ECR) was developed for use in ALPHA [53]. ECR exploits the cyclotron frequency $\omega_c = eB/m$, of trapped electron plasmas to measure the magnetic field on the axis to sub-Gauss precision. To perform ECR, a small 'target' electron plasma is extracted from a larger 'reservoir' plasma and is transferred to the axial trap location of interest. A pulse of microwaves is then injected into the trap via a waveguide, which interacts with the target plasma. When the microwaves are resonant with the cyclotron frequency it results in heating of the electron plasma, which can be measured using techniques discussed in section 2.1.6. This process is repeated with multiple different microwave frequencies; plotting plasma temperature as a function of microwave frequency results in a resonance peak, the maxima of which provide a precise measurement of the on-axis magnetic field.

ALPHA-g contains a similar setup to ALPHA-2, but with a vertical trap axis. It contains two identical atom trap configurations, along with an Ioffe-Pritchard trap built for precision measurements at the centre. The details of the ALPHA-g apparatus are beyond the scope of this thesis. For a more detailed discussion of the ALPHA-g trap, see chapter 6 in [54].

2.1.6 Sticks

To perform diagnostic measurements of confined plasma, and undertake other actions within the beamline, ALPHA employs vertical translating 'sticks' which move various instrumentation in and out of the beamline. There are nine sticks built into the ALPHA beamline: The CT has an upstream and downstream stick (USCT and DSCT), the AT also has upstream and downsteam sticks (USAT and DSAT), the beamline diagnostic stick (BDS), the positron diagnostic stick (PDS), the lower diagnostic stick (LDS), the upper diagnostic stick (UDS), and the positron accumulator stick (PB2). The locations of some of these sticks on the beamline is shown in figure 2.1. The selection of instrumentation contained on any given stick depends on the stick in question, however the instrumentation can be any selection from: a microchannel plate (MCP) detector, inspection mirror (Insp mirror), electron gun (Egun), Faraday cup (FC), 313 nm laser mirror, a beryllium ablation source, and an empty section to allow particles to pass through. The configuration of instruments on each stick is summarised below in table 2.1.

MCP

An MCP is a standard piece of hardware used to detect single charged particles, and measure the transverse size and shape of charged particle plasmas within the ALPHA experimental setup. The MCPs used within ALPHA are supplied from PHOTONIS, they are constructed from an array of tiny glass tubes (microchannels) fused together to form a thin disc, with a metal coating on the front and back surface. The front surface can be biased with a voltage which accelerates the charged particles of interest towards. The charged particle produces a shower of electrons upon impact with the front surface of the MCP, which are accelerated

	Instrument						
Stick	MCP	Egun	FC	Insp mirror	Phosphor screen	313 nm	Be^+ source
USCT	-	-	-	-	US	-	-
DSCT	US	US, DS	DS	DS	-	-	-
USAT	DS	DS	-	-	-	DS	DS
DSAT	US, DS	US, DS	DS	-	-	US	-
BDS	US, DS	US, DS	US, DS	-	-	-	-
PDS	US, DS	US, DS	US, DS	US, DS	-	-	-
LDS	US, DS	US, DS	US, DS	US, DS	-	-	-
UDS	US	US	-	-	-	-	-
PB2	-	-	-	-	DS	-	-

Table 2.1
Summary of hardware on each stick. Each stick can have up to two of each instrument, with the orientation which the instrument is facing specified within the table

through the microchannels by a potential difference with the back surface, producing an avalanche of electrons which can then be detected on a phosphor screen. A camera can capture the fluorescence of the phosphor by imaging the screen through a vacuum viewport. Plasmas trapped within Penning traps in ALPHA can be imaged by manipulating their confining potentials such that they are ejected towards an MCP. The transverse distribution of the plasma can be determined from MCP images, allowing for RW parameters to be tuned for optimum plasma size and shape. The intensity of the MCP image provides an arbitrary measure of particle number, which can be calibrated against Faraday cup measurements (described below) to be used as a measure of the absolute number of charged particles. The MCPs in ALPHA can also be used to detect individual charged particle; this provides a detection technique for the ionisation of antihydrogen (and possibly hydrogen) during 1S-2S spectroscopy, which is discussed in further detail in section 3.6.2.

Electron gun

An electron gun is an instrument which produces a narrow collimated beam of electrons. The electron guns in ALPHA have two parts: a hot barium oxide cathode filament which produces a stream of electrons through thermionic emission, and anode electrode plate which accelerates the electron beam. The beam of electrons is directed into the various Penning traps within ALPHA, where they are used for sympathetic cooling of antiprotons, and for ECR magnetometry techniques.

Faraday cup

A Faraday cup is a cup built out of a piece of conducting material with a well known capacitance, used to measure the charge of particle directed towards it. When charged particles are directed onto the conductive material of the Faraday cup, it gains a small net charge from impinging particles. The Faraday cup can then be discharged; this produces a small current

proportional to the number of dumped charged particles, which is measured using an SRS SR560 amplifier. Faraday cups are a tool for determining the number of charged particles in a given trapped plasma. Faraday cups can be used to determine the temperature of a trapped plasma, by lowering the one side of the electrostatic potential which axially confines the plasma within a Penning-Malmberg trap, and measuring the charge that escapes. The energy distribution of the plasma is directly sampled as the confining potential is lowered [55], by fitting the energies with a thermal distribution it is possible to extract the temperature of the plasma.

Mirrors

Some sticks contain an inspection mirror, the role of such a mirror is to allow a person to view into the beamline through a vacuum viewport to inspect hardware, check alignment and look for possible obstructions. The USAT and DSAT sticks also contain a mirror which is highly reflective for 313 nm light, which is used to direct laser light into the trap for on-axis cooling of Be^+ ions that are used for the sympathetic cooling of positrons [56].

Beryllium ablation source

The USAT stick contains a beryllium metal target (>99% purity, 0.5 mm thickness) [57]. To produce Be^+ ions through laser ablation, the target is exposed to 5 ns pulses of 355 nm laser light at a 50° angle through a vacuum viewport. A negatively charged acceleration plate directs the Be^+ ions into the Penning trap stack within the AT, where they can be laser cooled by the 313 nm laser to sympathetically cool positrons.

2.2 | Antihydrogen

Once both positrons and antiprotons have been trapped within the AT, and sympathetically cooled using Be^+ and e^- respectively, they can be carefully combined to form antihydrogen in a process known colloquially as 'mixing'. The coldest antihydrogen atoms formed will have energies low enough to be trapped in the Ioffe-Pritchard trap. The trapped sample of antihydrogen can be Doppler cooled using a pulsed 121-nm-laser [32]. Antihydrogen can be detected destructively in the silicon vertex detector through the formation of pions during the annihilation of the constituent antiproton on the trap wall [58]. The details of antihydrogen formation, trapping, cooling and detection are discussed in this section

2.2.1 Formation

Throughout the entire mixing process, displayed in figure 2.8, the 313 nm laser light impinges on the plasmas from the upstream direction, as illustrated by the blue arrows. Mixing takes place in electrostatic potentials located as close as possible to the magnetic minimum of the Ioffe-Pritchard trap, such that any trapped antihydrogen does not gain any extra kinetic energy after the formation process. Just before mixing, positive (Be^+ and e^+) and negative ($\bar{p}$) plasmas are confined in neighbouring electrostatic potential wells, as displayed in figure 2.8 **a**.

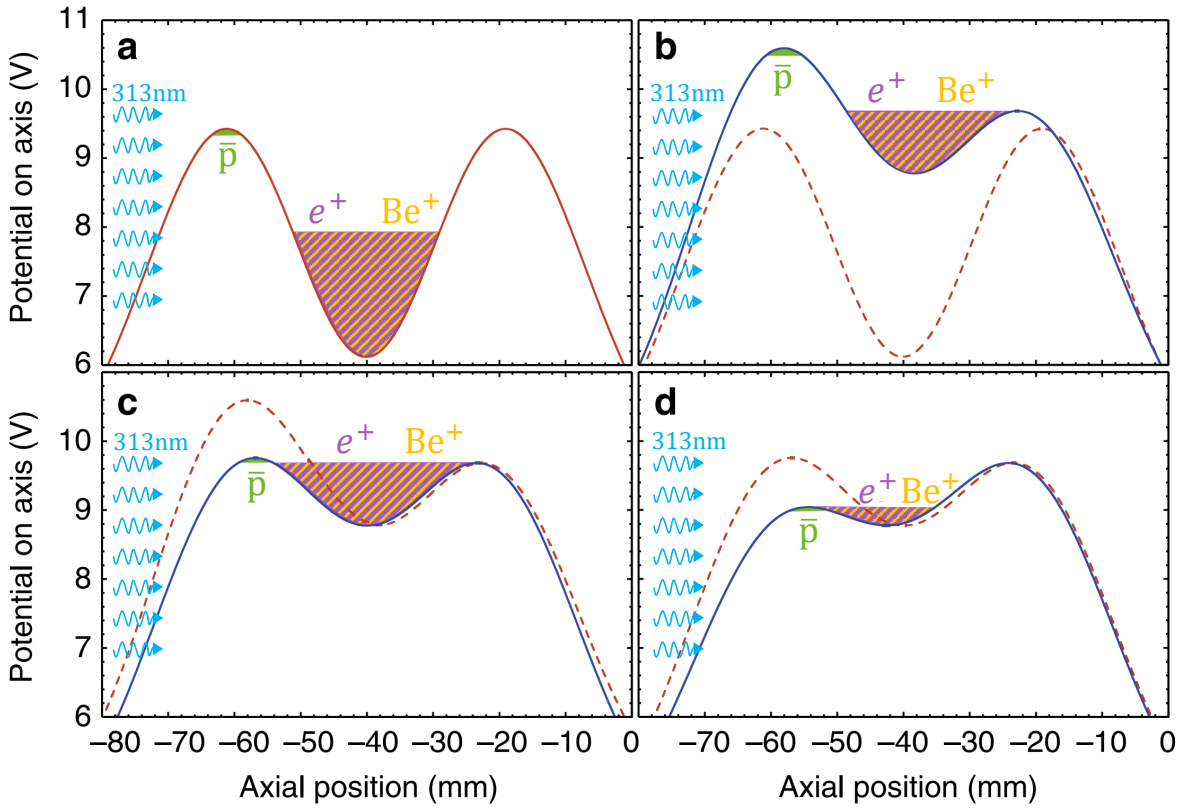

Fig. 2.8. The manipulations of the electrostatic potential required to slowly merge (smerge) positron and antiproton plasmas to form antihydrogen. Dashed and solid curves represent the potentials before and after each step. The green displays the axial extent of the negative $\bar{p}$ plasma, whereas the purple and amber display the axial extent of the mixed e^+ and Be^+ positive plasma. The blue arrows displayed the direction of impinging photons which cool the Be^+ plasma. The specific sub figures display: (a) Before evaporative cooling. (b) Evaporative cooling. (c) Arrangement of wells which nearly overlap the plasmas before mixing. (d) The mixing of the plasmas to form antihydrogen. Figure edited from [59].

The Be^+ and e^+ plasma first undergo evaporative cooling, as shown in figure 2.8 **b**, further cooling the positive plasma mixture. The depth of the potential well confining the antiproton plasma is then lowered such that the two plasmas nearly overlap in space, as displayed in in figure 2.8 **c**. Finally, as displayed in figure 2.8 **d**, the antiproton confining potential is gradually (over 1 s) lowered to slowly merge the oppositely charged plasmas together. During the combination of plasmas impinging 313 nm photons continuously cool the Be^+ plasma, which sympathetically cools the positrons [56], and in turn the antiprotons through the thermalisation of the plasmas. When the plasmas are combined, it is understood that antihydrogen is formed through a three body recombination process [60] between an antiproton and two positrons. During this process the antiproton and one of the positrons forms a bound state, whilst the additional positron carries away any excess kinetic energy from the recombination.

2.2.2 Trapping and accumulation

Antihydrogen is understood to be electrically neutral, which has been tested experimentally as described in section 2.3.1, so can not be trapped in Penning traps. However, it can be trapped using its magnetic moment in the Ioffe-Pritchard trap. The potential energy due to the interaction between an antihydrogen atom's magnetic moment $\vec{\mu}$ and an external field $\vec{B}$ is given by $U(B) = -\vec{\mu} \cdot \vec{B}$. Antihydrogen is formed with a magnetic moment which is either aligned or anti-aligned with the direction magnetic field which forms the trap. The antihydrogen which are aligned with the magnetic field are known as 'high-field seekers', as they will energetically favour stronger magnetic fields, this attracts them to the electrode walls where they annihilate, as a result they cannot be confined. Antihydrogen which has an anti-aligned magnetic moment are known as 'low-field seekers', they will favour weaker magnetic field regions and are thus attracted to the center of the trap, which means they can be confined. Antihydrogen formed through the mixing process described has thermal distribution which is approximately equal to the temperature of the positron plasma at the time of mixing. Of the low-field seeking antihydrogen formed, only the fraction with kinetic energies less than the trap depth ($\approx 0.5\,\mathrm{K}$) will be trapped. The antihydrogen is formed in a highly excited Rydberg state, with magnetic moments that are substantially larger than the magnetic moment in the ground state [61]. The antihydrogen will radiatively cascade towards the ground state states, experiencing a progressively shallower magnetic confining potential. This is equivalent to the trap volume expanding resulting in adiabatic cooling of the antihydrogen [61]. Once in the ground state, the confining potential of the trapped antihydrogen is given by

$$U(\rho, \varphi, z, m_F) = \mu B(\rho, \phi, z), \tag{2.3}$$

where B is the magnetic field strength, which varies with cylindrical coordinates ρ, ϕ and z. The magnitude of the magnetic moment of the trapped state μ is close to the Bohr magneton. There are two possible trapped ground states of antihydrogen, typically named c and d states. They have marginally different magnetic moments from the Bohr magneton due to different antiproton spins, which is discussed in more detail in section 3.2.1.

In 2016, a method for iterative antihydrogen accumulation was introduced using a technique called "stacking" [59]. This method was developed further in 2023 to incorporate laser-cooled beryllium ions to improve trapping efficiency. Once the initial antihydrogen sample is produced and trapped using the mixing procedure described above, additional batches of antiprotons, beryllium ions, and positrons can be delivered to the atom trap to repeat the formation process. The result of this is a trapped antihydrogen sample that grows approximately linearly with each consecutive four-minute mixing cycle, or "stack", as shown in figure 2.9. When this method is implemented over an extended period it enables the accumulation of significant amounts of antihydrogen in the ALPHA-2 trap, reaching around 10,000 antihydrogen trapped in 2023 with the first integration of laser-cooled beryllium ions.

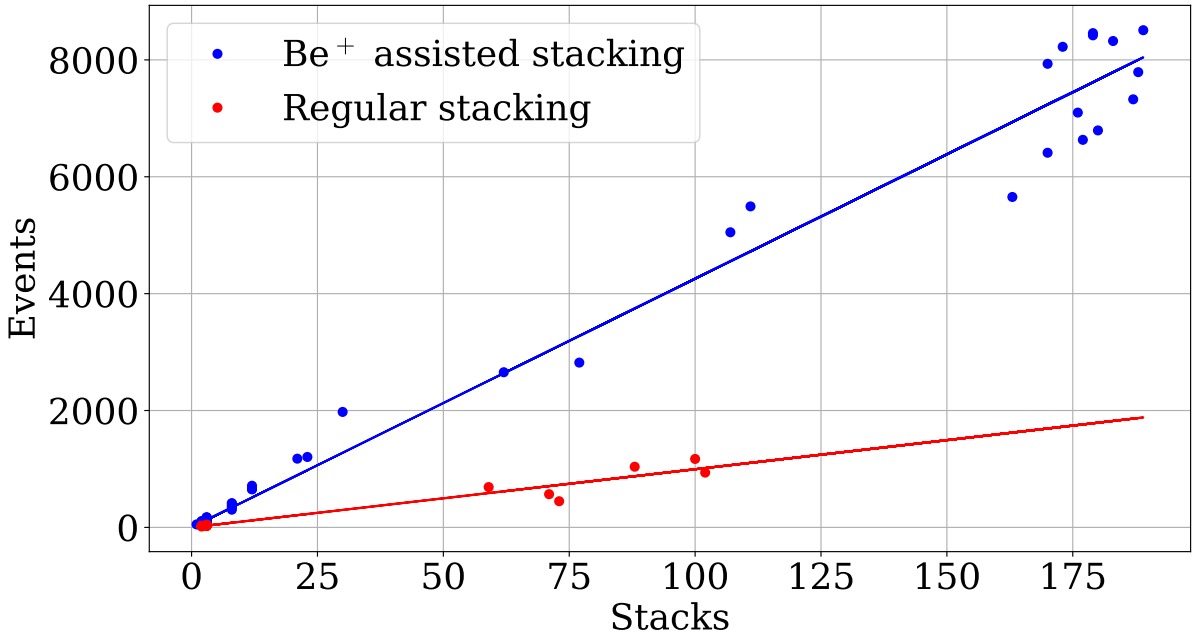

Fig. 2.9. Antihydrogen accumulated within ALPHA-2 via stacking in 2023. Events are passed cuts (described below in section 2.2.4), and after accounting for efficiency, it is estimated that more than 10,000 antihydrogen atoms were accumulated within the larger stacks in 2023 using Be^+ assisted stacking. The number of $\bar{H}$ is assumed to be linear, displayed by the solid lines.

2.2.3 Cooling

Magnetically trapped antihydrogen in ALPHA has a thermal distribution which is energetically truncated at the trap depth, around 0.5 K. Whilst this is a very low energy distribution, it is possible to increase the precision of fundamental antihydrogen measurements discussed in section 2.3 if the trapped sample can be cooled further. There are two possible methods which have been developed to cool trapped antihydrogen: laser cooling and adiabatic cooling.

Antihydrogen was laser cooled in ALPHA-2 for the first time in 2018 [32], by exciting the $1S_d$–$2P_a$ transition (states indicated in figure 2.2) with a pulsed 121-nm-laser, which decays back to a trappable ground state [32]. The cooling laser is directed into the trap along the axis where it interacts with trapped antihydrogen. When the laser is red-detuned from the transition frequency of atoms at rest, antihydrogen atoms preferentially absorb photons which are counter-propagating with their velocity due to the Doppler effect. The antihydrogen will receive a momentum kick from the photon which is opposite to the direction of its velocity, slowing it down. The excited antihydrogen will then decay back into the ground state, and emit a photon in a random direction, which means that on average the laser will impart a force on the antiatoms which opposes their motion, cooling the sample. The pulsed 121-nm-laser only cools the antihydrogen along the axial dimension; however, due to non-trivial energy mixing dynamics between the axial transverse dimensions [62], the result is three-dimensional cooling.

In order to measure the cooling effect of the 121-nm-laser on the trapped antihydrogen, the 121-nm-laser is used to probe the $1S_d$–$2P_{c-}$ transition (states indicated in figure 2.2) [30]. The $2P_{c-}$ state can decay to the untrappable $1S_a$ state, resulting in detectable annihilation on the inner electrode wall. This observation yields two key insights into the energy distribution of the trapped antihydrogen: Firstly, the linewidth of the $1S_d$–$2P_{c-}$ spectrum provides information on the axial energy distribution, as it is significantly influenced by Doppler broadening. Secondly, the time interval between the 121-nm-laser pulse and the annihilation event provides information on the duration it takes for an antihydrogen atom to travel from the trap axis to the inner electrode, the time-of-flight (TOF), which can be used to determine its transverse velocity.

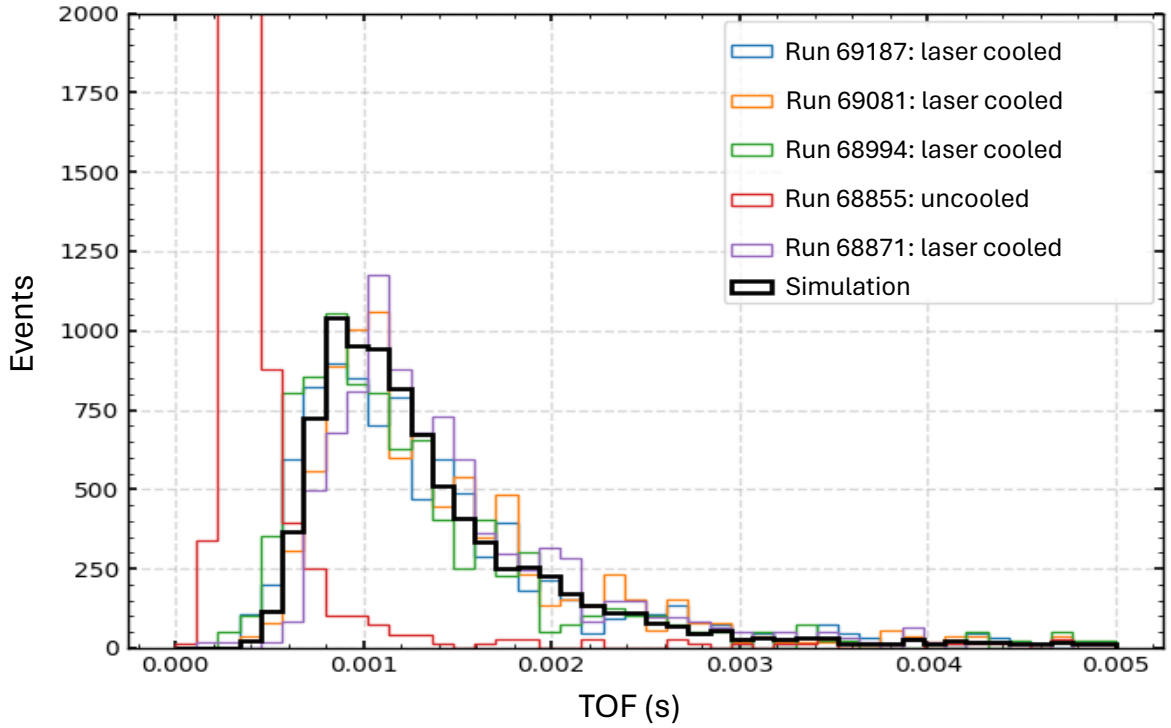

Fig. 2.10. TOF distribution of four laser cooled runs, and one uncooled run. The laser cooled runs display very similar TOF distributions, which demonstrates reproducibility of laser cooling. The cooled runs also display a similar TOF distribution to simulations. Figure provided by Andrew Evans, and is preliminary work which is subject to change.

The initial experimental campaign conducted in 2018 [32] demonstrated that the 121-nm-laser was effective in cooling trapped antihydrogen. The coldest laser-cooled sample, which had been laser cooled throughout the stacking process (refered to as 'stack and cool'), exhibited a narrower $1S_d$–$2P_{c-}$ linewidth compared to the wider linewidth observed in the uncooled sample. This reduction in linewidth indicates a decrease in axial velocity, leading to a decrease in Doppler broadening as a result of laser cooling. Likewise, the 'stack and cool' sample displayed an average TOF of 1.00±0.03 ms, while the uncooled sample had a TOF of 0.42±0.01 ms, indicating a significant reduction in the transverse velocity of the trapped antihydrogen. Although the energy distributions of the laser-cooled antihydrogen samples from the 2018 experimental campaign did not exhibit typical thermal characteristics, the 'stack and

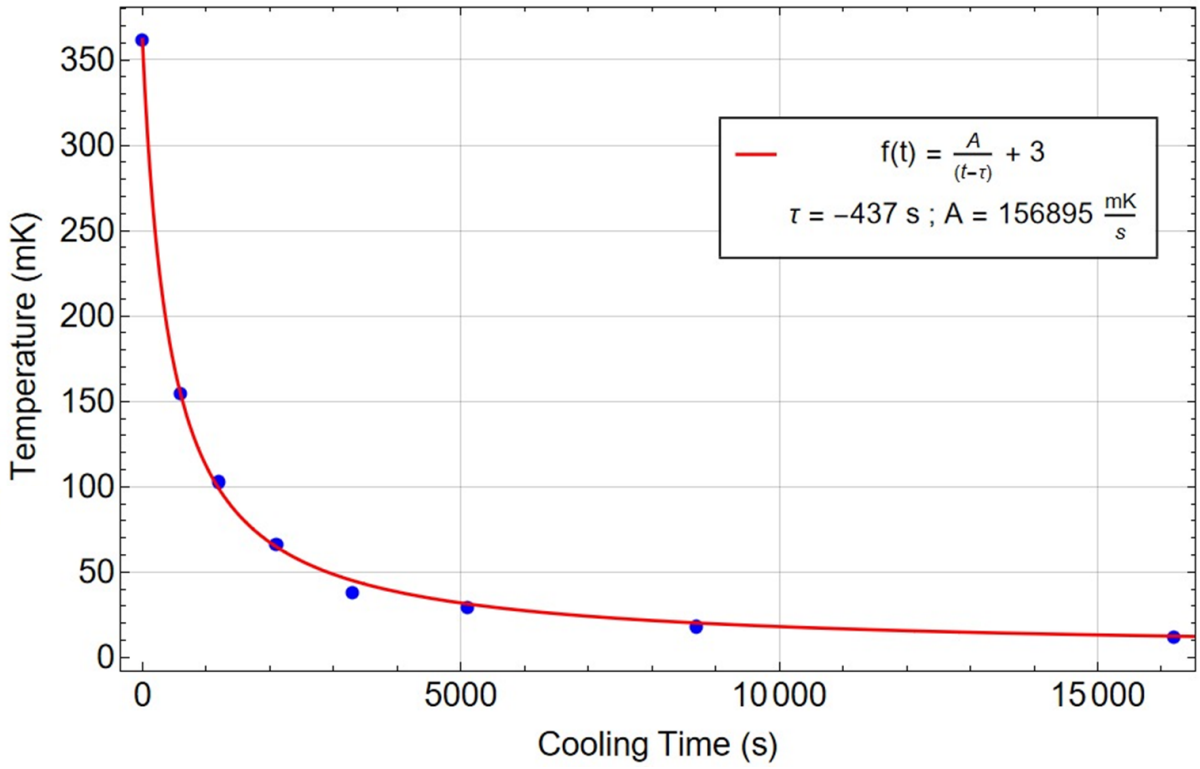

Fig. 2.11. The evolution temperature, which is estimated from fits to the TOF distribution, measured at intervals during the laser cooling. Figure produced by Levi Oliveira de Araujo Azevedo.

cool' sample has an average kinetic energy equivalent to that of a thermal distribution at a temperature of around 50 mK, which is significantly below the ~0.5 K trap depth,

Laser cooling studies conducted in 2018 took place over the course of only a few weeks, during which there was insufficient time to systematically study the cooling process. In 2023, more dedicated time was allocated to studying laser cooling, such that it could reproducibly cool antihydrogen samples to a consistent energy distribution. By exposing the antihydrogen sample to 121-nm-laser light with a detuning of -300 MHz from the $1S_d$–$2P_a$ transition for over 4 hours, the sample was found to be cooled to a reproducible energy distribution, as displayed by the TOF distributions in figure 2.10. This is because the effectiveness of the 121-nm-laser in cooling the antihydrogen was observed to saturate after approximately 3 hours, beyond which further exposure does not result in any significant further energy reduction of the antihydrogen sample. Figure 2.11, which displays the evolution temperature estimated from fits to the TOF distribution measured at intervals during the laser cooling. The antihydrogen that had been cooled to this 'saturation regime' exhibited average kinetic energy equivalent to that of a thermal distribution at a temperature of around 10 mK.

Trapped antihydrogen within ALPHA can also be cooled adiabatically, through ramping the mirror coils such that the trap volume dynamically expands. A proof of principle experiment in the adiabatic cooling of antihydrogen through these techniques was performed in 2016. The results are discussed extensively in [39], and comparison to simulation suggests a reduction in

the energies of trapped antihydrogen by a factor of ≈1.6. This technique was not implemented for the work of this thesis, but may provide methods for even colder antihydrogen in future work.

2.2.4 Detection

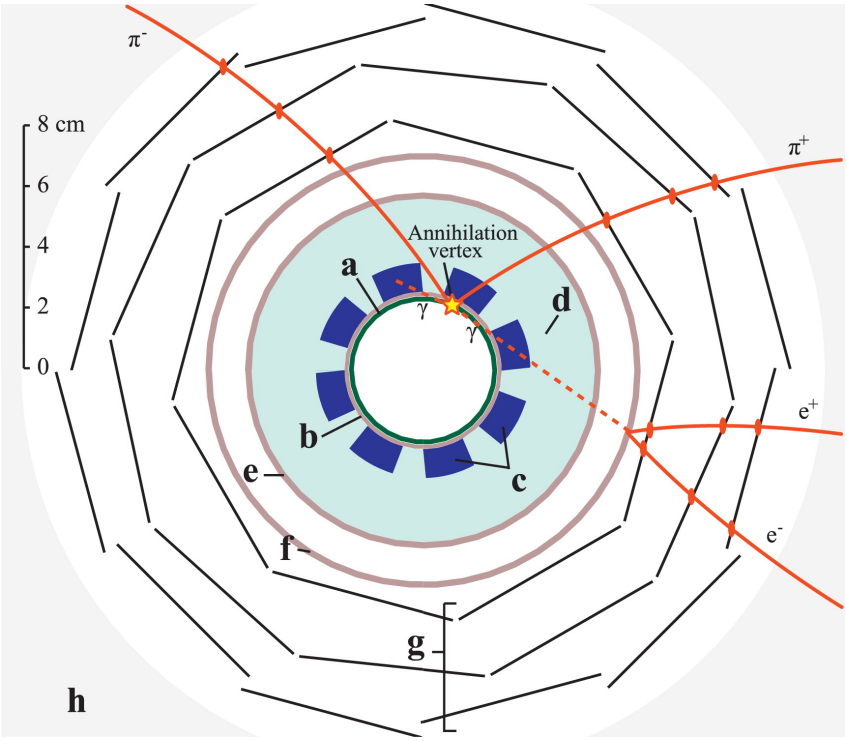

Fig. 2.12. Cross section of SVD. **a)** electrode wall, **b)** magnet winding form, **c)** octupole windings, **d)** liquid helium volume, **e)** inner isolation vacuum wall, **f)** outer isolation vacuum wall, **g)** SVD formed from three layers of silicon modules represented by the black lines, **h)** Section of the Carlsberg magnet. An example antiproton annihilation event is displayed by the orange star. The paths of two charged pions and one neutral pion (which decays into two photons, one of which is absorbed by the octupole, and the other which undergoes pair production) are displayed. Figure from [63].

Antiproton annihilation, predominantly on the electrode walls, is the physical process that provides the detection signal for most of the antihydrogen experiments performed within ALPHA. The annihilation of an antiproton results in the emission of pions, on average three charged pions and two neutral pions [63][58]. The neutral pions decay rapidly into gamma ray photons, whereas the charged pions have lifetimes which allow them to to travel a reasonable distance when moving at relativistic speeds. Charged particles (either pions or electron-positron pairs produced from the gamma ray photons) can be detected in ALPHA-2 by the silicon vertex detector (SVD), displayed in figure 2.12, and in ALPHA-g by a radial time projection chamber (TPC). As 1S-2S spectroscopy (which is performed in ALPHA-2) is the main topic of this thesis we shall only discuss the SVD here; a detailed discussion of the radial TPC can a found in [64].

The SVD is formed from 72 position sensitive silicon modules, split into three layers which surround the ALPHA-2 trap concentrically in the space between the outer vacuum chamber and the Carlsberg magnet, as displayed in figure 2.12. As a charged particle travels through through the SVD it deposits energy on the silicon modules, this is detected as a 'event' by dedicated microchips on each module which readout the signal. If a pion produces a hit on all three layers of the SVD, its path can be reconstructed; the intersection of multiple reconstructed pion paths determines the annihilation location, as shown in figure 2.12. Analysis of reconstructed path can help to distinguish between actual annihilation events, and cosmic rays. An SVD event that meets the conditions set out in table 2.2 [63] classified as a passed cut (PC), and is likely to be an antiproton annihilation event.

N_{tracks}	Vertex radius, R_{cut} (cm)	Linear residual, δ_{cut} $\left(\text{cm}^2\right)$
$= 2$	< 4	> 2
> 2	< 4	> 0.05

Table 2.2
Events satisfying these conditions are classified as passed cuts. From [63]. Paramter details provided in text.

The variable N_{tracks} is the number of reconstructed paths, which must be two or more, given that cosmic rays tend to produce a single continuous path. R_{cut} denotes the radial distance from the trap center to the annihilation location, which must be less than 4 cm to fall within the penning trap electrodes; events occurring beyond this radius cannot be an antiproton annihilation. δ_{cut} is the squared residuals of the path to a straight line fit, indicating how well an event matches a linear path (a value of zero indicates a perfect linear fit). Cosmic ray particles are expected to travel in a straight line trajectories within the detector [63], so the less linear the path the more likely it is caused by an annihilation. If N_{tracks} equals two, the residual from the linear fit must exceed two. In the case that N_{tracks} is greater than two, which is unlikely for a cosmic ray, then the linear fit residual condition is more relaxed. Antiproton annihilations are typically classified as passed cuts with an efficiency of 68%. Despite attempts to eliminate cosmic background, passed cuts still contain a cosmic ray background count rate of approximately $0.045\,s^{-1}$. Estimating the quantity of antiproton annihilations happening within a time period τ from the number of passed cuts is given by

$$N_{\bar{p}} = \frac{N_{PC} - \tau \times 45 \times 10^{-3}}{0.68}, \tag{2.4}$$

where $N_{\bar{p}}$ is the estimated number of antiproton annihilations, and N_{PC} is the number of pass cuts. Multivariate analysis (MVA) classification techniques that employ machine learning can be applied to more stringently classify annihilations from the background [65][66]. These MVA methods are frequently tailored to suit the particular antihydrogen experiment being conducted.

2.3 | Measurement of antihydrogen properties

Antihydrogen can be formed and trapped using the methods and instrumentation described above. Once trapped, antihydrogen can be subjected to experimental studies, which enable its fundamental properties to be measured. Here, we will briefly review past measurements of the fundamental properties of trapped antihydrogen made by ALPHA. We shall pay specific attention to the 1S–2S spectroscopy experiments, as this thesis represents a continuation of this work.

2.3.1 Charge neutrality

Antihydrogen is expected to be electrically neutral, just like standard hydrogen, as CPT symmetry requires the charge of an antiparticle to be equal and opposite to its equivalent particle. In 2014 a limit on the charge of antihydrogen was determined for the first time [67], producing a bound on the charge of antihydrogen of $q_{\overline{\mathrm{H}}} < (-1.3 \pm 1.1(\text{statistical}) \pm 0.4(\text{systematic})) \times 10^{-8}$, where $q_{\overline{\mathrm{H}}}$ is expressed in multiples of the elementry charge. The experimental method involved producing an electrostatic potential gradient along the length of the trap using the Penning-Malmberg trap electrodes. This produces an axial electric field along the length of the trap which would deflect charged antihydrogen to one side of the trap or the other side of the trap depending on its charge, neutral antihydrogen would be unaffected. By studying the axial annihilation locations and comparing to simulation it is possible to produce bounds on the antihydrogen charge.

In 2016 [68] an improved measurement made in ALPHA set a new bound of $q_{\overline{\mathrm{H}}} < 7.1{\times}10^{-10}$. The new methodology involved subjecting magnetically trapped antihydrogen to stochastic kicks from electric fields produced by the Penning-Malmberg trap electrodes. If antihydrogen has a charge it would undergo a random walk in energy, and would eventually be stochastically heated from the magnetic trap, whereby an annihilation could be detected by the SVD. Measurements with and without stochastic heating (null trials) were interleaved, and any difference between the stochastic and null trials would be indicative of antihydrogen charge. No difference was observed, and a comparison to simulation provided the bound.

2.3.2 Gravitational attraction

The weak equivalence principal (WEP) states that all particles (or antiparticles) fall with the same acceleration in a gravitational field, therefore the behavior of antimatter within a gravitational field is expected to be the same as matter. During 2022 we observed the effect of Earth's gravitational field on the motion of antimatter, to ascertain whether antimatter falls with the same acceleration as regular matter. The result, published in 2023 [33], was that antihydrogen behaved in a way which is consistent with the gravitational acceleration of regular hydrogen, and a repulsive 'anti-gravity' was definitively ruled out.

The experimental method involved accumulating antihydrogen for multiple hours to produce a magnetically trapped sample of approximately 200 anti-atoms within the ALPHA-g experimental setup, which is displayed in figure 2.1. The mirror coils which provide the axial confinement are ramped down simultaneously, allowing for trapped antihydrogen to escape on axis from either the top or the bottom of the magnetic trap, where they are detected by the TPC. If the currents in the top and bottom mirror are the same, then antihydrogen is expected to escape from mostly the bottom in the case of attractive gravity (and from the top in the case of repulsive). Different currents can be applied to the top and bottom mirror coils, producing a vertical gradient in magnetic field which can compensate for the effects of gravity. If we assume that the gravitational acceleration g to be $9.81\,\mathrm{ms}^{-2}$ towards earth then a magnetic field gradient of $-1.77\times10^{-3}\ \mathrm{Tm}^{-1}$ can completely compensate for the acceleration due to gravity. If we consider magnetically trapped hydrogen moving vertically in one dimension, it is possible to balance the effect of gravity by imposing a field difference of about -4.53×10^{-4} between the mirror coils field maxima, which we will refer to as a 'magnetic bias' of $-1g$. By finding this 'balance point' for trapped antihydrogen, which entirely compensates the effects of gravity to produce symmetric annihilations when the trap is lowered, one can deduce its gravitational acceleration of antihydrogen. However, in reality antihydrogen follow three dimensional trajectories within the trap, so the gravitational acceleration is determined through comparison to simulations of hydrogen in the trap. The experimental campaign involved repeating the mirror ramp down procedure many times, with multiple different magnetic bias, and observing the relative fraction of antihydrogen that escapes from the top and bottom of the trap. The balance point of the experimental data is seen to be close to $-g$, as expected from a one-dimensional model. A Bayesian likelihood analysis of comparisons between the experimental data and the simulation determined the gravitational acceleration of antihydrogen towards earth to have a value of $a_{\bar{g}} = (0.75 \pm 0.13(\text{statistical} + \text{systematic}) \pm 0.16(\text{simulation}))g$. The probability of our experimental data having occurred under equal but repulsive gravity was determined to be so small as to be quantitatively insignificant (below 10^{-15}), and the probability of the data occurring under the hypothesis that gravity does not act on antihydrogen was determined to be 2.9×10^{-4}.

2.3.3 Hyperfine spectroscopy

The first quantum transition which was ever probed in antihydrogen was the ground state hyperfine transition, which was observed for the first time in 2012 [31]. In this measurement, resonant microwaves induced positron spin flips in trapped low-field-seeking antihydrogen, driving a transition to a high-field-seeking ground state. These untrappable antihydrogen atoms subsequently annihilate on the electrode walls, producing a measurable signal in the SVD. In 2017 this measurement was improved upon [69], measuring the ground state hyperfine splitting of antihydrogen to be consistent with hydrogen with a precision of 4 parts in 10^4. In this experimental campaign, the individual $1S_d \rightarrow 1S_a$ and $1S_c \rightarrow 1S_b$ spectra (energy levels

displayed in figure 2.2) could be resolved, which have an asymmetric lineshape with a sharp onset frequency due to the Zeeman effect within an inhomogeneous magnetic field. However, the frequency difference between the onset of the two spectra provides a measurement of the ground state hyperfine splitting which is independent from magnetic field strength. The result was a hyperfine splitting of 1420.4±0.5 MHz.

2.3.4 1S–2P spectroscopy

The 1S–2P Lyman-α transition was first observed in antihydrogen in 2018 [30], where ground state antihydrogen was excited from the $1S_d$ state to the $2P_{c-}$ state (states indicated in figure 2.2) by linearly polarised pulsed 121-nm-laser light [70]. Once in the excited $2P_{c-}$ state, the antihydrogen can decay back down to either the trappable $1S_d$ state or the untrappable $1S_a$ state–which annihilates on the electrode, detectable by the SVD. Plotting the number of detected annihilations against laser frequency traces out a lineshape, with peak at the transition frequency. The lineshape produced by this experimental campaign resulted in a 1S–2P Lyman-α transition frequency of $2,466,051.7 \pm 0.12$ GHz (1σ uncertainty), corresponding to an agreement with measurement in hydrogen to a precision of $5{\times}10^{-8}$. The uncertainty on this transition is dominated by the Doppler broadening of the spectrum due to the motion of trapped antihydrogen parallel to the laser beam, making it a non-ideal candidate for CPT invariance tests. However, the measurement was an essential step towards the development of antihydrogen laser cooling techniques, described in section 2.2.3, which uses the same pulsed 121-nm-laser to excite $1S_d$–$2P_a$ used for cooling.

2.3.5 1S–2S spectroscopy

The 1S–2S transition is a requires two photons to be excited, which provides two distinct advantages for measuring the spectrum with precision. Firstly, in the case that the two photons are counter propagating, the Doppler effect is suppressed to first order. Secondly, because there is no 1P state, the 2S state is unable to decay by emitting one photon; this gives the meta stable 2S state a long lifetime of 0.12 s which results in a narrow natural linewidth. Once excited to the 2S state, the antihydrogen can escape the trap through two processes: ionisation of the positron to the continuum via the absorption of a third 234 nm photon, or Stark mixing to between the 2S-2P state followed by a decay to an untrappable state. These two detection routes are discussed in more detail in section 3.6.

The 1S–2S transition was first observed in antihydrogen in 2016 [29], where its frequency was found to agree with the hydrogen transition at a relative precision of $2{\times}10^{-10}$. In this initial experiment, trapped antihydrogen is accumulated and then held for for 600 s, and then the magnetic trap is ramped down and the antihydrogen annihilations are counted. During the 600 s hold, the antihydrogen undergo one of three experimental trials: 1) 'on resonance', the antihydrogen is exposed to resonant 243-nm-laser light, the $1S_d$-$2S_d$ and $1S_c$-$2S_c$ transition are driven for 300 s each with laser light at the expected transition frequency; 2) 'off resonance',

in which antihydrogen is exposed to 243-nm-laser light which is tuned too 200 kHz below the $1S_d$-$2S_d$ and $1S_c$-$2S_c$ expected transition frequency for 300 s each; 3) 'no laser', the antihydrogen is not exposed to laser light during the 600 s hold. The 243-nm-laser light which illuminates the antihydrogen is enhanced to 1 W by an optical build-up cavity within the ALPHA-2 experimental setup. Following 11 experimental trails, it was found that the on resonance trials on average had 58±6% less trapped antihydrogen following the magnetic trap rampdown. This was found to be in good agreement with simulations with hydrogen parameters, and it was concluded that the antihydrogen was removed due to the excitation of the 1S–2S transition by the resonant laser light.

In 2017 the spectrum of the $1S_d$-$2S_d$ transition was characterised for the first time [35]. The transition frequency was found to agree with hydrogen to a relative precision of 2×10^{-12}, which corresponds to an improvement by two orders of magnitude over the 2016 measurement. The characterisation of the spectrum involved collecting data for nine different laser detunings: –200, –100, –50, –25, 0, 25, 50, 100, 200 kHz, where the 0 kHz detuning is the expected transition frequency, accounting for the Zeeman shift at the magnetic minimum of the Ioffe-Pritchard trap. The experimental campaign consisted of 86 trails taken over a period of ten weeks, each studying one of the nine frequencies. During each trial, antihydrogen is accumulated for three stacks, and then the trapped antihydrogen is exposed to 300 s of 1 W of 243-nm-laser light at one of the nine detunings, which was blinded to the experimental operator. Any annihilations during the 300 s exposure are counted by the SVD, referred to as the 'appearance' mode of detection. The antihydrogen is then exposed to 32 s of microwaves resonant with the $1S_c$-$1S_b$ transition, which ejects any $1S_c$ states. Assuming that the microwave ejection is 100% effective, only the $1S_d$ states which were not removed by the 243-nm-laser would remain in the trap. The magnetic trap is then ramped down, and the remaining antihydrogen was counted by the SVD, referred to as the 'disappearance' mode of detection. Once the experimental campaign was complete the experimental trails were unblinded and sorted by frequency, and used to map out a spectrum using a simple scaling, displayed in figure 2.13. The scaled appearance mode is given by $r_l(D) = L(D)/L(0)$, and the scaled disappearance mode data is given by $r_s(D) = [S(-200\mathrm{kHz}) - S(D)]/[S(-200\mathrm{kHz}) - S(0)]$, where D is the detuning, and L and S are the number of appearance and disappearance mode annihilation events respectively. Ultimately, the transition frequency was determined by fitting the experimental spectrum to a simulated hydrogen line shape. The uncertainty on transition frequency determination is given by table 2.3, and is the most precise published measurement of the 1S-2S transition frequency in antihydrogen at the time of writing.

In 2018, the 1S–2S spectrum of antihydrogen was characterised again [32][71], this time both the $1S_d$–$2S_d$ and $1S_c$–$2S_c$ were characterised. The $1S_d$-$2S_d$ transition was determined at a level of precision similar to that in the 2017 measurement, and the $1S_c$–$2S_c$ spectrum was characterised for the first time. The 2018 data was collected using a new experimental protocol, where both the spectra can be measured within one day. First, a sample of trapped antihydrogen is accumulated within the trap. The antihydrogen is then exposed to short pulses

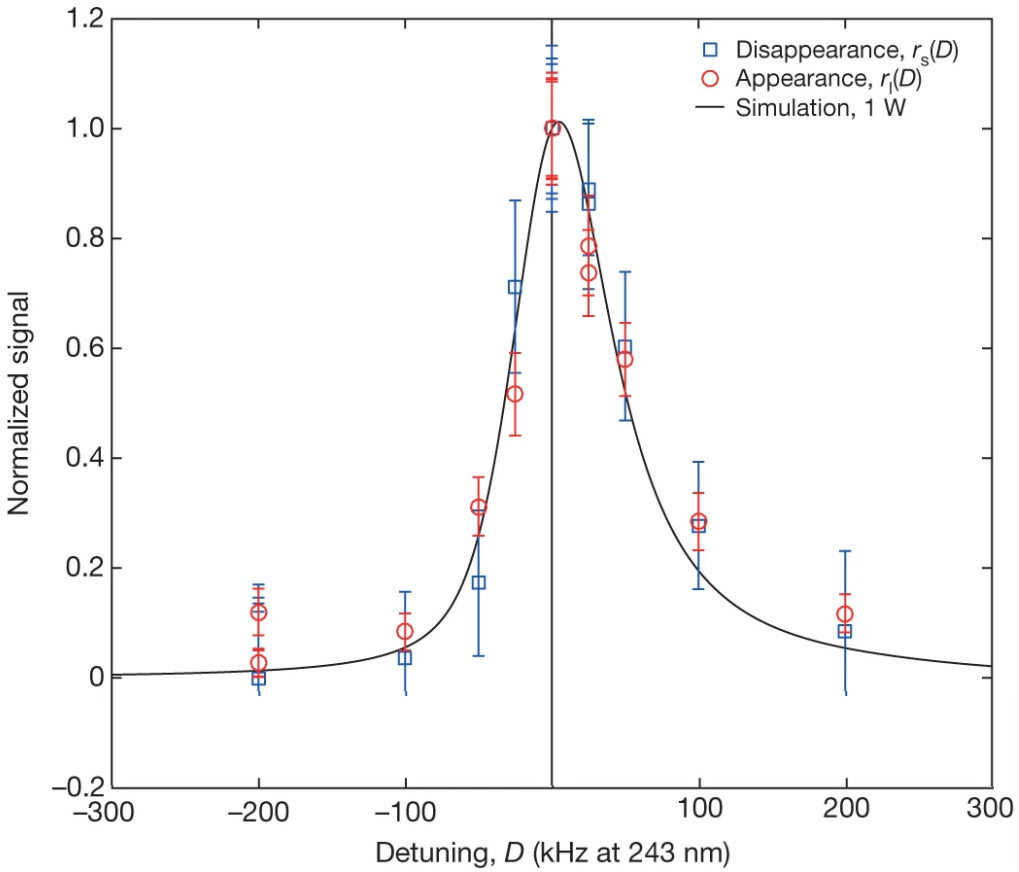

Fig. 2.13. The 1S–2S spectrum, characterised in [35]. Red points show data from the appearance mode of detection, whereas blue points show the disappearance mode of detection. The simulated curve is displayed in black. The vertical error bars represent counting uncertainties (one standard deviation). Figure taken from [35].

Uncertainty	Estimated size (kHz)	Comment
Statistical uncertainties	3.8	Poisson errors and curve fitting to measured data
Modelling uncertainties	3	Fitting of simulated data to piecewise-analytic function
Modelling uncertainties	1	Waist size of the laser, antihydrogen dynamics
Magnetic-field stability	0.03	From microwave removal of $1S_c$-state atoms (see text)
Absolute magnetic-field measurement	0.6	From electron cyclotron resonance
Laser-frequency stability	2	Limited by GPS clock
d.c. Stark shift	0.15	Not included in simulation
Second-order Doppler shift	0.08	Not included in simulation
Discrete frequency choice of measured points	0.36	Determined from fitting sets of pseudo-data
Total	**5.4**	

Table 2.3
Estimated uncertainties for the transition frequency (at 121.6 nm). From [35].

of 243-nm-laser light, iterating through a predefined sequence of frequencies. Short pulses of one or two seconds are required to avoid depletion of the antihydrogen sample, and there are dark periods of varying length between the pulses during which the laser shutter is closed. Antihydrogen lost during laser exposures are detected in the SVD, and annihilation events can be plotted against the laser frequency to map out a spectrum. The 2018 experimental campaign also marked the first laser cooling of antihydrogen, which presented the opportunity to measure a laser cooled 1S–2S spectrum; this is expected to be narrower due to reduced transit time broadening (discussed in more detail in section 3.4). Three experimental runs were conducted with the new protocol, runs 1 and 2 measured both $1S_d$-$2S_d$ and $1S_c$–$2S_c$, whereas run 3 only probed the $1S_d$–$2S_d$ spectrum. Runs 2 and 3 employed laser cooling on the $1S_d$ states during the stacking plus another 6 hours of laser cooling before spectroscopy, whereas run 1 did not have any laser cooling. The $1S_d$–$2S_d$ spectra for runs 1 and 2 are displayed in 2.14 (labeled B and A respectively), as can be seen the laser cooling in run 2 results in a narrower spectrum.

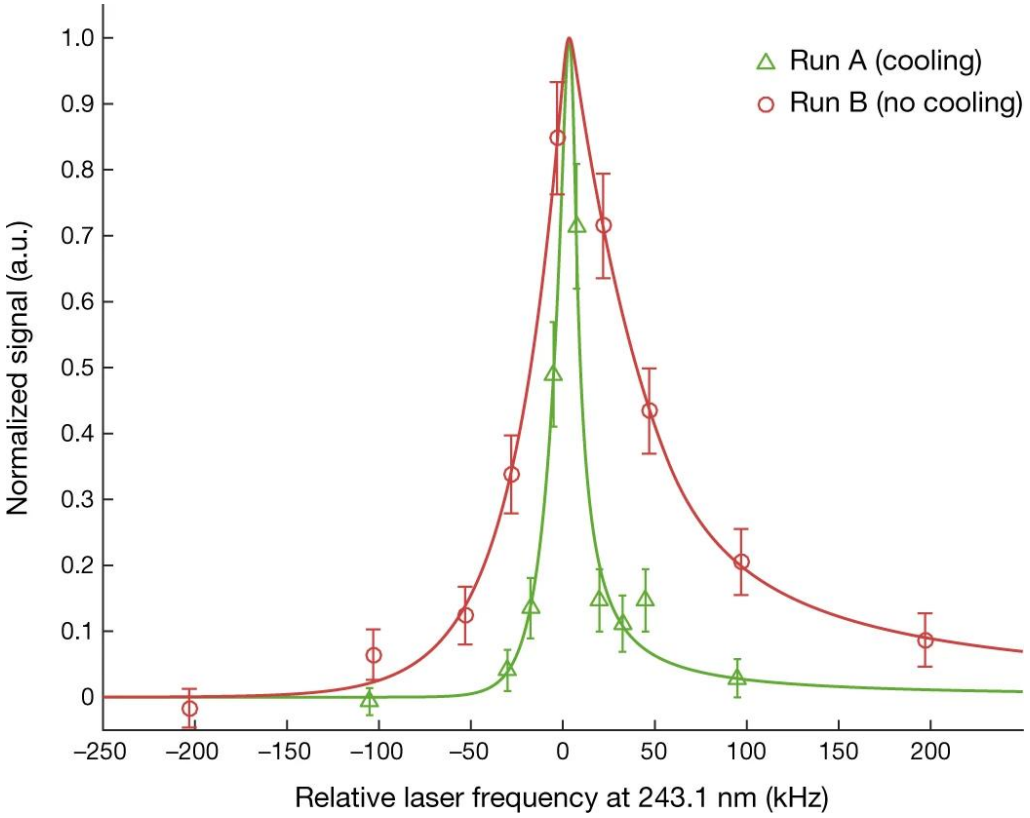

Fig. 2.14. Cooled and uncooled $1S_d$-$2S_d$ spectra measured in 2018. Both spectra have been normalised to their respective fitted heights, and the frequency-independent background has been subtracted to highlight the differences in line shape. The laser cooled fit is not well constrained due limited frequency points. Figure from [32]

Unfortunately, the laser cooled samples suffered from excessive depletion when probing the $1S_d$–$2S_d$ transition, which is expected to have caused significant distortion of the spectrum. All spectra were fit with an analytical function, which had their shape fixed by simulation data,

which could be used to extract the transition frequency. However, the effects of depletion, alongside a limited number of frequency points, prevent the laser cooled $1S_d$–$2S_d$ spectrum being used to extract a transition frequency.

Although not achieved in 2018, the laser cooling techniques and the 1S–2S spectroscopy protocol developed that year offer an exciting route to significantly improving the precision of measuring the 1S–2S transition frequency in antihydrogen. This thesis discusses the work towards improving this precision, and presents the experimental data from 2023 which will be used to extract an improved 1S–2S transition frequency. Laser cooling alone is not enough to achieve a significantly improved measurement, as there are still many large uncertainties in table 2.3 to be addressed. The beryllium assisted stacking procedure developed in 2023, discussed in sections 2.2.1 and 2.2.2, allows larger antihydrogen samples to be trapped–reducing much of the statistical uncertainty. The uncertainty derived from the frequency reference was reduced significantly through the upgrades to metrology instrumentation, which is discussed in detail in chapters 4 and 5. Many of the remaining sources of systematic uncertainty are addressed in chapter 7, which accounts the 2023 experimental campaign for a more precise determination of the 1S–2S transition frequency with laser cooled antihydrogen.

CHAPTER 3

Theoretical considerations

> *A week in the lab can save you an entire afternoon in the library.*
>
> — **Unknown person**
> PSAS 2024

A consequence of CPT symmetry is that if there is a matter bound state with energy eigenvalue E_n, then an equivalent antimatter bound state will have the same energy eigenvalue [17]. As a result, antihydrogen should exhibit spectral lines identical to those of hydrogen. Thus, measuring the 1S-2S transition frequency in antihydrogen serves as an accurate test for CPT symmetry [16] when compared to equivalent measurements made with hydrogen [34]. In the future, it is intended to conduct hydrogen experiments within ALPHA, such that it can be directly compared to antihydrogen, which would reduce systematic sources of uncertainty and reduce dependence on theoretical models. Currently, the theoretical models described in this chapter are necessary to compare with hydrogen and search for CPT symmetry violations.

This chapter delves into the theoretical aspects of the 1S-2S transition of antihydrogen in ALPHA. We start by reviewing the expressions for the field-free energy levels of hydrogen, and then in the presence of a magnetic field–which are identical for antihydrogen. We shall then cover two-photon transitions in the transit-time limit and derive the associated theoretical lineshape. Following this we shall summarise the key broadening mechanisms that will affect our measured lineshape, and discuss spectroscopy detection methods. We shall then dicuss modified lineshapes, which account for systematic shifts and broadening and which occur within ALPHA. Finally, we examine the simulations which are used to make predictions about spectroscopy in ALPHA.

3.1 | Field-free energy levels

In free space the complete expression for the energy levels of hydrogen, $\mathcal{E}_H$ is typically split into three parts: the Dirac energy, the Lamb shift, and the hyperfine splitting (HFS).

$$\mathcal{E}_H = \mathcal{E}_{\text{Dirac}} + \mathcal{E}_{\text{Lamb}} + \mathcal{E}_{\text{HFS}}. \tag{3.1}$$

The complete structure of antihydrogen for the levels which are of most interest to this thesis ($n = 1, 2$) are displayed in figure 3.1

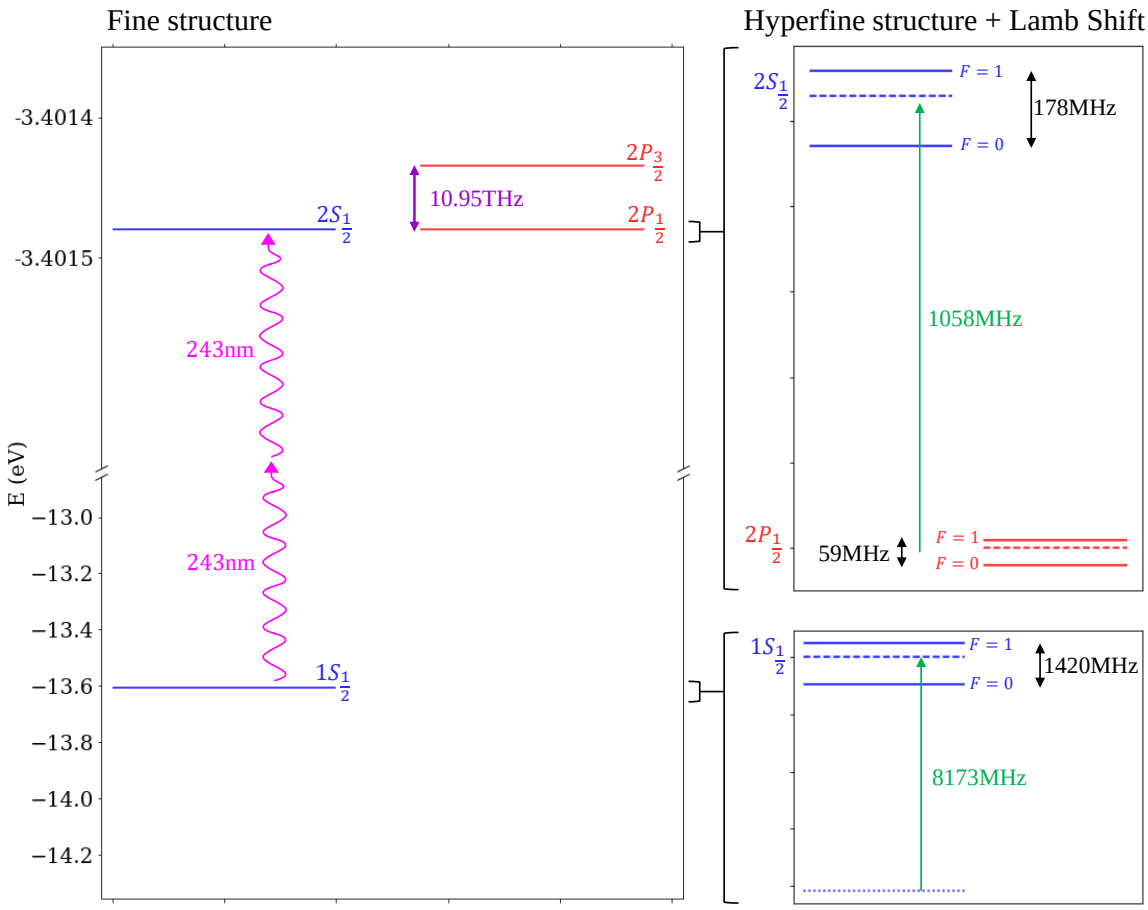

Fig. 3.1. The hydrogen energy levels displayed up to $n = 2$. The left hand plot displays the fine structure predicted by the Dirac energy relation. The two photon 1S-2S transition is displayed in pink, and the fine structure splitting of the 2P state in purple. The right hand plots present zoomed in sections which display the effects of the Lamb shift (green arrows) and hyperfine splitting (black arrows).

3.1.1 The Dirac energy

Dirac's model of quantum mechanics cohesively incorporates special relativity, from which naturally emerges the quantum mechanical property of spin. Spin, $\vec{s}$, is an intrinsic form of angular momentum which is carried by elementary particles such as the electron, with its own quantum number s. When the Dirac equation is applied to a hydrogen-like electron bound state, interactions between the electrons spin and its orbital angular momentum $\vec{\ell}$, among other relativistic effects, produces a fine structure in the energy levels. The energy-relation for

the fine structure of hydrogen is given by:

$$\mathcal{E}_{Dirac}(n,j) = mc^2\left[1+\frac{\alpha^2}{\left(n-\left(j+\frac{1}{2}\right)+\sqrt{\left(j+\frac{1}{2}\right)^2-\alpha^2}\right)^2}\right]^{-\frac{1}{2}}, \tag{3.2}$$

here α is the fine structure constant, j is the total angular momentum quantum number, and m is the reduced mass of the electron, given by

$$m = \frac{m_e m_p}{m_e + m_p}, \tag{3.3}$$

where m_e and m_p are the rest masses of the electron and proton respectively. Deriving equation 3.2 from the Dirac equation is beyond the scope of this thesis, but is covered in [72].

3.1.2 The Lamb shift

The energy relation 3.2 expresses that the energy of a state is dependent on only two quantum numbers: the principal quantum number n and the total angular momentum j. However, in 1947, an energy difference between the $2S_{1/2}$ and $2P_{1/2}$ was measured for the first time in the Lamb–Retherford experiment [73], which could not be explained through the Dirac equation. The discovery of what came to be known as the Lamb shift acted as a catalyst for major progress within quantum physics, which would produce techniques for renormalisation and development of quantum electrodynamics (QED).

The correction due to the Lamb shift increases the energy of all of the S states–with the largest effect on the $1S$ state, and decreases $\propto 1/n^3$ with the principal quantum number. The Lamb shift is the most complex part in theoretically determining the spectrum of hydrogen, with many contributing effects which must be understood through quantum field theory and renormalisation. The effects contributing to the Lamb shift, ordered by magnitude [74] are: electron self-energy; vacuum polarisation; radiative-recoil corrections; two-photon corrections; three-photon correction; finite nuclear size and polarisability; and nucleus self-energy.

3.1.3 Hyperfine splitting

The (anti)proton provides the confining potential for the (positron) electron, but it is also a quantum mechanical object with its own spin $\vec{I}$, quantised by quantum number $I = 1/2$. The spin of the proton produces a magnetic moment $\vec{\mu}_I = g_I \mu_N \vec{I}$, where g_I is the nuclear g factor (≈ 5.5857 [74]), and μ_N is the nuclear magneton [75]. The hyperfine splitting arises due to interactions between the proton's magnetic moment and the magnetic field generated by the electron's spin and orbital angular momentum. The angular momentum of the proton and electron couple, resulting in a total angular momentum for the atom $\vec{F}$ with quantum number

F which can take integer values between $|j-1/2|$ and $j+1/2$. This causes each fine structure state to split into multiple hyperfine substates, displayed for the $1S_{1/2}$, $2S_{1/2}$ and $2P_{1/2}$ states in the right hand side of figure 3.1.

The interaction between the proton's magnetic moment $\vec{\mu}_I$ and the magnetic field produced by the electrons results in the Hamiltonian

$$H_{\mathrm{HFS}} = -\vec{\mu}_I \cdot (\vec{B}_{\mathrm{spin}} + \vec{B}_{\mathrm{orbit}}) = A\vec{I} \cdot \vec{j}, \tag{3.4}$$

where $\vec{B}_{\mathrm{spin}}$ and $\vec{B}_{\mathrm{orbit}}$ are the magnetic fields generated by the spin and orbital angular momentum respectively, and A is the hyperfine structure constant, which is state dependent. The angular momenta $\vec{I}$ and $\vec{j}$ are in units of $\hbar$, the reduced Plancks constant. The expectation value of the Hamiltonian H_{HFS} provides the energy shift due to the hyperfine interaction, which is given by:

$$\mathcal{E}_{\mathrm{HFS}} = A\langle \vec{I} \cdot \vec{J} \rangle = \frac{A}{2}\{F(F+1) - I(I+1) - j(j+1)\}, \tag{3.5}$$

importantly, because the electric quadrupole interaction is zero for S states, this formula highly accurate. Highly precise experimental determination of the hyperfine splitting has been completed for the low principal quantum number states ($n = 1, 2$) [76][77].

$$\left.\frac{A}{h}\right|_{1S} = 1420405751.768\,\mathrm{Hz} \quad \text{and} \quad \left.\frac{A}{h}\right|_{2S} = 177556834.3\,\mathrm{Hz}. \tag{3.6}$$

A precise theoretical treatment of the hyperfine splitting requires complex contributions regarding the bound state nature of the proton [78] which are beyond the scope of this thesis–however the hyperfine structure constant can be well approximated using the following expression [79] [80]

$$A = \frac{2\pi\hbar c R_\infty \alpha^2 (m_e/m_p) g_I}{j(j+1)(\ell+1/2)n^3}, \tag{3.7}$$

where R_∞ is the Rydberg constant.

3.2 | In magnetic fields

The energy levels of the hydrogen atom in a field-free environment can be found by combining the Dirac energy, Lamb shift and hyperfine splitting in accordance to equation 3.1. However, in ALPHA large magnetic fields are used for the confinement of antihydrogen within an Ioffe-Pritchard trap. Magnetic fields shift the energy levels of hydrogen (and antihydrogen) through the Zeeman effect and diamagnetism.

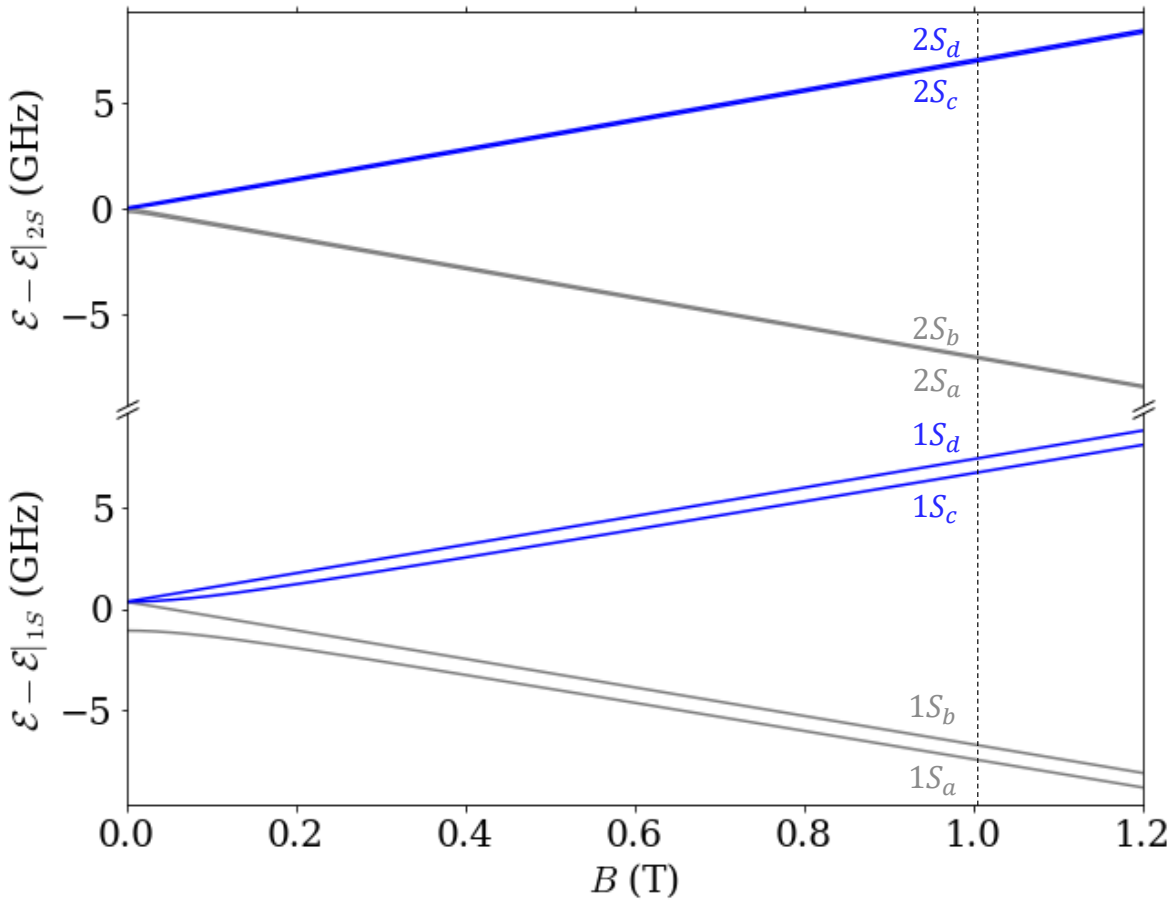

Fig. 3.2. The dependence of the 1S-2S hyperfine structure on external magnetic field (B). The blue line display trappable states, whereas the grey display untrappable states. The dotted horizontal line displays the nominal trapping field within ALPHA2.

3.2.1 The Zeeman effect

For each hyperfine state F there are $2F + 1$ magnetic substates, denoted by the magnetic quantum number m_F which takes the integer values between F and $-F$ and quantifies the projection of total angular moment $\vec{F}$ along an arbitrary axis z. The m_F states are degenerate in a field-free environment; however, in the presence of a magnetic field along z, the energy of the atom will depend on the projection of its magnetic moment along z, breaking the degeneracy of the m_F substates. The Zeeman effect can be approached using either the weak field approximation–where the external field can be treated as a perturbation of the $|F, m_F\rangle$ basis, or strong field approximation–where the external field dominates and the $|j, I, m_j, m_I\rangle$ basis is used. Neither limits provide an accurate estimation of the energy in intermediate fields, nor do they offer an accurate enough approximation for precision experiments in weak and strong limit. A complete picture considers superpositions of both basis states, and is known as the intermediate field Zeeman effect.

For the S states, $j = s = 1/2$, the electronic charge distribution is spherically symmetric, and the energy levels can be determined in a straightforward way. For S states the Hamiltonian

can be simplified to [81]

$$H = A(\vec{I}\cdot\vec{S}) + 2\left(-\mu_e(n)\vec{S} + \mu_{\rm p}(n)\vec{I}\right)\cdot\vec{B}, \tag{3.8}$$

where $\mu_e(n)$ and $\mu_p(n)$ are the magnetic moments of the (positron) electron and (anti)proton respectively, both of which depend of the principal quantum number, as they scale with binding energy. For S states this the magnetic moments are given by [35][82][83]

$$\mu_e(n) = \mu_e^{\rm free}\left[1 - \frac{\alpha^2}{3n^2} + \frac{\alpha^4}{2n^3}\left(\frac{1}{2n} - \frac{2}{3}\right) + \frac{\alpha^3}{4\pi n^2} + \frac{\alpha^2}{2n^2}\frac{m_e}{m_p}\right], \tag{3.9}$$

$$\mu_p(n) = \mu_p^{\rm free}\left[1 - \frac{\alpha^2}{3n^2} + \frac{\alpha^2}{6n^2}\frac{m_e}{m_p}\left(\frac{3 + 4\times 1.793}{1 + 1.793}\right)\right], \tag{3.10}$$

where $\mu_p^{\rm free}$ and $\mu_p^{\rm free}$ are the magnetic moments of the unbound proton and electron respectively. The Hamiltonian in equation 3.8 is solvable, resulting in energy eigenvalues given by Breit–Rabi formula [81] [84]:

$$\mathcal{E}_{HFS}(B)_{F=I\pm 1/2} = -\frac{A}{4} - 2\mu_p(n)m_F B \pm \frac{A}{2}\sqrt{1 + 2m_F x + x^2}, \tag{3.11}$$

where

$$x = \frac{2B\left(\mu_e(n) + \mu_p(n)\right)}{A}. \tag{3.12}$$

3.2.2 Diamagnetic Shift

The application of the external field can produce an extra magnetic moment that opposes the external field through diamagnetism. Due to their charge, electron orbitals can essentially be viewed as current loops with zero resistance. The application of an external field induces currents that generate a magnetic moment that opposes the field. The Hamiltonian due to diamagnetism is

$$H_{dia} = \frac{e^2}{8m_e e}B^2\left(x^2 + y^2\right) \tag{3.13}$$

Where x and y are the coordinates perpendicular to the external field (the area of induced current loop is proportional to $x^2 + y^2$). In the case of the S states the spherical symmetry means that the operators $x^2 = y^2 = \frac{1}{3}r^2$. We find the energy eigenvalues for the S states from first-order perturbation theory.

$$\mathcal{E}_{dia}\big|_{nS} = \frac{2}{3}\frac{e^2}{8m_e e}B^2\left\langle r^2\right\rangle \tag{3.14}$$

Evaluated for the $1S$ and $2S$ states these are:

$$\mathcal{E}_{dia}\big|_{1S} = \frac{e^2 a_0^2}{4m}B^2 \quad \text{and} \quad \mathcal{E}_{dia}\big|_{2S} = \frac{7e^2 a_0^2}{2m}B^2 \tag{3.15}$$

3.3 | 1S-2S transition frequency in ALPHA

Experimental determination [34] of the 1S-2S transition hyperfine centroid frequency is at a higher precision than the transition frequency calculated through theory alone, which is mostly limited by the evaluation of the Lamb Shift [78]. To adjust the measured hydrogen frequency to account for shifts due to the magnetic trap, one only needs to evaluate the Breit-Rabi formula and diamagnetic shift to determine expected transition frequency in ALPHA. The Ioffe-Pritchard trap in ALPHA can only confine the low-field seeking states of antihydrogen; the d-state, with $|F=1, m_F=1\rangle$; and the c-state, with $|F=1, m_F=0\rangle$. These undergo a two-photon transition to their equivalent 2S states. Using the measurement of the 1S-2S transition hyperfine centroid frequency, we get:

$$f_{1S-2S} = f_{MPQ} + \frac{1}{h}\left(\mathcal{E}_{HFS}(B)\big|_{2S} - \mathcal{E}_{HFS}(B)\big|_{1S}\right) + \frac{1}{h}\left(\mathcal{E}_{dia}(B)\big|_{2S} - \mathcal{E}_{dia}(B)\big|_{1S}\right) \tag{3.16}$$

Where $f_{MPQ} = 2\,466\,061\,413\,187\,035 \pm 10$ Hz. Evaluating explicitly for the $d-d$ and $c-c$ transitions gives [81]

$$f_{d-d} = f_{MPQ} + \frac{1}{4h}\left(A\big|_{2S} - A\big|_{1S}\right) + \frac{\mu_e(2)-\mu_e(1)}{2h}B + \frac{13e^2a_0^2}{4mh}B^2, \tag{3.17}$$

$$\begin{aligned} f_{c-c} = f_{MPQ} &+ \frac{1}{4h}\left(A\big|_{2S} - A^2\big|_{1S}\right) + \frac{13e^2a_0^2}{4mh}B^2 \\ &- \frac{1}{2h}\sqrt{A^2\big|_{1S} + \left(\mu_e(1)+\mu_p\right)^2 B^2} + \frac{1}{2h}\sqrt{A^2\big|_{1S} + \left(\mu_e(2)+\mu_p\right)^2 B^2}. \end{aligned} \tag{3.18}$$

3.4 | Transit time limited two photon lineshape

The 1S-2S transition has $\Delta\ell = 0$, which is forbidden by the electric dipole interaction– however, it can be excited through the simultaneous absorption of two photons [85]. The two-photon excitation has two benefits: Firstly, in the case that the two photons are counter-propagating, the lineshape is free from first-order Doppler broadening; Secondly, in a field-free environment two photons are required for the 2S state to decay back down to the ground state, which increases the lifetime of the state and narrows the natural linewidth. In ALPHA, $\overline{\mathrm{H}}$ are magnetically trapped within a volume larger than the laser beam, which they move into and out of during their trajectory in the trap. The finite interaction time of the atoms traversing the laser beam, the transit time, is much shorter than the natural lifetime and is the dominant cause of broadening of the 1S–2S spectrum measured in ALPHA. The effect of finite transit time on the line shapes of two-photon transitions can be derived following the procedure first introduced by François Biraben [86], and has been elaborated upon in many subsequent publications [36, 81, 87]. Here, and in Appendix A, I review this derivation.

The $1S$ state is excited to the $2S$ state through all possible intermediate virtual nP states [81]. To evaluate such a process, a standard tool to use is second-order time-dependent

perturbation theory. The perturbing Hamiltonian due to the laser light in the enhancement cavity which induces the transition is $H_I(t) = e\vec{r} \cdot \vec{E}(t)$. Given that $\langle 2S| H_I |1S\rangle = 0$ due to electric dipole transition selection rules, and assuming that the atom is initially in the $1S$ state such that its probability amplitude C_{1S} is 1 at $t = 0$, then the transition amplitude can be calculated by [88]

$$C_{2S}^{(2)}(t) = \frac{-1}{\hbar^2} \sum_n \int dt'' \langle 2S| H_I\left(t''\right) |nP\rangle e^{i\omega_{2SnP}t''} \int dt' \langle nP| H_I\left(t'\right) |1S\rangle e^{i\omega_{nP1S}t'}, \quad (3.19)$$

where $\omega_{2SnP} = E_{2S}/\hbar - E_{nP}/\hbar$ and $\omega_{nP1S} = E_{np}/\hbar - E_{1S}/\hbar$. The perturbing Hamiltonian is determined from the standing wave electric field produced by the Gaussian beam within the build up cavity, which has the form

$$\vec{E}(t) = \hat{\epsilon} E_0 \left[w_0/w(z)\right] \exp\left[-r^2/w^2(z)\right] \cos[kz] \cos\left(\omega_{\mathrm{L}} t\right), \quad (3.20)$$

where $\hat{\epsilon}$ is the polarisation of the lasers, w_0 is the minimum beam waist which occurs at the center of the cavity, r is the radial distance from the center axis of the beam, $w(z) = \sqrt{w_0^2\left(1 + z^2/Z_{\mathrm{R}}^2\right)}$ is the z dependent beam waist, $Z_{\mathrm{R}} = \pi w_0/\lambda$ is the Rayleigh length, and ω_L is the angular frequency of the laser $(2\pi f_L)$. The integrals in equation 3.19 are evaluated more explicitly in appendix A, following procedures outlined in literature [86][81][87]. The result is an expression for probability of exciting the $1S - 2S$ transition with two counter propagating photons during one pass of the laser. This is given by [36]

$$P_{2S}(f_0|v_\perp, \rho, z) = |C_{2S}|^2 = 32\pi \frac{\xi^2 I_0^2}{\hbar^2 \varepsilon_0^2 c^2} \frac{w_0^4}{w(z)^2 v_\perp^2} e^{-4\rho^2/w^2} e^{-\left[2\pi w (f_L - f_0)/v_\perp\right]^2}, \quad (3.21)$$

where $\xi \simeq 12.3\varepsilon_0 a_0^3$ [81], $f_0 = (E_{2S} - E_{1S})/2h$, ε_0 is the vacuum permittivity, and ρ is the distance of closest approach to beam axis during the $\overline{\mathrm{H}}$ trajectory, displayed visually in figure 3.3. The expression given in equation 3.21 is for a $\overline{\mathrm{H}}$ with perpendicular velocity $v_\perp$, during a single pass of the laser. To determine the lineshape of the entire ensemble of trapped atoms, $\bar{P}_{2S}$ we integrate over position and perpendicular velocity of a thermal distribution of temperature T. These integrals are evaluated more explicitly in appendix A, resulting in a double exponential lineshape [86]

$$P_{\mathrm{Biraben}} = \chi \exp\left(\frac{-4\pi w_0 |f_L - f_0|}{u}\right) = \chi \exp\left(\frac{|f_L - f_0|}{\gamma}\right), \quad (3.22)$$

where $u^2 = 2k_B T/M$, k_B being the Boltzmann constant, and M being the mass of an $\overline{\mathrm{H}}$. χ is given by [36]

$$\chi = \frac{16\pi^2 w_0^3}{u} \frac{\xi^2 I_0^2}{\hbar^2 \varepsilon_0^2 c^2} \bar{n}_{2D}, \quad (3.23)$$

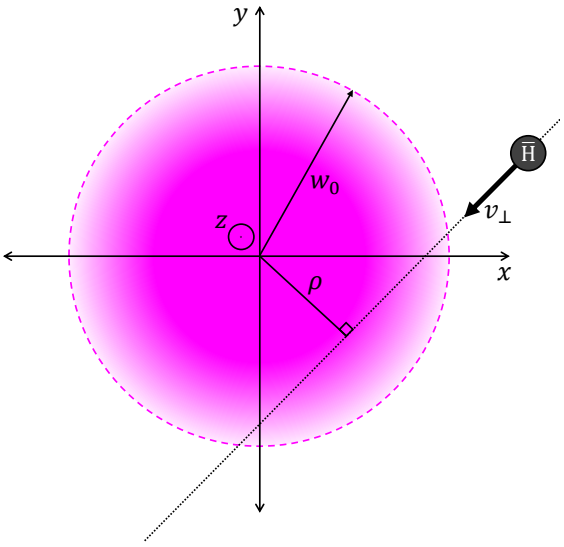

Fig. 3.3. Motion of antihydrogen in $x-y$ plane as it traverses the laser beam. The $\overline{H}$ are outside the beam at $t=-\infty$. The light field grows as it moves towards the beam, passing at its distance of closest approach of the beam axis ρ at $t=0$. Following this the light field diminishes again as the atom moves away. Based on figure from [86].

where $\bar{n}_{2D}$ is the average 2D cross sectional density of the $\overline{H}$ in the laser beam, I_0 is the intensity of the laser. Note that P_{Biraben} is a rate, with units of s^{-1}. Equation 3.22 is derived by treating the laser light as a small perturbation, as a result it is less accurate for higher laser powers, and for small detunings–near resonance perturbation theory breaks down, rounding off the infinitely shape peak of the double exponential. The double exponential given has a linewidth which is proportional to u/w_0. This is a consequence of transit time broadening–a wider beam or a colder sample results in more time spent in the beam, and produces a narrower linewidth.

3.5 | Other shifts and broadening effects

Finite transit time is the dominant broadening effect of 1S–2S spectra that have been measured in ALPHA. However, there are other broadening effects relevant for antihydrogen in ALPHA that must be considered.

3.5.1 Magnetic trap effects

For laser spectroscopy, currents on the Mirror coils have been optimised to produce a magnetic trap with a large flat region in the centre. The axial magnetic field for the trap configuration used for laser spectroscopy is shown in 3.4. In the flat region of the trap, the magnetic field, B_0, is measurable through ECR. The resonance frequency, f_0, adjusted for both Zeeman and diamagnetic shifts in this region, can be then calculated via equation 3.16. The magnetic trap, however, is not an infinite square well. While the $\overline{H}$ are more likely to be excited to the 2S state within the flat region of the trap, there is a small probability that the

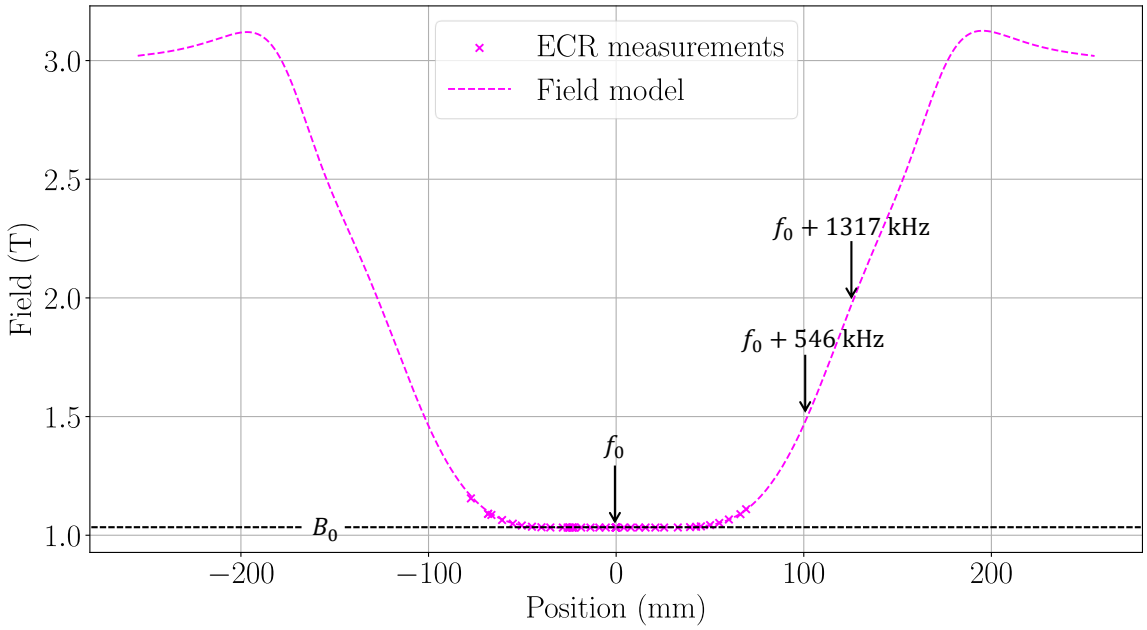

Fig. 3.4. Measurements and model of the on-axis magnetic field used for laser spectroscopy. The flat field region has a field strength of $B_0 \approx 1.032\,\mathrm{T}$, and a corresponding 1S-2S frequency of f_0. The relative resonance frequencies in regions of the trap where the field is 1.5 T and 2 T, determined via equation 3.17, are displayed.

$\overline{\mathrm{H}}$ are excited to the $2S$ state outside this region. Any antihydrogen excited to the $2S$ state in non-flat magnetic field regions will exhibit additional Zeeman and diagmagnetic shifts, as they occur at a magnetic field strength different from B_0. This induces an asymmetry in the observed lineshape, as there is an increase in excitation probability at positive detunings which are resonant with the transition in non-flat regions of the trap. The result is a line shape with a 'blue-tail' and rounded peak, which is shifted to frequencies above those expected at B_0. The effects of the magnetic trap on the lineshape can be diminished by using a magnetic trap configuration with a larger flat region and more abrupt edges so that $\overline{\mathrm{H}}$ spend less time in the non-flat region of the trap. Additionally, using a colder sample of $\overline{\mathrm{H}}$ also reduces the magnetic trap effects, as the colder $\overline{\mathrm{H}}$ will explore less of the high field regions of the trap and will spend proportionally more time in the flat region. Modifications to the double exponential lineshape which account for the magnetic trap effects are explored in [36] and in section 3.7 later in this chapter.

3.5.2 Stark Effect

The energy levels of antihydrogen will be shifted and broadened by the presence of external electric fields. Constant electric fields produce a DC Stark shift on the transition, whereas rapidly oscillating electric fields induce an AC Stark shift.

DC Stark shift

The energy levels of hydrogen are shifted by the presence of a constant (or slowly varying) electric field, known as the DC Stark shift. The DC Stark shift on the 1S state is negligibly small, equal to $\frac{\Delta\mathcal{E}_{1S}}{h} = -2.25(4\pi\varepsilon_0)a_0^3E^2 \approx -5.6\times10^{-8}\ \mathrm{Hz}\left(\frac{E}{\mathrm{Vm^{-1}}}\right)^2$ [81]. However, in 1 T the $2S$ state is in close proximity to the $2P$ states, which induces a larger DC Stark shift. The total DC Stark shift on the 2S state in 1 T, calculated using 2nd order perturbation theory, can be approximated as [81]

$$\frac{\Delta\mathcal{E}_{2S}}{h}\Big|_{1T} \approx -0.17\mathrm{Hz}\left(\frac{E_\parallel}{\mathrm{Vm^{-1}}}\right)^2 + 0.041\mathrm{Hz}\left(\frac{E_\perp}{\mathrm{Vm^{-1}}}\right)^2 \tag{3.24}$$

where $E_\parallel$ and $E_\perp$ are components of the electric field parallel and perpendicular to the magnetic field respectively. Due to their motion within a B field the $\overline{\mathrm{H}}$ will experience an extra component of $E_\perp$ in their rest frame, which can be determined through Lorentz transforms. The total $E_\perp$ experienced by the $\overline{\mathrm{H}}$ is given by $E'_\perp = \gamma(E_\perp + v_\perp B)$, where $v_\perp$ is the velocity perpendicular to $\vec{B}$ and γ is Lorentz factor. In the absence of any applied electric field, as is the standard case for spectroscopy in ALPHA, the only component of $\vec{E}$ which remains is $E'_\perp = \gamma v_\perp B$. The DC Stark shift therefore takes a range of values, from the distribution of $\overline{\mathrm{H}}$ velocities within the trap–resulting in broadening as well as a systematic shift. The magnitude of this effect can be reduced by either reducing the magnetic field, or by cooling the sample, resulting in lower $\overline{\mathrm{H}}$ velocities.

AC Stark shift

The time varying electric fields due to the laser induces a systematic shift on energy levels through the AC Stark effect. To determine the size of the shift on the $1S$ and $2S$ levels one must calculate the shift which occurs due to the $1S \rightarrow nP \rightarrow 1S$ and $2S \rightarrow nP \rightarrow 2S$ transitions respectively. The AC Stark shift coefficients, β_{AC}, for the $1S$ and $2S$ states when exposed to laser light near the 2-photon resonance frequency have been calculated [89] as -2.67827×10^{-5} Hz m^2 W^{-1} and 1.39927×10^{-4} Hz m^2 W^{-1} respectively. The shift of each energy level can be determined through $\Delta E_{AC} = h\beta_{AC}I$, where I is the intensity of the laser light (in W m^{-2}) which is resonant with the two-photon $1S-2S$ transition. The shift on the $1S-2S$ transition frequency due to the AC stark effect is therefore given by

$$\Delta f_{\mathrm{AC}}(2S) = f_{AC+}e^{-2r^2/w^2} = 1.667\times10^{-4}\,\mathrm{Hz}\frac{I_0}{\mathrm{W\ m^{-2}}}e^{-2r^2/w^2}, \tag{3.25}$$

where f_{AC+} if the maximum possible AC Stark shift, and I_0 is the intensity at the center of the laser. Taking into account the standing wave pattern formed by the counter-propagating beams, the central intensity is given by [81]

$$I_0 = \frac{4P}{\pi w_0^2}, \tag{3.26}$$

where P represents the circulating power within the cavity. Different $\overline{\text{H}}$ atoms will undergo the $1S-2S$ transition at varying radial displacements from the beam's center, leading to different AC Stark shifts. Therefore, the AC Stark effects systematically broaden the lineshape as well as shift it, smoothing out the peak of the double exponential. Modifications to the double exponential lineshape to incorporate the AC stark shift effects are discussed in section 3.7 of this chapter and derived in Appendix A.

3.6 | Detection routes

Many spectroscopy experiments measure photon absorption or emission to characterise a spectrum. However, obtaining a good signal-to-noise ratio requires a density of antiatoms beyond that currently produced at ALPHA. Although it is of future interest to use photon emission to characterise antihydrogen spectra, currently ALPHA mostly relies on antiproton annihilations as a detection mechanism for its experiments. Annhiliation can be used as a detection technique for 1S-2S spectroscopy, because once antihydrogen has been excited to the 2S state, there are routes for it to be detected via annihilation on the electrode walls. The two detection routes, shown in figure 3.5, are photoionisation by a third photon, and mixing into the $2P$ state–followed by subsequent decay into an untrappable $1S$ state.

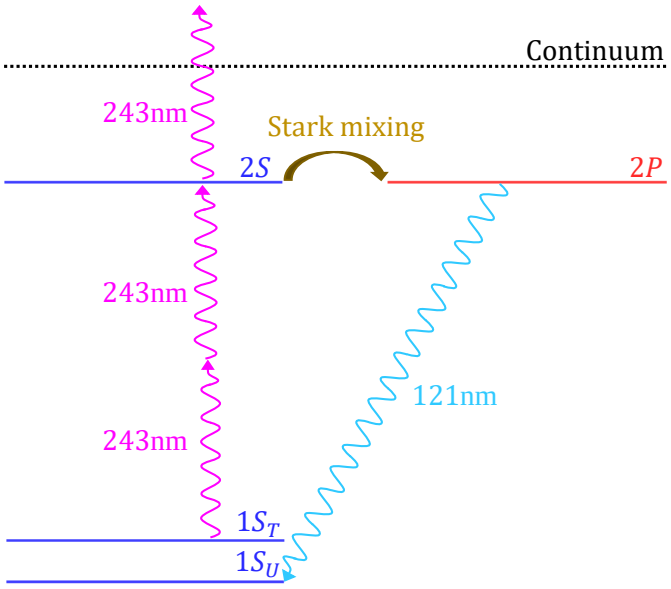

Fig. 3.5. Schematic of the two key detection routes for the $1S-2S$ transition in ALPHA. $1S_T$ and $1S_U$ represent the trappable and untrappable hyperfine ground states respectively. Verical axis not to scale.

3.6.1 $2S-2P$ mixing

In the presence of external electric fields there is Stark mixing between the $2S$ and $2P$ states. The $2P$ state can decay down to the ground states, both magnetically trappable and

untrappable, through the emission of a single 121 nm photon, as displayed in figure 3.5. The decay rate through this channel in a 1 T field, γ_{mix}, has been calculated using perturbation theory [81], and is given by

$$\gamma_{mix}\big|_{1T} \approx 0.015\mathrm{s}^{-1}\left(\frac{E_{\parallel}}{\mathrm{Vm}^{-1}}\right)^2 + 0.0055\mathrm{s}^{-1}\left(\frac{E_{\perp}}{\mathrm{Vm}^{-1}}\right)^2. \tag{3.27}$$

As described in section 3.5.2, the $\overline{\mathrm{H}}$ will experience an electric field in their frame of rest which is proportional to their velocity perpendicular to the magnetic field in the lab frame. At 1 T approximately 15% of the single photon decays from $2P$ will be to an untrappable high field seeking $1S$ state [81]. Untrappable states will annihilate on the electrodes, which will be detectable in the SVD. This route to annihilation is only possible once the $\overline{\mathrm{H}}$ has been excited to the $2S$ state by the laser, therefore providing a detection method for the $1S-2S$ excitation. Because the electric fields experienced by the $\overline{\mathrm{H}}$ is proportional to its velocity, this detection route to dependent on the temperature of the trapped sample; colder $\overline{\mathrm{H}}$ will mix less with the 2P state.

3.6.2 Photoionisation

Once excited to the $2S$ state, the positron is loosely bound enough to be excited to the continuum by an additional 243 nm photon from the $1S-2S$ laser, as displayed in figure 3.5. Once the $\overline{\mathrm{H}}$ has been ionised, the resulting antiproton is no longer confined by the magnetic minimum trap, and therefore will escape and annihilate on the electrodes. Because ionisation cannot occur directly through the absorption of a 243 nmn photon from the $1S$ state, this provides a detection method for the $1S-2S$ excitation. This detection route depends on the absorption of an additional photon, and will therefore increase with laser power. The rate of photoionisation has been determined numerically in [81], giving

$$\gamma_{ion}\big|_{1T} \approx I \cdot 7.57\times10^{-4}\mathrm{s}^{-1}\frac{I}{\mathrm{W\,m}^{-2}}. \tag{3.28}$$

The rate of photoioniation will also increase as the temperature of the trapped $\overline{\mathrm{H}}$ sample decreases– as colder $\overline{\mathrm{H}}$ will spend more time in the laser. Photoionisation reduces the lifetime of the 2S state, which induces additional broadening of the linewidth which is proportional to the photoionisation rate [81].

Photoionisation also provides an alternative detection method which does not depend on annhilation: ionised antiprotons can be recaptured in an electrostatic potential and subsequently ejected onto an MCP, which can be used as a detection method for the $1S-2S$ transition. Because this method relies on particle charge rather than annihilation, it has the advantage of also being applicable for hydrogen spectroscopy. This method therefore opens the door to direct comparison experiments, whereby hydrogen and antihydrogen spectroscopy is conducted within the same experimental apparatus.

3.7 | Modified lineshape functions

The double exponential function, outlined in section 3.4, describes a transit time limited two photon transition for atoms in a field-free environment. This is a different scenario from ALPHA, where antihydrogen is trapped within a magnetic minimum trap, which distorts the lineshape. One can make intuitive modifications to the double exponential to better accommodate the effects of the magnetic trap, producing a lineshape function which is expressible in a closed form. A simple modification is to make the change to an asymmetric double exponential, with different decay factors on either side of the peak. This modification follows

$$P_{\text{Biraben}} = \chi \exp\left(\frac{|f_L - f_0|}{\gamma}\right) \rightarrow P_{\text{asy}} = \begin{cases} \chi \exp\left(\frac{f_L - f_0}{\gamma_{\text{R}}}\right) & f_L \leq f_0 \\ \chi \exp\left(\frac{f_0 - f_L}{\gamma_{\text{B}}}\right) & f_0 < f_L \end{cases}, \tag{3.29}$$

where P_{asy} is the asymmetric double exponential lineshape function, and γ_R and γ_B are the independent exponential decay factors for the function below and above the peak, respectively. By making γ_B larger than γ_R it is possible to account for the asymmetry seen in our lineshape due to the magnetic trap, discussed in secion 3.5.1. Due to the broadening effects described in the sections above, and due to the breakdown of perturbation theory near resonance, the infinitely sharp peak of the double exponential is not what is observed in experiment. To smooth out the peak, we can take the convolution of the asymmetric double exponential, P_{asy}, with a Gaussian function with width of σ. This Gaussian convolution asymmetric double exponential (GCADE) function, P_{GCADE}, is given by,

$$\begin{aligned} P_{\text{GCADE}} =& \frac{1}{\sigma\sqrt{2\pi}} \exp\left(-\frac{1}{2}\left(\frac{x - x_0}{2\sigma}\right)^2\right) * P_{\text{asy}} \\ P_{\text{GCADE}} =& \chi \frac{\sigma\sqrt{\pi}}{\sqrt{2}} \left[\exp\left(\frac{\sigma^2}{2\gamma_{\text{R}}^2} + \frac{f_L - f_0}{\gamma_{\text{R}}}\right)\left(1 - \text{erf}\left(\frac{\sigma}{\sqrt{2}\gamma_{\text{R}}} + \frac{f_L - f_0}{\sqrt{2}\sigma}\right)\right) \right. \\ & \left. + \exp\left(\frac{\sigma^2}{2\gamma_{\text{B}}^2} - \frac{f_L - f_0}{\gamma_{\text{B}}}\right)\left(1 - \text{erf}\left(\frac{\sigma}{\sqrt{2}\gamma_{\text{B}}} - \frac{f_L - f_0}{\sqrt{2}\sigma}\right)\right)\right], \end{aligned} \tag{3.30}$$

where erf is the error function. The modifications to P_{Biraben} to produce the P_{asy} increases the number of parameters from four (χ, f_L, f_0, γ) to five (χ, f_L, f_0, γ_R, γ_B), and P_{GCADE} has one additional parameter σ. The modified lineshape functions are visualised in figure 3.6, alongside the P_{Biraben} lineshape.

The functions P_{asy} and P_{GCADE} are produced by intuitive modifications to P_{Biraben} and are convenient, since they have a closed form. However, their development does not follow a rigorous physical derivation, making it challenging to associate all their parameters with physical quantities, as is the case for P_{Biraben}. The closed-form functions can be associated with

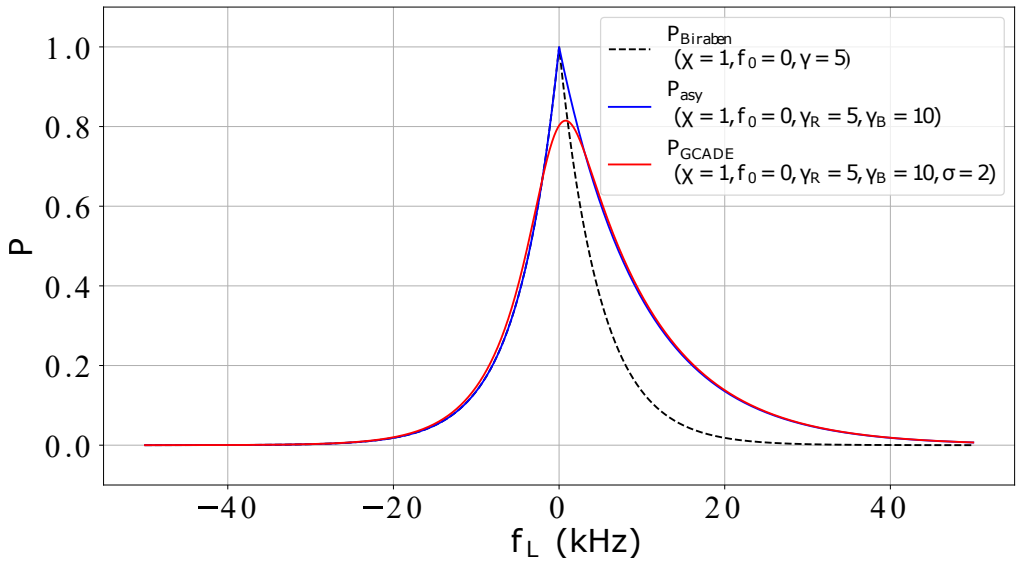

Fig. 3.6. Modified closed-form lineshape functions P_{asy} and P_{GCADE}, displayed alongside the standard lineshape P_{Biraben}.

the experimental parameters by fitting them to the results of simulations of 1S-2S spectroscopy in ALPHA to fix their shape. This procedure is discussed in more detail in chapter 8.

By making some assumptions about antihydrogen spectroscopy in ALPHA, it is also possible to derive lineshape functions based on physical principles [36]. So-called physics-driven functions are easier to relate to experimental parameters but do not necessarily have a closed form. The resonance frequency of the 1S-2S transition is dependent on the position of the antihydrogen in the magnetic trap due to the Zeeman and diamagnetic effects, as discussed in section 3.5.1. We can then make the assumption that excitations only happen when antihydrogen is within the laser beam, and that the magnetic field is approximately constant across the width of the laser beam. This reduces the dimensions of the picture; the resonance frequency, f_0, of the antihydrogen that gets excited is dependent only on its axial position z in the trap. We assume the axial position in the trap which is approximately the same as the axial position within the laser (the laser enters the trap at an angle of 2.3°, for simplicity we assume this is zero). How much the resonance frequency varies dependent on position is given by

$$f_0(z) = f_{x-x}(B(z)), \tag{3.31}$$

where f_{x-x} is the magnetic field dependent transition frequency for the $d-d$ or $c-c$ transition respectively, as given by equations 3.17 and 3.18, and $B(z)$ is the on-axis magnetic field in the trap. If we assume that the perpendicular velocity, $v_\perp$, is not dependent on the axial position z, then the transition probability only depends on z through how it varies the transition frequency. In this can the transition rate at a specific z is given by

$$P_{\text{Biraben},\,z} = \chi \exp\left(\frac{\left|f_L - f_0(z)\right|}{\gamma}\right), \tag{3.32}$$

which is the same as equation 3.22, except with a z dependence on f_0. Assuming our antihydrogen sample has a thermal energy distribution, then the on-axis probability density of trapped antihydrogen, $\mathcal{P}(z)$, is the same as atoms confined by the potential $U(z)$ at thermal equilibrium, which is proportional to [90]

$$\mathcal{P}(z) = N_z e^{-U(z)/k_B T} = N_z e^{-\mu_B (B(z)-B_0)/k_B T}, \tag{3.33}$$

where B_0 is the minimum on-axis field, and N_z is a constant which ensures normalisation in z. We can then integrate over this probability distribution, to produce a lineshape function for the entire trapped ensemble of antihydrogen in ALPHA [36], combining equations 3.33 to give

$$P_{\text{trap}}(f_L, \chi, T, B(z)) = \chi N_z \int_{z_{min}}^{z_{max}} \exp\left(\frac{-4\pi w_0 \left|f_L - f_0(z)\right|}{\sqrt{2k_B T/M}}\right) \exp\left(\frac{-\mu_B (B(z) - B_0)}{k_B T}\right) dz. \tag{3.34}$$

Because $B(z)$ does not have a convenient analytical form, the integral in P_{trap} must be completed numerically. While P_{trap} does not have a convenient closed form, it benefits from the fact that its parameters are related to physical quantities. The AC stark shift can also be incorporated into a physics-driven model, following the derivation in Appendix A. The resulting expression is

$$P_{\text{trap, AC}} = \chi N_z N_{AC} \int_0^{\sqrt{\frac{2}{3}} f_{\text{AC}_+}} \frac{w_0}{2\sqrt{2}} \frac{f_{AC}}{(\sqrt{\frac{2}{3}} f_{\text{AC}_+})^2 \sqrt{\log\left(\frac{\sqrt{\frac{2}{3}} f_{AC_+}}{f_{AC}}\right)}} df_{AC}$$
$$\int_{z_{\min}}^{z_{\max}} \exp\left(\frac{-\mu_B \left(B(z) - B_0\right)}{k_B T}\right) \exp\left(\frac{-4\pi w_0 \left|f_L - f_0(z) - \frac{f_{AC}}{2}\right|}{\sqrt{2k_B T/M}}\right) dz. \tag{3.35}$$

The lineshape function $P_{\text{trap, AC}}$ contains an extra integral over AC stark shift, f_{AC}, which also must be evaluated numerically. N_{AC} is a normalisation constant for the f_{AC} integral. Both physics driven lineshapes functions P_{trap} and $P_{\text{trap, AC}}$ are plotted, alongside the standard double exponential P_{Biraben}, in figure 3.7. As can be seen, the magnetic field integral produces asymmetries in the lineshape, and the AC stark shift integral shifts the lineshape and rounds off the peak.

3.8 | Simulations

As discussed in the previous section, the modified line shapes rely on simplifying assumptions about the nature of 1S-2S spectroscopy of antihydrogen within ALPHA. Computational simulations which model the dynamics of magnetically trapped hydrogen interacting with the spectroscopy laser can be used to produce more comprehensive theoretical predictions about 1S-2S spectroscopy in ALPHA. Differences between the spectra measured experimentally and

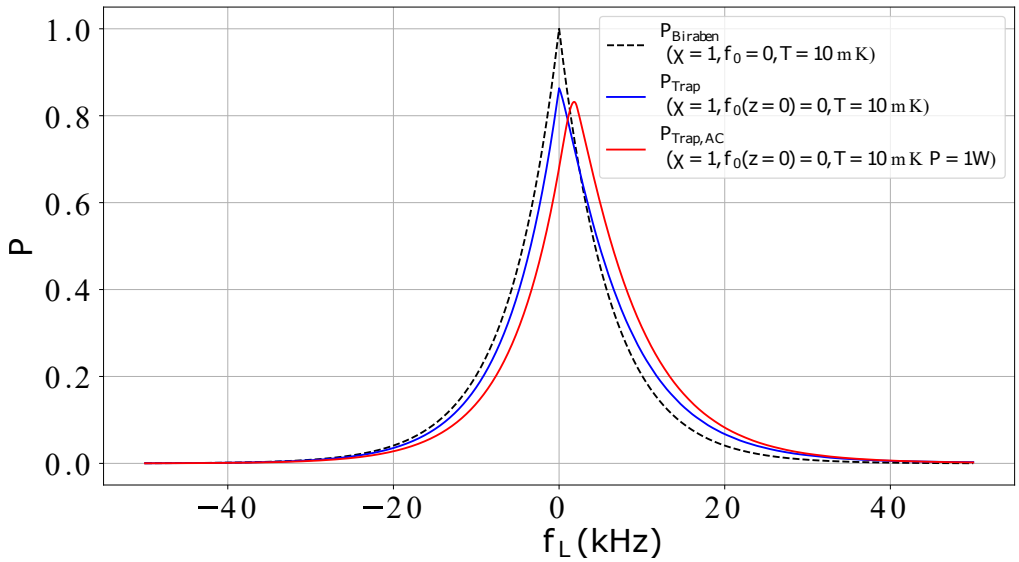

Fig. 3.7. Physics-driven lineshape functions P_{trap} and $P_{\text{trap, AC}}$, displayed alongside the standard lineshape P_{Biraben}. The magnetic field $B(z)$ input into these functions comes from models of the laser flat field.

those generated by simulations could be attributable to a deviation in the 1S-2S transition frequency, potentially indicating CPT symmetry violation. The simulation was originally developed by F. Robicheaux [81], and the code has since been developed by many ALPHA collaborators.

The atoms are simulated as classical particles moving in a potential $U = \mu B(z, y, z)$, where μ represents the magnetic moment of the confined antihydrogen. The three-dimensional magnetic field $B(z, y, z)$ is calculated on a spatial grid by employing a Biot-Savart approximation of the octupole and mirror coils, with interpolation used to compute the field at positions between grid points. A fourth order symplectic integrator [91] is employed to simulate the movement of atoms within the trap. At the start of the simulation, an atom is initialised in a high Rydberg state ($n = 25$) at a point within an ellipsoid that matches the size of the plasma of positrons used to generate antihydrogen, with velocities randomly selected from a thermal distribution. The rapid decay of the Rydberg state is modelled in the first few seconds of the simulation [61], which rapidly changes the magnetic moment until it reaches the ground state.

Should the simulation include laser cooling of antihydrogen prior to spectroscopy, it is performed subsequent to cascade cooling. A semiclassical treatment of laser cooling is used to simulate the interaction between the antihydrogen and the pulsed Lyman-α laser [92]. During each pulse, if the atom is within the laser waist, the simulation computes the probability of a photon being absorbed, which depends on the laser intensity, detuning (in the atom's frame of reference), and magnetic field at the antihydrogen's position. A random number is then drawn to determine whether the antihydrogen absorbs a photon. If a photon is absorbed, the antihydrogen receives an initial momentum kick of h/λ in the propagation direction of the laser, followed by a subsequent momentum kick of h/λ in a random direction due to the

emission of a photon. Antihydrogen atoms that remain trapped during the cooling process then proceed to the simulation of 1S-2S spectroscopy.

The 243 nm laser field is subsequently turned on, and the simulation iterates through the detuning array as per the experiment. If an atom approaches the laser beam, the code numerically solves the optical Bloch equations to calculate the probability of excitation to the 2S state, and a random number is drawn to determine if the atom is excited to the 2S state [81]. Once in the 2S state, at each time step the atom has a probability of: 1) staying in the 2S state, 2) decaying to the trappable 1S state via the emission of two photons, 3) decaying to the trappable 1S state through mixing to the 2P state and subsequent emission of a single photon, 4) decaying to a untrappable state through the same process, 5) being photoionised by a third photon (if in the laser). The probability of each of these depends on the atom's location and velocity within the trap, and at each timestep a random number is drawn to determine whether the atom undergoes any of these processes. The code halts if an atom hits the electrode wall after decaying to an untrappable state, or if an atom is photoionised. The code also terminates when the assigned laser illumination duration in the simulation has elapsed.

When the code terminates, the simulation time and laser frequency at this time is recorded, along with the position and internal state of the atom. This code is ran independently many thousands of times, with different randomly drawn initial conditions. The recorded information from the large number of simulations can be used to generate simulated lineshape, displayed in figure 3.8. Additionally, the simulations can be used to produce 'kickout curves', displayed in figure 3.9, which depict the temporal evolution of the simulated antihydrogen population being progressively removed from the magnetic trap during 1S-2S spectroscopy.

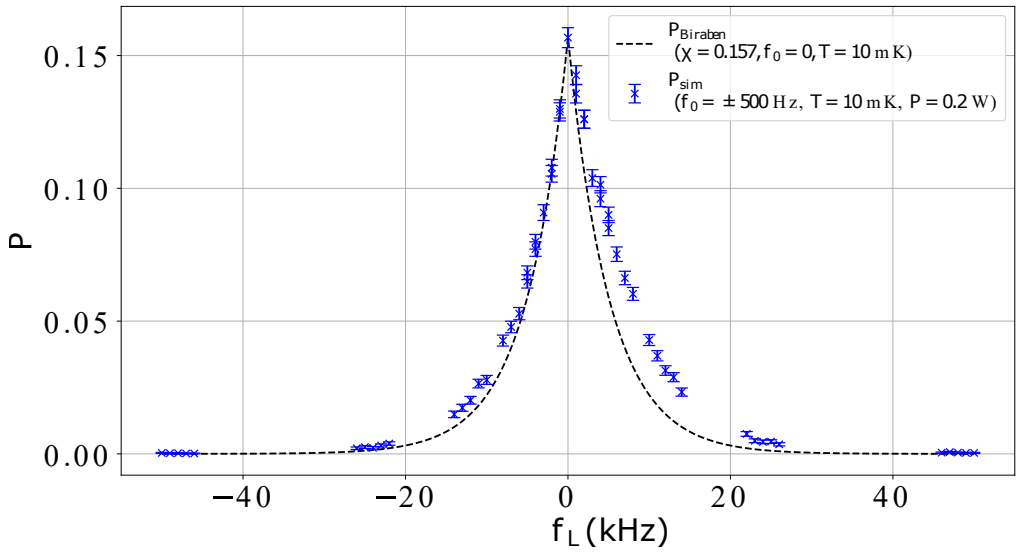

Fig. 3.8. Simulated spectrum with 200 s exposure per laser frequency. The resonance frequency f_0 has been modified by a random freuqency between -500 and 500 Hz to blind the simulation. Antihydrogen starts at 10 mK and undergoes no laser cooling.

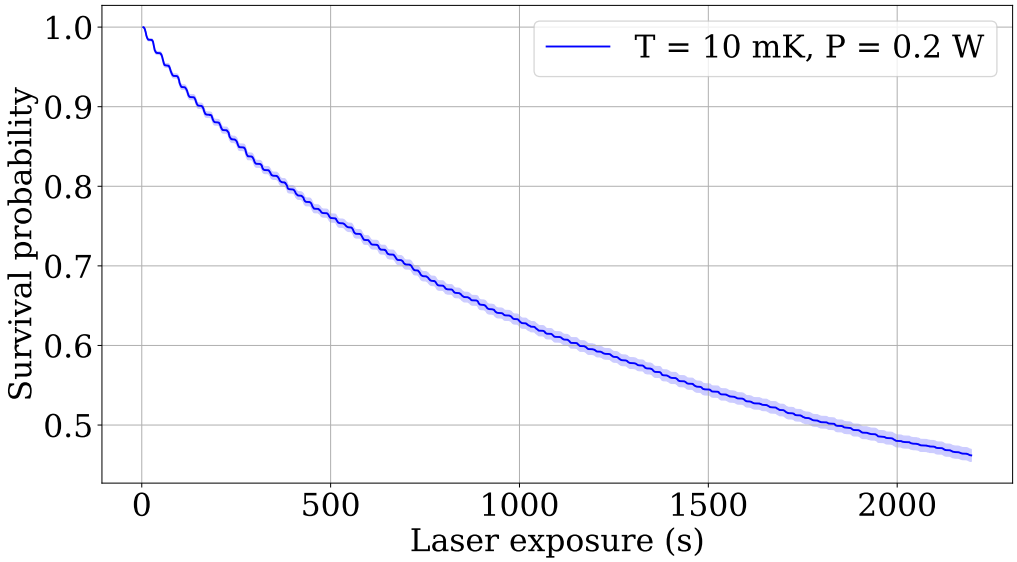

Fig. 3.9. Curve displaying atom survival probability. Shaded areas indicate counting uncertainty.

CHAPTER 4

Time-Frequency Transfer with a Hydrogen Maser

> *The maser is fine.*
>
> — **Team Metrology**

Frequency f is a parameter which, along with amplitude and phase offset, fully describes the nature of an infinite periodic oscillation; it defines the number of complete cycles per unit time $U(t) = U_o \cos(2\pi ft + \phi)$. Frequency is the measurable quantity which can be determined with the highest degree of accuracy [93], this is due to its repeating features (for example zero crossings) which can be counted directly. Laser spectroscopy of antihydrogen in ALPHA is a frequency measurement and the high precision of previous measurements of the 1S-2S transition frequency [35] reflects this. The second, which is the reciprocal of the Hertz, is the last remaining base unit in the SI system which still has a physical realisation [94]. As a result, the nature of frequency measurements is that they must be directly compared to a frequency standard–a device capable of providing a stable known frequency with a given accuracy. Previous characterisation of the 1S-2S transition spectrum in antihydrogen [35] was referenced to a GPS disciplined quartz oscillator, which introduced some significant uncertainty in determining the frequency. Upgraded metrology instrumentation has been planned since this measurement; in October 2020 the ALPHA collaboration obtained an active hydrogen maser for integration into its metrology system. Whilst hydrogen masers boast an impressive short to medium term stability, their long term stability is known to be plagued by slow drifts [95], which must be characterised and corrected. In 2022 the experiment also integrated a caesium fountain clock - a primary standard - for the means of correcting the maser (discussed in further detail in the following chapter 5). Additionally, alternative methods exist to measure the frequency drift of the maser, either instead of the caesium fountain (which was necessary prior to its arrival) or as a supplementary method. Specifically, the Global Navigation Satellite System (GNSS) can be used to transfer time and frequency data between metrology institutes to compare respective frequency standards with high levels of precision.

We start this chapter by reviewing the basics of how frequency standards work, and how we quantify their stability with measures such as Allan deviation. Following this we shall introduce

the active hydrogen maser acquired by ALPHA, briefly examining its principles of operation, its stability and drifting behaviours. We then turn to time-frequency transfer methods, discussing how one swaps between a time and frequency basis when comparing references. Following this we summarise the observables and products used in GNSS methods for time frequency transfer. We then examine the two time-frequency transfer methods, and how they are implemented by ALPHA: Common-view and Precise Point Positioning (PPP). Finally we examine the frequency behaviour of the maser as measured by these methods in the years of 2021 and 2022.

4.1 | Frequency standards and stability

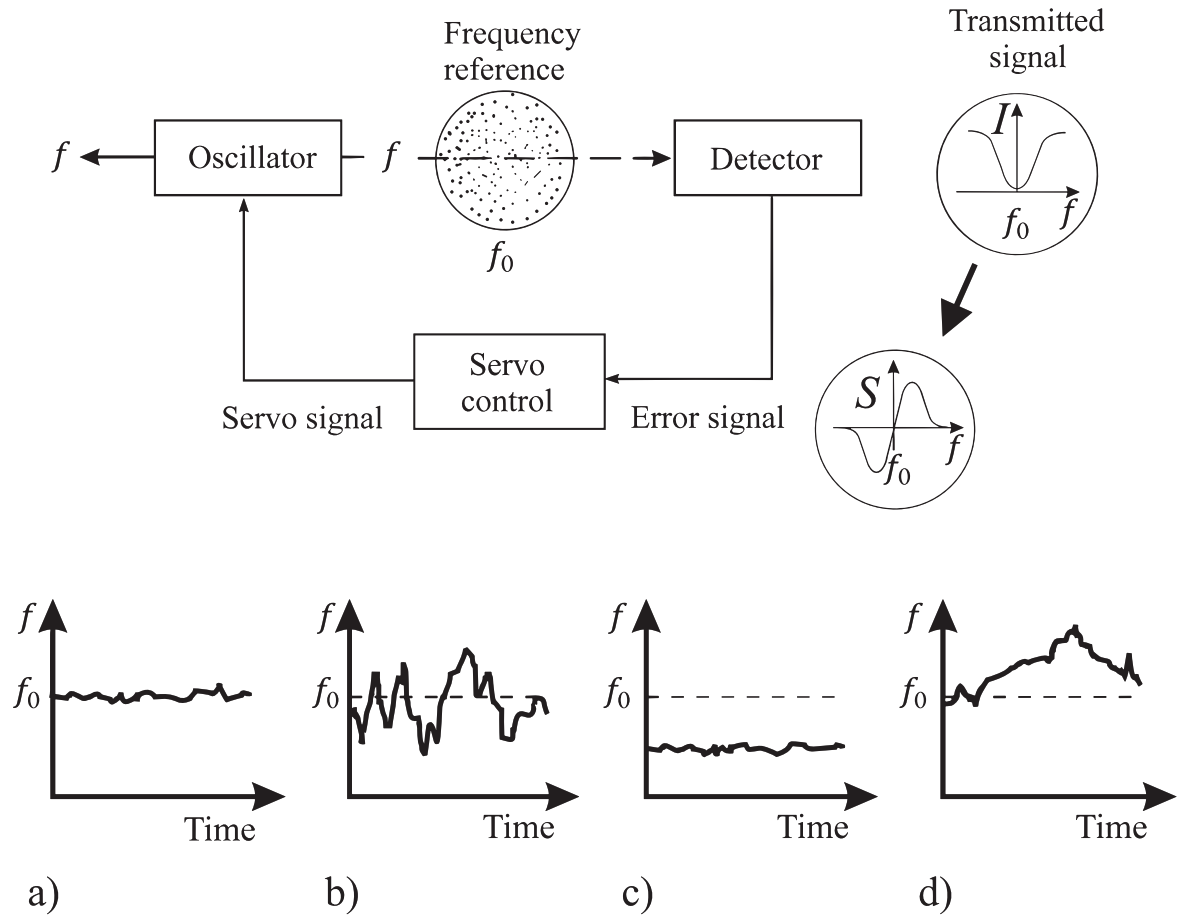

Fig. 4.1. Top: Operational principle of a frequency standard using feedback control. Bottom: Demonstration of accuracy and stability of a frequency standard. a) is both accurate and stable, b) is accurate but not stable, c) is stable but not accurate, d) is neither accurate nor stable. Figure has been adapted from [93].

A frequency standard is an instrument which provides a stable and known frequency which can be used for calibration or reference. The most accurate of these are atomic frequency standards, which reference their output frequency to an atomic transition. An atomic frequency standard typically operates through the interplay of four key components within a feedback loop: the atomic reference, the detector, the discriminator and the oscillator–depicted in figure

4.1. The oscillator provides a near-resonant frequency signal, f, which is compared to an atomic frequency reference which is resonant at f_0. The atomic transition signal is detected, and the discriminator converts the atomic signal into an error signal, S, which is proportional to deviation between the oscillator and reference frequencies $S \propto f - f_0$. The error signal is received by the servo control, which produces a servo signal that corrects the oscillator to minimise the frequency deviation. Through this loop the oscillator is regularly corrected such that its frequency is close to the reference frequency $f \approx f_0$.

The accuracy of a frequency standard is a measure of how close the output frequency is to the nominal frequency, whereas the stability of a standard is how much its frequency varies as time progresses. The accuracy and stability of a standard is illustrated by the four bottom plots of figure 4.1. Fractional frequency error, $y(t)$, is a unitless measure of a frequency standards accuracy at time t. Fractional frequency error is given by

$$y(t) = \frac{f(t) - f_0}{f_0}, \tag{4.1}$$

where $f(t)$ is the frequency of the standard at time t, and f_0 is the nominal frequency of the standard. Another useful measure of accuracy is average fractional frequency error $\bar{y}(t, \tau)$, which is the average fractional frequency between t and $t + \tau$. A measure of the stability of a frequency standard is Allan variance $\sigma_y^2(\tau)$, and its square root Allan deviation $\sigma_y(\tau)$. Allan variance is given by

$$\sigma^2(\tau) = \frac{1}{2N} \sum_{i=0}^{N} \left(\bar{y}(t + (i+1)\tau, \tau) - \bar{y}(t + i\tau, \tau)\right)^2. \tag{4.2}$$

Overlapping Allan variance is a form of the normal Allan variance which makes maximum use of the dataset by using overlapping samples to form the variance. This is given by

$$\sigma^2(\tau) = \frac{1}{2N} \sum_{i=0}^{N} \left(\bar{y}(t + \tau + i, \tau) - \bar{y}(t + i, \tau)\right)^2. \tag{4.3}$$

The overlapping form of Allan variance will be used throughout this thesis, unless explicitly stated otherwise.

4.2 | The hydrogen maser

A maser (**m**icrowave **a**mplification by **s**timulated **e**mission of **r**adiation) is an instrument which produces a stable reference frequency through amplification and stimulated emission of an atomic transition in the microwave region of the spectrum. There are different atomic or molecular species that can be used to construct masers, but hydrogen is the most ubiquitous. The hydrogen maser uses the ground state hyperfine transition, $|F = 1, m_F = 0\rangle \longrightarrow |F = 0, m_F = 0\rangle$, of atomic hydrogen as its reference frequency. This corresponds to the well known 21 cm line

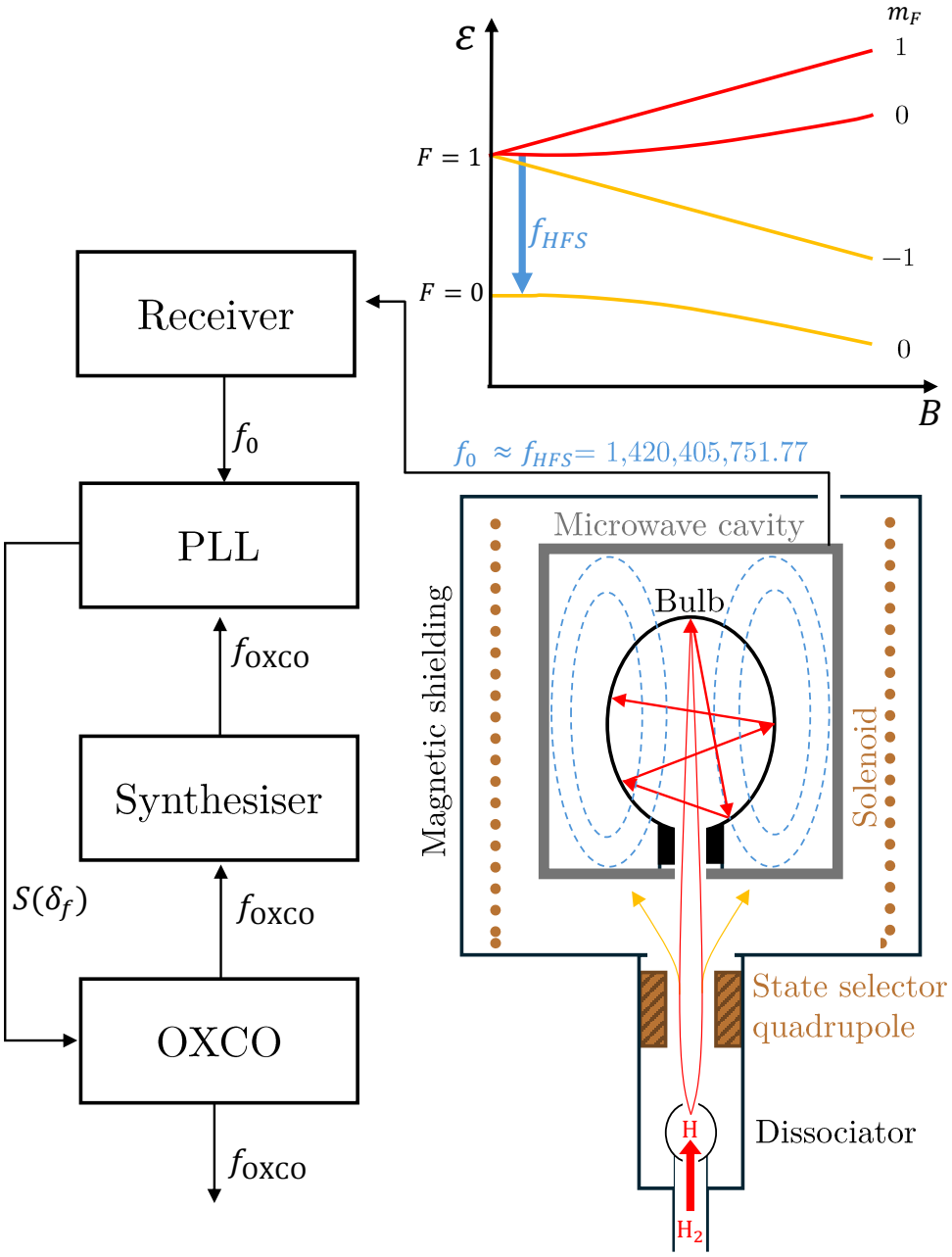

Fig. 4.2. Schematic of hydrogen maser, displaying the key hardware components, operational feedback loop, and the magnetic dependence of the ground state hyperfine energy levels.

in hydrogen, which has a transition frequency of 1,420,405,751.7667 ±0.0009 Hz [76]. The ALPHA collaboration acquired an iMaser 3000, constructed by T4Science, for its metrology upgrades. Hydrogen masers demonstrate remarkable short-term and medium-term stability, outperforming caesium fountain references; however, on longer timescales they begin to drift and require correction.

4.2.1 Physics package

To acquire a signal from a hydrogen transition, first atomic hydrogen must be produced. Molecular hydrogen, H_2 is supplied from a heated solid state metallic storage compound

$(LaNi5H)_x$, which releases molecular hydrogen as a function of temperature. The temperature is controlled to produce a stable hydrogen pressure in the dissociator bulb, which is then converted into atomic hydrogen by a plasma discharge. The atomic hydrogen leaves the dissociator bulb through a collimator, and directed through the state selector–a quadrupole magnet with a minimum field strength that increases radially from its axis of symmetry. The direction of atomic hydrogen flow is along the axis of symmetry, and the field gradient directs the atoms in the low field seeking hyperfine levels into a Teflon coated quartz storage bulb, displayed with the red arrows in figure 4.2, whilst deflecting the lower energy high field seeking atoms, displayed with the yellow arrows in figure 4.2.

The result of the state preparation is a population inversion within the bulb, where the high-field seeking population (the energy levels indicated in red in figure 4.2) exceeds the low-field seeking population (the energy levels indicated in yellow in figure 4.2), allowing for stimulated emission over absorption. The quartz storage bulb is located at the centre of a temperature-stabilised, silver-coated, glass-ceramic microwave cavity, which has the dimensions tuned such that the TE_{011} mode is resonant with the 21 cm line $f_0 \approx f_{HFS}$. The population inversion of the atomic hydrogen produces preferential stimulated emission over absorption, providing a gain medium which amplifies the microwave radiation of the surrounding cavity. For an active hydrogen maser, which the iMaser 3000 is, the gain provided by the hydrogen atoms is high enough that the microwave cavity can start and sustain its own oscillation. In the case of a passive maser the cavity is supplied an external frequency which is tuned to produce a maximum output from the hydrogen sample. The hydrogen atoms travel ballistically within the quartz bulb for around 1s, during which they interact with the microwave field and undergo many collisions with the Teflon coated walls of the bulb. During this time the atoms are confined to a spatial region which is smaller than the transition wavelength (21 cm) in every dimension, which results in a stimulated emission signal is free from first order Doppler broadening. The reduced atom-wall interaction due to Teflon coating, the long (≈1s) atom-field interaction time, and first order Doppler cancellation all contribute to producing a stable atomic frequency with a narrow linewidth.

4.2.2 Electronic package

Two radio frequency loops are connected to the cavity: a coupling loop for calibration purposes and a receiving loop which is responsible for extracting the atomic signal. The amplified frequency is extracted via the receiving loop to a low noise receiver, which amplifies the extremely low maser signal (around 10^{-13} W) by 20 dB. The signal is then down-converted to ≈ 405 kHz in three steps by mixing with intermediate frequencies derived from the maser oscillator, and oven-controlled crystal oscillator (OXCO), which plays an important role as the main oscillator, from which the reference frequency is extracted for use outside the maser. The 405 kHz signal is then phase-compared to the synthesiser output, which is derived from the OCXO, using a phase locked loop (PLL), the output of which is then sent to the OCXO as

a correction signal. In this manner the 5 MHz OCXO frequency is constantly corrected by the hydrogen reference. The 5 MHz OXCO output is used to synthesise a 10 MHz and 100 MHz signal, providing a total of three different stable and usable output frequencies for uses external to the maser. A one pulse per second (1 PPS) clock is derived from the 5 MHz output of the maser, which produces 1 Hz pulses which is used as a reference for a GNSS receiver.

4.2.3 Performance and stability

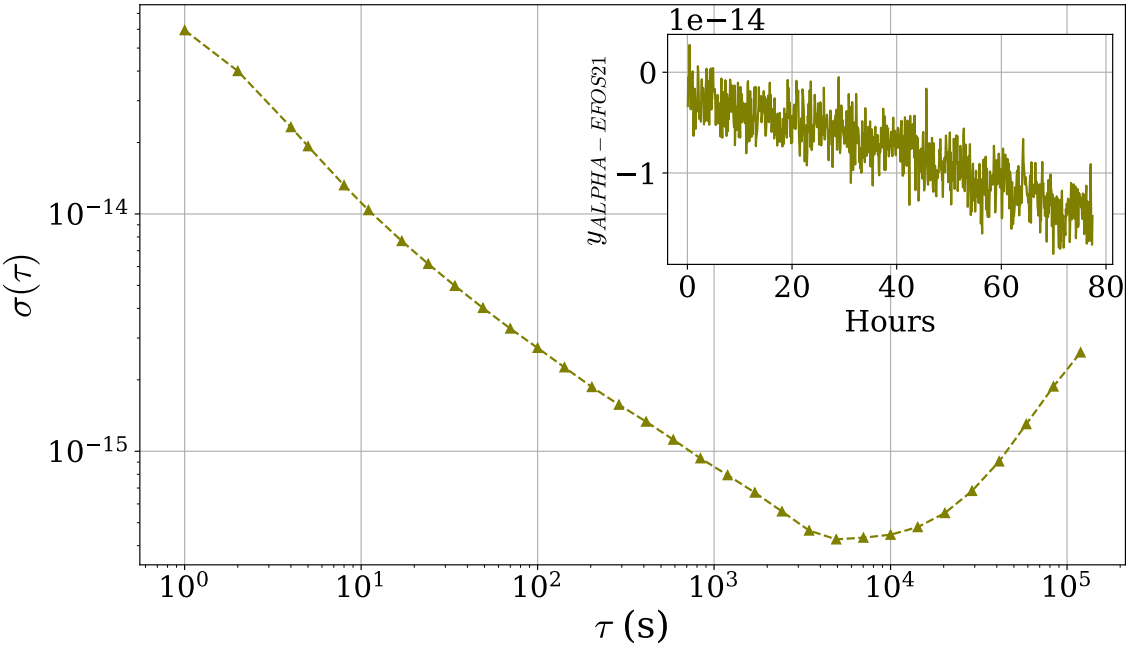

Fig. 4.3. Allan Deviation of our Hydrogen maser was measured on site by T4Science, through beatnote with their EFOS21 maser. Inset displays the beatnote fractional frequency, in five minute bins. Data provided by Gilles Cibiel at T4Science.

The hydrogen maser demonstrates an Allan deviation, $\sigma(\tau)$, which drops down to below 1×10^{-15}. The frequency stability for the maser acquired by ALPHA was measured directly at T4Science by beating it against a second maser (EFOS21); the Allan deviation of the measurement is displayed in figure 4.3. To perform such a precise measurement of the maser stability requires a second maser, such that the beatnote between the two maser frequencies can be measured. As a result we have been unable to repeat these measurements within our metrology lab. However we have been able to measure its stability through GNSS methods, discussed later in this chapter, and through comparisons to the caesium fountain clock (chapter 5).

The mechanisms which limit the frequency stability of the hydrogen maser are well known [93] [95]. For low averaging times ($\tau < 100s$) the stability of a maser is limited by white phase noise, causing the Allan deviation to vary as $\sigma(\tau) \propto \tau^{-1}$. The dominant cause of this phase noise is thermal noise entering the maser's RF receiver. For medium length time scales ($100s < \tau < 10^4 s$) the maser stability is limited by white frequency noise, causing the Allan deviation decreases as $\sigma(\tau) \propto \tau^{-1/2}$. This white frequency noise is a result of

predominantly thermal noise contributing to the linewidth of the atomic transition [95]. For longer averaging times above approximately $10^4 s$ and above the fractional frequency stability no longer decreases with τ and instead begins to increase. This behaviour which is indicative of systematic processes causing the output frequency of the maser to drift. For this regime the Allan deviation tends to vary as $\sigma(\tau) \propto \tau$ which suggests that the frequency is drifting linearly at first order. The linear drift of the maser can be characterised and subtracted as a time-evolving correction to the output, after which the Allan deviation varies according to $\sigma(\tau) \propto \tau^{1/2}$, which indicates a residual random-walking frequency drift. The main systematic processes liable for the frequency drift are the dimensional ageing of the microwave cavity material. This produces variations in the frequency shift produced from collisions with the interior surface of the quartz bulb–known as wall shift [96]–which changes slowly as the Teflon coating ages. The result is an output frequency that will slowly drift away from the nominal frequency over time if left uncorrected. Due to this long term drift the Hydrogen maser is limited in its use as an accurate frequency reference and cannot be used as a primary standard for definitions of the the SI second.

4.3 | Comparing clocks

Being able to determine and correct for the maser's frequency drift and offset, one has to compare directly to another accurate frequency reference. Frequencies can be directly compared if one has access to a second local reference with similar or better precision and accuracy, this became possible with the arrival of the caesium fountain clock in 2022, which is discussed in chapter 5. In principle it is also possible to directly compare the frequencies of two references which are separated by some distance, however transporting a highly stable reference frequency over large distance is problematic, and requires significant optical fibre infrastructure. However, if the output frequencies are used to produce a timescale (through the PPS output of the maser), two timescales can be compared through the GNSS using a satellite receiver. This allows us to precisely compare the timescale produced by our maser to the timescale produced by other metrology labs, or international standards such as the International Atomic Time (TAI). The frequency error on our maser can then be determined by observing how a difference between two timescales evolves over time.

A frequency standard can be straightforwardly used to produce a timescale by counting the number of cycles to track the evolution of time. This is summarised by

$$\tau_{\text{clock}} = \frac{n(t)}{f_0} = \frac{\int f(t)dt}{f_0}, \tag{4.4}$$

where τ_{clock} is the timescale kept by the clock, $n(t)$ is the number of cycles (which evolves with actual time t), f_0 is the nominal frequency of your standard, and $f(t)$ is the actual frequency of the standard–which for our maser evolves with time as due to the frequency drifts described above. If we consider the comparison between two timescales, timescale τ_A being derived from

our maser frequency f_A, and timescale τ_B originating from a second frequency reference f_B.

$$\tau_{AB} = \tau_A - \tau_B = \frac{\int f_A(t) - f_B(t)dt}{f_0}. \tag{4.5}$$

Now, lets assume that the second frequency reference, f_B is highly accurate and free of drift such that $f_B = f_0$. On the other hand our maser has some unknown frequency error $\delta f(t)$ which changes over time due to frequency drift, as a result we can say that $f_A = f_0 + \delta f(t)$. Plugging these into equation 4.5 we end up with

$$\tau_{AB} = \frac{\int \delta f(t)dt}{f_0}. \tag{4.6}$$

The integral can be differentiated out, allowing the fractional frequency error to be expressed as the time derivative of the delay between the two timescales,

$$y(t) = \frac{\delta f(t)}{f_0} = \frac{d\tau_{AB}}{dt}. \tag{4.7}$$

The relationship between the fractional frequency error $y(t)$ and timescale difference τ_{AB} expressed in equations and 4.7 means that any linear drifting term in frequency error will manifest itself as a quadratic drift between the two timescales.

4.4 | GNSS observables & IGS products

GNSS methods for time-frequency transfer allow two clocks to be compared by first comparing to an intermediate clock aboard the satellites, and then eliminating these satellite clocks from the comparison. Aspects of a GNSS signal that provide information on the separation between the satellite and the receiver, which can also be used to derive clock errors, are known as GNSS observables. For the time-frequency transfer techniques we shall discuss, two key GNSS observables are used: Pseudorange & Carrier Phase. Alongside GNSS observables, some GNSS time-frequency transfer techniques also require satellite data records kept by the international GNSS service (IGS), known as IGS products.

4.4.1 Pseudorange

GNSS signals contain pseudorandom binary codes which enable receivers to determine the signal's propagation time. The receiver determines the propagation time by comparing the code from the satellite signal with a replica code generated in the receiver. The propagation time between the satellite and the receiver provides, when multiplied by the speed of light, an observable known as pseudorange. The pseudorange is the 'apparent' range between the satellite and the receiver, which is different from the actual geometric distance between the satellite and the receiver. The difference between these can be understood to originate from, among other factors, clock errors in both the receiver and satellite. Pseudorange can be

expressed simply as [97]

$$P_R^S = c\left(\tau_R - \tau^S\right), \tag{4.8}$$

where P_R^S is the pseudorange observable, τ^S is the time that the signal is transmitted by the satellite as measured by the satellite clock, τ_R is the moment when the receiver records the signal, as indicated by its own clock. The pseudorange observable is understood to contain components of geometric range ρ, clock errors of the receiver and satellite dt_R & dt_S, delays due to the different propagation speed of electromagnetic waves through earths ionosphere, delays due to the different propagation speed of electromagnetic waves through earths troposphere T, as well as other noise components ε. Taking these terms into consideration it is possible to re-express the pseudorange as [97]

$$P_R^S = \rho + c\left(dt_R - dt^S\right) + \mathcal{I} + T + \varepsilon. \tag{4.9}$$

Ionospheric delays in pseudorange signals can be cancelled to first order using the 'ionosphere free' combination of two pseudorange observables P_{R1}^S and P_{R2}^S, which are distributed with a signal frequency of f_1 and f_2, respectively. GPS satellites transmit signals at at least two carrier frequencies: L1 at 1575.42 MHz, and L2 at 1227.6 MHz [98]. The ionospheric delay $\mathcal{I}$ is understood to be inversely proportional to the frequency of the signal squared, $\mathcal{I} \propto f^{-2}$, at first order [99]. Thus, the first order ionospheric delay can be eliminated via the combination [100],

$$P_R^S = \frac{P_{R1}^S f_1^2 - P_{R2}^S f_2^2}{f_1^2 - f_2^2}, \tag{4.10}$$

where P_R^S is the ionosphere-free combined psuedorange, which will be assumed value from now on unless stated otherwise, and can be expressed as,

$$P_R^S = \rho + c\left(dt_R - dt^S\right) + T + \varepsilon. \tag{4.11}$$

4.4.2 Carrier Phase

The carrier phase of the transmission signal is also a GNSS observable which can be used to obtain higher precision measure of the distance between receiver and satellite than the pseudorange alone. The phase of the satellite signal, as seen by the receiver, can be expressed as a function of time [101],

$$\phi^S = f^S t + f^S \frac{\rho}{c} - f^S dt^S, \tag{4.12}$$

whereas the receiver generated phase, which is synthesised from the frequency of the local oscillator, is given by

$$\phi_R = f_R t - f_R dt_R. \tag{4.13}$$

The measurement is the difference between the phase generated by the receiver's local oscillator, and the phase received from the satellite signal. This is given by

$$\begin{aligned}\phi_R^S(t) &= \phi^S(t) - \phi_R(t) \\ &= -f^S\frac{\rho}{c} - f^S dt^S + f_R dt_R + \left(f^S - f_R\right)t.\end{aligned} \tag{4.14}$$

We can then make the assumption that the receiver and satellite frequencies do not deviate significantly from the expected GPS band frequencies. In this case, $f^S = f_R \approx f$, and we can simplify the expression to be [101]

$$\phi_R^S(t) = -f\frac{\rho}{c} - f\left(dt^S - dt_R\right). \tag{4.15}$$

Carrier phase measurements made by the receiver can only be measured modulo one full cycle, and as a result the carrier phase measurement is ambiguous to an integer number of full cycles or wavelengths $N\lambda$ known as the 'ambiguity'. Therefore

$$\phi_R^S(t) = \Delta\phi_R^S(t) + N = -f\frac{\rho}{c} - f\left(dt^S - dt_R\right) \tag{4.16}$$

If we multiply equation 4.16 by the wavelength and rearrange, we end up with the definition of the carrier phase observable–which can be defined in similar terms to the pseudorange observable

$$L_R^S = -\Delta\phi_R^S(t) = \rho + c\left(dt_R - dt^S\right) + \lambda N + T + \varepsilon \tag{4.17}$$

Like pseudorange, this expression is dependent on the seperation between the receiver and satellite, troposphere propagation delays (added in by hand), the accuracy of their respective clocks, as well as the extra ambiguity term. As with the pseudorange observable, we use an ionosphere free combination of carrier phase observables $L_R^S = (L_{R1}^S f_1^2 - L_{R2}^S f_2^2)/(f_1^2 - f_2^2)$.

4.4.3 IGS Products

The IGS keep detailed records of essential satellite information, published daily on their web server. There are two products which are important for PPP: precise orbit product and the precise clock product. The precise orbit product is a record of the position and velocity of every GNSS satellite, at 5 minute intervals throughout a given day. It allows one to know the location of a given satellite in the International Terrestrial Reference Frame (ITRF) [102], at any given time. The product is openly available, and utilizes the Extended Standard Product-3 (SP3c) file format- which is described in [103]. The precise orbit product is available in three different and progressively more precise forms: Ultra Rapid, Rapid & Final. The ultra rapid product is published by the IGS at regular intervals four times per day, the rapid product is published after one day and 17 hours, and the final product is published after approximately 13 days. The precise clock product contains a record of the delays of satellite clocks at 30 second intervals throughout a given day–allowing one to know how much a satellites clock

deviated from the ITRF timescales at any given time. The clock product is available in two forms, Rapid and Final, with the same latency as the equivalent Orbit products.

4.5 | Common View

Common view (CV) is a simple technique which allows two oscillators in different places to be compared using the GNSS, by using the satellite clocks as an intermediary. The method works as follows: Two metrology labs receive the same signal containing the same pseudorange observable from the same satellite. The pseudorange observable can be compared to each timescale maintained by the local oscillator such that each lab measures the time difference between themselves and the satellite reference. This information is then shared between the two labs allowing for the time difference between the two stations to be determined. This is visualised in figure 4.4

Consider the pseudorange observable from a satellite S being measured by two receivers, A and B, simultaneously. The difference between the two pseudoranges is given by

$$P_A^S - P_B^S = c\,(dt_A - dt_B) + \rho_A - \rho_B + T_A - T_B + \varepsilon_A - \varepsilon_B. \tag{4.18}$$

By subtracting the pseudoranges from each other, the satellite clock errors dt^S are eliminated from the comparison. Furthermore, if the satellite is roughly equidistant between the two receivers then propagation and troposphere delay terms cancel out, $\rho_A - \rho_B \approx 0$, $T_A - T_B \approx 0$. Since the propagation delay is heavily influenced by environmental and atmospheric parameters (such as ambient temperature), we can get good cancellation when the distance between the two laboratory receivers is small relative to the distances between either receivers and the satellite. Multiplying out the speed of light c in equation 4.18, leaves just the difference between the clock errors, plus the added noise components. Assuming the clock error on the comparison clock, B, is small compared to our clock A, then $c(P_A^S - P_B^S) \approx dt_A$. The evolution of dt_A can be used to determine the frequency error through equation 4.7. At any given time both labs will be reading signals from around 20 to 30 different satellites–many of which will be the same. This procedure is then averaged over all the mutual satellite signals.

In practise the data is relayed between the two metrology labs by sharing CGGTTS (Common GNSS Generic Time Transfer Standard) files. These files are produced daily by the receiver, and are a record of all the satellites visible to the receiver recorded at 15 minute intervals throughout the day. For each visible satellite the CGGTTS file keeps a record of satellite elevation, azimuth, and the delay between the receivers local clock and the time communicated in the satellite signal. A more extensive summary of the CGGTTSS file format can be found in [104].

The Common view procedure using CGGTTS files can be defined algorithmically

1. Acquire two CGGTTS files: One for your own receiver, and once produced by a secondary metrology lab

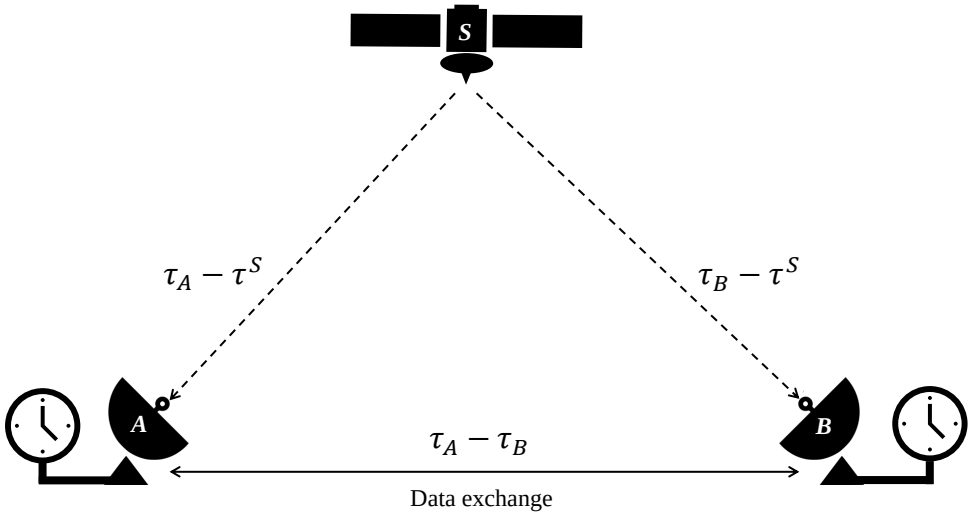

Fig. 4.4. The principles of common-view (CV) time-frequency transfer between lab A and B.

2. For a given time step, find all instances where the same satellites is visible to both metrology labs in the CGGTTS file

3. For each satellite in common, determine the delay between the two metrology labs, by eliminating the satellite clock difference via equation 4.18

4. Filter out satellites below a certain elevation, and those with delays more than three standard deviations from the time step mean

5. Take an average of all the remaining delays

6. Go to step 2 for the next 15 minute time step.

4.6 | Precise Point Positioning

Precise Point positioning offers an accurate and convenient approach to determining the position (and clock delays) associated with a GNSS receiver with centimeter (and picosecond) precision. It makes use of the data collected by the IGS and published in their satellite orbit and clock products, in combination with dual-frequency pseudo-range and carrier-phase observables that are retrieved by the receiver. PPP differs from Common-View methods in the sense that it does not require simultaneous observations from one or more close reference stations, and makes use of the carrier phase observable and IGS products. The pseudo-range and carrier-phase observables can be expressed as follows

$$P_R^S = \sqrt{(x_R - x^S)^2 + (y_R - y^S)^2 + (z_R - z^S)^2} + c\left(dt_R - dt^S\right) + T + \varepsilon_P \tag{4.19}$$

$$L_R^S = \sqrt{(x_R - x^S)^2 + (y_R - y^S)^2 + (z_R - z^S)^2} + c\left(dt_R - dt^S\right) - \lambda N_R^S + T_R^S + \varepsilon_L \tag{4.20}$$

Where x, y, z & dt are the positions and delays of the satellites and receivers as denoted by the subscripts and superscripts S and R repectively, ε_P and ε_L are any remaining non parameterised noise on the pseudorange and carrier phase observables respectively.

The goal of PPP is to calculate the receiver parameters x_R, y_R, z_R, dt_R using the satellite observables, with specific interest in dt_R in our case. Observable equations 4.19 and 4.20 contain satellite parameters x^S, y^S, z^S & dt^S which can be extracted from the IGS orbit and clock products on a daily basis. This reduces the number of unknown parameters to be determined. Furthermore, tropospheric delay, T_r^s, can be expressed as a function of the zenith path delay, zpd, using a mapping function, M, such that $T_r^s = Mzpd$ [105]. This relates the troposphere delay to the elevation angle of the satellite, which can also be extracted from the IGS Orbit product, further reducing the number of unknown parameters to be determined. If N_{sat} is the number of satellites visible to the receiver at a given time, what remains are $5 + N_{sat}$ unknowns to determine: (x_r, y_r, z_r, dt_r, zpd_r, N^1, ..., $N^{N_{sat}}$), and $2 \times N_{sat}$ observables ($\times 2$ because of both the carrier phase and psuedorange observable). Considering there are consistently more than 5 satellites visible to the receiver at any given time, we have an overdetermined system of equations. The PPP algorithm finds the optimal solution to the system of equations through the least squares adjustment [105], which is briefly summarised in the appendix B, allowing precise values of x_R, y_R, z_R and dt_R to be determined. The evolution of dt_R can be used to find the fractional frequency error through equation 4.7.

4.6.1 Implementation

How the PPP procedure is implemented at ALPHA is summarised graphically in Figure 4.5. The PolaRx5TR Receiver is connected physically to a satellite antennae on the roof of the metrology lab building. The antennae receives the carrier-phase and pseudorange GNSS observables, and this is relayed to the receiver where it is amplified. The receiver also receives a 10MHz and PPS signal from the maser, which is used to measure the observables to produce RINEX observation files.

RINEX observation files are a generic data file format for raw satellite observable data as collected by a receiver, relative to that receivers master clock. A RINEX file comes in two widely used types–RINEX2 & RINEX3. Our implementation uses RINEX2 files. RINEX files contain the satellite carrier phase and psuedorange observable information for multiple different frequencies. The organisation of the data within a RINEX file is difficult to interpret simply by reading it – but can be extracted via the PPP program. These observables are recorded every 30 second interval from all the satellites visible to the antennae, and a standard RINEX file records 24 hours worth of data. The RINEX file produced by our receiver is transferred to a folder in the metrology lab computer (alphametlab01) on a daily basis via FTP.

The PPP implementation is then carried out by two programmes on the metrology lab computer: a FORTRAN script (GPSPACE), which actually undertakes PPP calculation, and a

python programme (alphapppython), which collects the required files, decides when to run the FORTRAN script, and organises the output.

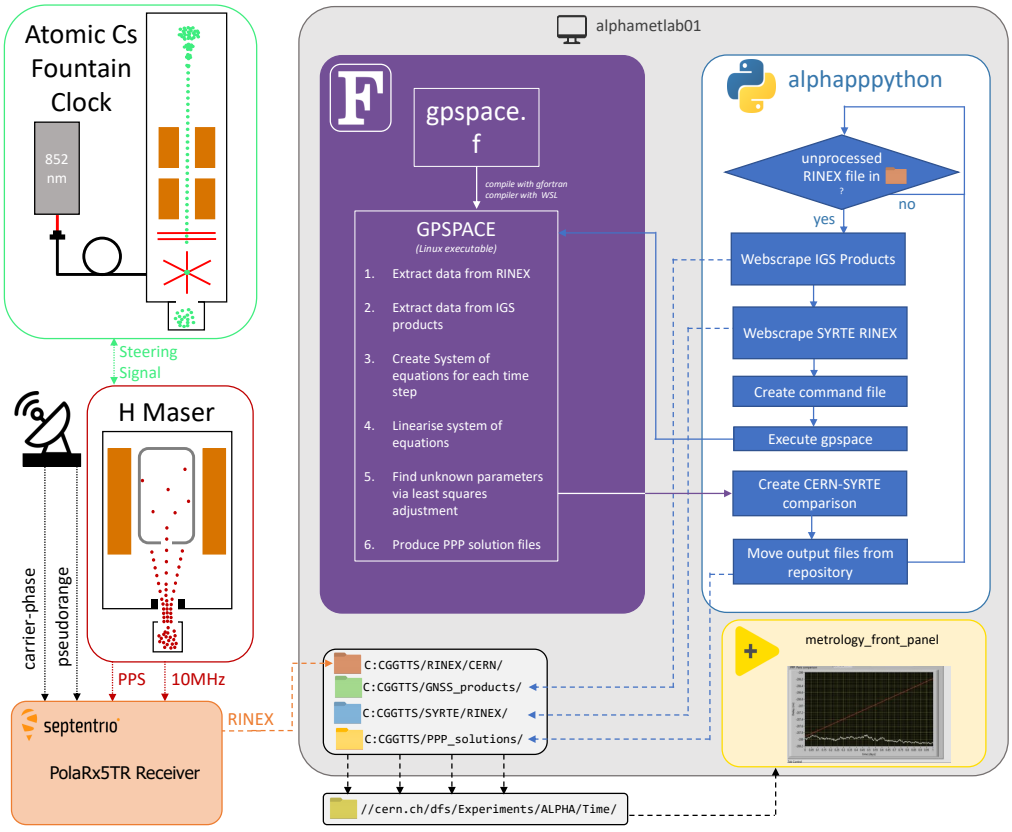

Fig. 4.5. PPP Scheme used by ALPHA. Dotted lines represent signals, dashed lines represent file transfers and solid lines display the algorithmic flow

The GPSPACE FORTRAN program is a well established open source script for running PPP, it was used operationally by Canadian Geodetic Survey (CGS) from the 90's until August 2018- after which the replaced it with a more updated program, however the source code is still widely used [106]. The program was produced at MIT over the course of many decades and with many developers- some of the the source code dates back to the 70s. As a result it is difficult to read, has no consistent coding style or practises and has no real documentation. However, the software has undergone very extensive testing over the years, and essentially bug free. The program has many different options and uses cases, many of which are not relevant for our own uses: to find the delay of our static master clock relative to GNSS time. At its basis the program completes the linearisation and parameter adjustment procedures described in appendix B. The file is compiled using the gfortran compiler in windows subsystem for Linux (WSL), and when executed takes uses four input files (which must be stored in the same repository) to carry out the PPP algorithm. The files it requires are: A RINEX File, IGS Precise orbit product file, IGS clock file, and a command file - all but the latter of which have been summarised previously. The command file is essentially a list of settings for our own PPP use case. The GPSPACE program then outputs five files: .ipx file, .sum file, .res file, .ses file,

and .pos file. It is only the last of these, .pos, which is of interest for finding the delay of our clock, which is contained within 'CLK(ns)' column.

The alphapppython programme collects and organises the required files, creates the command files, executes the gpspace script and organises and compares the outputs. It was produced to streamline and automate the PPP procedure. The program is ran in WSL for consistency with gpspace. When running the programs first step is to check for new unprocessed RINEX files which have not been used for PPP; this is done by comparing the PPP output files to the RINEX files. If there is no new file the program waits 60 seconds and then checks again, when a new file is found then the rest of the program is triggered. First the IGS sattellite orbit and clock products are web-scraped from the Center for Orbit Determination in Europe (CODE) website. Then RINEX files from other metrology labs corresponding to the same epoch are web-scraped and collected via ftp. Once all the required files are collected, a command file is produced for our RINEX file and for each of the web-scraped RINEX file, at which point the gpspace script is executed for each command file produced, and satellite data from each metrology lab is input into the PPP algorithm. The key information which we are interested in from the PPP algorithm is the the delay of our clock with respect to ITRF time. This is extracted for each metrology lab and saved in .clk files. Every permutation of .clk file pairs are then compared to produce comparison .clk files to allow our clock to be directly compared to the clock of a second metrology lab. These files are then all organised into a coherent file structure within the PC where they are later transferred to the CERN's distributed file system (DFS).

4.7 | Measurement and correction of hydrogen maser

The frequency synthesiser of the maser can be altered, allowing the frequency which is output by the maser can be adjusted without changing any of the parameters of the physics package, such as the cavity resonance frequency. The firmware built into the iMaser 3000 allows the synthesizer to be altered as in two distinct ways: Offset correction and drift compensation. Offset correction involves adjusting the frequency synthesiser in such a manner that it results in a step-wise correction in the frequency output by the maser, increasing or decreasing the output frequency. Drift compensation allows the linear drifts in the maser frequency to be compensated, by linearly adjusting the output of the maser to cancel out linear drifts. The goal was to correct the maser in these two different ways such that the maser output is maintained as close to the SI second in the reference frame of the metrology lab–particularly during experimental time for 1S-2S spectroscopy. The process of measuring and correcting the frequency error of the maser using the techniques described in this chapter was refined over time, and will hence be discussed chronologically.

4.7.1 2021

Common-view, being the more straightforward of the two methods described above, was the first technique implemented for measuring the fractional frequency error of the maser. A system to automatically implement common-view, exchanging CGGTTS files daily with SYRTE in Paris, was setup in early 2021. The comparison of the timescale maintained by our maser and the timescale maintained by SYRTE is displayed in figure 4.6; SYRTE regulates its maser timescales close to Coordinated Universal Time (UTC), as a result figure 4.6 shows the drift of our maser from UTC. The UTC is defined on a geopotential surface known as the geiod [107], whereas the metrology lab was measured by CERN's GIS service to have an orthometric height of 442 m above the geoid. This results in UTC running slow compared to the SI second in the metrology lab, due to gravitational red shift. To correct the frequency error on the maser, we want our timescale to run $1 + 4.827\times10^{-14}$ times faster than UTC, which corresponds to a maser fractional frequency offset of 4.827×10^{-14} compared to UTC. The equivalent data

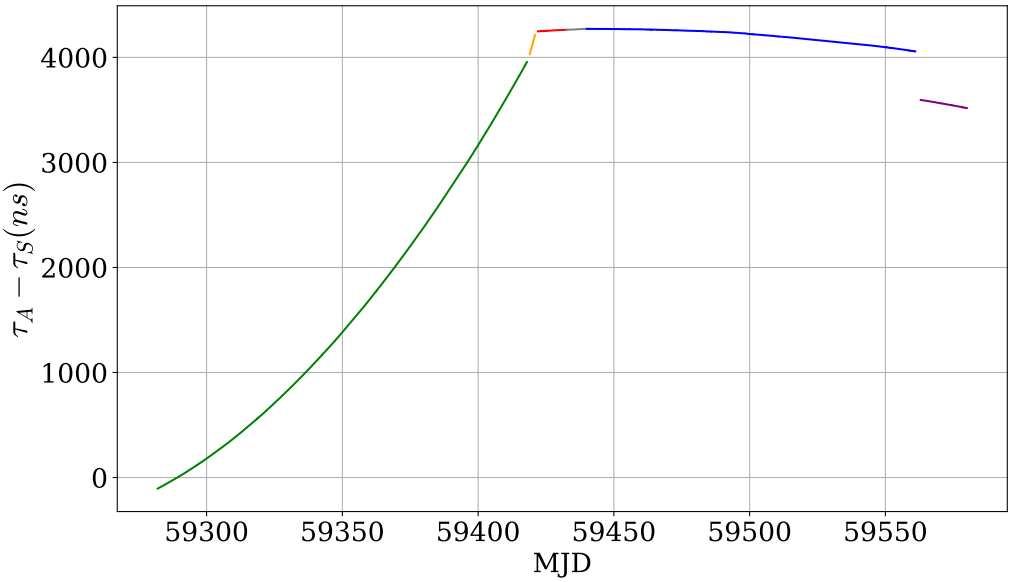

Fig. 4.6. Plot shows the drift between ALPHA timescale τ_A and SYRTE timescale τ_S. MJD is a measure of number of days, equal to the number of days since November 17, 1858. The different colors represent periods which have been subjected to different corrections.

converted into fractional frequency difference, with the same colour scheme, is displayed in figure 4.7. The fractional frequency difference was determined by binning the data in figure 4.6 to 1-day intervals, fitting a linear function to each of these intervals and extracting the slope to determine fractional frequency error in accordance to equation 4.7.

During 2021 the orthometric height of the metrology lab had not been measured with precision. Whilst learning how to correct the maser we decided it was pragmatic to steer the maser frequency towards UTC, corresponding to zero fractional frequency difference between ALPHA and SYRTE, rather than the SI second in the metrology lab. The green section of figures 4.6 & 4.7 display the behaviour of the maser timescale without any corrections. During this time its fractional frequency has a linear drift at rate of $\approx 2.8 \times 10^{-15}$ per day. The yellow

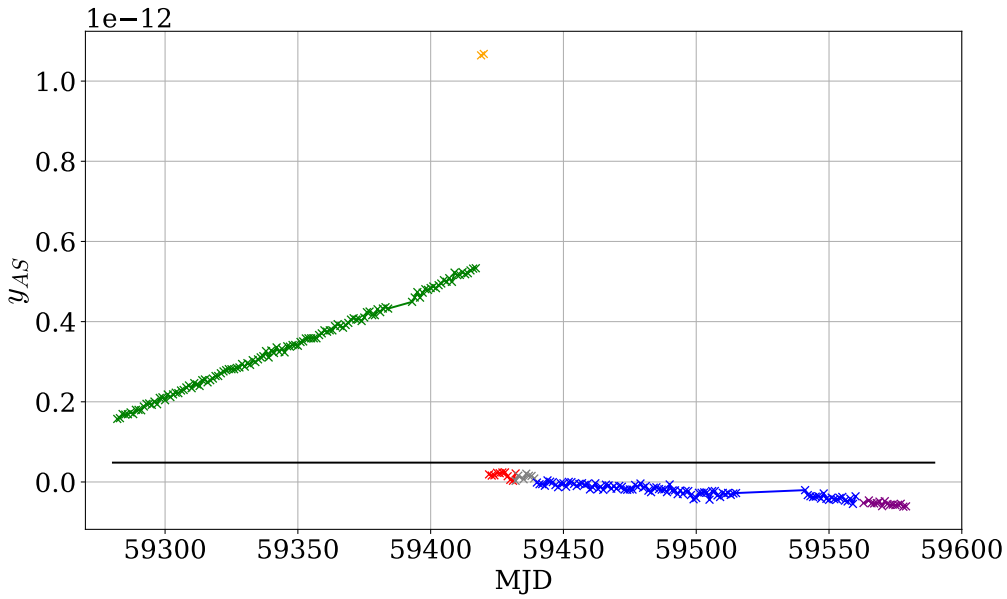

Fig. 4.7. Plot displays the fractional frequency error on the maser, y_{AS}, during 2021, measured relative to SYRTE. Fractional frequency was determined from the gradient of 1 day bins. The different colors represent periods which have been subjected to different corrections, as in figure 4.6. The black line corresponds to the maser frequency being at nominal value in the metrology lab frame, whereas $y_{CS} = 0$ corresponds to UTC.

follows an erroneous offset correct of $+5.3 \times 10^{-13}$, which was of the right magnitude, but in the incorrect direction to bring the maser closer to UTC. The red follows an offset correction of -5.3×10^{-13} to remedy the previous error and bring the maser frequency closer to UTC, which it does successfully. The grey follows the first implementation of a drift compensation, where a value of 2.8×10^{-15}/day is compensated for. Blue follows a further offset correction of $+1.42 \times 10^{-14}$, resolving the residual offset from UTC.

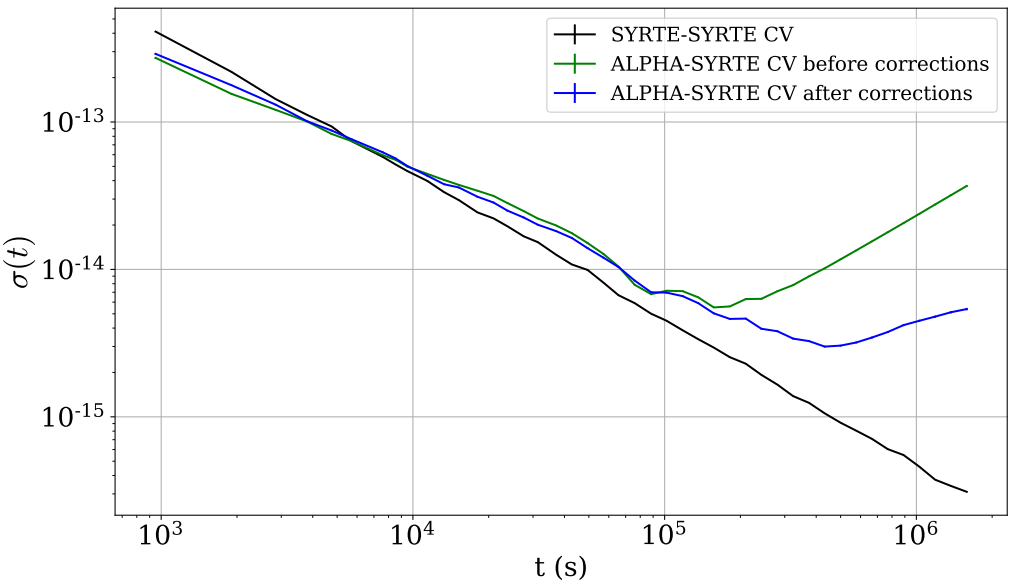

Fig. 4.8. Allan deviation of the green and blue periods in figure 4.6. A comparison between two masers with regularly corrected drift is plotted in black.

To determine the improvements in the maser frequency stability following the correction of fractional frequency error and linear drift, we can compare Allan deviation curves, which are displayed in figure 4.8. The black plot displays the common-view comparison between two masers maintained by SYRTE which are free of any drift terms–this provides a benchmark for the maximum stability measurable by common-view. The green curve displays the Allan deviation calculated from the green dataset in figures 4.6 & 4.7, the stability of the maser before any corrections were applied to the maser, whereas the blue displays the Allan deviation for the blue dataset in figures 4.6 & 4.7 after multiple corrections were applied. There are noticeable improvements in the stability of the maser following the corrections. The turning point of the blue curve is lower, and arrives later compared to the green. This corresponds to values of 5.6×10^{-15} and 3.3×10^{-15} for the blue curve and green curves respectively, corresponding a 1.7 factor improvement in maser stability as measurable by common view. The black curve displays the ultimate limit of the common-view method, and is a comparison between two masers maintained by SYRTE, which have their frequency regularly corrected such that they are free of drift.

4.7.2 2022

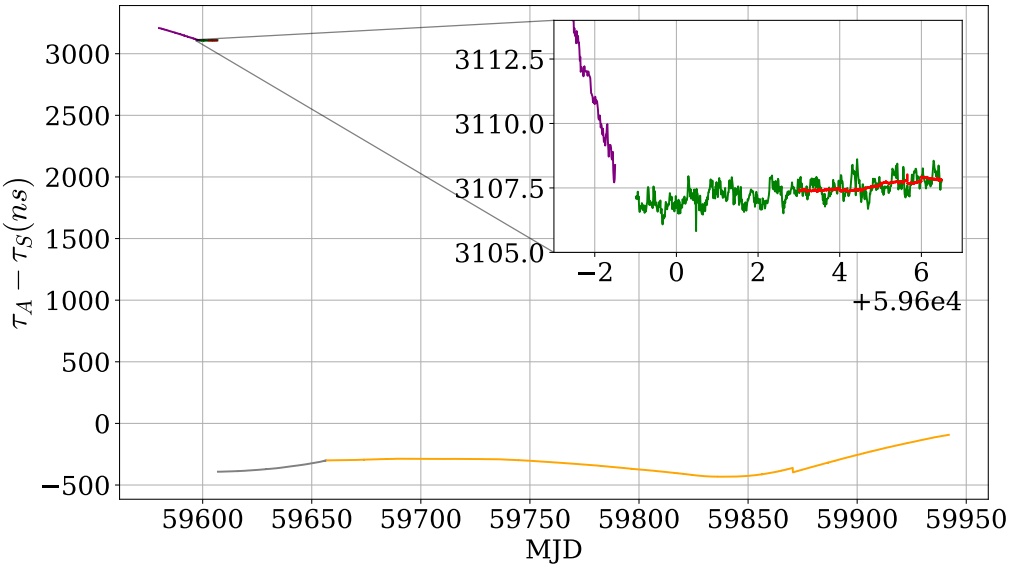

Fig. 4.9. Plot shows the drift between ALPHA timescale τ_A and SYRTE timescale τ_S. The different colours have been subjected to different corrections.

By 2022 we had developed and implemented the PPP system described in section 4.6.1, allowing for better determination of the maser frequency error and stability than with common-view. A comparison between the timescales maintained by our maser and the timescale maintained by SYRTE is displayed in figure 4.9. The same data converted into fractional frequency error is displayed in figure 4.10, again using one day bins. The purple dataset continues from 2021, still measured using common-view. The green dataset follows a simultaneous offset and drift correction of $+7.23\times10^{-14}$ and $+1.5\times10^{-15}$ per day respectively. Whilst the offset

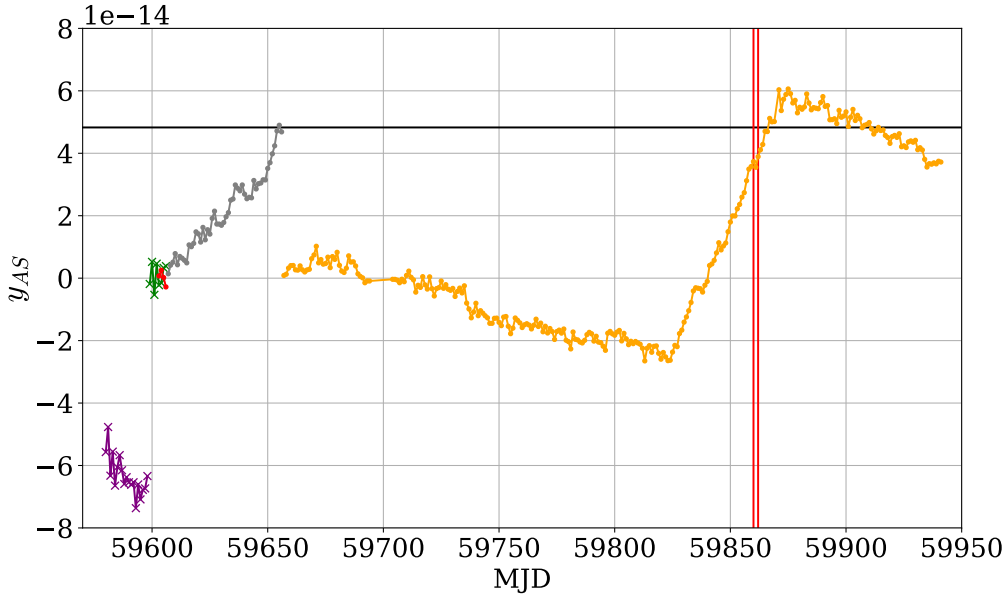

Fig. 4.10. Plot shows the drift between ALPHA timescale τ_A and SYRTE timescale τ_S. The different colours have been subjected to different corrections.

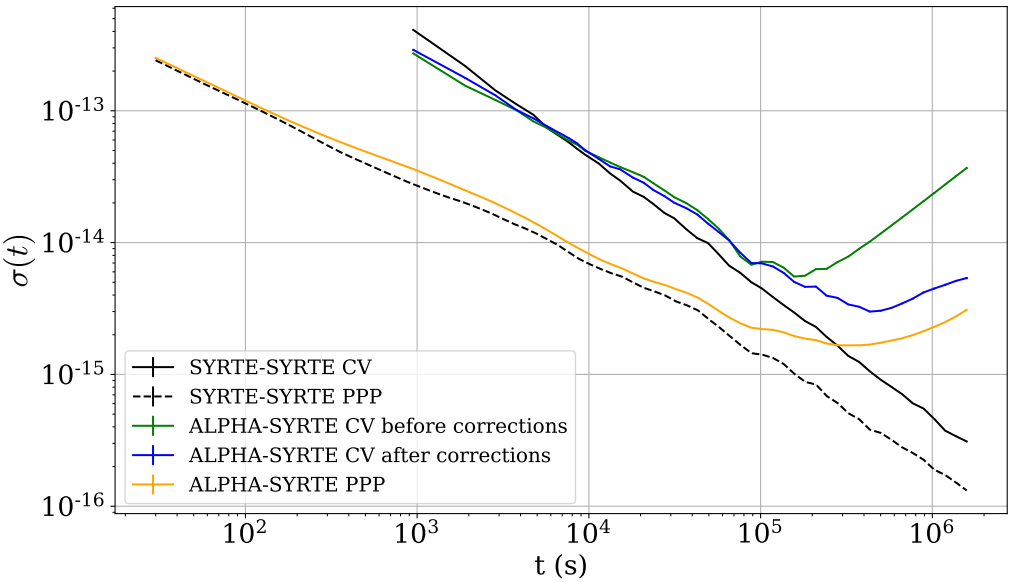

Fig. 4.11. Plot shows the drift between ALPHA timescale τ_A and SYRTE timescale τ_S. The different colours have been subjected to different corrections.

correction was correct, the drift correction was erroneous. The drift correction input into the maser controls should be the total accumulated drift of the maser, so what should have been input is the previous drift plus this drift term $(2.8 \times 10^{-15} + 1.5 \times 10^{-15})$.The red dataset is the same as the green dataset, except now measured using PPP–the increased stability from this technique is clearly visible in the inset of figure 4.9. The grey dataset follows a correction of the PPS clock which has no impact on frequency. The amber dataset follows a simultaneous offset and drift correction of $-4.605686 \times 10^{-14}$ and 2.2149×10^{-14} per day respectively; this time applying the drift correction correctly. The frequency drift in amber dataset changes

rapidly from negative to positive drift between MJD=59825 and MJD=89870, before shifting back to its previous negative drift. This change is not a result of any intervention on our behalf, but this behaviour has been occasionally observed in other masers [108]. The two horizontal red lines in figure 4.10 denote the days in 2022 where we were conducting 1S-2S spectroscopy, during this time the maser frequency is fortunately close to the nominal value (black horizontal line).

The Allan deviation curves displayed in figure 4.11 demonstrate the improved frequency determination and stability which results from PPP. The amber plot corresponds to the amber datasets in figures 4.9 and 4.10. The black dashed line displays a PPP comparison between two masers maintained by SYRTE that have their frequencies corrected for regularly and are therefore mostly free of drift, providing a benchmark for the capability of PPP. This is plotted alongside the data from figure 4.8 for comparative purposes. The amber curve consistently displays better frequency resolution and stability than any of the 2022 data, reaching a minimum Allan deviation of $\sigma(3.75 \text{ days}) = 1.661 \times 10^{-15}$

4.7.3 2023

By 2023 the caesium fountain clock was in operation and being used to inform the maser steering and correction protocol. As a result the measurement and correction of the hydrogen maser during 2023 are discussed in more detail at the end of the next chapter. The caesium fountain allows the frequency error of the maser to be measured with even higher precision than the GNSS methods, however the GNSS techniques still provide an important and essential secondary method during caesium fountain downtime. GNSS methods have also been important when diagnosing issues with the fountains, which have lead to systematic shifts in the fountain measurement, which became clear from differences differences between the two methods. Finally, as will be discussed in the next chapter, the GNSS methods were required to evaluate the performance of our caesium fountain against other primary standards.

CHAPTER 5

The Caesium Fountain Clock

> *Time is an illusion. Lunchtime doubly so.*
>
> **— Ford Prefect**
> The Hitchhiker's Guide to the Galaxy

Since 1967 the official definition of the SI second has been defined by the International Bureau of Weights and Measures (BIPM) as "the duration of 9192631770 periods of the radiation corresponding to the transition between the two hyperfine levels of the ground state of the caesium 133 atom" [94]. The precise measurement of the hyperfine transition in caesium, displayed in figure 5.1, leads not only to the exact definition of the second but, since the 2019 re-definitions, to the practical realisation of all other SI base units – other than the mole. Caesium is a group one alkali metal, with an unpaired electron in its outermost

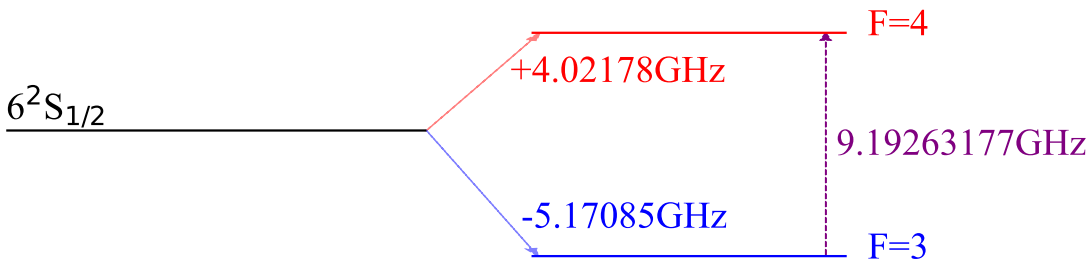

Fig. 5.1. The hyperfine splitting of the caesium-133 ground state and associated hyperfine transition defining the SI second

shell – providing a total electron spin for the atom of $S = 1/2$. The caesium-133 nucleus has a nuclear spin equal to $I = 7/2$ [109], which couples with the electron spin to produce two non-degenerate hyperfine states: the $F = 3$ state ($F = I - J$) produced by anti-parallel nuclear and electron spins, and the $F = 4$ state ($F = I + J$) produced by parallel nuclear and electron spins. The hyperfine energy shift on the ground state of caesium is given by [110]

$$\Delta E_{\mathrm{hfs}} = \frac{1}{2} A_{\mathrm{hfs}} (F(F+1) - I(I+1) - J(J+1)), \tag{5.1}$$

where $F = 3$ or $F = 4$, $I = 7/2$, $J = 1/2$ in the ground state, and $A_{hfs} = 2.2981579425$ GHz [110] is the magnetic dipole constant. Inserting these values into equation 5.1 we end up with two

values for hyperfine splitting; the $F = 3$ hyperfine state has a shift of $-\frac{4.5}{2}A_{\mathrm{hfs}} = -5.17085\,\mathrm{GHz}$, and the $F = 4$ hyperfine state has a shift of $+\frac{3.5}{2}A_{hfs} = +4.02178\,\mathrm{GHz}$. The difference between these states produce a ground state hyperfine transition frequency equal to 9.19263177 GHz, which provides the definition of the SI second, and reciprocally the definition of the Hertz.

The precision of the realisation of the SI second is limited solely by the measurement uncertainty of the caesium hyperfine splitting measurement, and therefore it is beneficial to produce a resonance signal with the narrowest possible linewidth. An atomic fountain (named because of the fountain-like motion of the atoms moving under the influence of gravity) uses laser cooling techniques and the Ramsey method of spectroscopy to measure the hyperfine transition of caesium with extremely high precision. The ALPHA collaboration acquired a caesium fountain clock in 2022, which was subsequently set up to be used as a primary reference for the SI second in the ALPHA metrology lab. This chapter will start with a review of the methods used in the operation of a caesium fountain, specifically laser cooling techniques and Ramsey spectroscopy. The chapter will then proceed to discuss hardware components and the operational cycle of the fountain, and evaluate its performance as a frequency reference for the ALPHA experiment. Finally, this chapter summarises the fountain performance in 2023, and possible automatic correction schemes for the fountain will be discussed.

5.1 | Laser Cooling Techniques

The caesium sample preparation within the fountain relies upon laser cooling techniques for the temperature reduction and temporary confinement of atoms before their launch. Producing cold atoms with laser cooling allows for longer atom interaction times which produces higher precision spectroscopy, as well as reducing the impact of many systematic effects. Briefly reviewed below are the general principles of laser cooling, before proceeding to its uses within an Optical Molasses (OM) and Magneto-Optical Trap (MOT).

By combining the energy of the photon, $E = \hbar\omega$, and the energy-momentum relation, $E^2 = p^2c^2 + m^2c^4$, it is straightforward to deduce the momentum of a photon,

$$\mathbf{p} = \hbar\mathbf{k}, \tag{5.2}$$

where $\mathbf{k}$ is the wave vector, pointing in the direction of the photon's propagation. Lasers produce a collimated monochromatic beam of photons, which can impart momentum in the direction of the beam onto atoms via absorption. Once excited via photon absorption, the atom will at some later point spontaneously emit a photon of equal momentum. The random direction of spontaneous emission means that the beam provides a net dissipative force on the atom equal to,

$$\mathbf{F} = R_{scatt}\mathbf{p}. \tag{5.3}$$

The scattering rate, $R_{scatt} = \Gamma\rho_{22}$, where Γ is the decay constant, and ρ_{22} is the excited population. The optical Bloch equations can be used to determine R_{scatt} [110],

$$R_{\text{scatt}} = \frac{\Gamma}{2}\frac{\Omega^2/2}{\delta^2 + \Omega^2/2 + \Gamma^2/4}. \tag{5.4}$$

In the expression above δ is the laser frequency detuning in the atom's frame of reference, which includes any Doppler shift from the atom's motion. The Rabi frequency, Ω, can be expressed in terms of the saturation intensity $\Omega^2 = \frac{I\Gamma^2}{2I_{sat}}$, such that the total dissipative force imparted by a laser beam is given by

$$\mathbf{F} = \hbar\mathbf{k}\frac{\Gamma}{2}\frac{I/I_{\text{sat}}}{1 + I/I_{\text{sat}} + 4\delta^2/\Gamma^2} \tag{5.5}$$

By providing a force, lasers can be used to slow atoms down and cool them. This is most obviously realised in atomic beams, when they are subjected to a counter-propagating laser beam. It can also be applied via Doppler cooling, whereby the laser beam is red-shifted relative to the atomic resonance such that its photons are preferentially absorbed by counter-propagating atoms, therefore cooling an atomic sample. This principle is applied within an optical molasses and a MOT - the key cooling and trapping techniques during the sample preparation stage within the caesium fountain. The physical principles of an optical molasses will be covered here first, despite being the second step of the sample preparation stage. This is a pedagogical choice, as many of the same principles required to understand the physics of molasses will be applied later to a MOT.

5.1.1 Optical Molasses

Atoms within a gas move with velocity components in all three spatial dimensions; laser cooling a gas to extremely low temperatures requires laser cooling in all three dimensions. This is the principle behind an optical molasses, which is composed of three counter-propagating pairs of laser beams that produce standing waves and cool in all three spatial dimensions. The counter-propagating beam produces equal and opposite forces on a stationary atom – however, the forces become unbalanced when one considers an atom in motion. The six laser beams are red-detuned from the transition frequency, atoms with a large enough velocity component will experience a blue Doppler shifting on the beam they are counter-propagating with, such that the laser frequency becomes closer to the transition frequency in the atom's frame of reference. In this way atoms preferentially absorb photons from laser beams they are counter-propagating with, and since the photon emission is spontaneous and in random direction, this results in a net reduction of momentum in the opposite direction of the atom's velocity. This effect can be viewed as a velocity dependent force acting on the atom. This force can be expressed as the difference between the forces acted upon the atom with a component of velocity v along

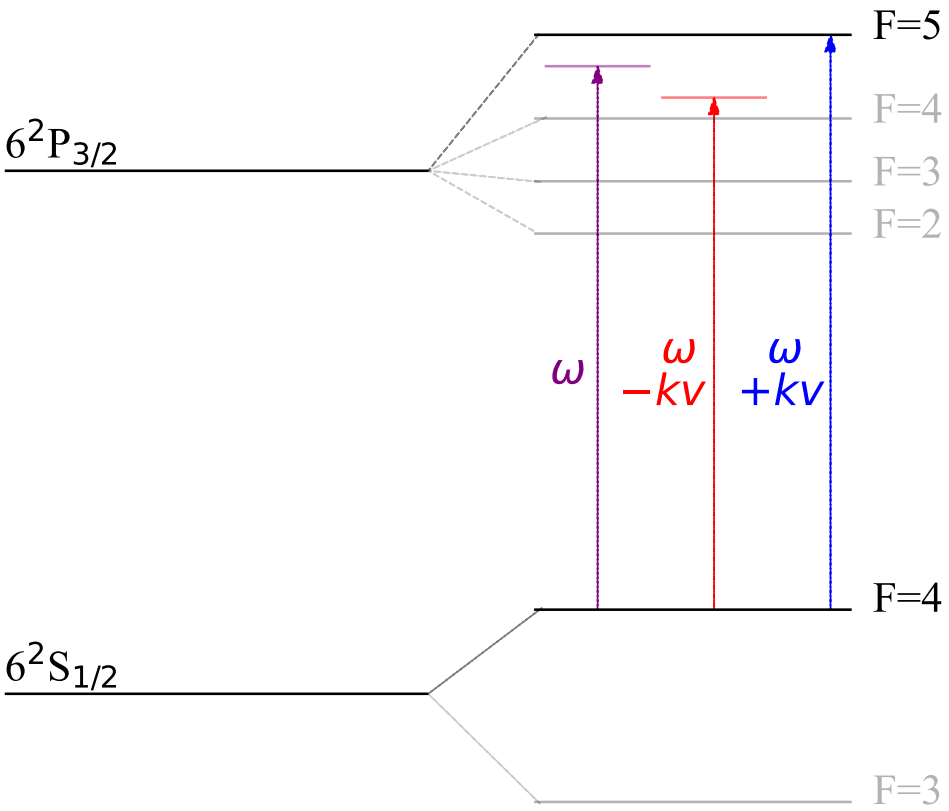

Fig. 5.2. The purple arrow displays the laser frequency for the caesium atom at rest, which is slightly red-detuned from the cooling transition. When atoms have velocity v, the antiparallel laser beam (blue) is Doppler shifted towards the transition frequency, whereas the parallel beam (red) is Doppler shifted further away

the the parallel and antiparallel beam axis.

$$\begin{aligned}\mathbf{F}_{\text{molasses}} &= \mathbf{F}\left(\omega-\omega_0-kv\right)-\mathbf{F}\left(\omega-\omega_0+kv\right)\\ &\simeq \mathbf{F}\left(\omega-\omega_0\right)-k\frac{\partial F}{\partial\omega}\mathbf{v}-\left[\mathbf{F}\left(\omega-\omega_0\right)+k\frac{\partial F}{\partial\omega}\mathbf{v}\right]\\ &\simeq -2\frac{\partial F}{\partial\omega}k\mathbf{v}=-\alpha\mathbf{v}.\end{aligned} \tag{5.6}$$

The laser light provides an incremental force, through the absorption of photons, which opposes the atom's motion. This is analogous to the frictional force on a particle moving through a viscous fluid, leading to the name "Optical Molasses" [111]. By differentiating equation 5.5 one can derive a value for the frictional coefficient α.

$$\alpha = 2k\frac{\partial F}{\partial\omega} \simeq 2k\frac{\hbar}{c}\left(\omega\frac{\partial R_{\text{scatt}}}{\partial\omega}\right) \simeq 4\hbar k^2\frac{I}{I_{\text{sat}}}\frac{-2\delta/\Gamma}{\left[1+(2\delta/\Gamma)^2\right]^2} \tag{5.7}$$

The above is derived by dropping negligible R_{scatt} and I/I_{sat} terms, as this technique is only possible at a low scattering rate, which can be achieved through a combination of

detuning and low intensity. A positive value of α is required to achieve cooling, which requires a negative (red) detuning δ.

The moving molasses technique

The optical molasses is used to cool the caesium atoms to microkelvin temperatures, and it is also used to launch the atoms upwards via the 'moving molasses' technique [112]. This involves producing a molasses that damps the velocity of the atoms towards zero within a frame of reference which moves with velocity $\mathbf{v}$ relative to the lab. To create such a molasses, the beam propagating antiparallel to the desired $\mathbf{v}$ direction is further red-detuned by some $\Delta\omega = k|v|$, and the beam propagating parallel to the $\mathbf{v}$ direction are blue-detuned $\Delta\omega$. In a reference frame moving at $\mathbf{v}$ the Doppler effect cancels these detunings, which means atoms moving in that frame of reference will experience the two laser beams of the same frequency. The atoms will have the same spread of velocities around their mean velocity as in the standard molasses, so the temperature is the same. This technique is used with the vertical beams in the caesium fountain to launch the cold atoms upwards to achieve an atomic fountain.

5.1.2 Magneto-Optical Trap (MOT)

Optical molasses can viciously confine atoms to a small region of space for times on the order of 0.1 seconds, but the atoms eventually diffuse out with their residual velocities. Optical molasses alone do not constitute a trap; however, using circularly polarised laser light and introducing a spatially varying magnetic field with a field minimum at beam intersection provides trapping capability in the form of a MOT [113]. The required spatially varying magnetic field can be produced by two coils in an anti-Helmholtz configuration which are positioned above and below the intersection of the molasses laser beams. These coils produce a quadrupolar magnetic field, the zero field of which overlaps with the intersection of the molasses laser beams. The field gradient of the quadrupolar magnetic is approximately constant along each axis (note, the gradient is roughly twice as strong along the axis which contains the coils), and the field varies linearly with position.

Each orthogonal pair of lasers has one clockwise σ^+ and one anticlockwise σ^- polarised laser, as displayed in figure 5.3, and all lasers are red-detuned from the transition frequency as in the optical molasses. The selection rules associated with circularly polarised light only allow for $\Delta m_j = \pm 1$ transitions [114]. The photon energy required to excite the allowed atomic transitions is shifted by the Zeeman interaction according to $\Delta E = \Delta m_J g_J \mu_B B$ [114]. As a result, atoms that are displaced from the beam intersection and field zero will experience the Zeeman effect which will cause the frequency of their allowed transitions to increase or decrease proportionally to their displacement, as displayed in the bottom of figure 5.3. As an atom is displaced in a positive direction across any of the three axes, for example, the $+x$ direction, the $\Delta m_j = -1$ transitions are shifted closer to resonance with the laser frequency. This leads to increased photon absorption from the σ^- laser beam, pushing the atoms in the negative direction back towards the intersection of the beams. Similarly, as atoms are

displaced in the negative direction their $\Delta m_j = +1$ transitions are shifted closer to resonance, and they absorb photons from σ^+ laser beam, which provides a scattering force in the positive direction back toward the center of the trap. The quantisation axis of the atoms and the light polarisation in these examples have been defined relative to a fixed direction in space parallel to an arbitrary laser beam

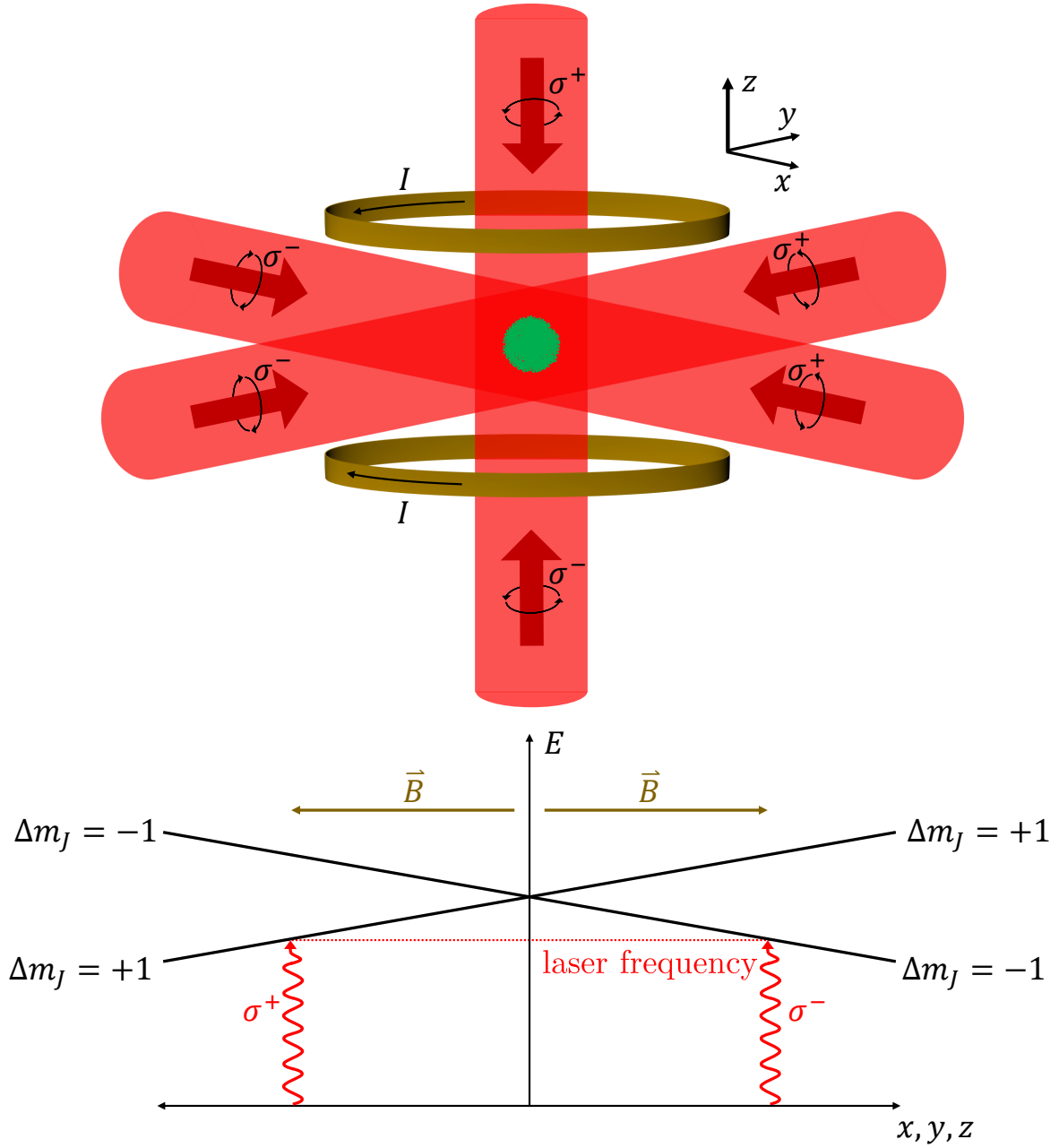

Fig. 5.3. **Top:** diagram of a MOT formed from three orthogonal pairs of counter propagating circularly polarised laser beams, and two anti-Helmholtz coils. **Bottom:** The mechanism of a MOT, illustrated by the position dependent Zeeman shift which leads to preferential absorption of counter propagating photons the further an atom is displaced from the center of the trap. This pushes the atoms back towards the center of the trap, resulting in confinement. Schematic inspired by figure in [114].

The principle of the MOT, described above, relies on the selection rules associated with circularly polarised light and the Zeeman effect due to a spatially varying quadrupolar magnetic field. The combination of these two effects produces a position-dependent light scattering force that confines the atoms towards the center of the trap. By adapting equation 5.6 to include the position-dependent linear variation of transition frequency $\omega_0 \rightarrow \omega_0 \pm \beta z$ where β is some constant to be derived from the physics of the Zeeman effect, it is possible to describe the MOT's confining force:

$$\begin{aligned}\mathbf{F}_{\text{MOT}} &= \mathbf{F}\left((\omega - kv) - (\omega_0 + \beta z)\right) - \mathbf{F}\left((\omega + kv) - (\omega_0 - \beta z)\right) \\ &\simeq -2\frac{\partial F}{\partial \omega} k\mathbf{v} + 2\frac{\partial F}{\partial \omega_0}\beta\mathbf{z} \ .\end{aligned} \tag{5.8}$$

The $\omega_0 + \beta z$ describes the $\Delta m_j = 1$ transition which is excited by the σ^+ beam, whereas $\omega_0 - \beta z$ describes the $\Delta m_j = -1$ transition - excited by the σ^- beam. Considering the Zeeman effect in a field that varies linearly with displacement, with a field zero at $x, y, z = 0$, it is straightforward derive the constant β:

$$\Delta\omega_0 = \beta z = g_J \mu_B B = g_J \mu_B \frac{dB}{dz} z. \tag{5.9}$$

Considering that equation 5.5 is a function of detuning, it is pragmatic to make the substitution $\partial F/\partial\omega_0 = -\partial F/\partial\delta = -\partial F/\partial\omega$ such that equation 5.8 can be rewritten as,

$$\mathbf{F}_{\text{MOT}} \simeq -2\frac{\partial F}{\partial \omega}(k\mathbf{v} + \beta\mathbf{z}) = -\alpha\mathbf{v} - \frac{\alpha}{k}\beta\mathbf{z} \ . \tag{5.10}$$

If α is positive (produced by a red detuning as discussed earlier) then the second term in equation 5.10 describes damped simple harmonic motion with the first term describing the damping due to the molasses and the second term describing the restoring force on the trapped atoms due to the MOT. In this way atoms can be trapped and cooled in a MOT, in a way that is straightforward to load for subsequent cooling steps.

Repump laser

For effective cooling via an optical molasses and trapping within a MOT, momentum must be quasi-continuously imparted on the caesium atoms through constant absorption-spontaneous emission cycles. For this to be possible, the specific transition must be a closed optical loop, such that after an absorption and a spontaneous emission the atom is returned to its original state. This is almost the case in caesium; the excited cooling state $|6^2P_{3/2}, F = 5\rangle$ can only decay to $|6^2S_{1/2}, F = 4\rangle$ through single photon emissions, which is vastly more probable than multi photon emission. However, there is some non-zero overlap between with the $|6^2S_{1/2}, F = 4\rangle \rightarrow |6^2P_{3/2}, F = 4\rangle$ transition, providing a small probability that the atom will end up in the $|6^2P_{3/2}, F = 4\rangle$ state. The $|6^2P_{3/2}, F = 4\rangle$ state can decay to either the $|6^2S_{1/2}, F = 4\rangle$ or $|6^2S_{1/2}, F = 3\rangle$ state, the latter of these causing the atom to exit from the cooling optical-loop. To avoid this problem, a repump laser, which is resonant with the

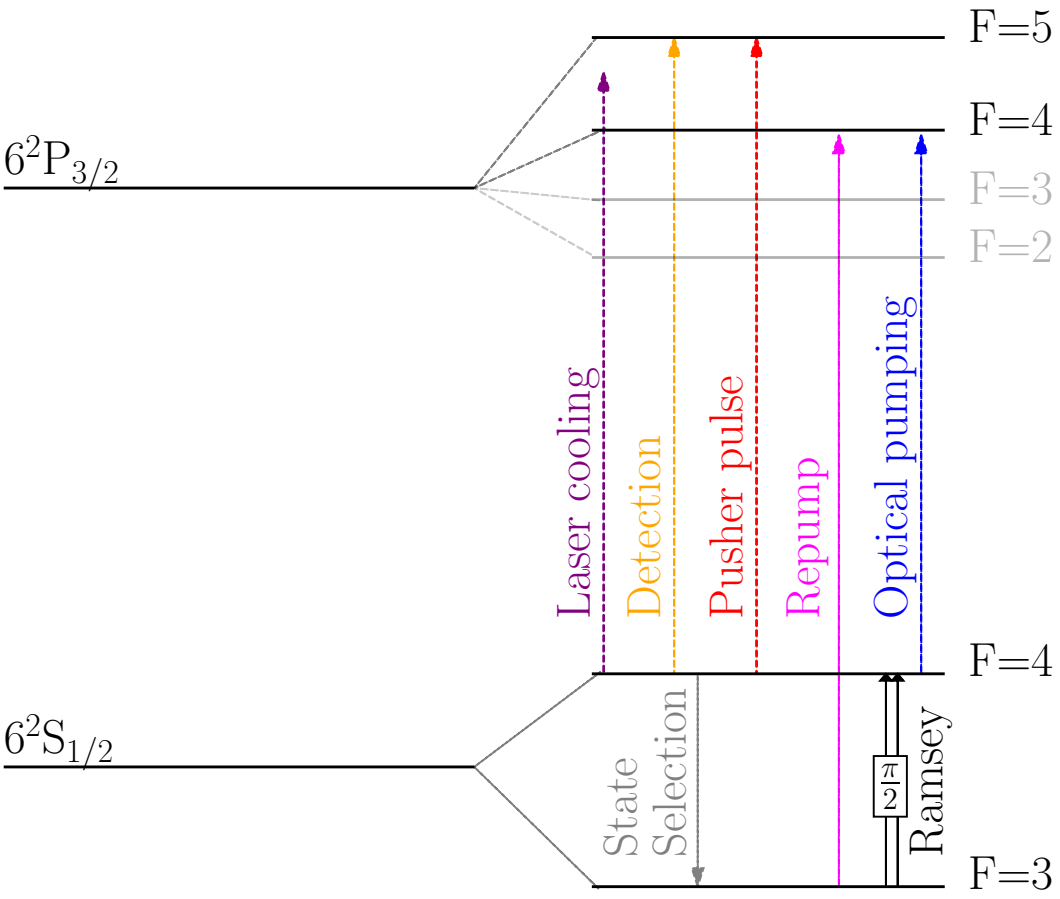

Fig. 5.4. The relevant energy levels for ^{133}Cs, annotated with arrows which show the specific transitions which are used in fountain operation.

$|6^2P_{3/2}, F = 3\rangle \rightarrow |6^2S_{1/2}, F = 4\rangle$ transition, is overlapped with one of the cooling beams and excites any atoms in the 'dark' $|6^2P_{3/2}, F = 3\rangle$ state back into the cooling optical loop, as displayed in figure 5.4

5.2 | Ramsey spectroscopy in Atomic fountains

Longer interaction time between the resonant microwaves and the atomic sample naturally reduces the linewidth; however, it is problematic to maintain atoms stationary in an interaction region without external perturbations which will affect the measurement. The Ramsey method of spectroscopy [115] was developed to circumnavigate interaction time limitations. Instead of applying resonant microwaves over some period of time, the atoms are instead exposed to two successive identical microwave interactions of time τ separated by an intermediate period of time T during which their quantum states evolve freely. When interrogating an atomic spectrum in this manner the linewidth is found to be inversely proportional to the elapsed times between interactions T. The resulting probability function for the excitation is characterised by *Ramsey Fringes*, with an outer envelope characterised by the probability function for standard

single interaction time τ. The emergence of these fringes can be understood visually by considering the behaviour of the Bloch vector during each stage of the Ramsey sequence. The Bloch vector $\mathbf{R} = (u, v, w)$ provides a convenient way to describe a two-level system, and can be defined in relation to the Density Matrix ρ [114] by,

$$\begin{aligned} u &= \rho_{12}e^{-\mathrm{i}\delta t} + \rho_{21}e^{\mathrm{i}\delta t} = \widetilde{\rho}_{12} + \widetilde{\rho}_{21}, \\ v &= -\mathrm{i}\left(\widetilde{\rho}_{12} - \widetilde{\rho}_{21}\right), \\ w &= \rho_{11} - \rho_{22}, \end{aligned} \tag{5.11}$$

where δ is the detuning of any incident radiation from the atomic resonance between the two levels, the diagonal terms (ρ_{11} and ρ_{22}) measure the populations and the off-diagonal terms (ρ_{12} and ρ_{21}) measure the coherence. The total vector $\mathbf{R}$ is a unit vector which points to a specific location on the Bloch Sphere, where the north and south poles ($w = 0$ or 1) represent a pure $|0\rangle$ or $|1\rangle$ state respectively. The dynamical behaviour of the Bloch vector in a Caesium Fountain clock can be described by the Optical Bloch Equations [114][116] with no decay,

$$\begin{aligned} \dot{u} &= \delta v \\ \dot{v} &= -\delta u + \Omega w, \\ \dot{w} &= -\Omega v, \end{aligned} \tag{5.12}$$

$$\dot{\mathbf{R}} = \mathbf{R} \times (\Omega, 0, \delta)^T = \mathbf{R} \times \mathbf{W}, \tag{5.13}$$

where Ω is the Rabi frequency of the transition, and we have defined the rotation vector W. Decay terms can be neglected from the system of equations in the case of radio frequency hyperfine transitions, due to the extended lifetime of the states. If we consider the case that the Bloch vector is initially in a pure state of $(0, 0, 1)^T$; it can be read from equations 5.12 and 5.13 that when Ω is non-zero (i.e the atom is exposed to driving radiation) the orientation of the vector will rotate. If we consider an atom continuously exposed to resonant radiation ($\delta = 0$), we find that the Bloch vector rotates around the u axis with frequency Ω, which is characteristic of Rabi oscillations [117]. It is possible to produce population inversion via exposure to resonant radiation for a period of length $\tau_\pi = \pi/\Omega$, or to produce an equal superposition via $\tau_{\pi/2} = \pi/2\Omega$ - these are referred to as π and $\pi/2$ pulses respectively [116]. In the case of non-resonant radiation, the detuning term δ is non-zero; this tilts the rotation vector W such that it has a w component.

An interesting feature of the equations 5.12 and 5.13 is the dynamics of the Bloch vector without driving radiation. When the Bloch vector is rotated to the equator via a $\pi/2$ pulse with finite detuning, the Bloch vector will continue to evolve even after the driving radiation is turned off. At this point, $\Omega = 0$, and the vector begins to rotate around the equator with frequency δ. The Bloch vector continuing to rotate even when not exposed to external radiation may seem puzzling; however, the Bloch vector formalism contains an implicit coordinate transform into a system that rotates with the frequency of the incident radiation. This coordinate transform is

denoted by the substitution $\rho \rightarrow \widetilde{\rho}$. When on resonance, this is the same as the frequency as the normal eigenfunction evolution–however when δ is finite it involves transforming to a detuned coordinate system. The relative phase between the normal eigenfunction oscillation and the detuned coordinate system rotation frequency manifests itself as an angular rotation in the equatorial plane of the Bloch sphere, even in the absence of driving radiation.

The δ dependent free equatorial rotation of the Bloch vector during time T is the key component of Ramsey's experimental method of separated fields. As mentioned earlier, the Ramsey method consists of three stages: 1) expose atoms to radiation for time τ, 2) allow free evolution for an intermediate time T, 3) re-expose atoms to identical radiation for time τ. The length of τ is chosen to be $\tau = \pi/2\Omega$ such that both exposures are $\pi/2$ pulses, and T is made as long as possible to maximise precision. These three stages are conducted in an atomic fountain, by exploiting the trajectory of an atomic sample when launched upwards and allowed to fall back down due to gravity, as displayed in figure 5.5. The atoms pass through a microwave cavity twice: once on their ascent, and a second time on their descent, passing through a microwave-field-free region during the intermediate time. The power of the microwave cavity is tuned such that the time spent by the atoms moving through the cavity equates to a $\pi/2$ pulse.

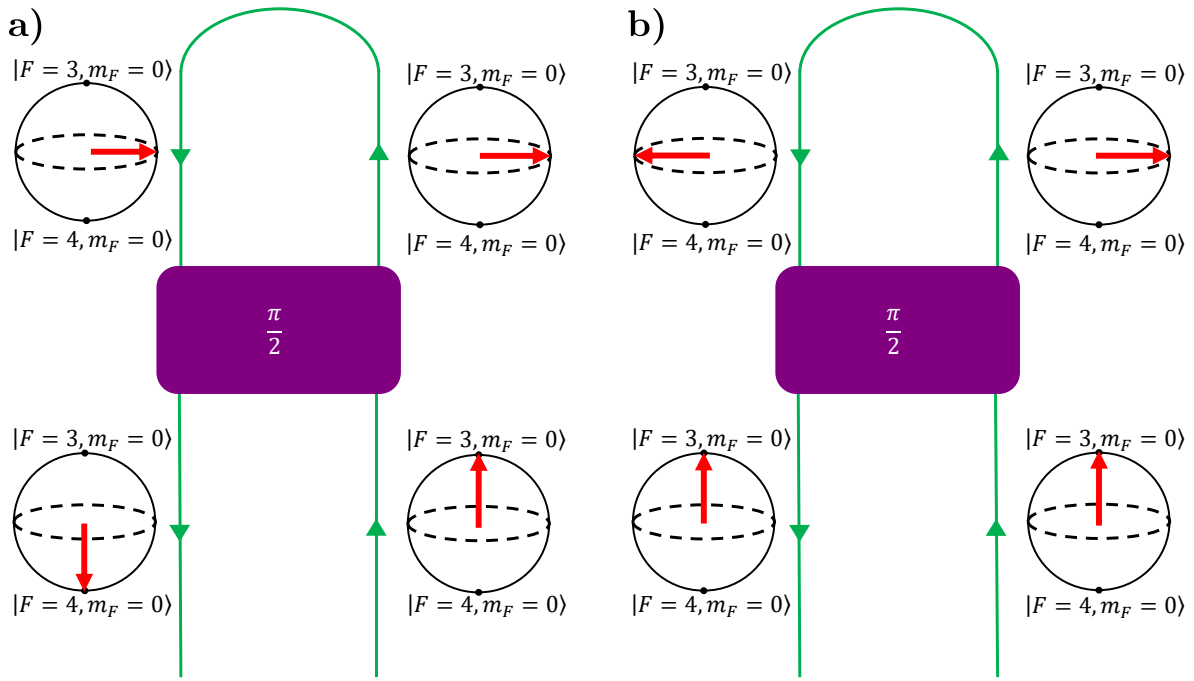

Fig. 5.5. The dynamics of a caesium atoms Bloch vector during its trajectory within the fountain, **a)** no detuning $\delta = 0$ and **b)** $\delta = \pi/T$

Let us consider first the cases of resonant microwaves, which is displayed in figure 5.5a. Assuming that the atoms are initially in the ground state, $\mathbf{R} = (0, 0, 1)^T$, passing through the cavity the first time will provide a $\pi/2$ pulse that will rotate the Bloch vector to $\mathbf{R} = (0, 1, 0)^T$ in the equatorial plane. During the free flight time, T, the Bloch vector will remain in the

same orientation as $\delta = 0$, and the second pass through the cavity provides the second $\pi/2$ pulse that will rotate the Bloch vector to the south pole $\mathbf{R} = (0, 0, -1)^T$. This zero-detuning case equates to the peak of the central Ramsey fringe. However, if we consider the effects of finite δ during the free flight time, we see that the Bloch vector rotates from $\mathbf{R} = (0, 1, 0)^T$ along the equator by angle $\varphi = \delta T$. In the case of $\delta = \pi/T$, displayed in figure 5.5b, the free flight evolution of the Bloch vector rotates it to $\mathbf{R} = (0, -1, 0)^T$, and the second $\pi/2$ pulse rotates the Bloch vector back to the north pole. This equates to the trough on either side of the central Ramsey fringe. At larger δ, we find maxima when δ equals an even multiple of π/T, and minima at odd multiples. The equatorial angle accumulated during the free evolution affects the projection of the Bloch vector on w after the second $\pi/2$ pulse, such that $w_{final} \propto -\cos(\delta T)$. If we consider that the probability of being in the excited state is equal to $|c_e|^2 = (1 - w)/2$, we find that the probability function displays characteristic Ramsey Fringes:

$$|c_e|^2 \propto \cos^2\left(\frac{\delta T}{2}\right). \tag{5.14}$$

The increased precision in determining the transition frequency via the Ramsey method is immediately obvious from equation 5.14. The peak width (FWHM) of the central peak is $\Delta\omega = \pi/T$, or $\Delta f = 1/2T$. The time T can be relatively long, in our fountain is approximately 0.5 s, resulting in a central peak width of $\approx$ 1Hz.

5.3 | The Caesium fountain apparatus

Now that the physical principles that underlie operation of the caesium fountain have been put forward, we shall describe the key hardware components which comprise the caesium fountain. We shall first discuss the physics packages, which is the section of hardware which acts as the fountain. We then describe the optical setup which performs the various laser operations required in the fountain. Finally we discuss the microwave generation for fountain operation.

5.3.1 Physics package

Figure 5.6 displays the physics package of the fountain system. This is the main part of the apparatus, where the caesium atoms undergo the operations of the fountain cycle. It was assembled at the National Physical Laboratory (NPL) and is based on previous designs, [118]. The internal volume of the apparatus is an ultra-high vacuum – to achieve this the system is baked for 8 weeks until a residual background gas pressure of 2×10^{-11} mbar is obtained. The ultra-high vacuum is maintained by a combination of ion getter pumps and non-evaporable getter (NEG) pumps. In addition, shaped graphite getter materials are added in the region between the MOT and microwave cavities to reduce the amount of Cs background gas in the detection region. The various stages of the experimental cycle occur within distinct sections of the physics package, each equipped with its own specialized instrumentation. The lower section

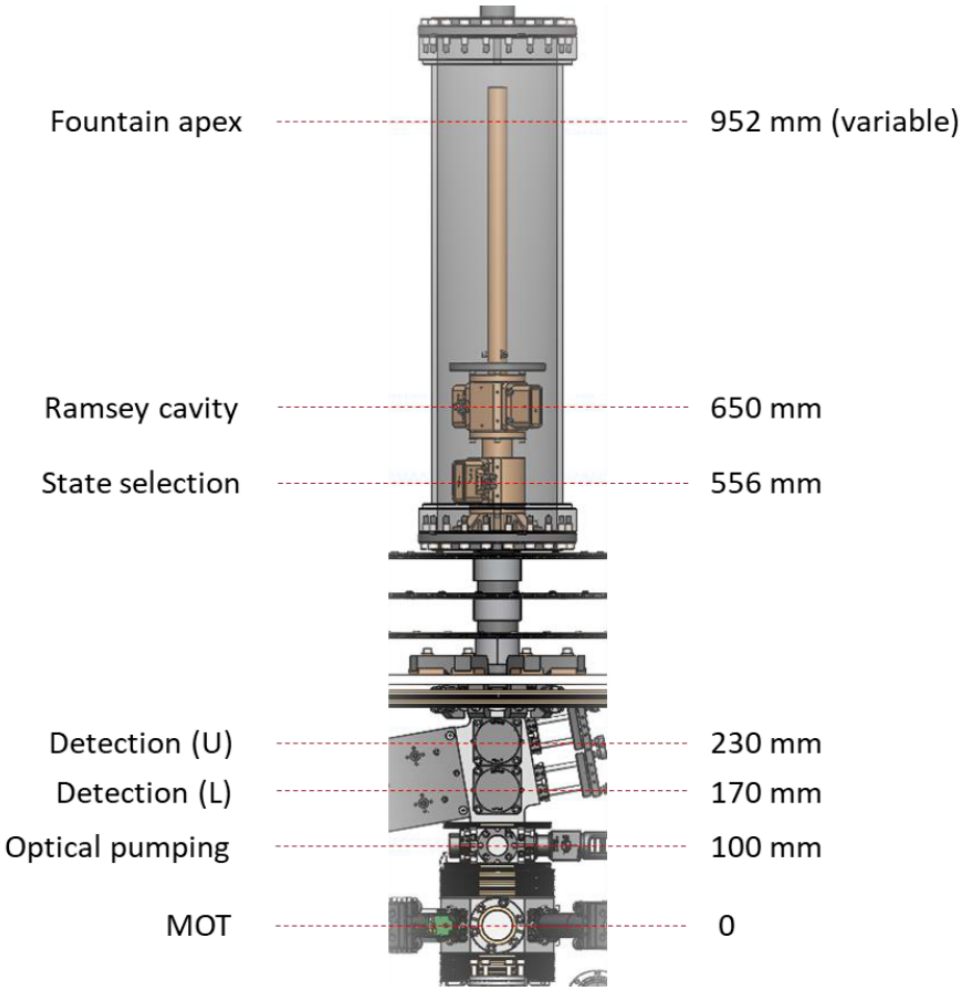

Fig. 5.6. Overview of the physics package, with the Cs atom cloud height of the different stages indicated. Provided my NPL.

of the apparatus performs state preparation and detection, it contains instrumentation for a magneto-optical trap (MOT), optical molasses (OM), optical pumping, and state detection. The upper section is where atoms are exposed to microwaves during their ballistic path. This region is enclosed by magnetic shielding and consists of microwave cavity situated beneath a copper flight tube.

Lower section

We shall describe the key components of the lower section starting from the bottom and heading upwards. The lowest component is the caesium reservoir. Caesium vapor is loaded into the reservoir chamber by crushing a sealed ampoule containing 1 gram of caesium. This reservoir is isolated from the primary fountain chamber by a valve, allowing for the potential future replacement of the caesium without having to vent the entire vacuum system. An extra, unopened ampoule is kept in reserve for future caesium supply once the initial one has been used up. The reservoir's temperature is regulated using Peltier elements, which are cooled by circulating water on their hot side. Above the caesium reservoir is the MOT and OM apparatus; this is formed by three orthogonal pairs of counter-propagating laser beams and a pair of

345-turn coils situated above and below the intersection of the beams. The 6 laser beams provide three-dimensional cooling; they are delivered from the light distribution module to the physics package by optical fibres, along with repumping light which is overlapped with one of the horizontal cooling beams (see section 5.3.2). The pair of vertical beams span the entire height of the physics package and are used for optical pumping and launch. The two coils are operated in an anti-Helmholtz configuration which provides the spatially varying quadrupolar magnetic field with a zero field that overlaps with the intersection of the optical beams. The apparatus has dual functionality: operating as a MOT when the coils are energized, and as an OM when they are not. The ambient magnetic field of the Earth is compensated by using three pairs of rectangular coils which surround the lower region of the apparatus and correct the three orthogonal components of the ambient field. Directly above the MOT are two coils in the Helmholtz configuration. These coils are used to produce a homogeneous magnetic field that breaks the degeneracy of the magnetic sublevels for optical pumping. Continuing upwards above the optical pumping coils we reach the two detection regions, the lower detection for $|F = 3\rangle$, and the upper detection for $|F = 4\rangle$, each with its own photodetector. Above the detection region are two small guiding coils which prevent magnetic field zero regions and spin flips in the atoms during their ascent to, and descent from, the upper region of the apparatus.

Upper section

The upper section of the physics package is where the Ramsey spectroscopy takes place, it comprises the state selection cavity, the Ramsey cavity and the free flight region. Both microwave cavities have cylindrical structure with openings in the endcaps for the atoms to pass through with dimensions carefully tuned such that the TE_{011} mode is resonant with the clock transition. The state selection cavity is used to transfer the population from the $|F = 4\rangle$ to the $|F = 3\rangle$ state before their interrogation by the Ramsey cavity. The state selection cavity is fed by a single rectangular cavity (TE_{012}), which is coupled to the main cylindrical cavity through a circular hole of 1.5 mm radius in the wall of the cavity. The Ramsey cavity provides a $\pi/2$ microwave pulse each time the atoms pass through, resulting in Ramsey type spectroscopy. The Ramsey cavity is symmetrically fed by two rectangular cavities, which couple via two 1mm radius holes which are placed symmetrically about the midplane in the cavity wall. The Ramsey cavity dimensions have been designed and tuned such that the TE_{011} mode in the main cylindrical part of the cavity is resonant with the clock transition when the cavity is at 22 °C. The two cavities are contained within the double-walled aluminium flight tube. The flight tube also attenuates any microwave leakage by acting as a waveguide below the cut-off. The temperature of the upper region of the fountain is controlled through the circulation of cooling water in a space between the outer walls of the upper section using a ThermoCube recirculating chiller. Around the outer walls of the upper section is the C-field coil which produces the 114 nT vertical magnetic field that breaks the magnetic sublevel degeneracy. The microwave cavities, flight tube, and coil are enclosed in three cylindrical layers of mu-metal magnetic shielding which provide an attenuation factor of over 10000.

5.3.2 Optical setup

The fountain utilizes two laser systems for its operation. The primary laser is a Distributed Bragg Reflector (DBR, Vescent D2-100-DBR-852-HP) which emits 852 nm light (with a typical linewidth of 250 kHz), which is used for laser cooling, optical pumping and detection. The secondary laser is a Distributed Feedback (DFB, Toptica DFB pro) laser with a typical linewidth of 3 MHz, which is used as a repumper to prevent the accumulation of atoms in the $F = 3$ state. The optical setup of the system is composed of three interconnected rack-mounted breadboards: the laser board which contains the lasers and most of the initial optics; the spectroscopy board which contains the Cs cells and instrumentation used for locking and controlling the laser frequencies; and the distribution board where the beams are split up and distributed via optical fibre to the physics package of the fountain. All beams are equipped with mechanical shutters operated by a small electromagnet. The optical layout of each of these boards is illustrated in Figure 5.7. The other end of each of the fibre is mounted in a cage assembly that is connected to flanges on the vacuum chamber. The power of each beam is monitored with small photodiodes attached to the side of each cage and logged at the start of each fountain cycle. Other than a few technical interventions, the entire optical system has displayed exemplary pointing and frequency stability, which has been demonstrated by continuous operation over several months.

The primary laser is used to excite the $|F = 4\rangle \longrightarrow |F = 5'\rangle$ transition; for frequency stability the laser is locked to this transition in a room temperature Cs cell on the spectroscopy board using Doppler-free saturated absorption spectroscopy. To achieve this, the laser current is modulated at 4 MHz and the two probe beams are differentially detected, with one of them being overlapped with a pump beam in the reverse direction. This produces a Doppler-free error signal for the locking servo to act on the laser current. A second slow feedback loop on the laser temperature is implemented to extend the locking range. A double-pass AOM operating between 70 to 100.5 MHz before the Cs cell is used to control the primary laser frequency. A second branch of the primary laser is sent to the fibre distribution board via a fibre-coupled tapered amplifier (TA, New Focus VAMP TA-7616). The arriving 200 mW beam is split into 8 different polarization-maintaining fibres which lead to the physics package. Six of these beams form the MOT: the four horizontal (X_1, X_2,Y_1,Y_2) beams are shifted to the cooling transition by a double-pass AOM with a fixed frequency of 100.5 MHz. The frequency of each of the two vertical beams (Z_{up}, Z_{down}) can be controlled independently using their own AOM – this enables the formation of a moving molasses [112]. The seventh beam, used for optical pumping, is delivered to the region directly above the MOT–where an additional polarizing beamsplitter produces a pure π polarization required for pumping. A retroreflector on the other side of the vacuum chamber ensures symmetric photon scattering to avoid deflection of the atom cloud. The frequency of optical pumping light is controlled via a double-pass AOM at 189.8 MHz which tunes the beam 10 MHz below the $|F = 4\rangle \longrightarrow |F' = 4\rangle$. The eighth and final beam originating from the primary laser is used for state detection. The light is delivered

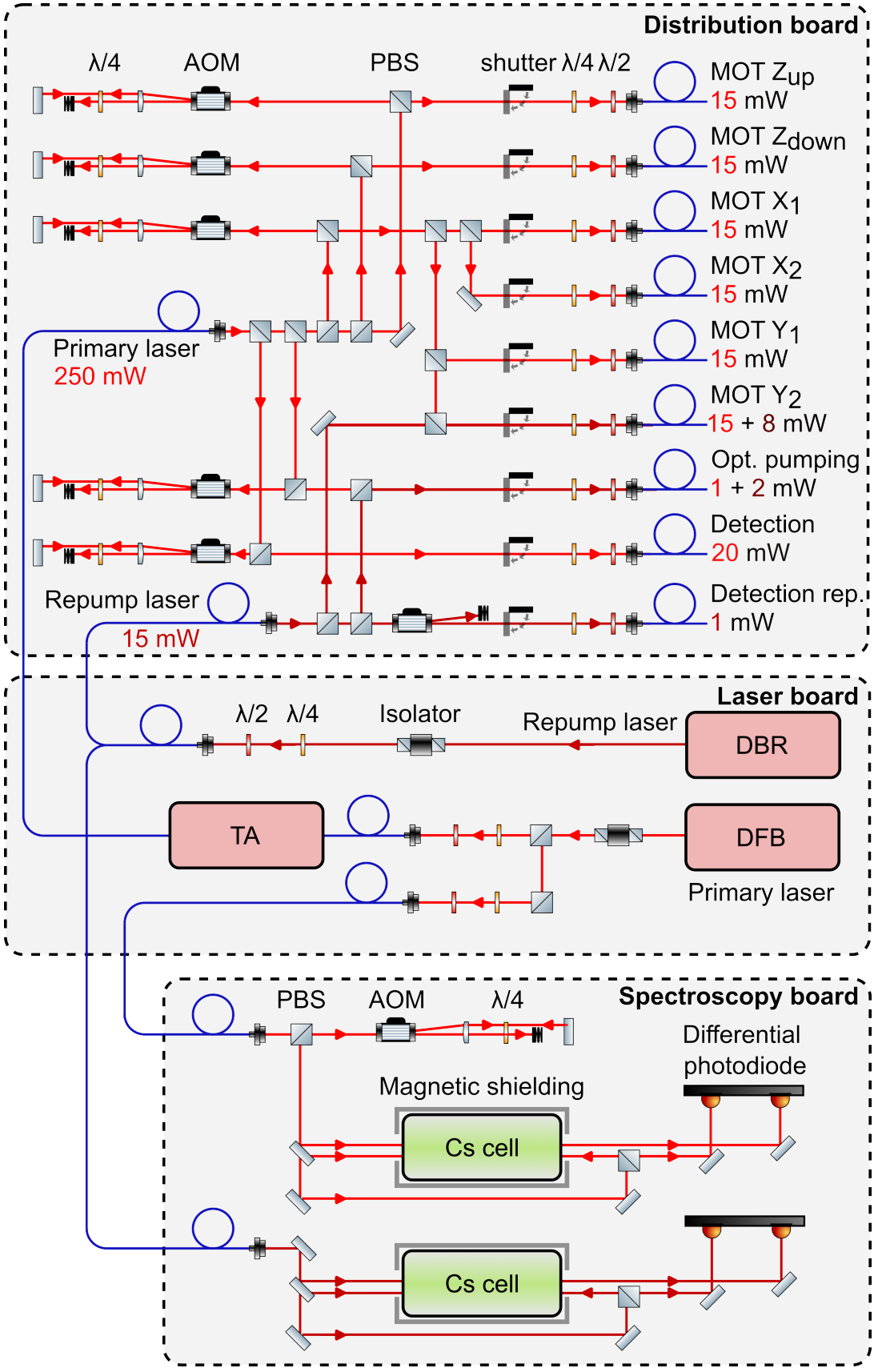

Fig. 5.7. Overview of the optical system. AOM: Acousto-Optical Modulator, PBS: Polarizing Beampslitter, $\lambda/2, \lambda/4$: retardation plates, DBR: Distributed Bragg Reflector, DFB: Distributed Feedback, TA: Tapered Amplifier.

to the detection region, where it is split by a polarizing beam splitter and directed into the vacuum chamber as the two parallel beams used for the upper and lower detection. Light in the lower detection is overlapped with a laser beam from the repumping laser for detection of the $|F = 3\rangle$. Fluorescent light is collected through two windows perpendicular to the detection beams and focused onto two low-dark count amplified photodiodes through a band-pass filter to reduce background. The florescence signal collected by the photodiodes is used as a measure of the relative populations in each state. A lens and retroreflector assembly behind the opposite vacuum window is used to effectively double the amount of light collected for each detection region. The frequency of the detection light is shifted to exactly the $F = 4 \longrightarrow F' = 5$ transition by an 80 MHz double-pass AOM.

The repump laser is used to excite the $F = 3 \longrightarrow F' = 4$ transition. The laser frequency is locked to this transition using a caesium cell, with a 20 kHz modulation of the diode current. The repump light is split into three separate beams on the fiber distribution board. The first beam is combined with the Y_2 MOT beams. Due to the red detuning required for cooling, there is a non-zero overlap between with MOT beam frequency and the $|F = 4\rangle \longrightarrow |F = 4'\rangle$ transition. This can cause atoms to exit the cooling loop, by decaying from the $|F = 4'\rangle$ into the $|F = 3\rangle$ 'dark' state. The repump beam is overlapped with the MOT to excite any atoms which decay into the dark state back into the cooling optical loop. A second repumping beam is combined with the optical pumping beam, to excite any atoms which decay from $|F = 4'\rangle$ state into the $|F = 3\rangle$ state during the optical dumping. The third beam is delivered through a seperate fibre, but later combined with the lower detection beam. The aim of this beam is to pump the $|F = 3\rangle$ states to the $|F = 4\rangle$ for state detection. The power of all beams can be adjusted by changing the radio-frequency power fed to the AOMs.

5.3.3 Microwaves

The microwaves used for the Ramsey spectroscopy are generated using a CS-1 model synthesizer from SpectraDynamics Incorporated; it is referenced by a 5 MHz signal from ALPHA-HM1. Inside the synthesizer the 5MHz reference frequency is converted to a 100 MHz signal using two ultra-low-noise quartz oscillators. The 100 MHz signal is fed to a dielectric resonant oscillator (DRO) that outputs 9.2 GHz. A 7.36823 MHz signal of a tunable direct digital synthesizer (DDS) with 48 bit resolution is mixed with the DRO output to yield the microwaves which are fed into the Ramsey cavity for driving the clock transition at 9192631770 Hz. Because the reference frequency is provided by ALPHA-HM1, it is possible to determine the frequency error on ALPHA-HM1 by measuring the difference between the clock transition frequency and the frequency of the microwaves in the Ramsey cavity.

Microwaves for the supply of state selection cavities are generated separately using a frequency chain built by NPL. A high-frequency voltage-controlled oscillator is phase-locked to the 10 MHz reference provided by ALPHA-HM1, generating the fourth harmonic signal at 9.210 GHz. By mixing this signal with a 17.36823 MHz RF signal provided by a direct

digital synthesizer results in a microwave output at the clock frequency. A current-controlled attenuator acting on the RF component controls the microwave power which is used to tune the selection cavity power to control the fraction of atoms transferred to the $|F = 3\rangle$ clock state. To avoid microwave leakage above and below the cavities, both microwave sources are rapidly detuned from resonance when atoms are not within them, detuning the Ramsey cavity by 1 MHz and the state selection cavity by 6 MHz. In addition to the frequency shift, the microwave power is reduced to zero in the selection cavity.

5.4 | The fountain cycle

In this section, we summarise the various stages of the fountain cycle in more detail

i) Sample capture and cooling

The first step of the fountain cycle is to accumulate and laser-cool the sample of atomic caesium which is used for the rest of the fountain cycle. First, caesium atoms are accumulated in a MOT, which is formed by a quadrupolar field produced by the anti-Helmholtz coils and the intersection of three orthogonal pairs of counter-propagating beams (X_1, X_2, Y_1, Y_2, Z_{up}, Z_{down}). The six beams forming the MOT have circular polarisation and a red-detuning of 19 MHz from the $|F = 4\rangle \rightarrow |F = 5'\rangle$ transition. Caesium atoms are confined and cooled in the MOT for 553 ms, the accumulated cloud of caesium can be observed visually through a small view port on the back of the MOT chamber using an IR viewer, where it will be seen as a 1-2 mm diameter bright spot. Following the MOT stage, the magnetic field and cooling beams are both switched off for a brief 5-10 ms 'dark period'. The cloud of caesium expands freely during the dark period due to diffusion, so by adjusting the duration of the dark period it is possible to control the size of the caesium sample. Following the dark period the cooling beams are restored at full power, subjecting the caesium sample to 40 ms of optical molasses cooling before launch.

ii) Launch

For 0.3 ms the horizontal beams are extinguished, and up and down beams are detuned by a further -2.54 MHz and +2.54 MHz respectively. The vertical beam detuning forms a moving molasses [112] which launches the atoms by producing a molasses in a frame of reference which is moving upwards at 4.3 ms^{-1} with respect to the lab frame. The horizontal beams are restored following the launch for 1.9ms for a final polarisation gradient cooling. During this period all of the cooling beams are further detuned rapidly to -13Γ and the beam intensity is gradually ramped to zero. This final cooling stage implements polarisation gradient cooling to produce a caesium sample temperature on the order of $\sim 1\,\mu K$

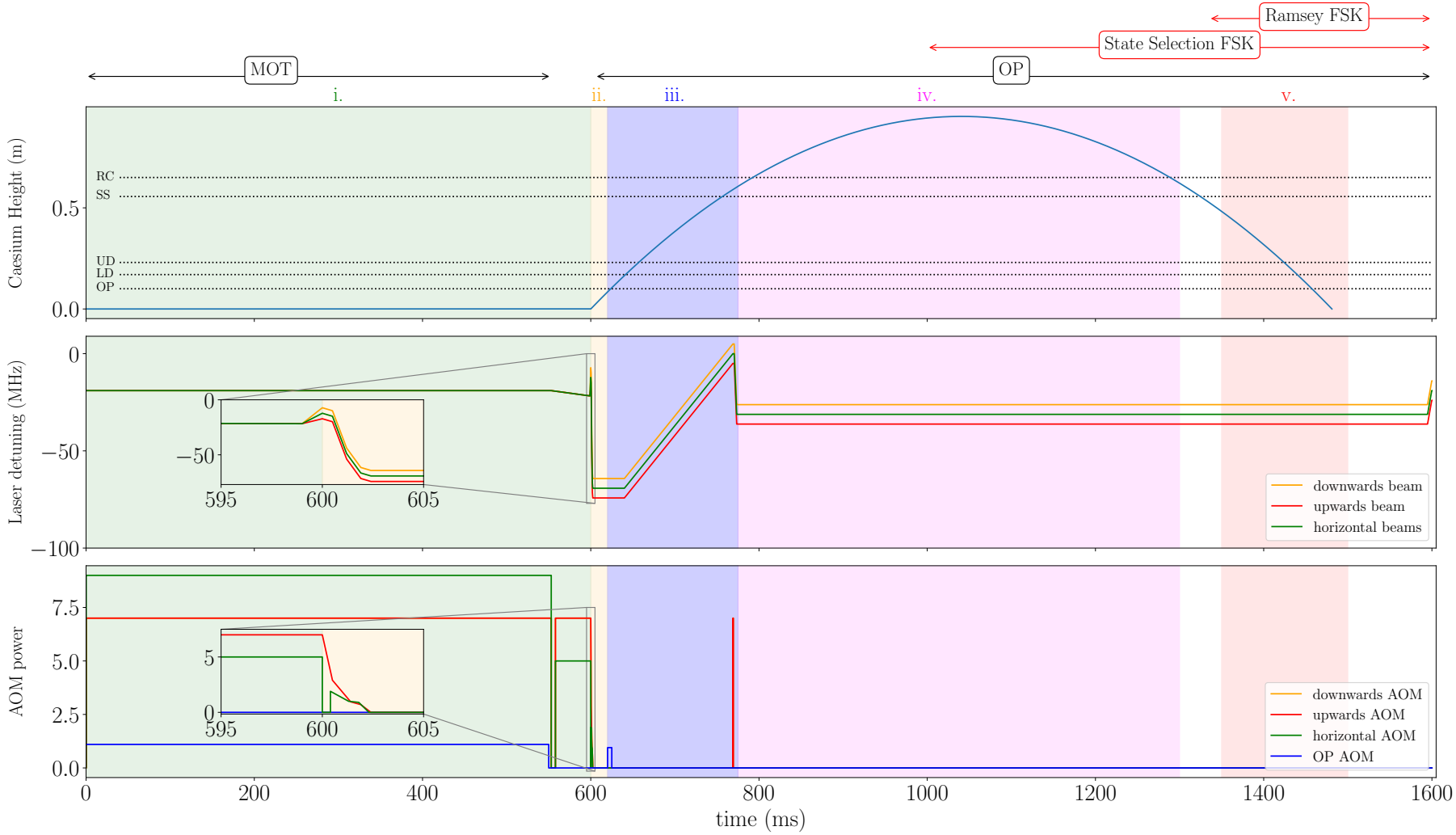

Fig. 5.8. Overview of the caesium fountain cycle, showing the evolution of laser power, laser frequency and atom height during during the cycle. (i.) capture and cooling of Cs atoms, (ii.) launch phase, (iii.) state preparation, (iv.) Ramsey spectroscopy, (v.) detection. The inset display details of the laser frequency detuning and power during the OM and launch phase, see text for more details. The black arrows indicate when current is running through the MOT and OP coils, while the red arrows show when the selection and Ramsey cavity are frequency shifted away from the Cs ground state hyperfine transition to reduce microwave leakage. The MOT sets the location of the zero in the top figure. OP: optical pumping, LD: lower detection region, UD: upper detection region, SS: state selection, RC: Ramsey cavity.

iii) Caesium state preparation

Following the launch stage the atomic sample is extremely cold; however, it will contain a mixture of substates. The objective of state preparation is to produce the highest possible population of atoms in the $|F = 3\rangle$ state, to maximise the signal in the subsequent spectroscopy and detection stages. Approximately 20 ms after the launch, the atomic sample traverses a beam consisting of repump and pulsed optical pumping laser light. The linear (π) polarisation of the optical pumping beam ensures that atoms are pumped into the $|F = 4, m_F = 0\rangle$ state due to the $\Delta m_F \neq 0$ selection rule (note that the m_F states are degenerate due to the local magnetic field). The optical pumping power can be set to maximise the $|F = 4, m_F = 0\rangle$ state to >90%; however, this requires high-power optical pumping which heats up the atomic cloud. As such, the optical pumping is optimised to ensure a state transfer of roughly 70% as a tradeoff between signal and temperature. The repumping beam is used to re-excite any atoms out of the $|F = 3\rangle$ dark state. After optical pumping the atoms pass through the state selection cavity. The state selection cavity is resonant with the $|F = 4, m_F = 0\rangle \rightarrow |F = 3, m_F = 0\rangle$ transition. When the atoms traverse the state selection cavity they experience a π pulse which transfers them to the lower state $F = 3$ state. After this, any atoms remaining in the $|F = 4, m_F = 0\rangle$ state are removed via a pusher pulse from the Z_{up} beam, which is resonant with the $|F = 4\rangle \rightarrow |F = 5'\rangle$ transition. Any remnant $|F = 4\rangle$ states are heated out of the sample by the pusher pulse. After sample and state preparation, the fountain will have an ultra-cold sample of caesium atoms, entirely in the $|6^2S_{1/2}, F = 3, m_F = 0\rangle$ state.

iv) Ramsey Spectroscopy

Following state preparation, the caesium sample continues to travel upwards until it traverses the Ramsey cavity. The microwave power in the Ramsey cavity is tuned such that the caesium sample receives a $\pi/2$ pulse during a single pass. The first pass of the cavity puts the atomic sample in a superposition of $|F = 4, m_F = 0\rangle$ and $|F = 3, m_F = 0\rangle$ state. This superposition is allowed to freely evolve for 0.5 s as the atoms continue their ballistic trajectory in the flight tube, reaching an apogee 90.05 cm. The atoms then fall back through the Ramsey cavity and experience the second $\pi/2$ pulse.

iv) Detection and correction

After passing through the Ramsey cavity a second time, the atoms continue their downward trajectory through the detection region, which consists of the upper and lower detection region. During detection, fluorescence is used to determine the relative populations of each groundstate sublevel. The upper detection beam is tuned to the $|F = 4\rangle \rightarrow |F' = 5\rangle$ transition, which induces fluorescence as the atoms traverse it. The fluorescence signal is detected via a photodetector and is proportional to the $|6S_{1/2}, F = 4\rangle$ population. The upper detection beam also accelerates the atoms, which pushes them off-resonance for when they are passing through the lower detection beam. The lower detection beam is overlapped with a repump beam, which rapidly pumps the $|F = 3\rangle$ atoms back to the $|F = 4\rangle$ state so that they can be detected in the

same way as the upper detection region. These signals are used to produce the ratio measure, P, which is a normalised measurement for the probability of the atoms undergoing the clock transition during the fountain cycle $|F = 3\rangle \longrightarrow |F = 4\rangle$ transition. The ratio P is given by

$$P = \frac{N_4}{N_4 + N_3}, \tag{5.15}$$

where N_4 and N_3 are the populations in the upper and lower levels of the clock transition receptively - measured through fluorescence. In normal clock operation, the Ramsey cavity

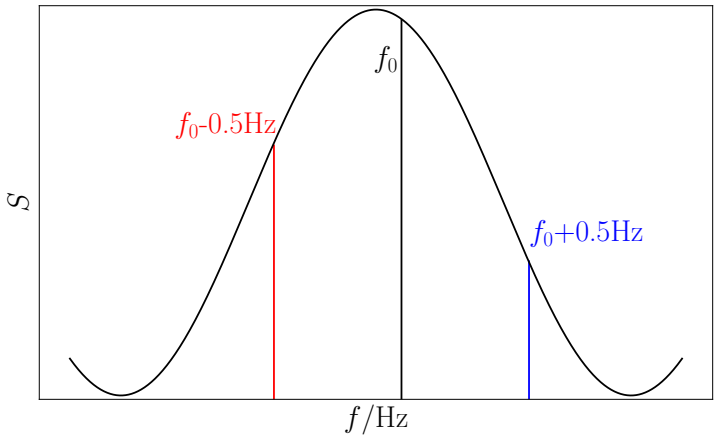

Fig. 5.9. Two frequency measurements are made on either side of the central fringe

switches back and forth between two frequency measurements on either side of the expected maxima of the central fringe: $f_0 + 0.5$Hz and $f_0 - 0.5$Hz, as displayed in figure 5.9. The ratios P_+ and P_- is measured at these points, which are the most sensitive to changes in frequency. If f_0 is on the maximum of the central fringe, these ratios should be equal. However, if not, then the difference between these ratios is used to produce a correction to the microwave synthesizer frequency, $v = (m/2) \cdot (P_+ - P_-)$ where m is the maximum slope of the central fringe. This correction is applied to the microwave synthesizer every second cycle of the fountain, resulting in the synthesizer frequency tracking the maximum of the central fringe.

5.5 | Evaluation of Systematic Biases

The extremely high precision of the clock frequency measured by the fountain means that it is more vulnerable to shifts produced by systematic effects. For the fountain to operate as a primary standard, these systematic shifts must be measured and accounted for when determining the clock transition frequency. Presented here is an evaluation and compensation of the key sources systematic bias - further analysis of future data may yield an even lower systematic uncertainty on the fountain.

Effect	Bias	Uncertainty
Second order Zeeman	60.621	0.009
Collisional shift	6	0.1
BBR	-15.736	0.043
Microwave leakage	0.48	0.1
AC Stark		0.02
Gravitational shift		0.015
Microwave lensing		0.03
Microwave generation		0.1
Cavity pulling		0.01
DCP $m = 0$		0.1
DCP $m = 1$		0.5
DCP $m = 2$		0.1
Phase transients		0.1
Second order Doppler		0.01
Total	51.37	0.56

Table 5.1
Uncertainty budget for the ALPHA-Cs1, all values are parts in 10^{-15}.

5.5.1 Second Order Zeeman shift

The stable and uniform 114 nT C-field, provided by an external solenoid, is used to break the degeneracy of the m_F magnetic sub-levels. This is important for shifting the non-zero m_F states far off-resonance for state selection. The clock transition $|F = 3, m_F = 0\rangle \rightarrow |F = 4, m_F = 0\rangle$ is unaffected by the first-order Zeeman shift; however, it does experience the second-order quadratic Zeeman effect. The second-order Zeeman effect produces the largest corrected systematic shift in our clock transition frequency. The second-order Zeeman shift on the clock transition can be determined from the Breit-Rabi formula to be [110][119],

$$\frac{\delta\nu_{0\rightarrow 0}^{(2)}}{\nu_0} = \frac{(g_J - g_I)^2 \mu_B^2}{2h^2\nu_0^2} B^2, \tag{5.16}$$

where g_J and g_I are the electronic and nuclear gyromagnetic moments, μ_B is the Bohr magneton, B is the C-field, h is Planck's constant and ν_0 is the hyperfine splitting of the ground state.

The caesium atoms follow path dictated by the moving molasses launch and the influence of gravity; it is essential to characterise the magnetic field which produces the second order Zeeman shift during their path. The second-order Zeeman shift on the clock transition is proportional to the time average squared magnetic field, $\langle B^2 \rangle$ during the path of the atomic sample. This shift depends on the C-field's absolute value, as well as its homogeneity and stability. To measure the magnetic field acting on the atoms during their flight, the $|F = 3, m_F = -1\rangle \rightarrow |F = 4, m_F = -1\rangle$ transition is used as a magnetometer for mapping out

the C-field. The $m_F = -1$ energy levels are affected by the first-order Zeeman effect and will therefore very sensitive to changes magnetic fields. The shift induced by the first-order Zeeman effect on the magnetically sensitive transition can be determined from the Breit-Rabi formula as

$$\frac{\delta\nu^{(1)}_{1\to1}}{\nu_0} = \frac{(g_J - g_I)\,\mu_B}{4h\nu} B. \tag{5.17}$$

The Zeeman shift on this transition is proportional to the time-averaged magnetic field $\langle B\rangle$ experienced by the atoms during their path between the two microwave exposures. By varying the launch height of the atoms and measuring this transition, a map of the C-field in the drift region can be constructed. As mentioned above, the shift on the clock transition is

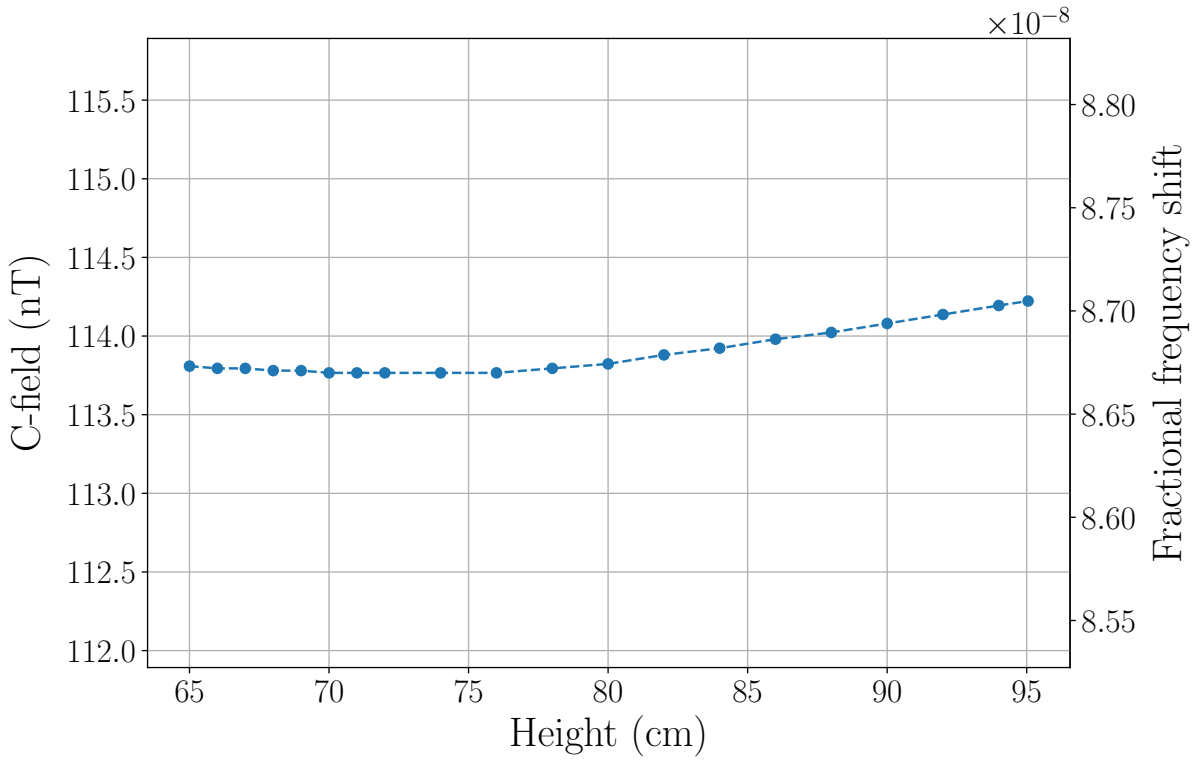

Fig. 5.10. A map of the C-field using the $|F = 3, m_F = 1\rangle \rightarrow |F = 4, m_F = 1\rangle$ transition. The right axis displays the fractional frequency shift, $\frac{\delta\nu^{(1)}_{1\to1}}{\nu_0}$, whereas left axis displays the C-field which induces the shift. The Ramsey cavity is situated at 65 cm, where 0 cm is the MOT location. Typical launch height is 95.05 cm.

proportional to $\langle B^2\rangle$ - however, we are only able to measure $\langle B\rangle^2$ in practice. The difference between these two values is our uncertainty on the shift, $\sigma_B = \langle B^2\rangle - \langle B\rangle^2$, and is equal to the variance in B throughout the atoms trajectory. In a perfectly homogeneous field the variance is zero, and the field map displayed in figure 5.10 demonstrates that the C-field is uniform to a 0.1 nT (<0.1%) level. This is sufficiently homogeneous that one can assume $\langle B^2\rangle = \langle B\rangle^2$ with negligible error ($\sim 10^{-18}$). Given that the C-field demonstrates sufficient uniformity, it is straightforward to combine equations 5.16 and 5.17 to produce an expression for the frequency shift induced on the clock transition as a function of the measured shift on the magnetically

sensitive transition:

$$\frac{\langle \delta\nu^{(2)}_{0\to 0}\rangle}{\nu_0} = 8\left(\frac{\langle \delta\nu^{(1)}_{1\to 1}\rangle}{\nu_0}\right)^2 . \tag{5.18}$$

When launching the atoms to the height used in standard operation, we measured $\langle \delta\nu^{(2)}_{0\to 0}\rangle$ to be 798.62Hz. This corresponds to a second-order fractional shift on the clock transition of 603.8×10^{-16} resulting from the atoms experiencing a time-averaged C-field of 113.95 nT during their trajectory. The dominant uncertainty associated with the second order Zeeman shift

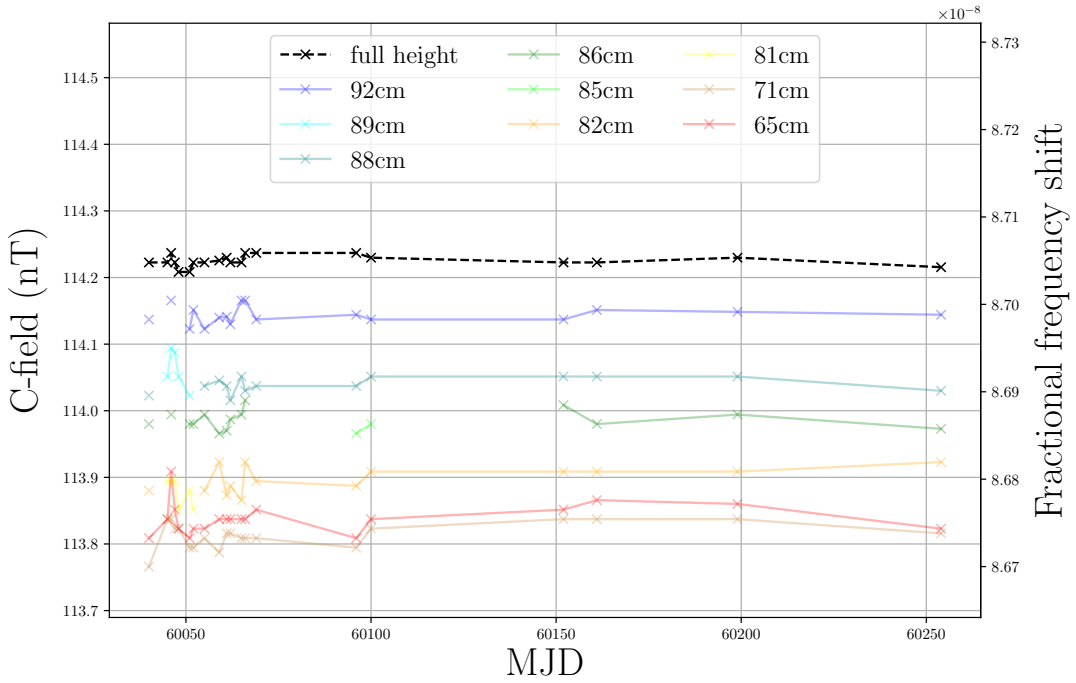

Fig. 5.11. Temporal drift of C-field. The full height (90.05 cm) is plotted in black, and lower heights plotted in different colours. The right axis displays the fractional frequency shift, $\delta\nu^{(1)}_{1\to 1}/\nu_0$, whereas left axis displays the C-field which induces the shift.

correction originates from the long-term stability of the C-field. In order to assess the long term stability of the C-field, a series of measurements of the C-field were taken at irregular intervals over a period of 214 days, displayed in figure 5.11. The average value of the C-field experienced by atoms launched to a height of 95.05 cm, denoted as $\langle B\rangle$, demonstrates excellent stability, with an average value of 114.224 ± 0.008 nT over the 214 day period. This corresponds to a second-order fractional shift on the clock transition of $(6.0621 \pm 0.0009)\times10^{-14}$.

5.5.2 Collisional shift

Another systematic frequency shift in fountain standards occurs as a result of collisions and interactions between the caesium atoms within the laser cooled sample; this perturbs the energy of both the $|F=3\rangle$ and $|F=4\rangle$ state during the ballistic flight between the Ramsey interrogations. The number of collisions between atoms is proportional to the atom density and can therefore be reduced by operating the fountain at a low density. However, a low

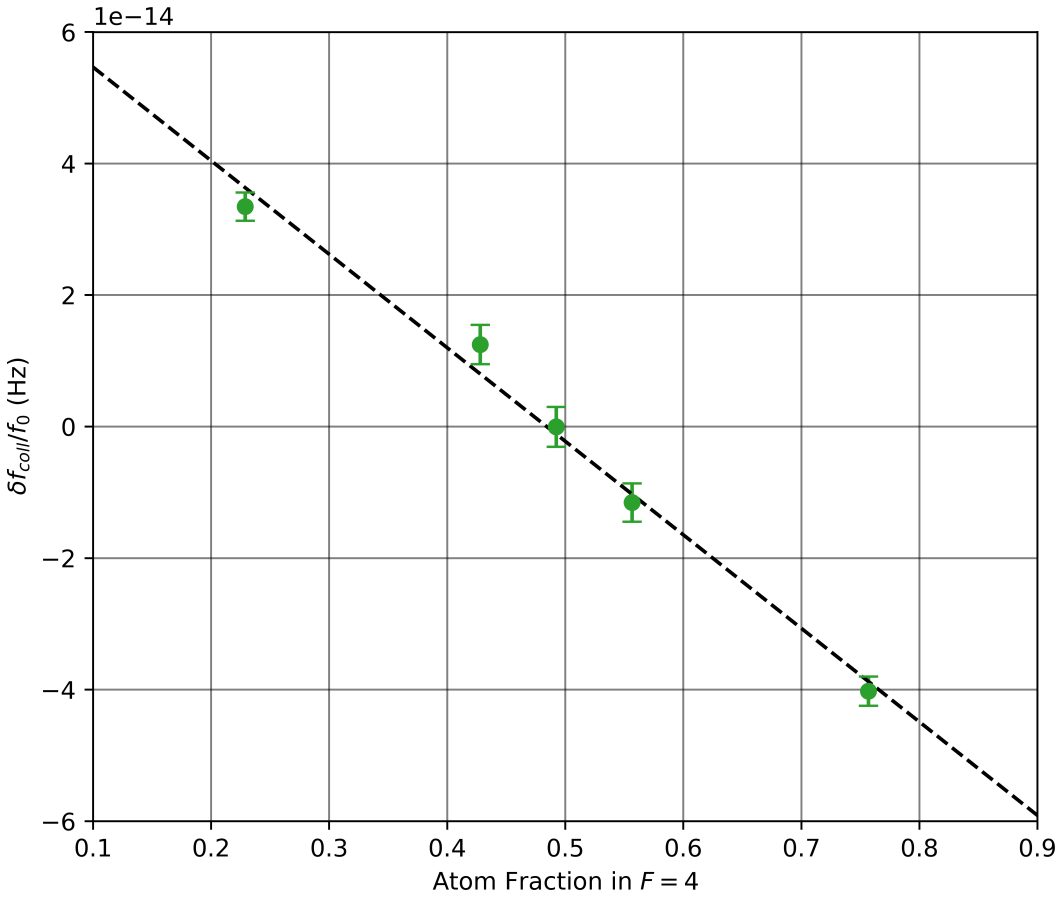

Fig. 5.12. Frequency difference between high density and low density operation of the fountain, for different atom fractions in the $|F = 4\rangle$ state after the first passage through the Ramsey cavity.

density sample results in a reduced signal-to-noise (SNR) ratio and short-term stability of the fountain. Generally, the collisional shift in fountains is corrected by taking measurements at multiple different densities, and extrapolating the measured frequency to zero atom density, assuming the the collisional shift is linearly proportional to density.

Within our fountain an additional technique is used to mostly cancel the collisional shift. According to theory [119], the frequency shift imparted on the clock transition by collisions at a single energy, E, is given by

$$\Delta\omega = n \sum_i \lambda_i(E)\rho_i, \tag{5.19}$$

where the sum is over the atomic hyperfine ground states, ρ_i is the population of state i, n is the number density, and λ_i are the collisional rate coefficients–which are calculated from scattering amplitudes. We assume that the only $|F = 3\rangle$ and $|F = 4\rangle$ states are populated, and as a result the sum in equation 5.19 only contains two terms. The collisional rate coefficients for the two states are strongly dependent on the collision energy; for low energies of a few μK and cloud sizes with a radius of approximately 1 mm, the collisional shift coefficients have opposite signs [120]. In the low-collisional-energy regime it therefore becomes possible to

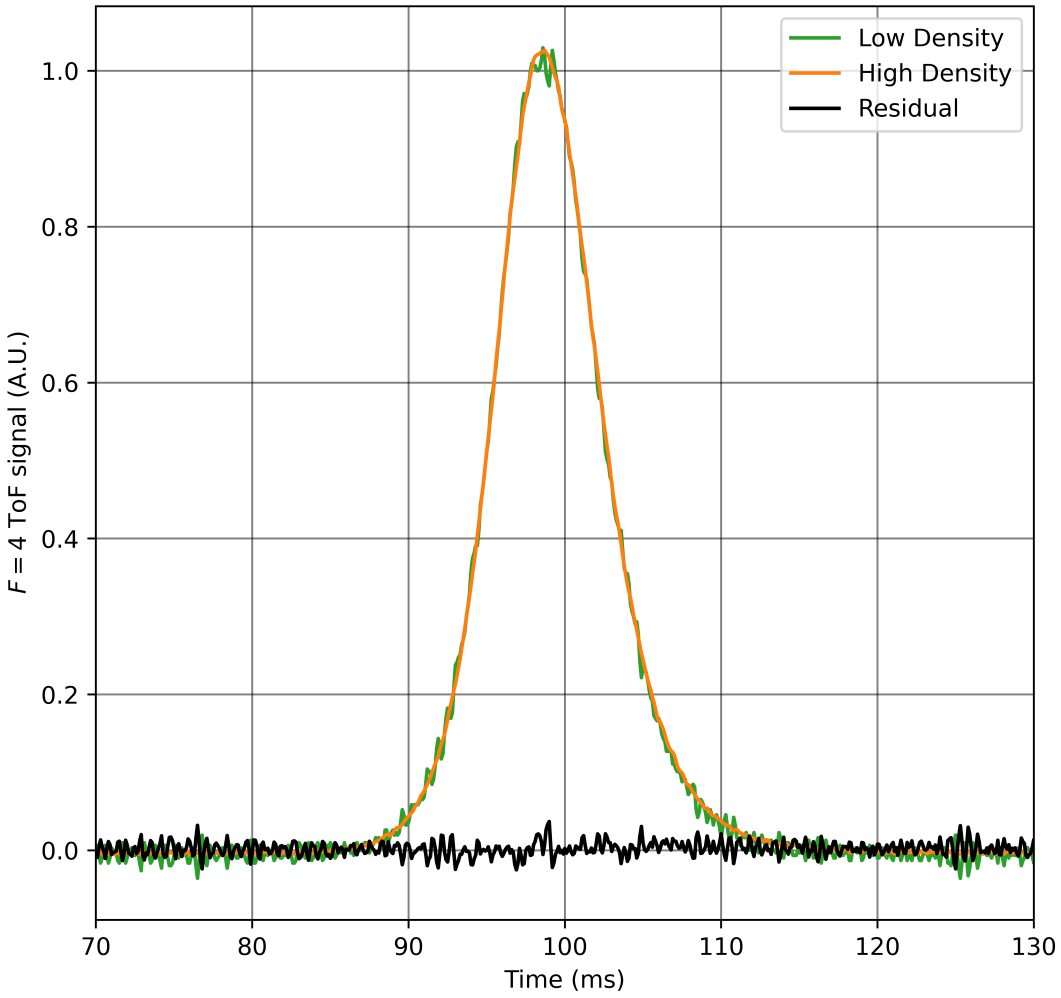

Fig. 5.13. Time of Flight (ToF) signal of the $|F = 4\rangle$ atoms for high and low density (HD and LD). The spatial profile of atoms passing through the detection region. Spatial profile of HD and LD atom clouds agree at the 2% level

choose a state population after the first Ramsey pulse which mostly cancels the collisional shift.

The initial atom cloud size is tuned by adjusting the expansion time after the MOT phase; an optimum cloud size is obtained by allowing the atoms to expand for 5 ms. All fountain parameters are optimised to reach a temperature of 3.2 μK, which is measured from the width of the time-of-flight (ToF) detection signal. The result is a caesium sample which is in low the collisional energy regime. The state populations are then tuned to maximise the cancellation of the collisional shift by adjusting the amplitude of the Ramsey pulses, as displayed in figure 5.12. The zero crossing of the linear relationship in figure 5.12 occurs at a $|F = 4\rangle$ population of 0.48, resulting in cancellation of the collisional shift with only a negligible reduction in fringe contrast.

Since the cancellation method requires fine tuning of cloud size and temperature, full cancellation is not always possible to maintain for extended periods of time. Any residual shifts due to collisions are corrected for by operating the fountain at two different alternating

densities and linearly extrapolating to zero density. This extrapolation is given by

$$f_{0,ext} = \frac{k \cdot f_{LD} - f_{HD}}{k-1}, \tag{5.20}$$

where f_{LD} and f_{HD} are the measured frequencies at low and high density, and k is the ratio between the two densities. It is only possible to measure the number of detected atoms through the time of flight; $k = N_{HD}/N_{LD} = 7$ if the linearity between the number of atoms and the density is assumed. A linearity between atom number and density requires that the atom cloud has an identical spatial profile at both densities. Since state preparation of the atomic sample continues until it is beyond the state selection cavity, we are unable to measure the cloud shape before it enters the Ramsey cavity. However, we can measure the spatial profile of the high and low density clouds at the detection stage of the fountain cycle using the ToF signal. This is displayed in Figure 5.13, which has residuals below 2%, indicating a nearly identical spatial profile for both cloud densities. The spatial profiles measured by the time of flight signal may not be representative of the initial spatial profile, which may have larger differences between the high and low density samples. To account for this uncertainty we assume a conservative estimate for the fractional error in k of 10%, which contributes an uncertainty on the extrapolated frequency given by [121]:

$$\sigma_{\text{ext}} = \frac{\sigma_k}{(k-1)^2} \Delta F'_{H-L}, \tag{5.21}$$

where σ_k is the uncertainty in k and $\Delta F'_{H-L}$ the measured collisional shift enlarged by its statistical uncertainty. Typical operating parameters of $\sigma_k = 0.6$ and $\Delta F'_{H-L} = 4 \times 10^{-15}$ result in a systematic uncertainty of 1×10^{-16}.

5.5.3 Blackbody radiation shift

The flight tube of the caesium fountain produces thermal electromagnetic radiation, which perturbs transition frequencies of the caesium atoms via the AC Stark and Zeeman effects. This can be modelled as the caesium atoms being surrounded by a cylindrical black body radiator at temperature T during their ballistic path, which induces a fractional frequency shift which is given by [122]:

$$\frac{\Delta f_{\text{BBR}}}{f_0} = \beta \left(\frac{T}{300\ \text{K}} \right)^4 \left[1 + \varepsilon \left(\frac{T}{300\ \text{K}} \right)^2 \right], \tag{5.22}$$

The coefficients β and ε have the numerical values of $(-1.718 \pm 0.003) \times 10^{-14}$ and 0.013 ± 0.001 respectively [123, 124]. The temperature of the flight tube is taken from the average value read by three T-type thermocouples positioned along the length of the water jacket. The thermocouples were calibrated to an uncertainty of 0.1 K, and typically agree within the calibration uncertainty–indicating no significant temperature gradients on the flight tube. We

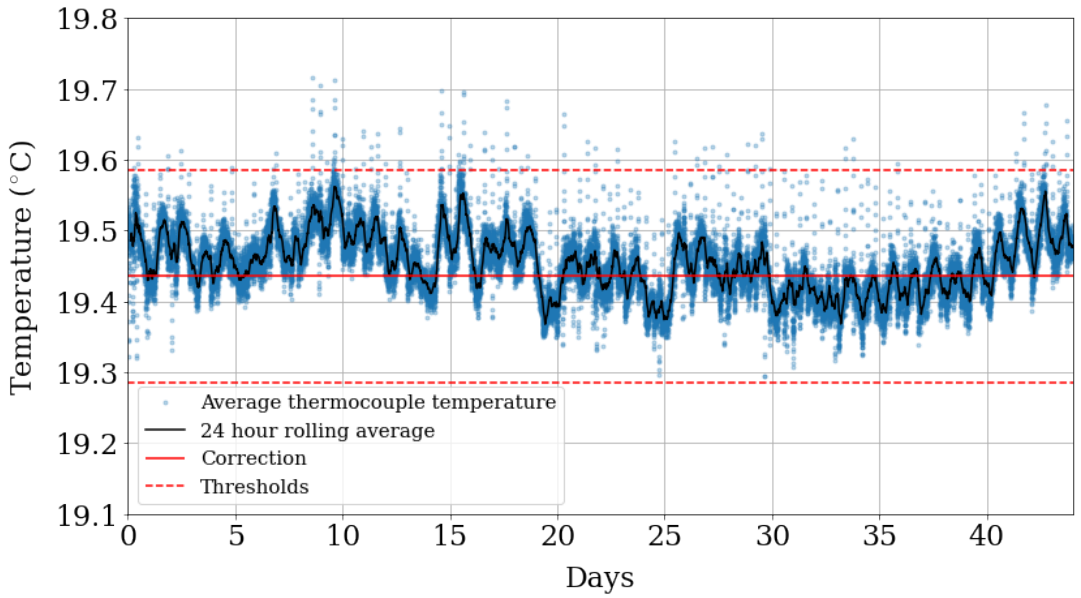

Fig. 5.14. Temperature variation of the fountain flight jacket, as measured by the three thermocouples along the drift tube. The blue data points are the average of all 3 thermocouples, sampled at 2 minute intervals. The black plot displays a 24 hour rolling average of the same data.

estimate the uncertainty on T is 0.2 K, which results in a total fractional uncertainty on the black body shift of 4.3×10^{-17}. The thermocouples monitor the temperature continuously, with example data displayed in figure 5.14. The correction for the black body shift is updated whenever the temperature changes by > 0.15 K for an extended period. The fractional systematic shift induced by the temperature data in figure 5.14 is -1.57308×10^{-14}

5.5.4 Microwave leakage

The operational principal of Ramsey spectroscopy involves two identical resonant interaction periods separated by an intermediate period during which the states can evolve freely. The fountain has been designed carefully to limit the leakage of microwaves into the regions outside the resonant cavities. The flight tube and copper tubes between and below the microwave cavities have been machined with diameters such that they act as a waveguide with a cut-off frequency well below the clock transition frequency. The effect of microwave leakage is further minimised by rapidly detuning the microwaves far off-resonance after the second passage through the Ramsey cavity, using a frequency shift key (FSK) protocol on the microwave synthesizer. The effect of residual microwave leakage on the transition probability is has a sinusoidal relationship with microwave amplitude [125], which is given by

$$\Delta P = c_L A_R \sin(A_R) \sin(\omega_{mod} T_R), \tag{5.23}$$

where c_L is a scaling factor that depends on the strength of the leakage field, A_R is the Rabi pulse area of the interaction of the atoms with the first pulse of microwaves on their ascent,

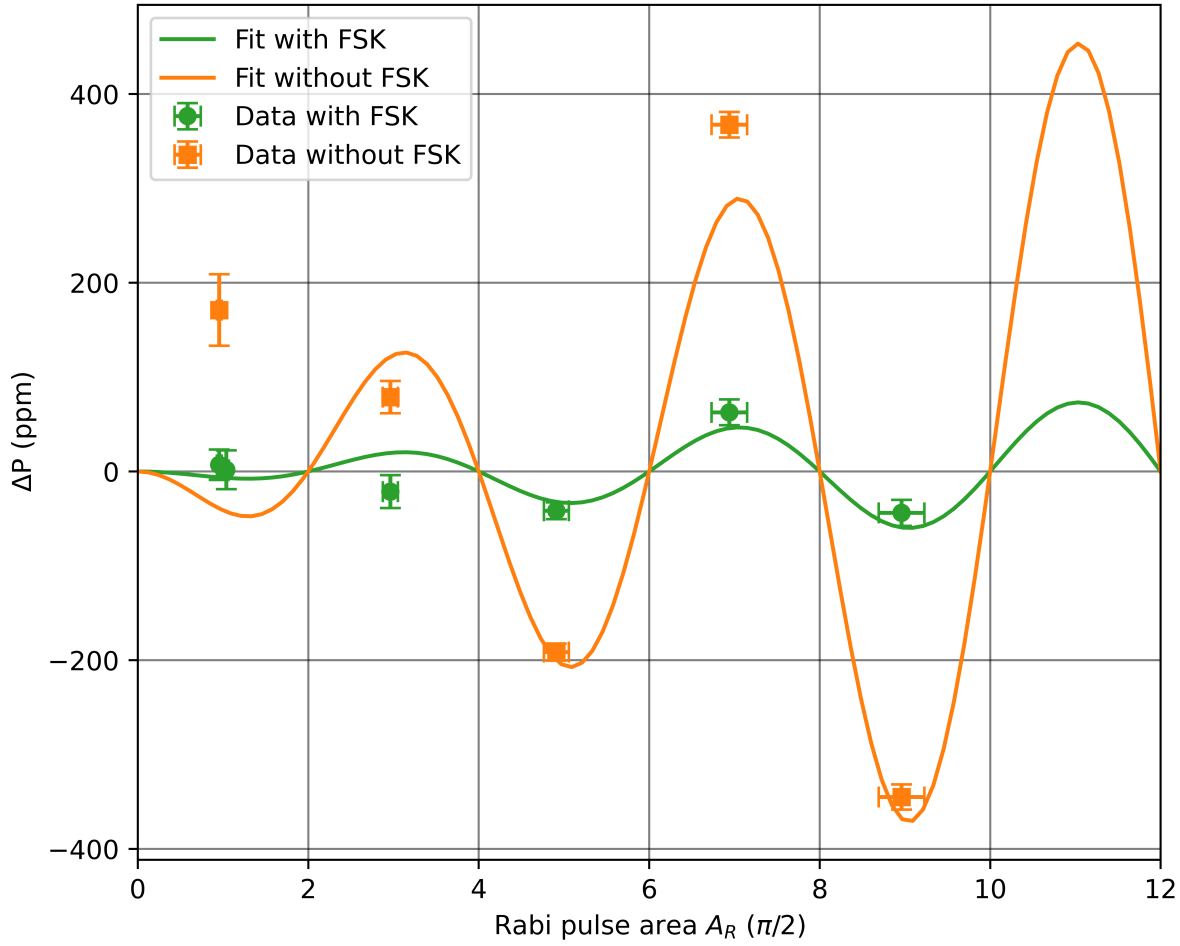

Fig. 5.15. Systematic shift in transition probability induced by microwave leakage as a function of the Rabi pulse area of the atoms on their ascent, which is in practice varied by changing the microwave amplitude fed to the Ramsey cavity. Two series of measurement are presented, one where the microwaves are detuned after the second passage through the Ramsey cavity, (with FSK) and one where the microwaves are left on resonance (without FSK).

$\omega_{mod} = 2\pi f_{mod}$ is the angular modulation frequency at which the atoms are interrogated, and T_R is the Ramsey interaction time between the two passages through the cavity.

To evaluate the effect of any residual microwave leakage on clock transition frequency, a series of measurements collected with varying microwave amplitudes, both with and without the FSK protocol. These measurements are displayed in figure 5.15. The data show good agreement with the model given in equation 5.23; the shift in transition probability is greater for larger microwave amplitudes. From the model fit the estimated effect of microwave leakage at a nominal Rabi pulse of $\pi/2$ is $4.8 \times 10^{-16} \pm 1.0 \times 10^{-16}$. This value should be interpreted as an upper bound on the effect during normal operation, and therefore we take the combined frequency bias and its uncertainty as the value for the microwave leakage uncertainty.

5.5.5 AC Stark Shift

Alongside the thermal electromagnetic radiation discussed in section 5.5.3, stray laser light can also perturb the clock transition frequency through the AC Stark shift. To avoid any stray light, all laser beams are extinguished during the Ramsey spectroscopy stage of the clock cycle–particularly the vertical laser beams which propagate along the full length of the flight tube are in view of the atoms at all times. The AOMs on the primary laser beams are used to strongly attenuate the amount of light delivered through the fibres by at least 30 dBm. Alongside this, all the beam paths are blocked using mechanical shutters before the optical fibres. To check for any residual AC Stark shift effects we collected a dataset without AOM attenuation during the clock measurement, alternating between normal operation and no AOM attenuation. The dataset without AOM attenuation had a measured frequency shift of $(-2.5 \pm 0.9) \times 10^{-15}$; accounting for a −30 dBm attenuation to this value results in a residual ac-Stark shift $< 10^{-17}$. The repumper beams for optical pumping and detection are not equipped with AOMs. To measure their influence on the clock transition, an equivalent excerise as described above was undertaken, except involving alternating between repumper shutters being open and closed. The resulting frequency shift in the dataset with open shutters was $(-16.4 \pm 1.4) \times 10^{-15}$, and accounting for a conservative estimate of −30 dB shutter attenuation, we estimate the repumper ac-Stark shift effect to be $< 2 \times 10^{-17}$.

5.5.6 Gravitational Shift

The caesium fountain operates as a primary frequency standard at the location of operation, but is used to provide a stable and precise frequency reference to the SI second to the antihydrogen spectroscopy experiments. There is an orthometric height difference between the free flight region of the caesium fountain and the magnetic trap where antihydrogen spectroscopy experiments occur. These two locations will have marginally different gravitational potentials there will therefore be a gravitational redshift when transporting references frequencies from one location to the other. For the fountain to be effective as an accurate reference for spectroscopy, the difference in gravity potentials at each location must be determined with accuracy. The relative gravitational redshift is applied as a frequency correction, and is given by [126]

$$\frac{\Delta\nu_g}{\nu_0} = \frac{W_{\bar{H}} - W_{Cs}}{c^2} = \frac{1}{c^2}\int_{H_{Cs}}^{H_{\bar{H}}} \mathrm{g} \cdot \mathrm{dH}. \tag{5.24}$$

Where $W_{\bar{H}}$ and W_{Cs} are the gravitational potential experienced by the caesium and antihydrogen atoms respectively, H is orthometric height from the geoid, H_{Cs} and $H_{\bar{H}}$ are the orthometric heights of caesium and antihydrogen atoms respectively, c is the speed of light and g is the local acceleration due to gravity. For small changes in height, the earth's gravitational field can be approximated as uniform and the following expression can be used:

$$\frac{\Delta\nu_g}{\nu_0} = \frac{g}{c^2} \cdot (H_{\bar{H}} - H_{Cs}) \tag{5.25}$$

The orthometric heights of the ALPHA antihydrogen trap, $H_{\bar{H}}$, and the caesium fountain, H_{Cs} were measured by CERN's GIS team as 435.75 m and 442.42 m respectively relative to the EGM2008 geoid [107]. Using equation 5.25, along with the local gravitational acceleration, $g = 9.80577858\text{ms}^{-2}$, measured at CERN by the Swiss Federal Office of Topography produces a correction factor of -7.28×10^{-16}. The orthometric heights are measured with an uncertainty of ~ 0.1m, which corresponds to a fractional frequency uncertainty on the redshift correction factor of $\sim 1.5 \times 10^{-17}$.

We shall also be irregularly be comparing to external standards for evaluative purposes (in section 5.7.2). In this case, the gravitational redshift correction is larger, reflecting the larger difference in orthometric height between our lab and the external reference.

5.5.7 Other systematic effects

The systematic effects described above have each been quantified using an empirical study and, in some cases, corrected for. However, there are other effects that will introduce an error in the frequency of the caesium fountain, which, at the time of writing, remain unmeasured. We shall briefly describe some of these effects here. Each of these effects are small; estimated to perturb the clock frequency by $< 1 \times 10^{-16}$. However, if in the future we wish to extract the best possible performance out of the caesium fountain, systematic studies to quantify and reduce these sources of frequency uncertainty may be necessary.

Microwave lensing

The transverse variation of the microwave field in the Ramsey cavity is approximately quadratic; this induces dipole forces [127] on the atomic wavepacket moving through the cavity–analogous to a lens. The changes in transverse momentum that occur due to this effect producs a frequency shift on the measured clock transition and focus the two dressed states differently, which can lead to differences in detection. However, our fountain has an identical cavity design as caesium fountain NPL-CsF3 at NPL, which was designed to minimize microwave lensing effects [128], and has been evaluated to a fractional frequency precision of 1.4×10^{-16}. The fractional frequency uncertainty due microwave lensing is therefore currently estimated to be $3{\times}10^{-17}$, which is not corrected for. If we wanted to more precisely calculate the frequency shifts which result from this effect, and correct for them, we can follow the procedure set out in the appendix of [129] using the specific geometries for our fountain.

Distributed cavity phase shift

If the atoms pass through different transverse positions in the Ramsey cavity during their ascent and descent it can produce a frequency shift on the clock transition through the Doppler effect, known as the Distributed cavity phase (DCP) shift, due phase variations of the microwave field within the cavity. In the ideal case where the atoms are launched with a uniquely vertical velocity and along the central axis of the cavity, the atoms will experience and identical microwave field on both ascent and descent, and any cavity phase variations would

perfectly cancel. Unfortunately in reality the atoms can have some horizontal component of velocity during their flight due to a tilt in the fountain apparatus, which produces a difference in the upwards and downwards trajectory of the atoms relative to the cavity axis. Also, the non-zero temperature of the atomic cloud causes expansion during its flight, and therefore the atom cloud is larger on the descent compared to its ascent. The DCP shift can be understood through a Fourier expansion of the microwave field within the Ramsey cavity in terms of its azimuthal modes m [130], and, considering that our atomic cloud stays close to the axis, we only need to consider modes where $m \leq 2$. According to this model, alongside studies performed in similar NPL designed systems, conservative estimates of the DCP shift are $< 1 \times 10^{-17}$, $< 5 \times 10^{-16}$, and $< 2 \times 10^{-16}$ for $m = 0, 1$ and 2 respectively. There are systematic studies with the fountain which would allow the DCP shift to be better parameterised and corrected for. Such systematic studies require extensive work which involves perturbing the flight of the caesium atoms by tilting the fountain apparatus; in doing so it is possible to increase or decrease difference between the upwards and downwards trajectory of the atoms, exacerbating or diminishing the DCP shift. The procedure required is described in [131] and would allow the DCP shift to be quantified, resulting in a lower uncertainty.

Cavity pulling

The first order cavity pulling effect occurs due to the atom cloud within the Ramsey cavity acting as a maser, introducing radiation damping which can affect the clock transition frequency. However, this effect is small for the low atom numbers used, additionally, it is automatically corrected for by the collisional shift extrapolation. As a result this effect is negligibly small. Second order cavity pulling can occur when the cavity is driven away from the atomic resonance frequency. The flight tube temperature is stabilised to 0.2 K using a water jacket, as is shown in Figure 5.14. This results in a microwave cavity which is stabilised within 30 kHz of the clock frequency. The resulting shift due to the second order cavity pulling is estimated as below 1×10^{-17} [132].

Microwave spurs

Spurious components produced by the caesium fountain microwave synthesiser in the spectrum of the microwave signal used to interrogate the caesium atoms can lead to systematic shifts–particularly if these spurs are within tens of Hz of the Rabi frequency. However, spurs which are symmetric around the Rabi frequency will lead to opposite sign shifts, and will cancel out. The output spectrum of the synthesiser was measured, and whilst spurs were found (-50 dBc, -40 dBc, and -40 dBc at $\pm$ 50 Hz, $\pm$ 60 Hz and $\pm$ 400 Hz, respectively), they were all measured to be symmetric around the main peak within 0.5dBc. This results in a residual shift below 10^{-16}.

Magnetic field environment (AD)

The metrology lab is situated next to the Antiproton Decelerator (AD) facility. To produce and decelerate the antiproton beam, the AD uses dipole and quadrupole magnets that are

ramped to different field strengths over the course of one production cycle. Inside the fountain laboratory, this appears as a background magnetic field that changes periodically, with a cycle time between 110 and 130 seconds. The clock frequency is insensitive to changes in the magnetic field at first order, and is measured within 3 layers of mu-metal shielding, which attenuate any external field fluctuations. In addition, any remaining effect should average out over time as the AD cycle and fountain cycle are asynchronous. However, to study any remaining subtle effect that this unique magnetic field environment might have on the clock performance, we have characterized the effect of the AD on the fountain frequency by operating the fountain in a mode which tracks the central fringe of the $|F = 3, m = 1\rangle \longrightarrow |F = 4, m = 1\rangle$ magnetically sensitive transition. These measurements can be compared to independent measurements of the laboratory's ambient magnetic field parallel to the C-field, which is measured simultaneously by a magnetometer. This data is displayed in figure 5.16, for both situations where the AD is cycling and when it is not. As can be seen, when the AD is cycling the magnetometer measures a periodic variation in the ambient field, with an amplitude of around 500 nT

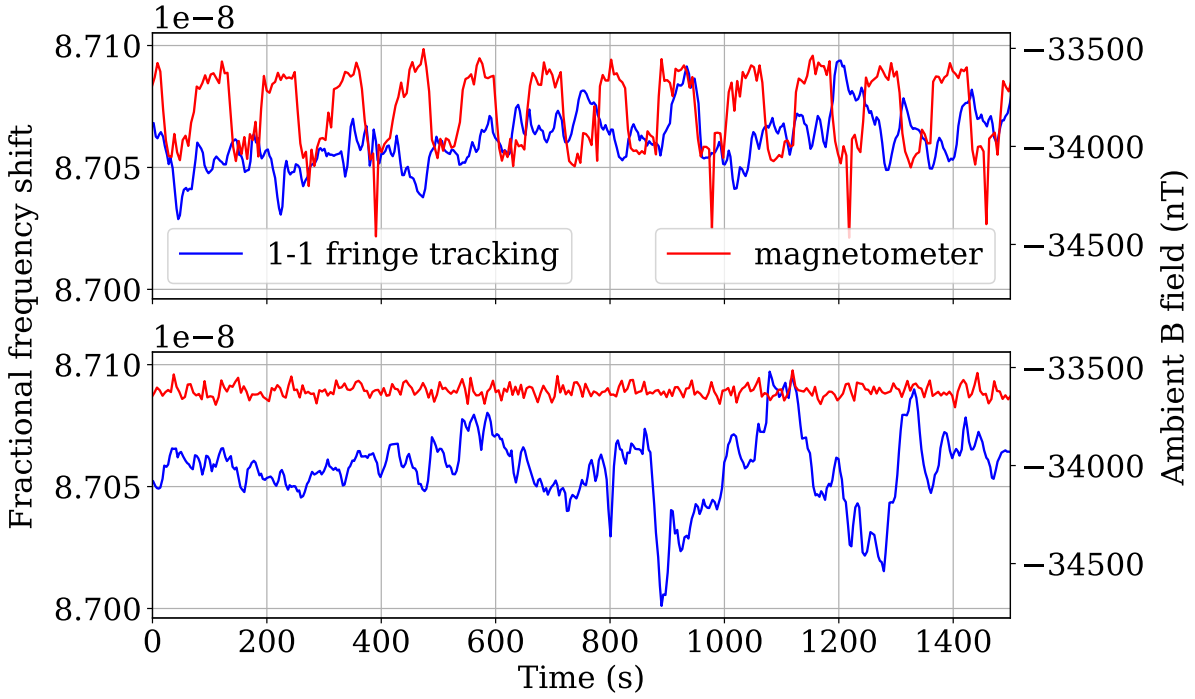

Fig. 5.16. Plot of the magnetically sensitive transition frequency $\delta\nu^{(1)}_{1\to1}/\nu_0$ (left axis), compared to ambient magnetic field measured by a magnetometer (right axis). The top plot displays behaviour when the AD is cycling, whereas the bottom displays behaviour when the AD is not cycling.

The magnetically sensitive transition can be converted into a measurement of the C-field through equation (5.17). The internal field of the fountain can then be plotted against simultaneous measurements of the ambient magnetic field in the laboratory to look for correlations, as displayed in 5.17. There is very weak correlation to the linear fit of the data (R = 0.07), which has a slope of 4.82×10^{-6}. Taking an exaggerated variation of 1500 nT in

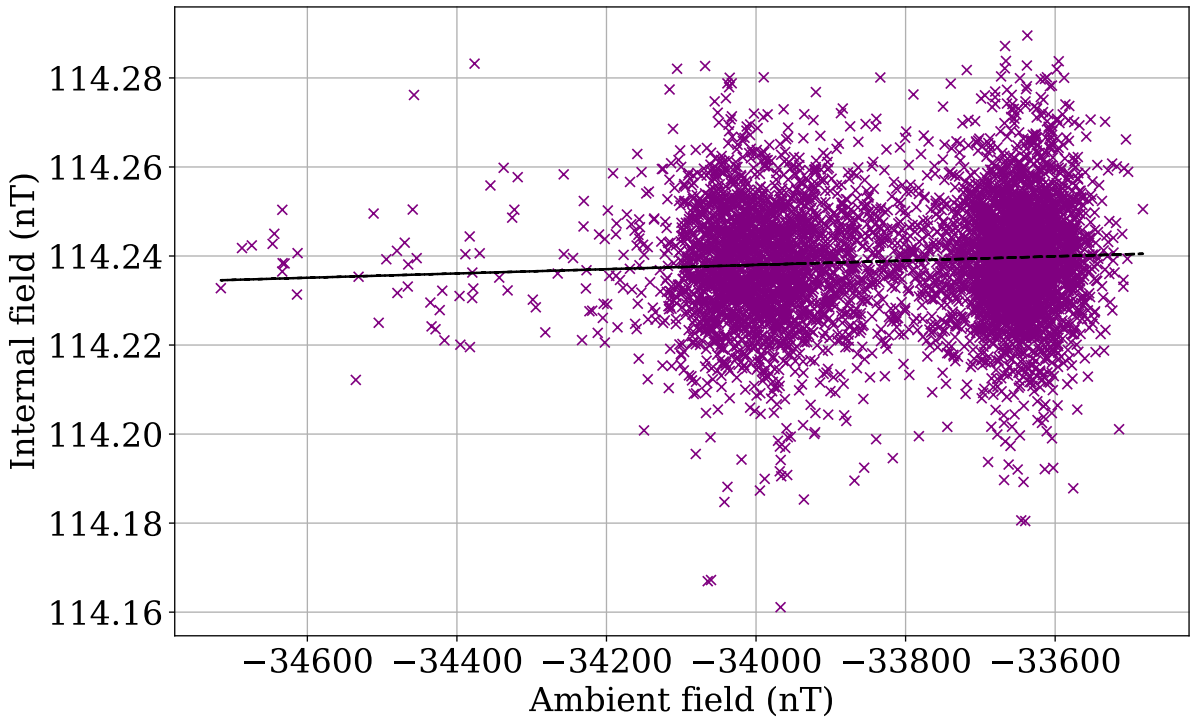

Fig. 5.17. Plot of external magnetic field parallel to the C-field against the internal magnetic field measured by the magnetically sensitive transition frequency. Measurements were taken over around 12 hours. Dashed black line displays linear fit.

the ambient magnetic field due to AD cycles corresponds to a variation of 0.007 nT in the internal field, which produces negligible variation in the clock transition frequency through equation (5.16). From this we can conclude that the variation in the ambient magnetic field due to the AD has no measurable impact on the clock frequency.

5.6 | Fractional frequency error of the maser

Ultimately, the caesium fountain measures is the difference, δ, between the frequency of microwaves in the Ramsey cavity, and the ground state hyperfine transition frequency of the caesium atoms within the cavity; displayed visually in 5.18. If all of the systematic shifts are accounted for, then the transition frequency of the caesium atoms provides a primary reference to the SI second. Because microwaves in the Ramsey cavity are derived from the maser, the difference δ provides a measure of the fractional frequency error of the maser. This can be calculated by plugging in measured values into the following expression

$$-y_{maser}(t) = \frac{1}{f_0}\frac{k\cdot\delta_{LD}(t)-\delta_{HD}(t)}{k-1} - \frac{\Delta f_{Zee}}{f_0} - \frac{\Delta f_{\mathrm{BBR}}}{f_0} \tag{5.26}$$

Where $\delta_{LD}(t)$ and $\delta_{HD}(t)$ are the high and low density measurements made at time t respectively, and $\Delta f_{Zee}/f_0$ and $\Delta f_{BBR}/f_0$ are the systematic shift in fractional frequency due to Zeeman and BBR effects, discussed in sections 3.2.1 and 5.5.3. The negative sign on $-y_{maser}(t)$ is due to the fact that a negative fractional frequency error of the maser results in

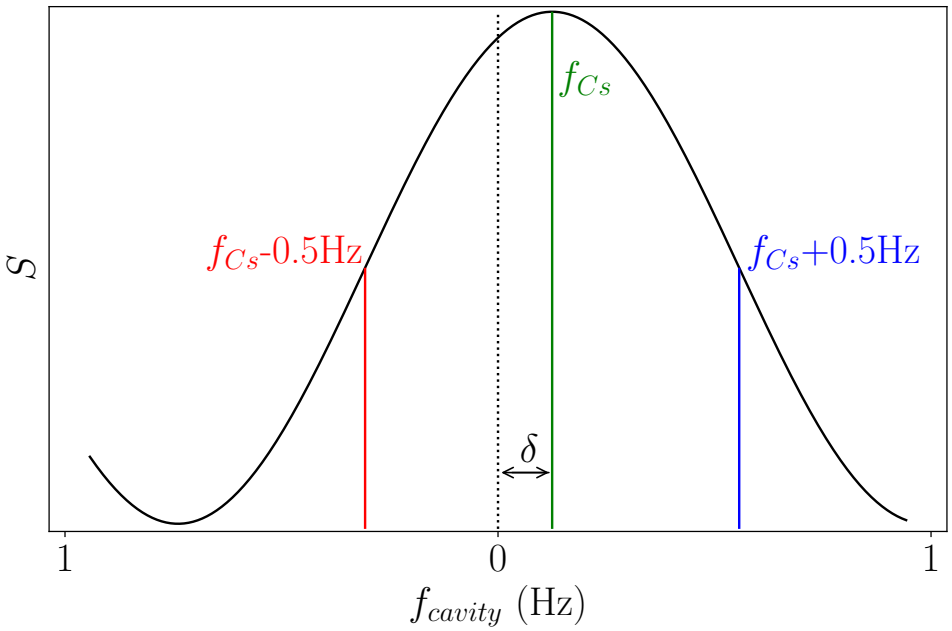

Fig. 5.18. Visualisation of fountain measurement. The peak of the central Ramsey fringe, f_{Cs} is displayed by the green line, which is determined through the two measurements taken 0.5 Hz above and below the peak, displayed by the blue and red lines. The zero of the cavity frequency, f_{cavity}, is the nominal clock transition frequency. The offset, δ, between the expected position of the the peak of the central fringe and the actual position is a measure of the difference between the nominal and actual frequency of the microwaves in cavity. This difference is derived from the fractional frequency error of the maser. The size of this difference has been exaggerated for visual purposes.

a caesium spectrum which is shifted in the positive direction. As discussed in 5.4, the fountain takes two 1.6 s measurement cycles to determine the maximum of the central fringe, 0.5 Hz above and below the central fringe peak. The fountain program is set such that for every five measurements it takes at with a high density sample of caesium atoms, it takes thirty measurements with a low density sample. Typically these measurements are binned hourly, and the mean values of the high and low density measurements are plugged into 5.26 to determine the mean fractional frequency error of the maser for that hour.

5.7 | Performance

5.7.1 Short term

The short term stability of the caesium fountain can be analysed using the overlapping Allan deviation of the fountain-maser comparison, which is displayed in figure 5.19 up to a 10^4 s averaging time. The Allan deviation of this comparison is expected to have white noise characteristics, averaging down as $1/\sqrt{(t)}$ up to around 10^4 s during which the fountain noise dominates; after this, maser flicker noise and drift becomes the dominant source of instability. Furthermore, the small difference between the behaviour of high and low densities indicates that the atom number is not limiting the stability of the fountain, even at low densities.

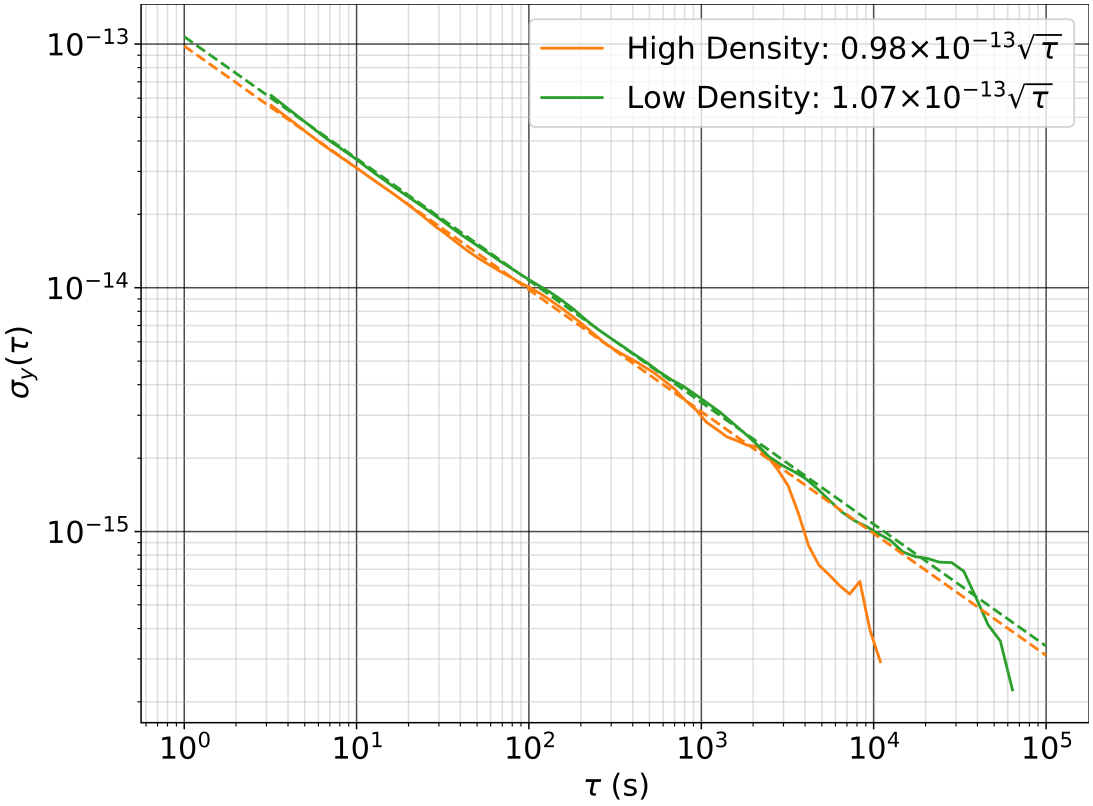

Fig. 5.19. Short-term stability of the fountain for both high density and low density operation. The dashed lines represent $1/\sqrt{\tau}$ fits to the data.

The short term stability can also be assessed in terms of this Signal-to-Noise (SNR) ratio, which is defined as the inverse of the shot-to-shot noise on the measured frequency, with the atom fraction in $|F = 4\rangle$ close to 0.5. The cancellation of the collisional shift, described in section 5.5.2, allows us to operate with large atoms numbers which boosts the SNR. The SNR plotted as a function of the square root of the integrated ToF signal, which is proportional to the number of detected atoms, in figure 5.20. It is displayed for two scenarios: The orange triangles show the SNR for a singular resonant $\pi/2$ pulse during the atoms descent; the blue points represent two equivalent pulses, each detuned by 0.5Hz to capture the SNR when operating in 'fringe tracking' mode. The SNR is modelled using three noise terms, a, bx, cx^2, where $x = \sqrt{N_{det}}$. These are added together in quadrature to give:

$$\mathrm{SNR}\,(x) = \frac{x^2}{\sqrt{\mathrm{a}^2 + \mathrm{b}^2 x^2 + \mathrm{c}^2 x^4}} \tag{5.27}$$

This function is fit to the data, displayed by the dotted lines. At very low atom numbers (ToF < 0.5) the constant contribution from technical noise dominates, which manifests itself as a parabolic increase $SNR(x) \propto x^2$. For intermediate atom numbers the fountain SNR follows trends expected from quantum projection noise, proportional to $\sqrt{N_{det}}$, which manifests itself as the linear increase section where $SNR(x) \propto x$. Finally at high atom number laser amplitude or frequency fluctuations produce dominant noise components proportional to the atom number, which produces saturation in figure 5.20 where $SNR(x) \not\propto x$.

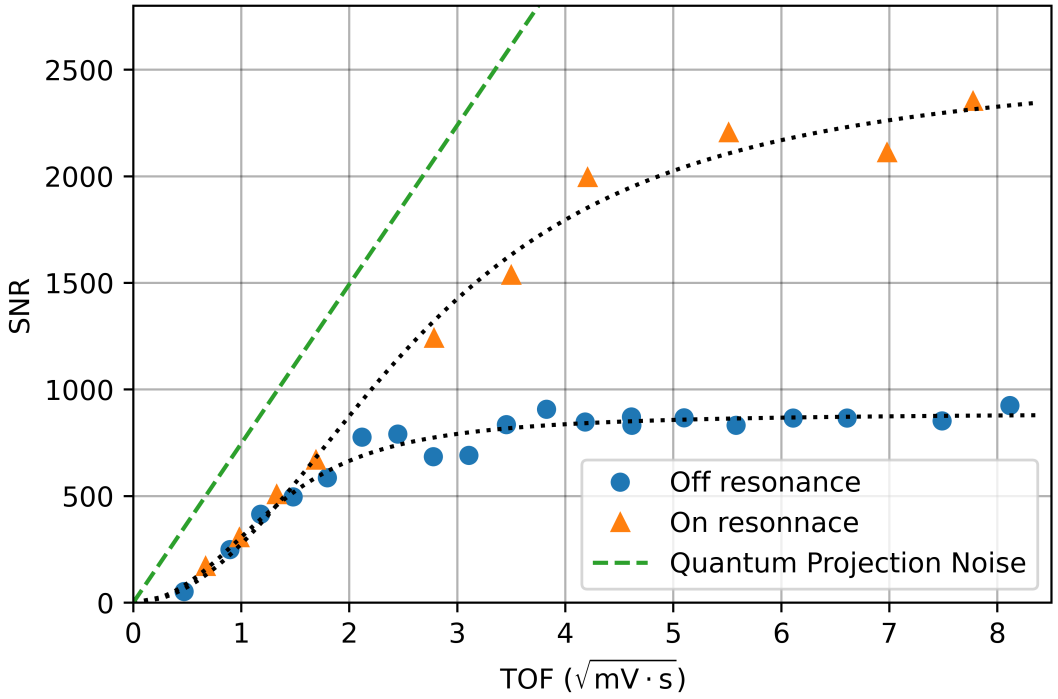

Fig. 5.20. Signal to Noise (SNR) ratio as a function of the square root of the Time-of-Flight (ToF) florescence signal (measured in mV on a photodiode), which is proportional to the number of detected atoms. Orange triangles were recorded on resonance, where frequency noise from the local oscillator is suppressed, whereas the blue circles were measured off resonance, where the SNR is limited by frequency noise. The dotted lines are fits to the data that include three different noise contributions.

5.7.2 Long term

Direct comparison to the maser allows characterisation of the caesium fountain instability at short time scales, however the maser drift dominates the comparison at long time scales. To evaluate the long-term stability of the fountain, time and frequency transfer methods are carried out using the hydrogen maser as an intermediate oscillator. The comparison involves three datasets: Dataset 1 is the local comparison between the fractional frequency of the caesium fountain and our maser at ALPHA; dataset 2 is the local comparison between the fractional frequency of the caesium fountain (NPL-CsF2) and maser at NPL; and dataset 3 is the GNSS comparison between the two masers, using both common-view and precise point positioning (PPP)–discussed extensively in chapter 4. By combining these three datasets, the frequency terms due to the hydrogen masers can be eliminated, leaving a comparison between our fountain and NPL-CsF2 conducted via GNSS methods.

The comparison is corrected for shifts due to second-order Zeeman, collisional, BBR, and microwave leakage effects. The comparison is also corrected for gravitational shift due to the 442.42 m orthometric height of the metrology lab, which results in a fractional frequency difference of $+4.827\times10^{-14}$ compared to CsF2, which is nominally kept at UTC. Figure 5.21 shows the mean fractional frequency difference between ALPHA-Cs1 and NPL-CsF2, y(F2 -

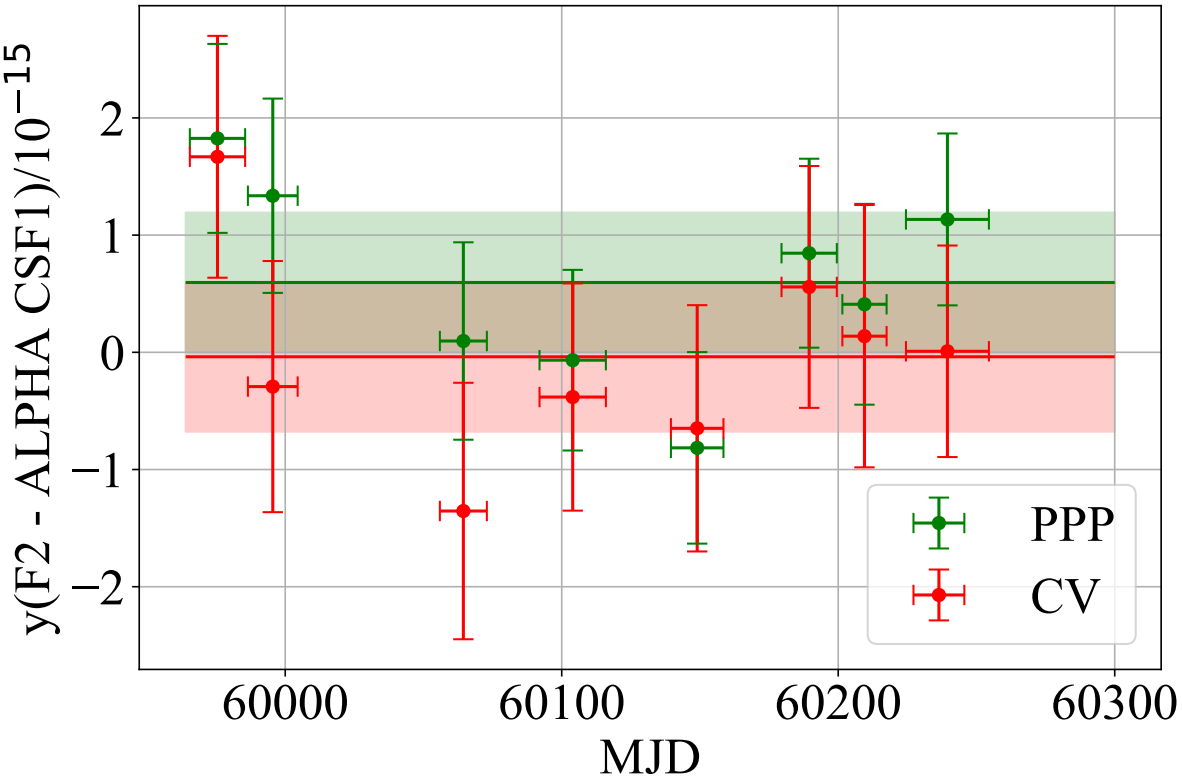

Fig. 5.21. Fractional frequency difference between ALPHA-Cs1 and NPL-CsF2. The horizontal axis is modified Julian date (MJD); the horizontal error bars indicate the duration of a measurement period. Vertical error bars represent the total uncertainty on the comparison, originating from the statistical uncertainty on the GNSS link and systematic uncertainty discussed in this chapter. The comparison was performed from January 2023 to November 2023, with occasional downtime. PPP comparison is displayed in green, whereas common-view is displayed in red. The total for the entire period is displayed by the horizontal line, with the shaded region representing total uncertainty.

ALPHA CSF1), for measurement periods that range from 16 to 30 days in duration, as indicated by the horizontal error bars. The vertical error bars represent the uncertainty originating from the GNSS comparison for each measurement period, added with the systematic uncertainties determined earlier in this chapter. The average of all measurement periods gives a fractional frequency difference of $-0.38 \pm 6.39 \times 10^{-16}$ and $5.96 \pm 5.97 \times 10^{-16}$ for the CV and PPP comparisons, respectively.

5.8 | 2023 operation

The caesium fountain arrived at CERN in 2022, and was set up during the final quarter of the year. Its operation in 2023 is displayed in figure 5.22. Whilst the fountain was being setup at ALPHA, a water leak was found in the temperature stabilising jacket, which meant that water could not be cycled through this part of the apparatus. Whilst this was inconvenient, the temperature stabilisation system was not considered critical for the fountain operation; a similar fountain at NPL had been operating without this feature for multiple years. As such,

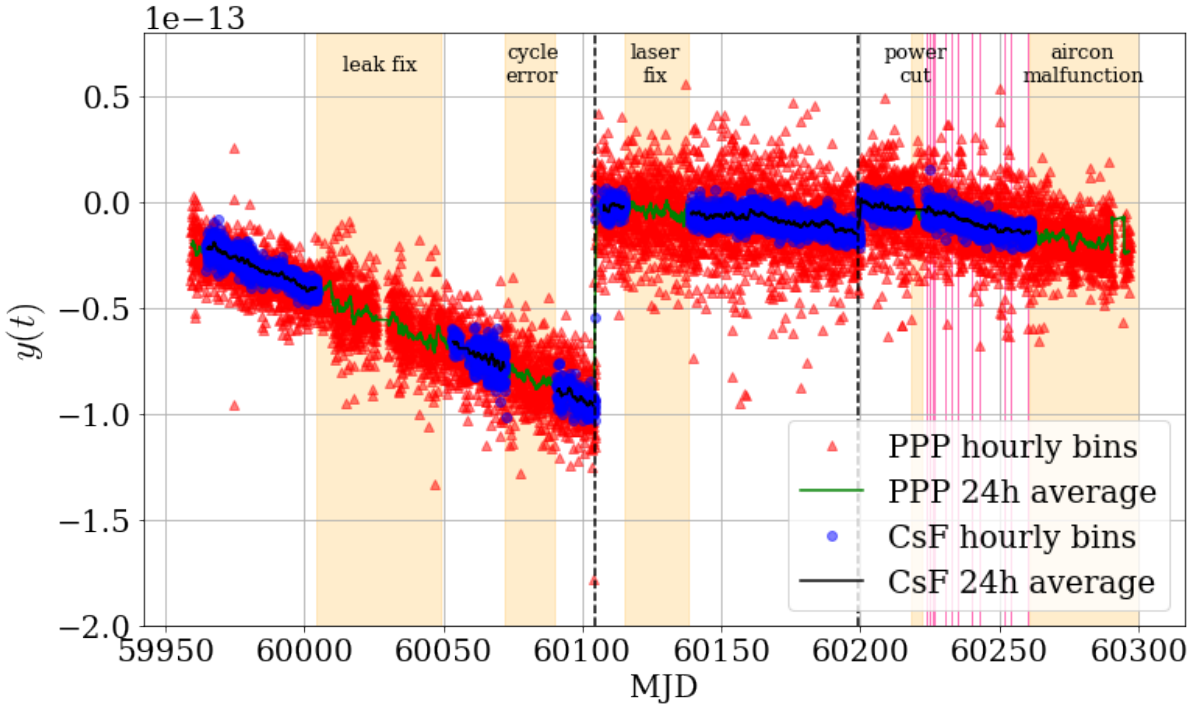

Fig. 5.22. Plot shows the fractional frequency drift of the maser, as measured by the CsF and PPP (compared to SYRTE). Two corrections were made during 2023, at times displayed by the dashed vertical lines. The orange shaded regions show the times when the fountain was nonoperational, with the specific reason annotated at the top the region. The pink shaded regions show the times we were undertaking 1S-2S spectroscopy experiments.

the decision was made to run the fountain without an operational water cooling jacket whilst a plan was made to rectify the leak. The fountain was operated in this way from the start of the year until the 1st of March (MJD = 590045 - 60004). A 49 day down time in operation occurred whilst the fountain underwent an intervention to resolve the water leak. By the 19th of April (60049), the fountain was operational again. In a bid to improve the fountains operation, the fountain cycle was made shorter by removing dead time in the fountain cycle, which was implemented on the 8th of May (60072). This introduced a systematic shift in the fountain frequency which was not discovered until the 26th of April (60090), after which we reverted to the standard fountain cycle. The source of this systematic shift is still unknown, and future work should be done to reduce the fountain cycle without introducing this shift. Following this the fountain was operational until the 20th of June (60126), when the primary laser failed. The laser was replaced, and the fountain was operational again (other than a brief power cut) until the 13th of November (60261), after which we decided to switch the fountain off until the end of the year due to aircon failures in the metrology lab

Ultimately the role of the caesium fountain primary standard is to measure and correct for the frequency error of the hydrogen maser which provides a reference to the 1S–2S laser system. One hour bins of maser frequency as measured by the fountain in 2023 are displayed by the blue points in figure 5.22, alongside equivalent one hour bins measured by PPP. The PPP system to SYRTE which maintains its timescale at UTC; to achieve the SI second in our

metrology lab we require fractional frequency offset of $+4.827\times10^{-14}$ from UTC as a result of the 442.42 m orthometric height of the lab. This offset is subtracted from the PPP data in figure 5.22 such that it measures the fractional frequency from the SI second in the lab, which aligns with the caesium fountain. The frequency error of the maser is clearly measured more precisely by the fountain than by PPP, but the PPP signal provides a method to check for consistency with other fountains. There were two maser corrections made in 2023, displayed by the dashed lines in figure 5.22, which were informed by the caesium fountain measurements. The first correction occurred on the 9th of June, and was both an offset and drift correction of $+9.6\times10^{-14}$ and -5.16×10^{-16} per day respectively.

At this point in the year we were approaching the ALPHA experimental run, as such we decided to implement a protocol for applying maser frequency corrections during the run. This protocol is:

- We compensate the drift when the absolute value of the measured fractional frequency drift becomes larger than 5×10^{-16} per day
- We correct the frequency offset when the absolute value of the measured fractional frequency offset becomes larger 1×10^{-14}
- If in either of the above thresholds is crossed at a time near a 1S–2S experiment, the corrections will happen at the next appropriate time (for example a thermal cycle of the ALPHA2 atom trap, during which the laser will not be used for spectroscopy for a matter of days)

During the experimental campaign the protocol set out above was only triggered once, when the maser fractional frequency offset became larger than 1×10^{-14} on the 14th of September (60199), where it was corrected by $+1.44\times10^{-14}$. Towards the end of the experimental program the offset again surpassed the threshold, however seeing as we were currently running 1S-2S spectroscopy we decided to leave the maser free running. When the run was over we dropped the steering protocol and left the maser free running so that it could be more conveniently characterised for the next experimental program.

5.9 | Automatic correction

The maser frequency error is allowed to vary within the protocol as set out in the previous section. Any smaller corrections to the laser frequency at the time of spectroscopy can be corrected in analysis by determining the frequency error of the maser at the time of spectroscopy. However, it would be convenient to set up a system which could automatically correct the maser frequency at regular intervals, such that the maser frequency is always nominally near the SI second. An investigation of automatic correction methods for the hydrogen maser was undertaken by CERN summer student Elisabeth Sweeney in 2023, under my supervision [133]. Multiple steering methods were investigated, which used the drift compensation and

offset correction features of the maser either at specific intervals or when the maser frequency crossed a specific threshold. After evaluating the performance of various steering methods it was found that the best automatic correction method uses only the offset correction feature, whereas linear drifts in the maser could be manually corrected irregularly throughout the year.

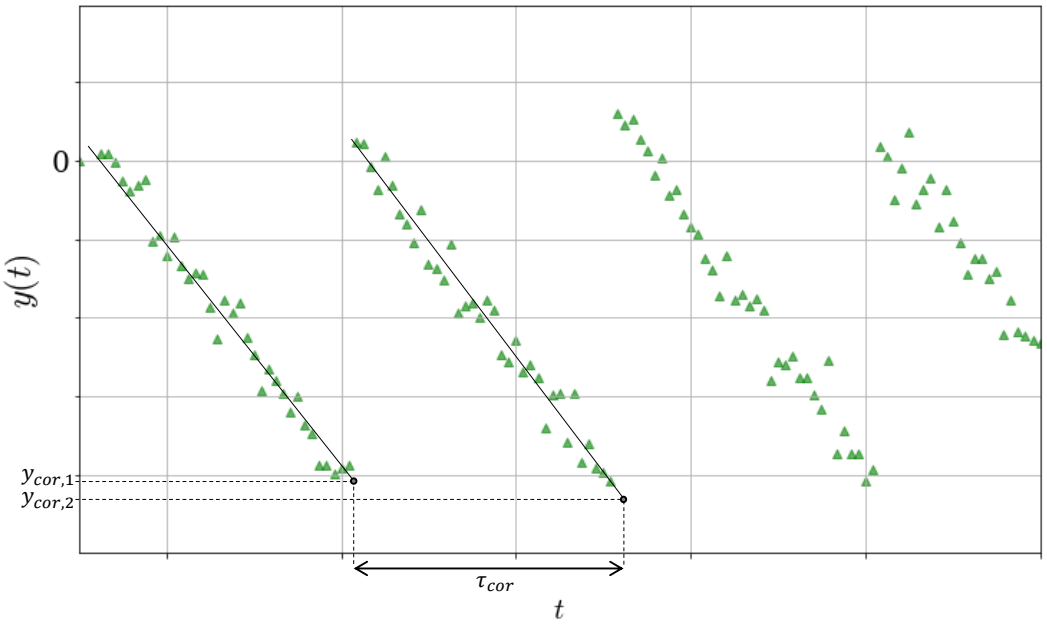

Fig. 5.23. Visualisation of automatic correction protocol. The linear drift has been exaggerated for visualisation purposes. A linear function used to inform the offset correction has been fit to the first two correction periods, resulting in corrections $y_{cor,1}$ and $y_{corr,2}$, which shift the fractional frequency error closer to zero. These two corrections are separated by the correction period τ_{cor}, which has not been optimised in this example.

The method involves applying an offset correction to the maser at regular correction intervals τ_{cor}. To determine the value of the offset correction, a linear function is fit to all the fractional frequency error data of the maser measured by the fountain since the last correction. The linear function extrapolated to the current moment provides a best determination of the instantaneous fractional frequency error, $y_{cor}(t)$ given the available data, displayed visually in figure 5.23. Once the time since the last steer reaches τ_{cor}, the current value of $y_{cor}(t)$ is automatically provided as an offset correction to the maser, which shifts the fractional frequency error back closer to zero. The optimum duration of τ_{cor} is dependent on the current linear drifting rate of the maser; for low linear drifts the maser's offset does not need to be corrected as often. However, if the linear drift of the maser is kept within the thresholds defined in the correction protocol, then a general correction period of 36 hours turns out to be a reasonable choice that provides a good stability.

To assess this stability, the steering protocol can be synthetically applied to real data. An example of some of this data is displayed in figure 5.24, as can be seen, the steering protocol maintains the fractional frequency of the maser at close to zero, whereas the free running maser slowly drifts away. The Allan deviation of this dataset can be taken to determine

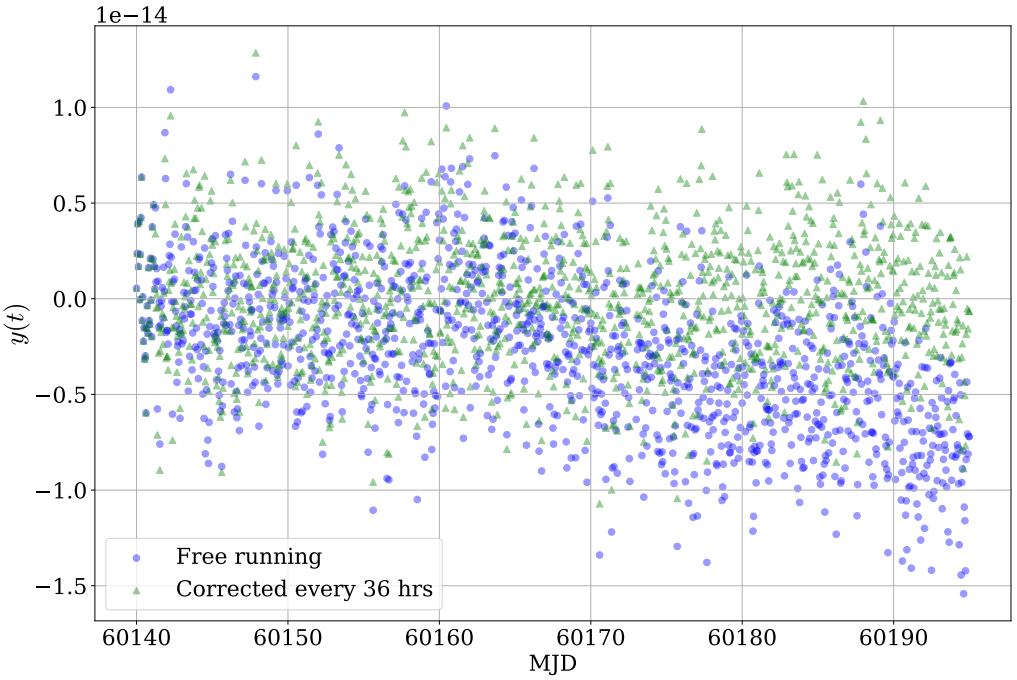

Fig. 5.24. Blue displays the fractional frequency error of the free running maser for a section of 2023, green displayes the steering protocol synthetically applied to the same data.

how the steering protocol changes the stability of the maser, this is displayed in 5.25. The steering protocol produces a small reduction in stability at short and medium time scales, due to the jumps in the dataset, but increases the long term stability as drift is corrected for. A software implementation of a program which would automatically apply this correction protocol is completed by Elisabeth Sweeney; its functionality is described in [133]. Although not implemented at the time of writing, much of the work to implement an automatic steering protocol has been completed and may be integrated into the ALPHA metrology suite in the future.

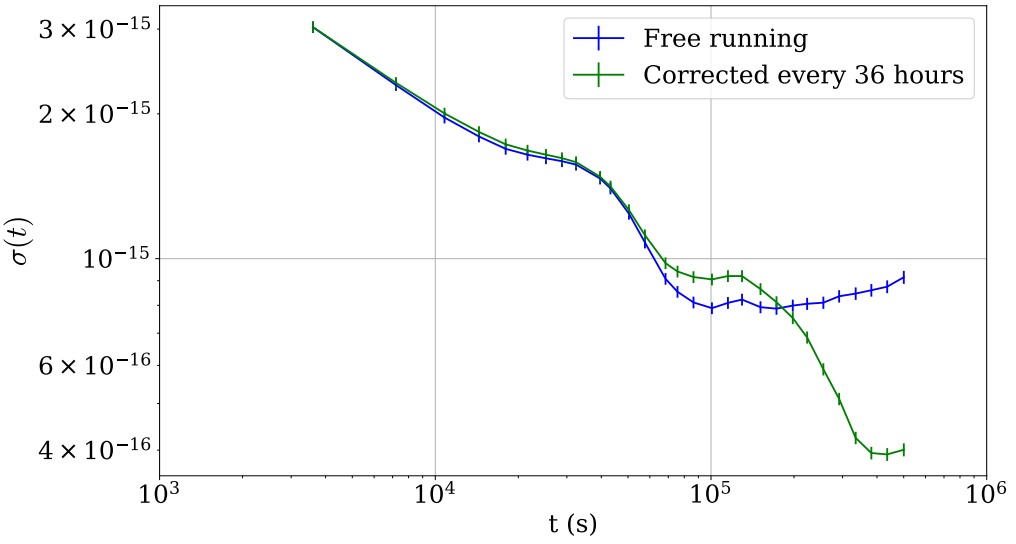

Fig. 5.25. Allan deviation of free running and corrected data displayed in figure 5.24

CHAPTER 6

The 1S–2S Laser System

> *One step forward, Ten steps back.*
>
> — **Laser physics ethos**

The 1S-2S transition in ALPHA-2 is driven by the absorption of two 243 nm photons of laser light, which has been amplified by an optical enhancement cavity situated within ALPHA-2. To measure the 1S-2S transition with a high degree of precision, we require a highly stable and precise laser system. The 243 nm laser light is provided by a commercially available Toptica TA-FHG pro laser [134], which produces 243 nm light through two successive frequency-doubling cavities. The laser is locked to an ultra low expansion (ULE) cavity for stability, and referenced to the maser (and ultimately the caesium fountain) via a frequency comb. The ultimate goal of the metrology upgrades outlined in the preceding two chapters was to improve the precision at which we are able to determine the frequency of the 243 nm laser light. The 1S-2S frequency metrology and laser instrumentation is visualised schematically in figure 6.1. In this chapter we shall first examine the 972 nm system and its frequency stability following the metrology upgrades. Following this we discuss the 243 nm light generation, it's stability, and how its delivery to the ALPHA-2 enhancement cavity.

6.1 | 972 nm

The 972 nm laser light is generated by an DL pro extended cavity diode laser (ECDL) in Littrow configuration, which provides the fundamental light source for the Toptica TA-FHG pro laser [134]. The laser frequency can be coursely adjusted by modifying the diode's temperature, or finely adjusted by varying the diode current. To produce sufficient 972 nm power for the frequency doubling stages, the output of the DL pro is coupled to a tapered amplifier (TA) operating at 4 A, which amplifies the 972 nm power from 35 mW to 2.36 W. Optical isolators are positioned before and after the TA to avoid optical feedback. An EOM placed after the TA introduces 5 MHz modulation, which is utilised to lock the frequency-doubling cavities through the Pound-Drever-Hall (PDH) technique [135].

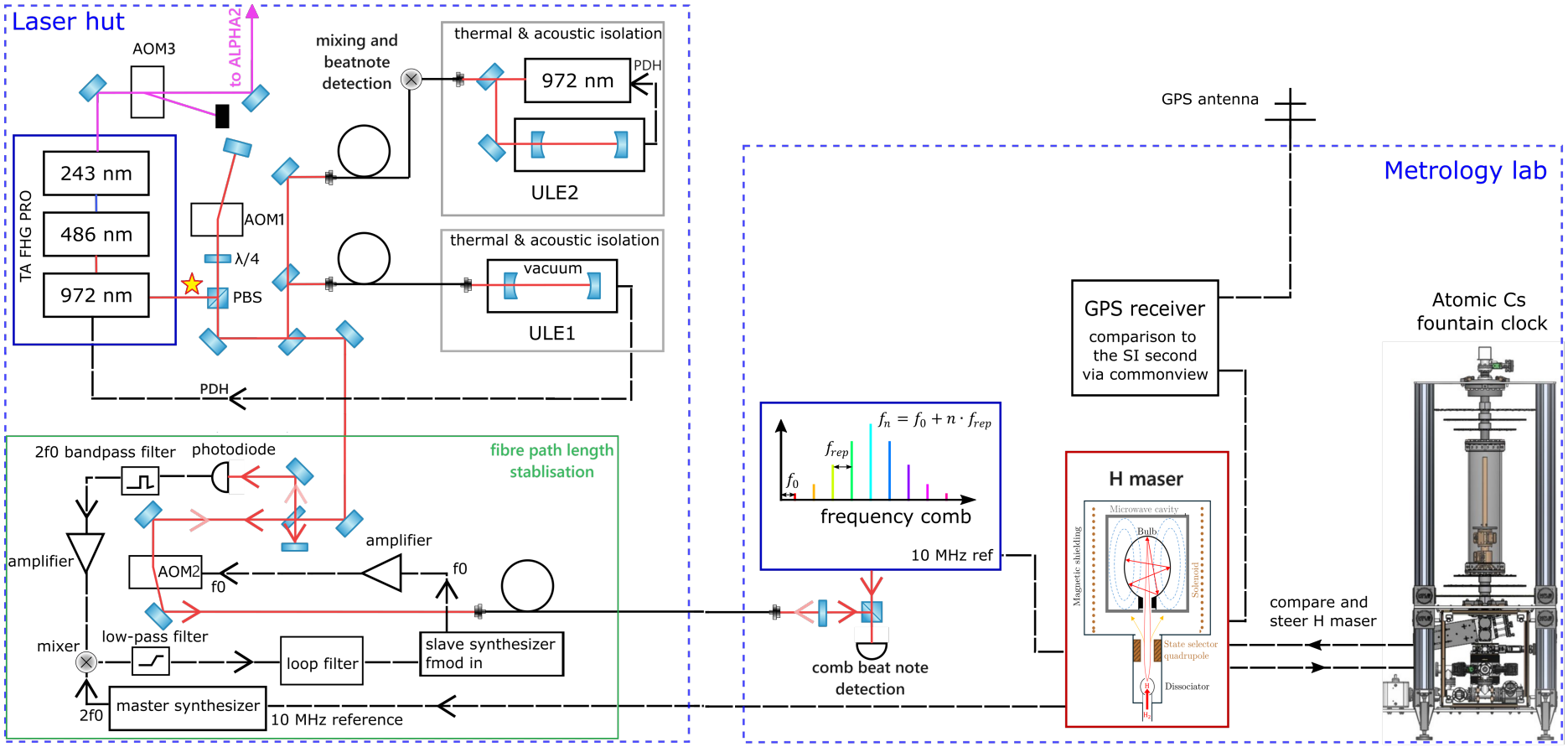

Fig. 6.1. The 1S-2S frequency metrology and laser instrumentation. Red lines indicate 972 nm laser light. Black solid lines indicate optical fibres. Black dashed lines indicate electrical connections. The left dashed blue box displays the components based within the laser lab, whereas the right dashed blue box displayed the components based within the metrology lab. The two labs are connected by a coaxial cable and an optical fibre, the latter of which is stabilised through the path length stabilisation components within the green box. All AOM drivers are referenced to the maser. The red and yellow star relates to a discussion in section 6.1.3. Figure produced by Janko Nauta and edited by the author.

6.1.1 Short term stability

The 972nm laser has a free running linewidth of around 300 kHz [134]. Although this is quite narrow for a diode laser, it is by far too broad to conduct 1S-2S spectroscopy in the sub-kHz regime. To stabilise its frequency, the 972 nm laser is locked to a high-finesse Fabry-Pérot reference cavity manufactured from ultra-low expansion glass (ULE). The 972 nm light is shifted to the cavity mode frequency using an AOM in a double-pass configuration (AOM1). AOM1 is used to control the frequency of the 243 nm light used for spectroscopy, and is also used to compensate the ULE frequency drift (see sections 6.1.2). The shifted light is delivered to the ULE cavity through an optical fibre, and then locked to the TEM00 mode of the ULE cavity (ULE1) via the PDH technique [135]. The ULE reference system was manufactured by Menlo and is based on the ORS 1500 system [136]. It is confined within a temperature controlled vacuum chamber, that is contained within an acoustically dampened enclosure that is supported by a vibration control platform module (Accurion Vario series). The short-term stability of the ULE mode is determined by beating the stablised 972 nm light it against an identical second 972 nm laser which is locked to an equivalent ULE (ULE2), as displayed by the cross in figure 6.1. The two beams are overlapped and directed into a beatnote detection unit (BDU) and the beatnote is counted by frequency counter. The Allan deviation of the counted beatnote is displayed in figure 6.2. For short averaging times below

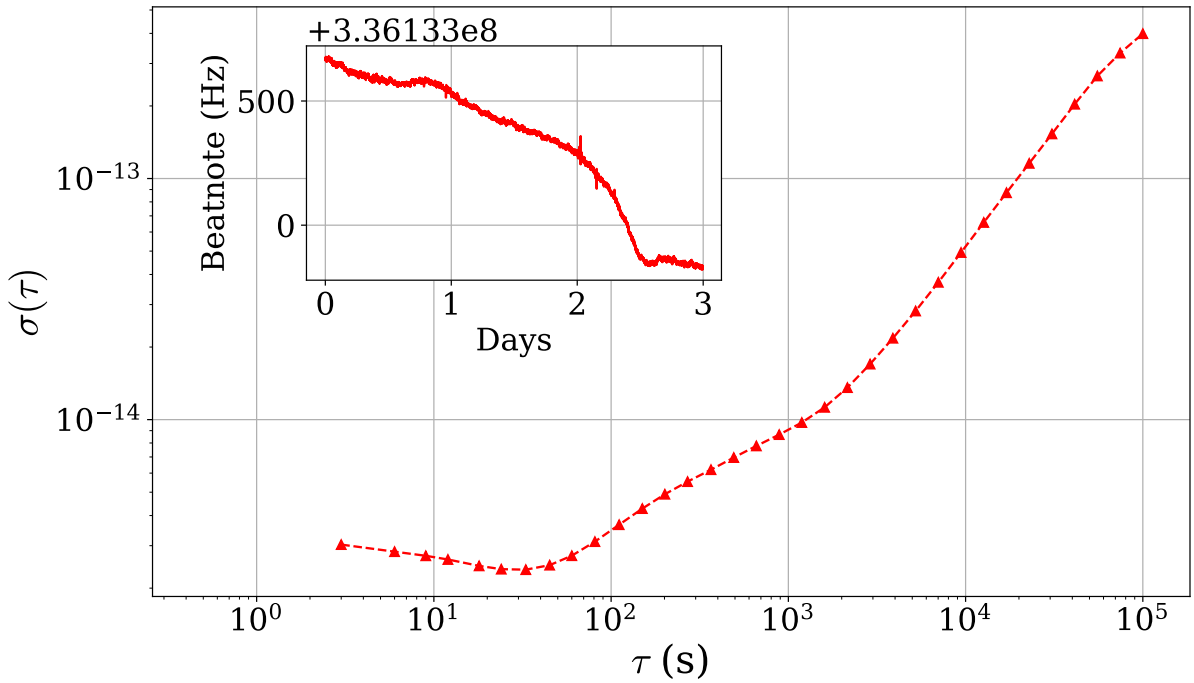

Fig. 6.2. Allan deviation of ULE1-ULE2 beat note, raw frequency counter data is displayed within the inset.

10^2 s the beatnote between the two ULE stabilised lasers is stable, with an Allan deviation below 5×10^{-15}. However as the averaging time increases above 10^2 s the Allan deviation steadily increases, indicating a drift in beatnote frequency, which can clearly be seen in the raw

frequency data displayed in the inset of figure 6.2. The beatnote frequency drifts over time because the frequency of the ULE modes changes over time, which occurs because of length contraction due to the recrystallisation process. Under ideal conditions the ULE modes have a stated linear drift of 53 mHz/s [136, 137], which has since decayed to a measured 23 mHz/s, but temperature fluctuations in the laser lab also produce non-linearity in the frequency drift of the cavity modes. The beatnote between ULE1 and ULE2 provides a measure of the stability of ULE1, however, this is a relative measurement between the cavities and does not provide an absolute measure of the frequency of the ULE1 mode. The absolute frequency of the ULE modes can be measured using a frequency comb, which is referenced to the maser, which is referenced to the SI second via the fountain. This provides the value of absolute frequency in Hertz of the 972 nm laser, which is used to calculate the frequency of the 243 nm laser light used for spectroscopy. The measured frequency drift of the cavities can also be measured using the frequency comb, and compensated for in AOM1, resulting in a 972 nm laser that is used for spectroscopy which does not drift with ULE1 and is stable on long timescales.

6.1.2 Long term stability & absolute frequency measurement

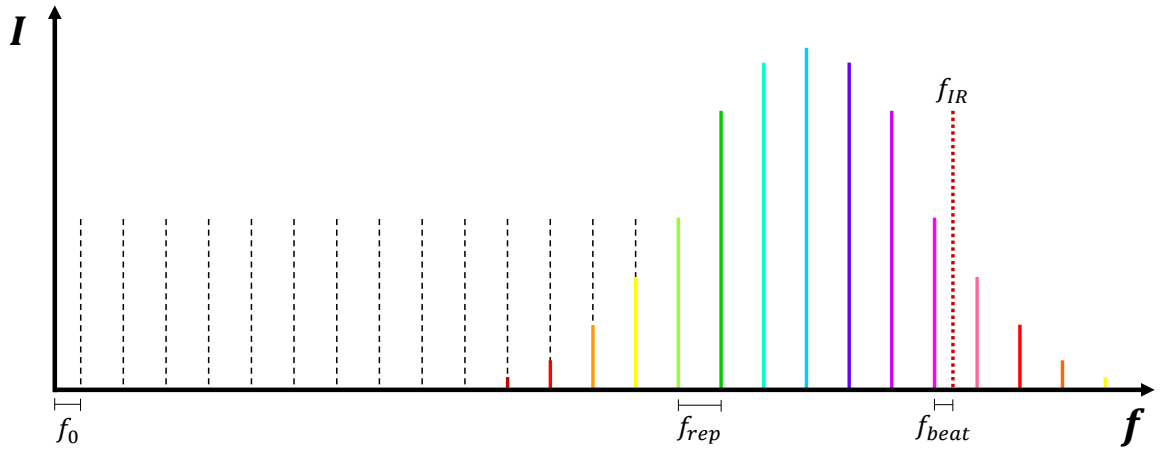

Fig. 6.3. Frequency comb spectrum. Dotted red line indicates the frequency of the 972 nm laser, f_{IR}. The offset, repetition and beat frequencies are also displayed by f_0, f_{rep} and f_{beat} respectively.

The absolute frequency of the ULE stabilised laser is measured using a Menlo Systems FC1500-250-WG frequency comb, which it referenced to the maser frequency. A frequency comb is a mode-locked laser that emits a train of evenly spaced pulses, separated by a constant repetition time T_{rep}. The Fourier transform of the pulse train yields a spectrum with discrete and regularly spaced frequency lines–like teeth on comb – spaced by the repetition rate $f_{\text{rep}} = 1/T_{\text{rep}}$. The spectral profile of a frequency comb in the frequency domain can be approximated by a series of equidistant delta functions separated by f_{rep}

$$f_{\text{comb}} = n \cdot f_{\text{rep}} \pm f_0, \tag{6.1}$$

where f_0 is the offset from zero frequency, which can either be above or below zero–resulting in the plus or minus sign. The frequency of the 972 nm laser, f_{IR} is determined using the beat note f_{beat} between the laser and the comb using the following formula

$$f_{IR} = n \cdot f_{\text{rep}} \pm f_0 \pm f_{\text{beat}}. \tag{6.2}$$

The value of f_{IR} can be above or below the nearest comb tooth, which results in a second plus or minus sign within the expression. The beat note is in the RF range so can be easily measured using a frequency counter, however the comb tooth number n and the signs of $\pm f_0$ and $\pm f_{\text{beat}}$ must also be determined to extract the exact value of f_{IR}. It is straightforward to determine the comb tooth by measuring f_{IR} with low precision using a wavemeter; as long as the wavemeter precision is better than $f_{\text{rep}}/2$ then n is determined from the nearest comb tooth to the laser frequency. The sign of f_{rep} can be determined by varying its value and observing a change in f_{beat}. For example, if f_{rep} is increased the spacing between the comb teeth becomes larger moving all comb teeth towards higher frequencies. In this case that f_{IR} is below its nearest tooth (negative sign) then f_{beat} will increase, if it is above (positive sign) then f_{beat} will decrease. Once the sign of f_{beat} is determined then the sign of f_0 can be determined by following a similar process. If the beat note sign is positive and we increase f_0, then if f_{beat} decreases we know then f_0 is positive, and if it increases then we know f_0 is negative. In the case when the beatnote sign is negative then this is inverted.

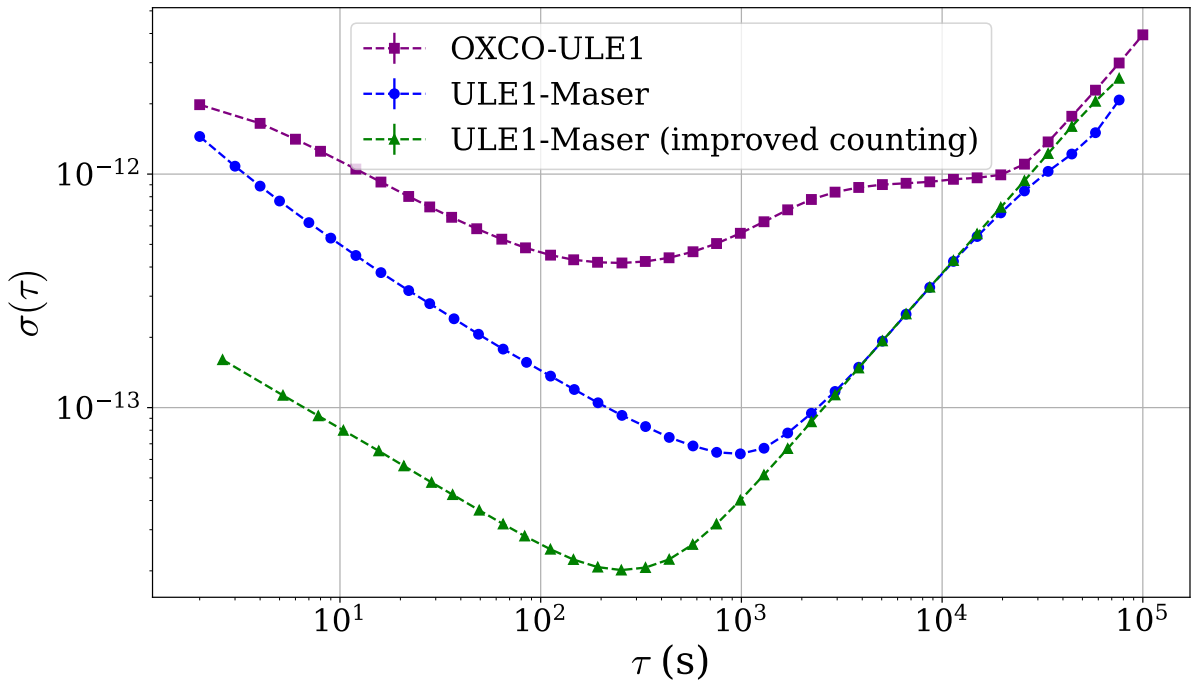

Fig. 6.4. Allan deviation of ULE1 stabilised laser, measured by the comb. The purple displays the comb measurements when referenced to the OXCO. The blue display the initial comb measurements when referenced to the maser. The green indicates comb measurements, following the comb move to the metrology lab and with improved frequency counters.

Once the integer n and the signs of the terms are known, the laser frequency $f_l R$ is calculated by equation 6.2 using the values of f_{rep}, f_0 and f_{beat}. Within the comb, the values of f_0 and f_{rep} are actively stabilised by the reference frequency provided by the hydrogen maser through a phase-locked loop and f_{beat} is measured with a counter. In measuring the frequency of the 972 nm laser with the comb we are therefore determining its value by comparing it to the reference frequency provided by the maser, which itself can be referenced to the SI second through the fountain. By measuring the ULE1 stabilised 972 nm laser with the frequency comb, one can determine its absolute frequency in Hertz with reference to the SI second. Before the metrology upgrades the comb was referenced to a GPS disciplined quartz oscillator (OXCO), and measurements were limited by frequency fluctuations of the OXCO. This is displayed by the purple Allan deviation plot in figure 6.4, which reduces down to a minimum value of 4.2×10^{-13} in 254 s. Replacing the OCXO with the hydrogen maser led to significant improvements in the stability, visible in the blue Allan deviation plot, which to reduces down to a minimum of 6.3×10^{-14} in 988 s. It was clear that as a result of the metrology upgrades that the limiting factor in the precision of the comb measurements had become the comb hardware itself, and the method in which we were counting the frequencies in equation 6.2. To address this, the comb counters were upgraded, and the comb itself was moved from the laser lab to the less noisy and more stable metrology lab with fewer temperature fluctuations and sitting much closer to the maser, reducing noise on the 10 MHz reference signal. We also changed the way in which we determined the frequencies within equation 6.2. Previously, f_{rep}, f_0 and f_{beat} were all taken to be their individually measured values. However, f_0, and f_{rep} are extremely stable, and instead what we mostly observed was measurement noise on these values. Furthermore, by entering the measured values of f_0 and f_{rep} into equation 6.2, we are double counting the noise - as the noise in f_0, and f_{rep} will manifest as noise in the measured f_{beat} Recently, we have decided to take f_{rep} and f_0 to be the fixed frequency value set on the synthesiser within the comb, and f_{beat} is the only remaining measured value in equation 6.2. In this way, measurement noise is reduced, while the noise of each of the frequency components still contributes to f_{beat} without double counting. This resulted in further improvements in the precision of the frequency measurement made by the comb, as displayed by the green Allan deviation in figure 6.4, which reduces down to 2.0×10^{-14} in 252 s. So, by 2023 the metrology upgrades resulted in an improved precision by around a factor of 20, compared to pre-2020 precision.

Path length stabilisation

After moving the comb to the metrology laboratory, 972 nm light is delivered from the laser laboratory to the metrology lab via an optical fibre for measurement. An active path length stabilisation system was introduced to reduce the impact of phase noise due to fluctuations in the optical fibre length, induced by acoustic and other vibrations. The system measures the phase noise by splitting the 972 nm beam into the two paths with a beamsplitter and eventually recombining them to form an interferometer. Measuring the phase noise provides an error

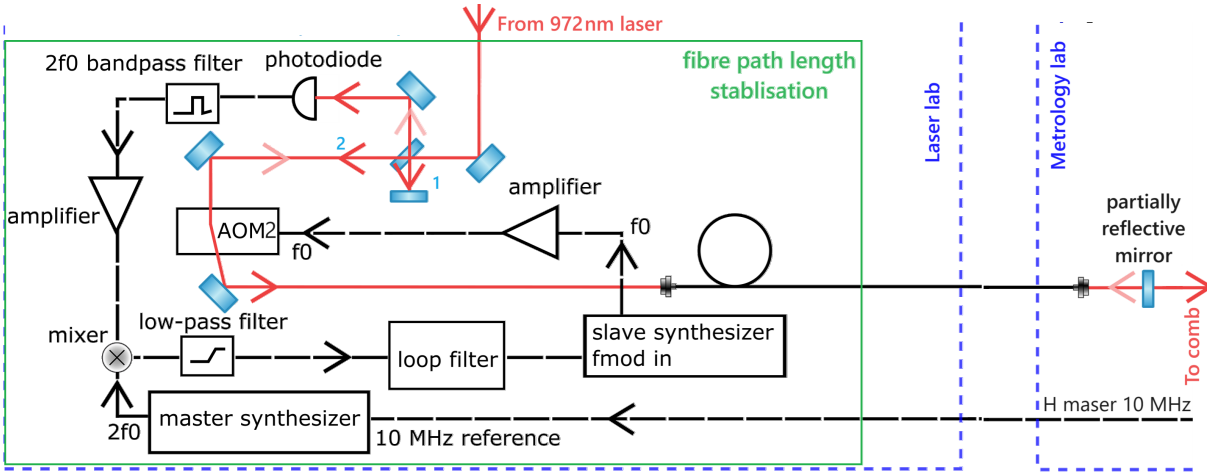

Fig. 6.5. Zoom in on the schematic shown in figure 6.1 to display the specific components used for path length stabilisation

signal which can be minimised with using an AOM, referred to as AOM2. The first path of the interferometer is a very short path from the beamsplitter to a nearby mirror which reflects it back to the beamsplitter. The second path is the round-trip from the beamsplitter through AOM2 and the optical fibre to the metrology lab, where part of the beam is reflected back into the fibre to the laser lab, and traversing AOM2 a second time before reaching the beamsplitter. The two beams are recombined at the beamsplitter and the interference between them can be measured to determine the phase noise on optical fibre path. During the second path the beam traverses AOM2 twice, which shifts the frequency of the light by $2 \times f_{\mathrm{AOM2}} \approx +2 \times 75\,\mathrm{MHz}$, as a result the beat note between the two paths of the interferometer should correspond to $2 \times f_{\mathrm{AOM2}} = 150\,\mathrm{MHz}$ plus any phase noise in the fibre path. This beatnote is detected on a photodiode, any frequencies far from 150 MHz are removed by a bandpass filter, and then the signal is amplified and mixed with a $2 \times f_{\mathrm{AOM2}}$ signal from a master synthesiser. The 150 MHz reference signal is removed with a low pass filter, leaving a signal that corresponds to the phase noise on the fiber path of the interferometer. The phase noise signal can act as an error signal with many zero crossings; a PID loop is used to lock onto one of these zero crossings by modulating the frequency, f_{AOM2}, which is used to drive AOM2. This locks the phase in the two arms of the interferometer; the phase noise in the fibre is thus compensated for within the bandwidth of the feedback look, which is much higher than the typical kilohertz noise that is observed in the fibre.

To measure effect of the path length stabilisation, the ULE1 stabilised laser is sent to the metrology lab, reflected back, and beat against the ULE2 stabilised laser light in the laser lab. The beat note is then down mixed with a similar frequency from a synthesiser ($\approx 336\,\mathrm{MHz}$) and fed into a digital scope which determines the linewidth via a fast Fourier transform (FFT), both with and without path-length stabilisation. The result is displayed in figure 6.6, with Gaussian fits to the two spectra. It is visually clear that without the stabilisation the beat note

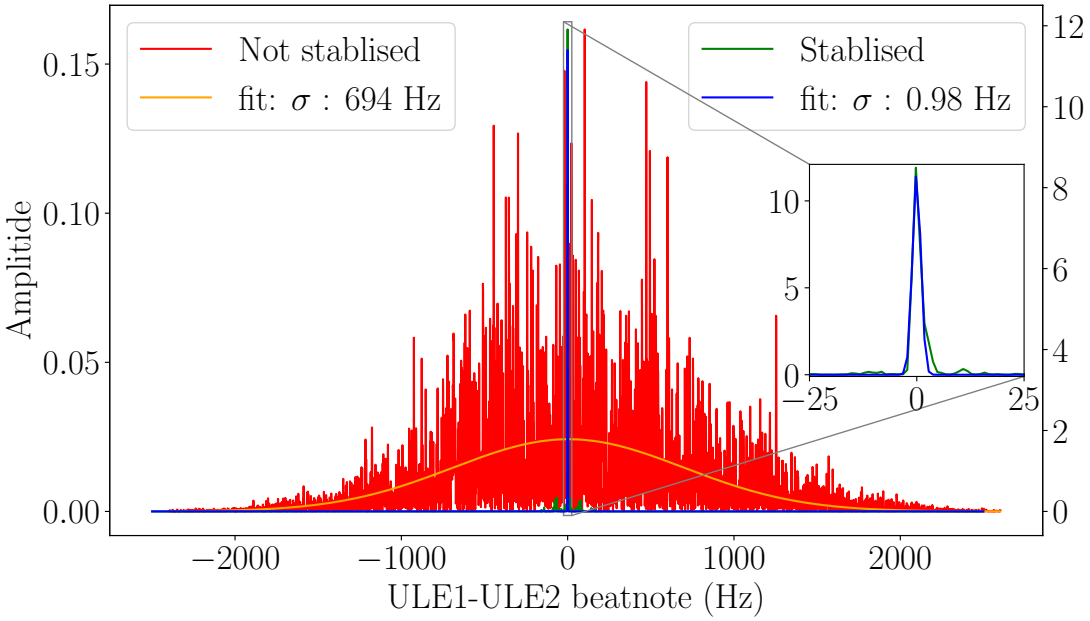

Fig. 6.6. FFT of one second of beatnote data between ULE1 and ULE2, where ULE1 has been sent on return journey through the long fibre. The beatnote with the fibre not being stabilised is displayed in red, and orange displayed a Gaussian fit to this data. The green displays the beatnote with fibre path length stabilisation on, and the blue displays a Gaussian fit. The green and blue plots have been plot to the right hand y-axis to produce a similar vertical scale in the red and green plots.

spectrum is dominated by phase noise in the fibre, resulting in a linewidth which is over 700 times wider than with the stablisation.

6.1.3 Total stability

The comb measures the absolute frequency (relative to the SI second) of the cavity stabilised laser, which can then be used to correct the slow moving frequency drift of ULE1. The Allan deviation of the comb measurements after its movement to the metrology lab, displayed in green in figure 6.4, reaches a minimum at 252 s, which corresponds to the averaging time at which the laser frequency can be most precisely determined. A linear function can be fit to the most recent 252 s of comb measurements, and forecast to the current time to provide the best possible determination of the instantaneous ULE1 frequency given the available data. This value can be used to adjust the frequency of AOM1 such that it compensates for the ULE frequency drift, resulting in a laser frequency which does not drift with the ULE on long time scales. The raw (1 s) comb measurement is plotted in green in figure 6.7 alongside the 252 s forecast used for correcting AOM1, plotted in amber.

So, the laser frequency is stabilised on short timescales by locking it to the ULE mode, but the frequency of that mode drifts over time. However, the frequency of the ULE mode is measured using the comb and compensated for in real time using AOM1, which corrects the

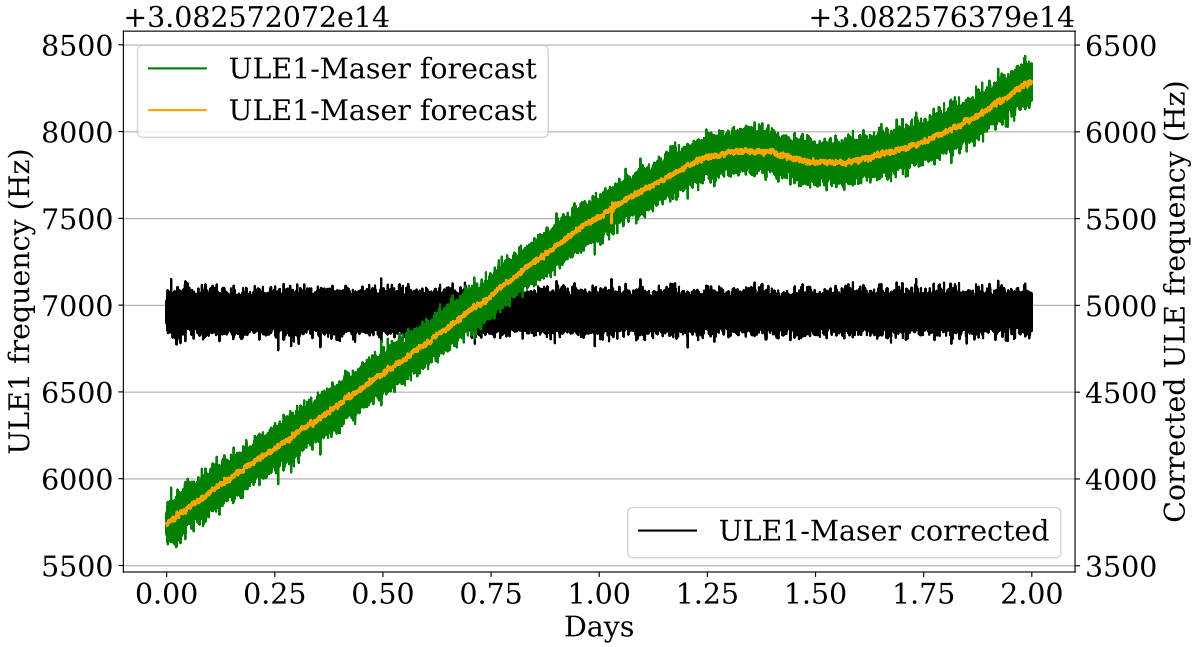

Fig. 6.7. Comb measurement of frequency over 2 days. Green is the 1 s average of measurements, amber is a 252 s forecast. Black is the difference between the green and amber plots

frequency based on the linear forecast from 252 s of comb measurements. Considering all of this, what is the frequency stability of the 972 nm laser used for for the generation of 243 nm light? And how accurately can we know its frequency? This is the same as asking what the frequency of the 972 nm light is before the AOM's, at the location of the yellow and red star in figure 6.1. It is possible to model the stability of this frequency from the difference between the raw (1 s) comb measurement of the ULE1 frequency and the 252 s forecast used for correcting the ULE1 frequency drift. This is displayed in black in figure 6.7, and is clearly stable over long time scales. The Allan deviation of the black and green datasets have been plotted in figure 6.8 with the same colour scheme, alongside the Allan deviation of the ULE1-ULE2 beatnote in red, and the Allan deviation of the maser as measured by the caesium fountain in blue.

The corrected frequency data in black is clearly free from the linear drifts which are visible in the green uncorrected frequency data; the black Allan deviation decreases down below the 10^{-15}, whereas the green turns over before ever reaching 10^{-14}. The black Allan deviation curve is a measure of how accurately we can determine the 972 nm laser frequency compared to the SI second, given a specific averaging time. This is true until the black Allan deviation falls below the blue Allan deviation (after $\sim 10^4$ s averaging time) after which the blue plot represents the uncertainty, as the limiting factor becomes the knowledge of the maser frequency. On the other hand, as discussed in section 6.1.1, the stability of the 972 nm laser frequency at short time scales is indicated by the red Allan deviation of the beatnote between ULE1 and ULE2 - at short time scales the frequency stability is better than our ability to measure the frequency. At longer timescales, when the Allan deviation of the black curve falls below the red curve ($\sim 5 \times 10^2$ s), the stability of the corrected laser is indicated by the black Allan

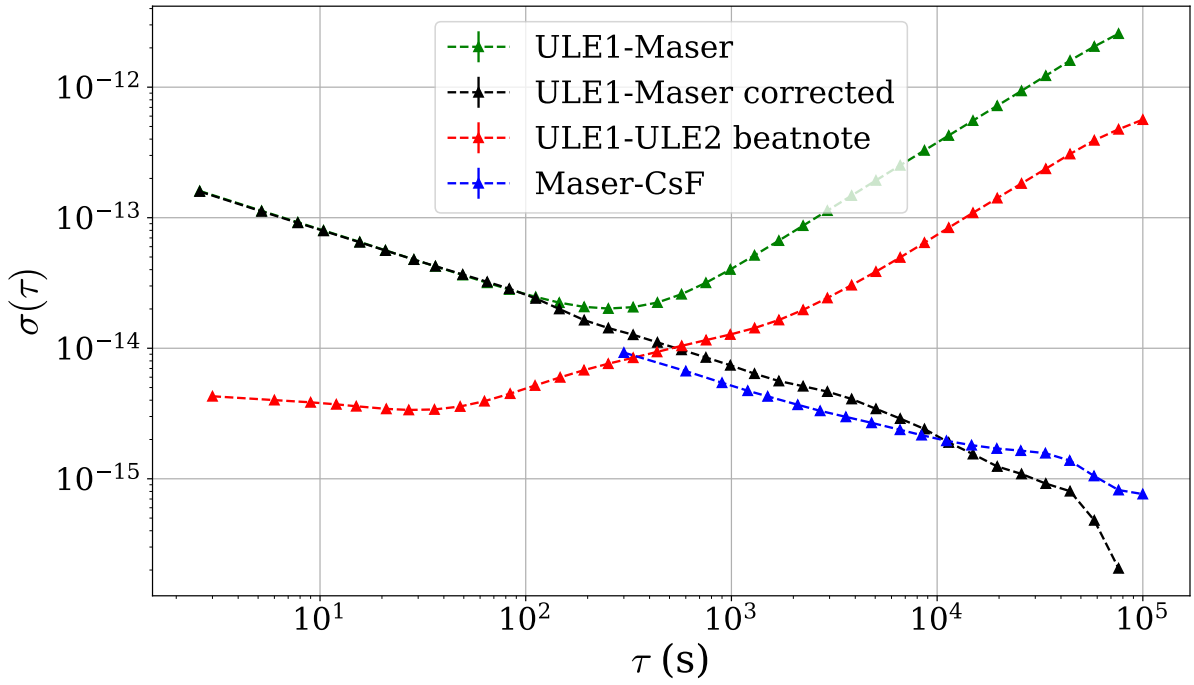

Fig. 6.8. The key Allan deviation curves for the 1S-2S laser system.

deviation. At even longer timescales, once the black curve has fallen below the blue curve, the ultimate stability of the laser is limited by the maser stability. From this evaluation, we can say that we can state that the accuracy and stability of the stabilised and corrected 972 nm laser that is used for spectroscopy can fall below the 10^{-15} level, given a sufficiently long period of comb measurement. However, the ultimate limit on the frequency stability of our system is capped by the systematic uncertainty of the Cs fountain, discussed in the previous chapter.

6.2 | 243 nm

The 243 nm laser light is produced by the Toptica laser using sequential second-harmonic generation (SHG). SHG is a non-linear optical process where two photons of identical frequency interact with a non-linear material, which then emmits a single photon with twice the frequency [138]. The single-pass efficiency of SHG is small, so resonant enhancement bow-tie cavity are used to increase the efficiency of the second harmonic generation. Initially, the 972nm light goes through the first SHG cavity, generating 486 nm second-harmonic laser light, which is subsequently directed to a second SHG cavity to produce the intended 243nm fourth harmonic (FHG). The 243 nm light can then pass out of the laser box, through bench optics (described in section 6.2.2), and eventually reaches the cryogenic enhancement cavity surrounding the antihydrogen trap for uses within the experiment. Both second harmonic generation (SHG) and fourth harmonic generation (FHG) cavities are locked using the Pound-Drever-Hall (PDH) technique [135]. the 2.5 W of 972 laser light coming out of the TA is converted by the SHG into approximately 1 W of 486 nm light and the FHG produces approximately 150 mW of 243 nm light when new. While the power of the 486 nm laser has remained relatively constant,

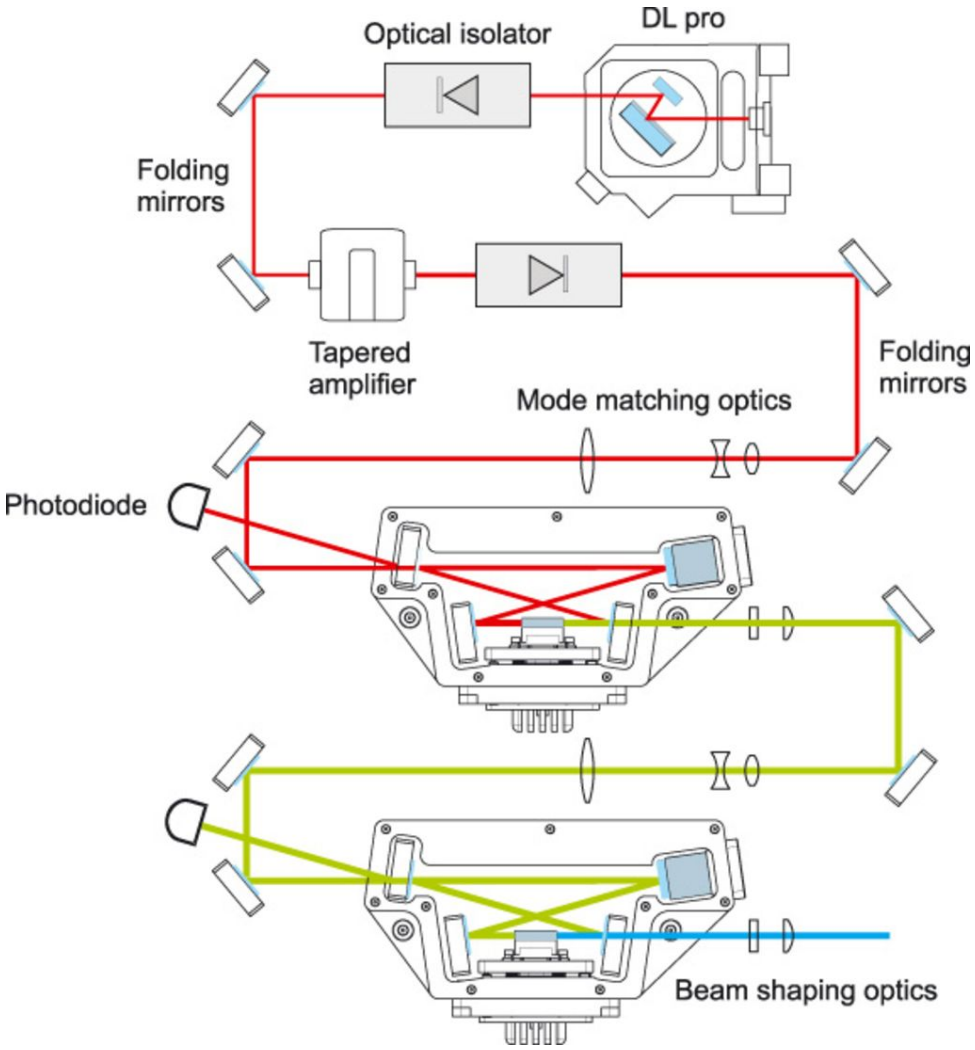

Fig. 6.9. 243 nm light generation within the Toptica TA-FHG pro laser. The 972 nm light (red) passes through two frequency doubling cavities, producing first 486 nm light (green), and then 243 nm light (blue). The output powers of the three stages are 2.5 W, 1.2 W and 150 mW respectively when new. [134]

the output power of the 243 nm light from the FHG cavity has been observed to decrease gradually over time most likely due to the formation of damaged spots on the FHG crystal from prolonged operation. To minimise the formation of damaged spots, the FHG remains unlocked when the laser is not being used for spectroscopy, and there have been irregular interventions which involve translating the FHG crystal to find new spots, leading to a recovery in the 243 nm power output. However, in two instances, the FHG cavity had to be replaced when the 243 nm power dropped significantly. Replacing the FHG cavity produced significant improvements in the 243 nm laser power.

6.2.1 Frequency stability and control

The 243 nm light generated through FHG inherits its frequency stability from the 972 nm laser. However, each frequency doubling step scales up the frequency noise of the 972 nm light. The scaling factor is $\sqrt{2}$ when the frequency noise on the two photons that combine is

uncorrelated, or by a factor of 2 when the frequency noise is correlated. As a conservative estimate, we assume a fourfold decrease in frequency stability when producing 243 nm laser light from 972 nm via FHG.

The frequency of the 972 nm light used to generate 243 nm can be determined by subtracting the frequency of AOM2 and twice the frequency of AOM1 (due to double pass configuration) from the frequency measured by the comb. Multiplying this result by four yields the frequency of 243 nm light. This is expressed mathematically as

$$f_{243} = 4 \times \left[\left(n \cdot f_{\text{rep}} \pm f_0 \pm f_{\text{beat}} \right) - f_{\text{AOM2}} - 2 \times f_{\text{AOM1}} \right], \tag{6.3}$$

where the term in brackets is the comb measured frequency defined in equation 6.2, where the comb mode number n, and signs of $\pm f_0$ and $\pm f_{\text{beat}}$ have been determined. f_{AOM1} is used to shift the laser light into resonance with a ULE mode, and compensate for the frequency drift of the mode, as discussed in section 6.1.3. Additionally, f_{AOM1} is used vary the frequency of laser light for spectroscopy, so has typical operating range of 210 MHz to 255 MHz to be able probe both the $1S_d - 2S_d$ and $1S_c - 2S_c$ transition. The values of f_{rep} and f_0 are fixed, whereas f_{beat}, f_{AOM1}, and f_{AOM2} are continually measured with Keysight frequency counters. The noise on f_{beat} is the dominant source of instability on f_{243}.

When conducting spectroscopy we tend to define the laser frequency as a detuning, δ_L, relative to the expected transition frequency. This is given by the expression

$$\delta_L = f_{243} - \frac{f_{x-x}(B_0)}{2}, \tag{6.4}$$

where $f_{x-x}(B_0)$ is the expected transition frequency of the $1S_d - 2S_d$ or $1S_c - 2S_c$ transitions in magnetic field B_0, given by equation 3.17 or 3.18 respectively. The magnetic field is B_0 is the value measured in the middle of the magnetic trap ($r = 0$, $z = 0$).

6.2.2 Pre-cavity optics

Once the 243 nm laser light exits the laser box, it covers a distance of around 7 m, passing through various optical elements before reaching the ALPHA-2 enhancement cavity. This is displayed schematically in figure 6.10. We shall briefly describe the role of each of these optical components, roughly following the path of the 243 nm light.

EOM

A QUBIG electro-optic modulator (EOM) is used to add 6.25 MHz sidebands to the laser spectrum, which are essential for locking the enhancement cavity in ALPHA2 via the PDH technique [135]. The EOM has been oriented in a 5-axis alignment mount such that the axis of its birefringent crystal matches the polarisation of the laser.

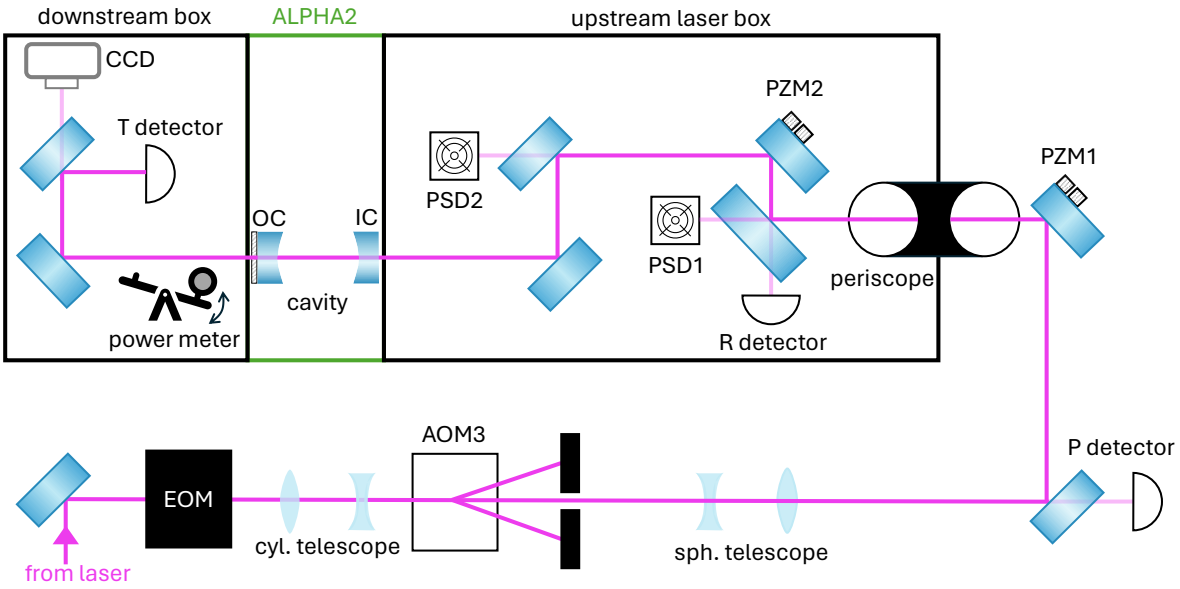

Fig. 6.10. A schematic illustrating the path of the 243 nm beam and the optical elements involved. The photodiodes labeled as R detector and T detector detect the transmission and reflection from the cavity, respectively. The P detector, also a photodiode, is used for stabilising the power through AOM3. The telescopes denoted as cyl. and sph. are cylindrical and spherical, respectively. The mirrors PZM1 & PZM2 are controlled by piezoelectric actuators to maintain the beam's position on the position-sensitive detectors PZT1 and PZT2. IC and OC are the input and output couplers of the enhancement cavity, respectively.

Telescopes

The laser beam exiting the laser box is elliptical and astigmatic, with a larger width in the horizontal direction due to the phase matching process which occurs in the FHG crystal. This eliptical beam will not couple well to the ALPHA-2 cavity, so a cylindrical telescope is employed to reshape the beam to an approximately Gaussian beam, and minimise the astigmatism. In 2023, numerous lenses were tried out to determine the most effective cylindrical telescope setup, and the chosen configuration involved a primary lens with a horizontal focal length of 100 mm, followed by a secondary lens positioned around 50 mm away with a horizontal focal length of -50 mm. The combined effect of these two lenses horizontally compresses the beam by a factor of two. The spherical telescope is used for mode matching the beam to the enhancement cavity, such that the minimum beam waist is located at the middle of the build up cavity. The spherical telescope consists of two lenses, with the first lens having a focal length of -50 mm, and the second lens having a focal length of 250 mm.

AOM3 for power control

In 2023, a novel system was implemented to control the power of the 243 nm laser and as a result the power within the enhancement cavity. The laser power reaching the cavity is controlled using AOM3, which is placed in the beam such that only zeroth-order transmitted beam is directed towards the cavity. By increasing the amplitude of the RF signal (V_{pp}), the ratio of laser power in the higher order modes relative to the zeroth mode is increased, thereby

enabling the adjustment of the power of the 243 nm beam directed into the enhancement cavity. To ensure that the coupling with the buildup cavity is not affected, it is crucial that the spatial profile of the zeroth mode changes only in intensity with V_{pp}, without altering its shape. Figure 6.11 presents the horizontal spatial profile of the zeroth mode at various control voltages, normalised by the peak height minus the background level, measured using a beam profiler. As can be seen, the shape of the horizontal profile remains roughly constant until V_{pp} surpasses 1200 mV. The percentage of laser power reaching the cavity (measured using a power metre) and passing through the cavity (measured by the T detector) is plotted in Figure 6.12 relative to the AOM being turned off, as a function of V_{pp}. As is clear, there is an approximately linear relationship for V_{pp} values ranging from 200 to 1400 mV.

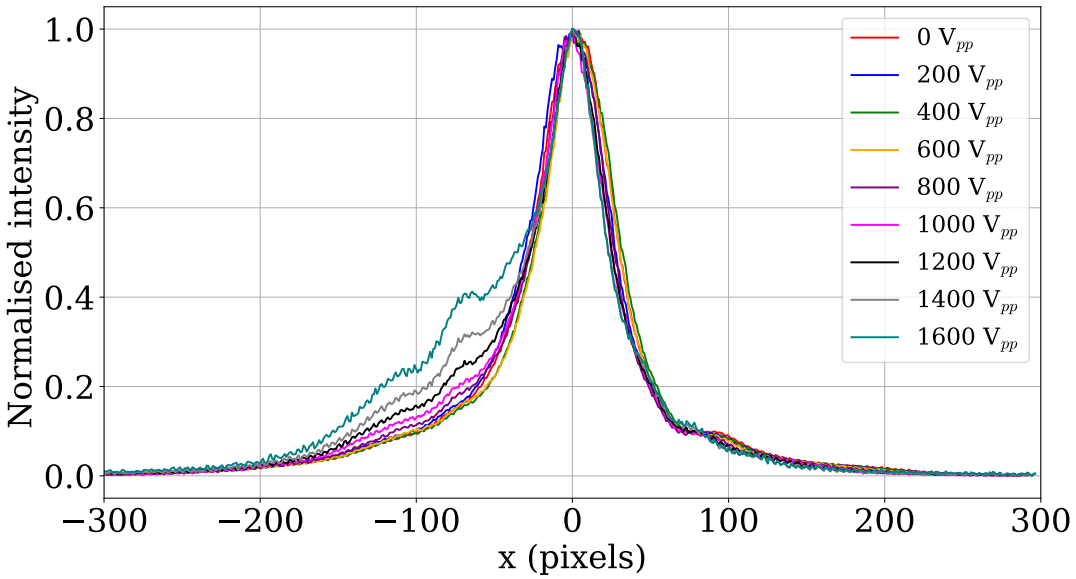

Fig. 6.11. Normalized horizontal spatial profile of the zeroth order generated by AOM3. The plots are normalized by the peak height minus the background level. Legends display the V_{pp} values applied to the AOM in in mV.

The V_{pp} value is regulated by a PID loop that uses the power on a photodiode, identified as the 'power control detector' in figure 6.10, as feedback signal to stabilize the power in the zeroth mode following AOM3. This system allows the 243 nm laser power which is circulating in the enhancement cavity (which is determined by measuring its transmission, as discussed below in Section 6.2.4) to be controlled remotely to the desired level by varying the set point of the PID loop.

Beam stabilisation

Active beam position stabilisation is required to ensure a stable coupling to the ALPHA-2 enhancement cavity. Two position sensitive detectors (PSD) are placed within the upstream laser box, where they detect the position of the beam picked-off through the back of two 243 nm mirrors. Each of the PSD's is paired with a piezo actuated mirror, which can be used to remotely finely adjust the angle of the mirror and thus the position detected on each of the PSD's. Once an optimum alignment into the enhancement cavity has been found, a PID loop

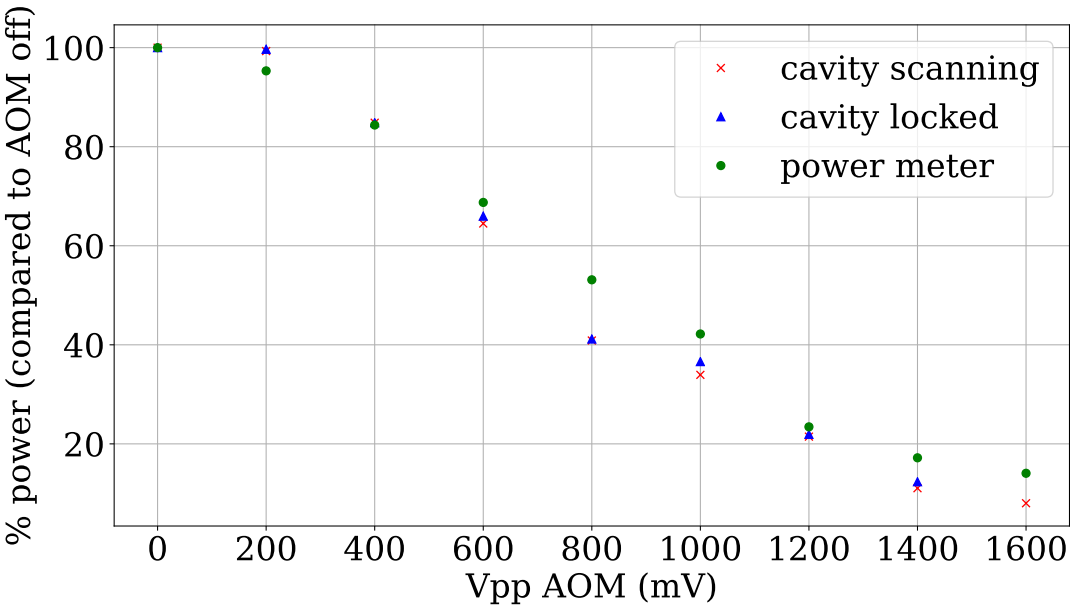

Fig. 6.12. percentage power as a function of V_{pp}. The green points have been measured with a power meter before the enhancement cavity. The red and blue points are measures of transmitted power after the cavity by the T detector, when scanning and locked respectively.

locks the position of the beam, which results in a significant improvement in the stability of the enhancement cavity modes and negates the need for frequent realignment.

6.2.3 The ALPHA-2 enhancement cavity

Much of the work developing the ALPHA-2 enhancement cavity is discussed in detail within chapter 4 of [137] and in [139]. Therefore, only a brief overview will also be provided here. The 243 nm laser beam power is typically around 100 mW when leaving the laser box, and is even lower due to losses by the time it has reached the experiment (approximately 50 mW). Consequently, an optical cavity is required to increase the power of laser light within the experiment. An optical cavity is formed out of two partially reflective mirrors, often curved mirrors, which amplify the optical intensity through the constructive interference between multiple reflections of the laser light within the cavity. Constructive interference occurs when the length of the cavity has been precisely tuned to a half-integer number of wavelengths of the input light, resulting in the formation of a standing wave formed from counter-propagating photons. This also has the added benefit of providing counter-propagating photons for the Doppler-free two photon excitation of the 1S-2S transition. Only specific ranges of mirror curvatures, R_1 and R_2, and separations, L, form a 'stable' cavity, whereby consecutive round trips of the beam within the cavity are exactly mapped onto each other, in both transverse directions and beam diameter. Any mirror curvatures and separations outside the stable range will result in beam which continually grows with each round trip within the cavity, until it is larger than the cavity mirrors and becomes lost. The criterion for a stable cavity is given by

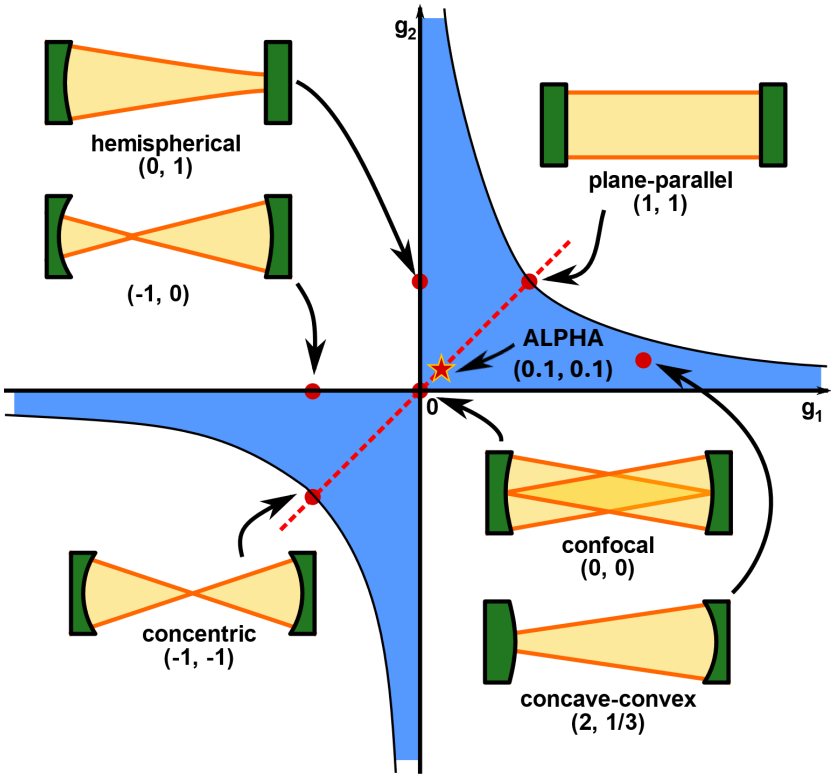

Fig. 6.13. Cavity configurations defined in terms of g_1 and g_2. Stable cavity configurations only occur within the blue regions. The stable cavity configuration used within ALPHA-2 is displayed by the red and amber star. Figure adapted from [140].

[141]

$$0 \leqslant \underbrace{\left(1-\frac{L}{R_1}\right)}_{g_2}\underbrace{\left(1-\frac{L}{R_2}\right)}_{g_2} \leqslant 1. \tag{6.5}$$

The range of mirror curvatures and separations that constitute a stable cavity, expressed in terms of g_1 and g_2, is displayed visually by the blue regions in figure 6.13. The enhancement cavity used within ALPHA-2 has equal mirror curvatures of 1 m which are a separated by 0.92 m, forming a nearly confocal cavity with equal g_1 and g_2 of 0.08; denoted by the red star in figure 6.13. The optical cavity intersects the ALPHA-2 trap at an angle of approximately 2.3° from the trap axis, displayed in figure 6.14 **a**. The reflection (R), transmission (T) and absorption (L) of input and ouput coupling mirror (IC and OC) of the cavity were determined by measuring the cavity mirrors in 2017, summarised in the table below. Since the cavity was

	R	T	L
IC	0.99	0.007597	0.002403
OC	0.995	0.0004865	0.0045135

integrated into ALPHA-2, it is likely that the mirrors have degraded with time due to frequent baking of the vacuum space. This could have led to potential changes in the values of R, T, and L.

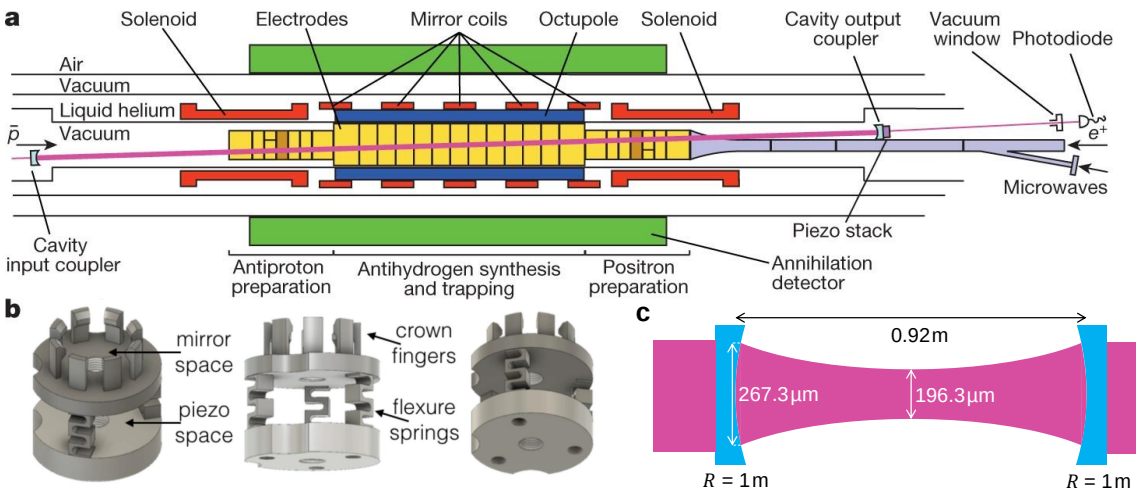

Fig. 6.14. **a** Schematic diagram displaying the orientation of the enhancement cavity and beam within ALPHA-2. **b** mechanical drawings of aluminum piezo-mirror mounts [139]. **c** Dimensions of beam within the enhancement cavity.

The input and output coupling mirrors are mounted within a specialised cryogenic mount machined from a single piece of aluminium, where the cavity mirrors are secured by the mechanical tension of eight flexing fingers. The output coupler mount, the mechanical drawing of which is displayed in figure 6.14 **b**, includes a slot for a cylindrical piezo actuator, which is held in position under pressure and can be actuated by applying a voltage to adjust the cavity length. The input coupler is secured in a similar finger mount, which does not have the piezo space. Having added 6.25 MHz sidebands to the laser spectrum via the EOM, a PDH error signal can be produced using the reflection signal (measured by the R detector in 6.10) of the cavity. The output coupler piezo voltage can be locked using the zero point of the PDH signal, which actuates the length of the cavity to achieve resonance, minimising the reflection signal and maximising the transmission signal measured by the T detector.

6.2.4 Downstream detection

Downstream of ALPHA-2 is a second laser box that houses the equipment to measure the 243 nm light transmitted through the enhancement cavity, as displayed in 6.10. The downstream laser box contains three key instruments: a camera, a photodiode (referred to as the T detector), and a power meter. When perfectly aligned and mode-matched, the enhancement cavity only resonates with the fundamental Gaussian mode (TEM_{00}). The camera allows the transverse spatial profile of the cavity mode to be observed, which provides an important functionality when aligning the laser into the cavity. The photodiode allows for continuous measurement of the transmitted power, which is directly read into a national instruments PCI eXtensions for Instrumentation (PXI) crate at a sampling rate of 1 kHz since 2023. Once calibrated, the photodiode signal enables the continuous monitoring of the power circulating within the enhancement cavity, with time resolution of 1 ms. Once the cavity is

aligned and locked, the power meter can be moved into the beam to measure the power the transmitted power P_T. The circulating power within the cavity, P_{circ}, can be calculated using the equation,

$$P_{circ} = \frac{P_T}{T_{OC}}, \tag{6.6}$$

Where T_{OC} is the transmission of the output coupling mirror, which was measured in 2017. This measurement provides the calibration of the photodiode, enabling the real-time estimation of the circulating cavity power. This calculation relies on T_{OC}, which, as mentioned previously, has not been directly measured since the cavity was installed, and could have changed over time. The circulating power within the cavity can also be determined by comparing the kickout rate of $\bar{H}$ during 1S-2S spectroscopy to simulations, which is discussed in more detail in section 8.2.1.

CHAPTER 7

Spectroscopy results

> *The spectrum has actually been really reproducible today!*
>
> — **Ted**
> 2023 antiproton run

There have been two experimental campaigns to investigate the 1S-2S spectrum post-LS2. The initial campaign took place briefly in 2022 and replicate the results of the 2018 uncooled spectrum [71]. The subsequent campaign in 2023 involved the measurement of multiple spectra using substantial samples of laser-cooled antihydrogen. The 2023 campaign was far more comprehensive, incorporating systematic investigations to mitigate the sources of error that were prominent in previous measurments. This chapter discusses these two experimental campaigns, outlining the experimental conditions in which they were performed, and presents the experimental data and spectra. The following chapter focuses on analysing the 2023 dataset to extract the 1S-2S transition frequency.

7.1 | 2022

The 2022 antiproton run was dedicated to the ALPHAg experimental campaign [33], detailed in section 2.3.2. During October 2022, a 4-week thermal cycle of the primary ALPHA-g solenoid, allowed for a brief opportunity to conduct experimental studies in ALPHA-2. The first three weeks of this period were dedicated to optimising parameters for antihydrogen production, while the last week was allocated to further investigate laser cooling and replicate of the spectroscopy from 2018. The original plan was to conduct two 1S-2S spectroscopy trials: the first involving an uncooled sample of antihydrogen and the second intended to measure the spectra of laser-cooled samples of antihydrogen. Unfortunately, technical issues with the 121 nm laser arose after the first trial, so the second experimental trial followed the same experimental protocol. Although these two experimental trials had the potential to improve the precision of the 1S-2S transition, given the improved metrology, the primary goal was to confirm that we could repeat previous measurements following a four year break.

7.1.1 Experimental protocol

The spectroscopy experimental procedure in 2022 remained the same as in 2018 [71], consisting of the following steps:

1. Accumulate a sample of trapped antihydrogen in the flat trap (see section 2.2.2).
2. Measure the central field of the trap using ECR magnetometry, use this measurement to adjust the frequency of the laser to account for magnetic field effects
3. Optimise the alignment of the 243 nm laser into the enhancement cavity, using light which is over 200 MHz detuned from the transition frequency.
4. Iterate over the preset list of laser detunings from the expected $d-d$ transition frequency, exposing the $\bar{H}$ for the specified exposure time and counting the number of annihilation events for each frequency.
5. Repeat previous step for $c-c$ transition.
6. Repeat steps 4 and 5 a preset number of sweeps; each repeat is one "sweep".
7. Perform a second measurement of the central field of the trap using ECR.
8. Ramp down the trap, and count the number of annihilations to determine the number of atoms remaining.

The two spectroscopy trials, identified by ALPHA run numbers 65695 and 65700, were completed in 2022 were taken under very similar experimental conditions. Both trials interrogated the same detunings (δ_L: -200, -100, -50, -25, 0, 25, 50, 100, 200 kHz). Both trials were carried out using the flat field setup from 2018 (displayed in figure 2.7, and also compared to the 2023 flat field in figure 7.3), where antihydrogen was accumulated for approximately 17 hours resulting in 2500-3000 trapped anti-atoms. The trapping rate was about 12-14 antihydrogen per stack, as this was before the development of beryllium-assisted accumulation. The conditions of the two trials are summarised in table 7.1.

trial #	trap config	kickout	laser cooling	*d-d*	*c-c*	# sweeps	average power (mW)	# $\bar{H}$	comments
65695	flat	None	none	yes	yes	300 (*c-c* & *d-d*)	427	949	2 s exposure per detuning. Cavity power very unstable throughout spectroscopy
65700	flat	None	none	yes	yes	300 (c-c & d-d)	446	1133	3 s exposure per detuning.

Table 7.1
Conditions of the two experimental trials from 2022.

Leading up to trial 65695, the maximum power we could achieve in the build-up cavity was approximately 700 mW, a decrease from the 1000 mW used in 2018. To compensate for the reduced laser power, our strategy was to expose the confined antihydrogen to twice as many frequency sweeps, but kept the laser exposure time at two seconds, the same as in 2018. Unfortunately, after about 15 minutes of laser exposure in trial 65695, the laser power began

to decline rapidly, which also impacted the reliability of the cavity lock. The spectroscopy was interrupted several times, to adjust laser alignment into the cavity, resulting in temporary improvements. Finally, after approximately 3 hours of spectroscopy the cause of the problem was determined: The beam was clipping on the shutter. The insufficiently secured mounting of the shutter had caused it to gradually rotate over time due to repetitive opening and closing cycles. After resolving this problem the laser and cavity power remained stable. The power drift is shown in figure 7.1. The timescale of the power decay is slow compared to the frequency sweeps, so we can assume that it provides no frequency bias in the spectrum. Trial 65700 was completed two days later. Our maximum circulating cavity power had stabilised at around 550 mW, so for trial 65700 we decided to increase the laser exposure time to three seconds, based on the observation from the previous trial that at these lower laser powers the depletion of the $\bar{H}$ sample was not so severe. During this spectroscopy measurement, the cavity power remained stable, as can be seen in figure 7.1, having fixed the problem with the shutter during the previous measurement.

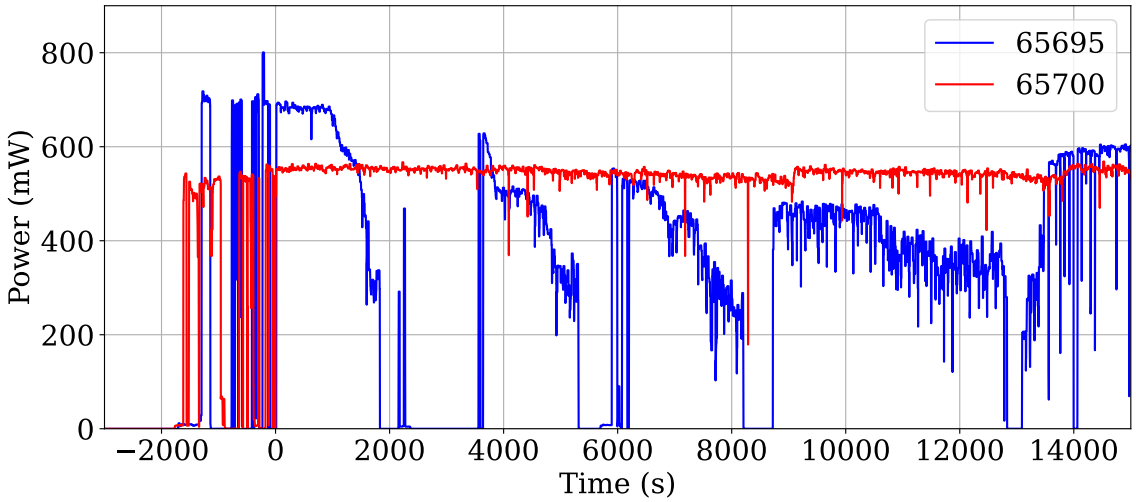

Fig. 7.1. Calculated power circulating in the ALPHA-2 cavity during the 2022 experimental trails. Plots display the 20 s rolling maximum of cavity power.

7.1.2 Results

The $\bar{H}$ which are lost from the traps during laser exposure can be determined from the number of detected pass cuts, via equation 2.4. The atoms lost can then be plotted against the laser detuning to produce a spectrum. The spectra obtained during the brief experimental period in 2022 are displayed in figure 7.2, normalized to the total losses observed during the spectroscopy, alongside equivalent spectra from 2018. It is clear that the two trials conducted in 2022 effectively replicate the uncooled spectrum from 2018 for both the $d-d$ and $c-c$ transitions. During trail 65700 we were fighting a deminishing vacuum within ALPHA-2, which was overdue a thermal cycle. Consequently, trial 65700 is expected to exhibit a higher background signal from annihilations with background gas.

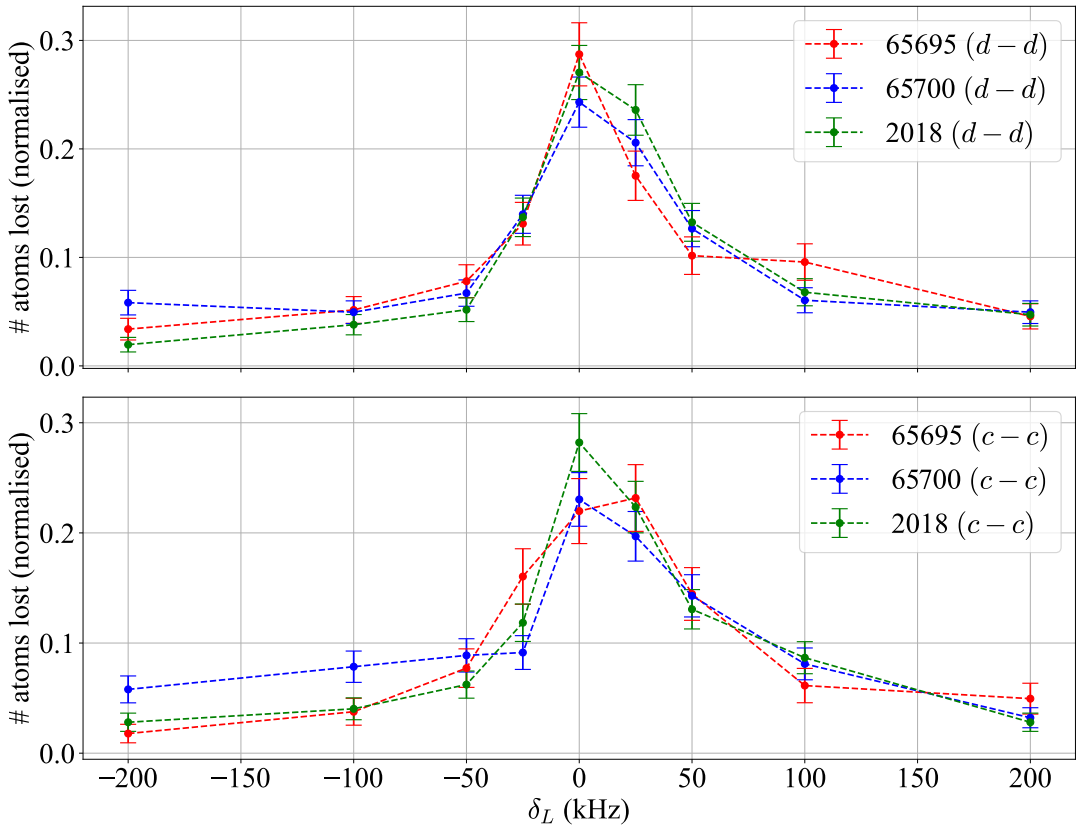

Fig. 7.2. Spectra measured during the 2022 experimental campaign, plotted alongside equivalent spectra measured in 2018 for comparative purposes. Each spectrum is normalised to the sum of all frequencies The top plot displays the $d-d$ spectra, and the bottom plot displays the $c-c$ spectra.

While the spectra measured in 2022 a provide a comparable level of precision as the 2018 spectra, they have not yet been extensively analysed to extract the 1S-2S transition frequency. This is because of the subsequent collection of the more comprehensive and precise dataset from the 2023 experimental campaign, offering a better opportunity to improve the precision in determining the 1S-2S transition frequency.

7.2 | 2023

In 2023 the antiproton run was entirely spent focusing on antihydrogen experiments within ALPHA-2, with a precision measurement of the 1S-2S spectrum being one of the key experimental objectives for the year. One of the major developments during the 2023 antiproton run was antihydrogen production from positrons that had been cooled sympathetically with laser-cooled Be^+ ions, discussed in sections 2.2.1 and 2.2.2. This led to a notable increase in the quantity of trapped $\bar{H}$ per mixing cycle, enabling the accumulation of approximately over 10,000 $\bar{H}$ within ALPHA-2. A higher number of trapped antihydrogen atoms presents an opportunity to substantially decrease the statistical uncertainties when determining the frequency of the 1S-2S transition, which was the most significant uncertainty in table 2.3. In September 2023 we had an operational Lyman-α laser, which was able to reproducibly laser

cool trapped $\bar{H}$ to roughly the same energy distribution, as discussed in section 2.2.3. Lower energy $\bar{H}$ take more time to traverse the 243 nm laser, resulting in a narrower linewidth as discussed in section 3.4. A narrower spectrum is more sensitive to changes in frequency, and allowing the transition frequency to be extracted with greater precision.

These two important experimental milestones, along with the improvements in laser frequency stability described in chapter 6, positioned us by October 2023 to commence an experimental campaign to improve the precision of the 1S-2S transition frequency of antihydrogen. This goal was primarily accomplished by measuring the spectra of large samples of laser-cooled antihydrogen within the conventional flat magnetic trap configuration. Additionally, in order to systematically reduce another significant source of uncertainty, identified in table 2.3 'Modelling errors', we also collected spectra of $\bar{H}$ confined within alternative magnetic trap configurations. The reason spectra do not exhibit a peak at the 1S-2S transition frequency is due to the magnetic trap's shape distorting the shape of the spectrum, resulting in an asymmetry and a shift in the peak's location, as discussed in section 3.5.1. The modelling uncertainties in previous measurements originate from the reliance on simulation to accurately account for the effect of the field shape on the spectrum. In order to minimise the impact of magnetic trap effects, an ECR magnetometry campaign was conducted to produce the flattest field possible, which is illustrated by the 'Flat' field in 7.3. Furthermore, to systematically study magnetic trap effects, and reduce the uncertainty arising from it, we measured spectra in three additional magnetic trap configurations, which were given the names 'harmonic-up', 'harmonic-down', and 'raised-flat', displayed in figure 7.3.

The harmonic-up and harmonic-down field configurations can be produced by modifying the currents in the mirror coils. These configurations will introduce more distortion to the spectrum compared to the flat trap, and in differing ways. The harmonic-up configuration will shift the peak of the spectra towards higher detunings, whereas the harmomic-down configuration will shift the peak of the spectra towards lower detunings. The raised-flat configuration can be produced by increasing the current of the Carlsberg magnetic, resulting in a trap that maintains a similar shape to the flat trap but with approximately a 4% stronger field in the flat region. This will shift the peak location relative to the standard flat trap due to the Zeeman effect but does not cause further deformation of the spectrum's shape.

The majority of the 1S-2S spectra measured in 2023 were produced by illuminating the $\bar{H}$ with around 200 mW of 243 nm light in the build-up cavity. This is a significantly lower than the 1 W used in 2018, which was far to0 high and led to excessive depletion of the $\bar{H}$ sample within the first few sweeps. At the start of each experimental trial, the cavity power was tuned to 200 mW using AOM3 in figure 6.10, and nominally maintained at this value throughout each experimental trail through irregular adjustment. The upgrades in downstream detection described in section 6.2.4 allowed the cavity transmission to be recorded with 1 kHz resolution, compared to the 1 Hz previously. Lower 243 nm power, enhanced control, and higher resolution data compared to previous measurments is expected to reduce relative uncertainties run-to-run occurring due to mean laser power. Alongside these operational improvements, an

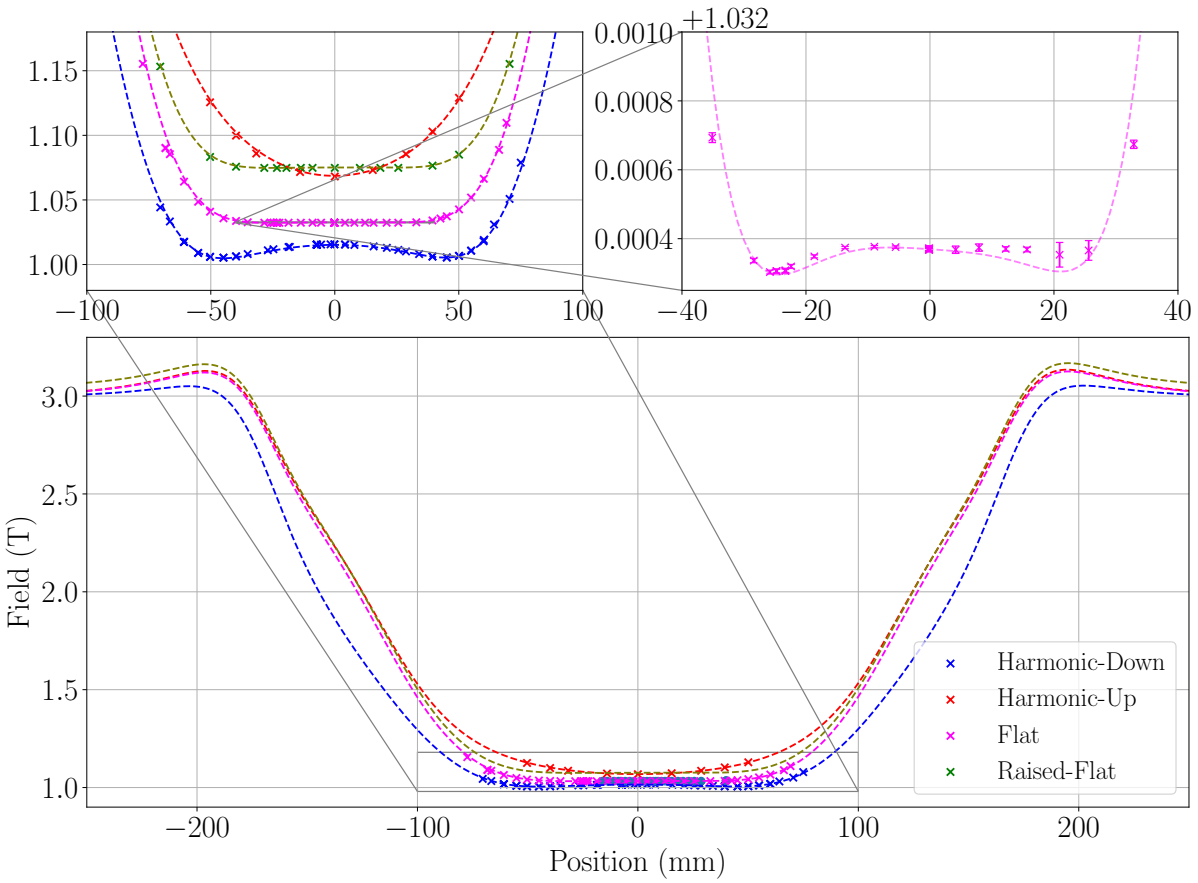

Fig. 7.3. Magnetic field strength on the axis for the different configurations. The data points indicate the field measured by ECR, while the dashed lines show the expected value derived from field models. First zoom (top left) clearly displays the different shapes of the different magnetic trap configurations. The initial zoom (top left) illustrates the distinct shapes of the different configurations. The second zoom (top right) highlights the inability of our field models to accurately determine the on-axis field at the sub-Gauss level.

experimental trial was conducted with around 100 mW of 243 nm light, to systematically study the effect of laser power on the spectrum.

Almost all of the spectra measured in 2023 were recorded by illuminating the $\bar{H}$ with eleven distinct frequency detunings, δ_L = -48, -24, -12, -6, -3, 0, 3, 6, 12, 24, 48 kHz. This is a greater number than the nine detunings used in 2018, and the choice of detunings is better selected to characterise the 1S-2S spectrum of laser-cooled antihydrogen. One experimental trial was conducted with an altered selection of detunings, δ_L = -48, -18, -9, -4.5, -3,-1.5, 1.5, 4.5, 9, 18, 48 kHz, which would further characterise the shape of the spectrum, and systematically study the effect of frequency selection.

Table 7.2, outlines the strategies implemented in 2023 to reduce the different sources of uncertainties identified in previous measurments. We are obliged to address these various sources of uncertainty, however, the uncertainty table arising from the 2023 experimental study is expected to be more comprehensive, encompassing additional sources of uncertainty that

become significant at increased precision.

Uncertainty	2023 approach
Statistical	Be+ Stacking, laser cooling
Frequency reference	Metrology upgrades
Mean laser power	Lower power, different power studies
Motional DC stark shift	Laser cooling
Frequency choice	Frequency choice studies
Modelling errors	Magnetic field studies

Table 7.2
Approaches taken to reducing specific uncertainties in the 2023 experimental campaign.

7.2.1 Experimental protocol

The spectroscopy experimental protocol in 2023 is very similar to the procedure conducted in 2022 and 2018. However as it is not possible to laser cool the d-states and c-states at the same time, we were unable to conduct $d-d$ and $c-c$ spectroscopy simultaneously as in 2022. The spectroscopy protocol consisted of the following steps:

1. Accumulate a sample of trapped antihydrogen in the flat trap via stacking.
2. Eject the antihydrogen in the c-state from the trap using resonant microwaves to induce a positron spin flip (this step is omitted if conducting $c-c$ states spectroscopy also)
3. Laser cool the remaining sample of d-states with a 300 MHz detuned pulsed 121 nm laser for a minimum of 4.4 hours
4. Measure the central field of the trap using ECR magnetometry, use this measurement to select the 0-detuning of the laser
5. Optimise alignment of the 243 nm laser into the cavity, using light which is over 200 MHz detuned from the transition frequency.
6. Iterate over the first preset list detunings from the expected $d-d$ transition frequency, list-1, exposing the $\bar{H}$ for the specified exposure time at each frequency.
7. Iterate over detuning list-2. (list-1 in reverse)
8. repeat steps a preset number of sweeps; each repeat of steps 4-7 is one "sweep".
9. Perform a second measurement of the central field of the trap using ECR.
10. If c-states are still present, repeat steps for c-states
11. Ramp down the magnetic trap.

Eleven experimental trials were conducted in 2023 according to the protocol detailed above, resulting in twelve measured spectra (the additional spectra arises from trial 691172, where both the $d-d$ and $c-c$ spectra were measured). The conditions of each of these experimental trial is summarised in table 7.3, which specifies the magnetic trap configuration, the microwave kickout, laser cooling, number of sweeps, and average power.

Trial #	Trap config	Kickout	Laser cooling	*d-d*	*c-c*	# sweeps	Average power (mW)	Comments
69026	flat	c-state μ-wave kickout before spectroscopy	successful	yes	no	40	202	
69029	flat	c-state μ-wave kickout after spectroscopy	not successful	yes	no	40	188	Two minutes of accidental laser heating after laser cooling, resulting in an improperly cooled sample
69037	flat	c-state μ-wave kickout after spectroscopy	not successful	yes	no	40	190	121 nm laser frequency was set incorrectly, resulting in an improperly cooled sample
69092	flat	c-state μ-wave kickout before spectroscopy	successful	yes	no	40	205	
69117	flat	d-state 243 nm laser kickout after spectroscopy	successful	yes	yes	50 (*d-d* & *c-c)*	200 (*d-d)* 201 (*c-c)*	
69126	up	c-state μ-wave kickout before spectroscopy	successful	yes	no	50	208	Laser cooled in flat trap, morph to harmonic-up trap before spectroscopy
69184	down	c-state μ-wave kickout before spectroscopy	successful	yes	no	43	216	Laser cooled in flat trap, morph to harmonic-down trap before spectroscopy. Cavity lock unstable.
69225	flat	c-state μ-wave kickout before spectroscopy	successful	yes	no	60	211	Ion-recapture as a secondary detection method during spectroscopy
69287	flat	c-state μ-wave kickout before spectroscopy	successful	yes	no	60	206	Different frequency detunings: -48, -18, -9, -4.5, -3,-1.5, 1.5, 4.5, 9, 18, 48 kHz
69290	flat	c-state μ-wave kickout before spectroscopy	not successful	yes	no	200	104	Improper laser cooling, the cause of which is unclear.
69377	raised	c-state μ-wave kickout before spectroscopy	successful	yes	no	50	214	

Table 7.3
Conditions of the eleven experimental trials from 2023

The $d-d$ spectra taken in 69026, 69092 and 69117 were performed under almost identical conditions: laser cooling of antihydrogen in a flat trap configuration, with spectroscopy conducted using an average laser power of approximately 200 mW over 40-50 sweeps using the same selection of laser detunings. During trial 69117 the *c*-states were not removed before the $d-d$ spectrum was measured, which is unlikely to make any significant impact on the $d-d$ spectrum,except for a higher background rate due to annihilation on gas. After the measurement of $d-d$ spectrum in trial 69117, the remaining *d*-states were removed with 200 s of zero-detuning laser light. Following the laser kickout, the *c*-states were laser cooled with the 121 nm laser, and the $c-c$ spectrum was recorded for the first time with a laser-cooled antihydrogen sample. Trial 69287 was conducted under conditions similar to those of 69026 but with a different set of laser detunings. Trial 69225 was also performed under similar conditions to 69026, except that ion recapture was performed during spectroscopy as an additional detection technique. During laser exposure, ionised antiprotons could be re-confined

within the Penning trap, and then dumped to the MCP following each exposure, as discussed in section 3.6.

The spectra measured in trials 69126, 69184 and 69377 were taken under different trap configurations - harmonic-up, harmonic-down and raised-flat - to systematically study the effects of magnetic field. Other than the trap configurations, the remaining experimental parameters are nominally the same, except for a slightly lower number of sweeps in trial 69184. While the spectra were recorded in harmonic-up and harmonic-down fields for trials 69126 and 69184, laser cooling of the $\bar{H}$ initially occurred in the flat field. This is because the laser cooling parameters has been extensively optimised for the flat field configuration. Following cooling the flat-trap was slowly morphed into the harmonic trap, leading to a slight modification in the energy distribution of the trapped $\bar{H}$ due to adiabatic heating or cooling. This is not the case for trial 69377, which was laser cooled in the raised-flat configuration. Additionally, it is worth mentioning that the enhancement cavity lock exhibited instability during the spectroscopy in trial 69184.

The remaining trials, 69029, 69037 and 69290, were affected by issues which lead to them not being laser cooled to as cold as the other trials. In the case of trial 69029, this was caused by an accidental frequency change in the 121 nm laser, leading to two minutes of inadvertent laser heating towards the end of the laser-cooling period. In trial 69037, an incorrect setting of the 121 nm laser frequency resulted in ineffective cooling. As for trial 69290, the $\bar{H}$ sample produced results which are indicative of improper laser-cooling, although the specific reason for this remains unclear. The spectrum during this experimental trial was measured with 100 mW of laser power, to systematically study the effect of power on the spectrum. This spectrum was recorded over 200 sweeps rather than 50, to account for the expected fourfold decrease in excitation rate with half the laser power.

7.2.2 Results

For each spectroscopy trial, the $\bar{H}$ sample which was accumulated over 185 antiproton-positron mixings. For each experimental trial, the duration from the completion of antihydrogen accumulation to the last ramping down of the magnetic trap can be divided into time intervals, during which the $\bar{H}$ is exposed to a particular experimental process, and time intervals between the processes. For each of these intervals, the number of antiproton annihilations can be approximated by equation 2.4. The number of $\bar{H}$ remaining within the magnetic trap at the end of the i^{th} interval can be approximated by the reverse cumulative sum

$$\overline{\mathrm{H}}_i = \sum_{j=0}^{N} A_j - \sum_{j=0}^{i} A_j, \tag{7.1}$$

Where N is the total number of intervals the experimental trial has been split into, A_j is the number of detected annihilations in interval j, and $\overline{H}_i$ is the estimated number of $\bar{H}$ remaining

at interval i. This can be used to track the evolution of the number of $\bar{H}$ remaining during the experiment, which is displayed in figure 7.4 for trial 69026.

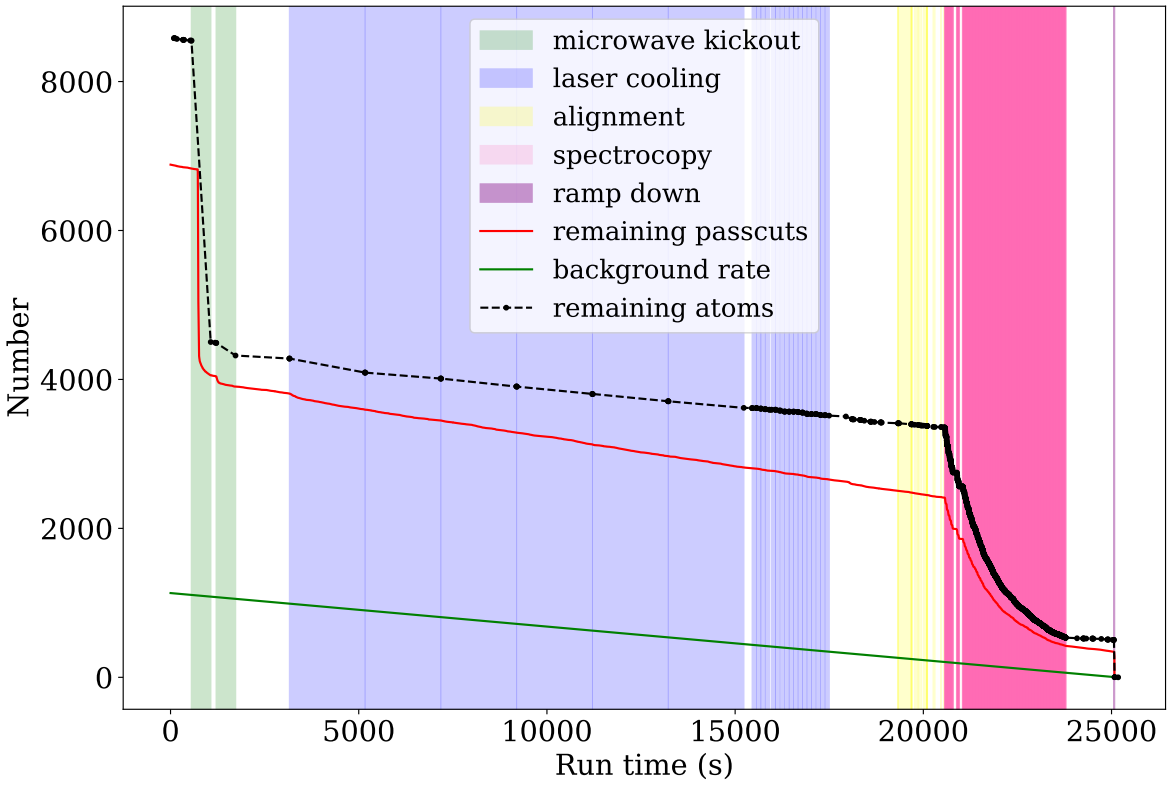

Fig. 7.4. Total number of trapped $\bar{H}$ remaining during trial 69026, plotted in black. The green shaded regions denote the temporal windows where $\bar{H}$ is subjected to resonant microwaves. The blue denotes temporal windows where the $\bar{H}$ are being laser cooled. The yellow regions denote when the $\bar{H}$ is being exposed to non-resonant 243 nm light for the sake of alignment. The pink denotes periods where the $\bar{H}$ is being exposed to one of the eleven 243 nm detunings for spectroscopy. Purple denotes the ramp down of the magnetic trap. The quasi-continuous evolution of passcuts is displayed in red, alongside the expected rate from background in green.

As can be seen, there is a sharp decrease in the number of remaining $\bar{H}$ during microwave kickout, where most of the c-states will annihilate. There is a steady decrease in the number of remaining $\bar{H}$ during laser cooling, alignment, and the other intermediate windows where no processes are taking place. This can be attributed to the annihilation of $\bar{H}$ by the background gas. During spectroscopy, there is an approximately exponential decrease as $\bar{H}$ are either ionized or undergoes a spin-flip subsequent to the transition to the 2S state. The remaining $\bar{H}$ annihilate during the ramp down of the magnetic trap. The reverse cumulative sum denoting the pass cuts remaining has also been plotted, which is quasi-continuous at this scale; as it is not corrected for cosmic background and therefore does not require segmentation into intervals. The expected contribution due to the cosmic background is displayed in green.

The antiproton annihilations during a trial can be categorised according the specific physical process occurring at the time of annihilation. This classification can be used to produce budgets of $\bar{H}$ losses resulting from different mechanisms. The budget table for all eleven experimental trials is presented in table 7.4. It is important to note that the atom numbers in this table

have been estimated from number of passed cuts, and adjusted for background rates and efficiency. The final analysis will involve an MVA (discussed in section 2.2.4), as such these number may change. The losses of $\bar{H}$ are sorted into seven categories: spectroscopy (also categorized by laser frequency), kickout, cooling, miscellaneous, alignment, miscellaneous laser, and ramp-down. These categories are self-explanatory, except for miscellaneous and miscellaneous laser. Miscellaneous refers to any annihilations that happen when none of the processes described in the other categories are occurring. Miscellaneous laser refers to counts occurring between laser exposures during spectroscopy. The experimental trials listed in table 7.4 are divided into three groups: trials conducted in the flat trap, trials conducted in a different magnetic trap configuration, and trials where laser cooling was unsuccessful. The reported errors represent one standard deviation counting errors, which are calculated as the square root of the number of contributing pass cuts divided by efficiency, with no background subtraction.

The $\bar{H}$ losses during spectroscopy can be plotted against laser detuning to produce a spectrum. All twelve spectra from the eleven runs are displayed in figure 7.5, where the $\bar{H}$ losses have been normalised by the sum of all losses during spectroscopy. The five spectra displayed in the top plot are the $d-d$ spectra measured in the flat trap, alongside the $d-d$ from trial 65700 in 2022. The spectra demonstrate excellent reproducibility and have a far narrower linewidth than the uncooled 1S-2S spectrum from trial 65700. Trial 69225 displays a slightly different shape compared to the other spectra shown in the upper plot. This difference may be attributed to the ion recapture technique, described in section 2.2.4, favoring the capture of the least energetic trapped antihydrogen, which results in a slightly broader spectrum in the SVD data due to it originating from the more energetic subset of trapped antihydrogen. The $c-c$ spectrum shown in the second plot from the top represents the first measurement of this line with laser-cooled antihydrogen, and it is notably the most narrow $c-c$ spectrum observed to date. It exhibits a more pronounced 'blue tail', an asymmetry resulting a broader spectrum at positive detunings, compared to the $d-d$ spectrum. This behaviour is in line with expectations, as the $c-c$ transition is more sensitive to the residual Zeeman shift. The third plot from the top displays the magnetic field studies. As expected, the harmonic-up shows a more prominent blue tail and shifts the peak to higher detunings, while the harmonic-down results in a red tail and shifts the peak to lower detunings. Trial 69377 displays approximately the same shape as the other flat spectra, but offset due to the stronger Carlsberg field. This shift to all frequency points has been put back in by hand, as during spectroscopy the detunings were chosen to be the same as the other runs, relative to the raised field minimum. The lower graph displays the spectra of $\bar{H}$ samples that were not properly cooled, which are visually broader compared to the other spectra measured in the flat trap. This broadening is expected because of the shorter average transit time.

		Spectroscopy frequency																	
	run	**1**	**2**	**3**	**4**	**5**	**6**	**7**	**8**	**9**	**10**	**11**	**kickout***	**cooling**	**misc.**	**alignment**	**misc. laser**	**FRD**	**total**
Standard Magnetic trap	**69026**	47.7	65.7	103.1	229.7	384.2	528.6	471.7	319.0	121.1	52.8	59.8	4216.1	736.8	285.0	30.5	437.5	500.4	**8589.7**
	69026 error	8.7	10.2	12.7	18.7	24.1	28.1	26.6	22.0	13.7	9.2	9.8	79.4	49.1	32.2	10.1	26.2	27.2	**122.1**
	69092	44.6	54.6	115.5	237.1	402.0	566.0	498.6	354.8	142.8	57.3	60.4	3951.4	727.9	294.9	160.8	161.7	522.3	**8352.7**
	69092 error	8.4	9.3	13.4	19.0	24.6	29.1	27.4	23.2	14.9	9.5	9.8	76.9	51.3	33.8	18.4	16.4	27.7	**122.1**
	69117 ***(d-d)***	79.6	96.7	121.6	262.0	391.7	670.1	561.3	369.6	166.5	80.6	76.5	113.2	1438.2	888.3	176.1	239.3	629.6	**8948.2**
	(c-c)	50.0	66.5	92.9	177.4	218.8	250.0	262.7	197.7	153.1	98.2	57.7		1278.0		6.7	307.2		
	69117 error ***(d-d)***	11.2	12.3	13.8	20.0	24.3	31.7	29.0	23.7	16.0	11.3	11.0	13.6	60.6	53.8	18.0	20.1	30.5	**138.8**
	(c-c)	8.9	10.3	12.1	16.6	18.4	19.6	20.1	17.5	15.4	12.5	9.5		58.6		5.7	22.5		
	69225**	29.7	62.0	111.6	210.1	266.2	429.6	355.1	273.9	173.3	52.9	56.5	5682.2	905.9	494.8	140.7	439.0	698.8	**10382.3**
	69225 error	6.9	10.0	13.2	18.0	20.2	25.6	23.3	20.5	16.4	9.2	9.5	92.0	53.8	42.2	18.2	26.3	32.1	**135.2**
	69287***	48.8	92.4	198.3	315.7	381.0	541.2	670.8	446.5	272.9	109.2	53.0	4964.6	835.3	537.9	80.3	168.5	888.5	**10604.9**
	69287 error	8.8	12.0	17.5	21.9	24.0	28.6	31.7	26.0	20.4	13.1	9.2	86.0	52.8	43.9	14.0	16.4	36.2	**136.5**
B field studies	**69126**	49.0	59.9	82.2	142.8	209.5	265.6	289.1	290.4	195.6	100.7	71.3	4692.5	1188.2	575.0	41.3	175.9	651.7	**9080.7**
	69126 error	8.8	9.8	11.4	14.9	18.0	20.2	21.0	21.1	17.4	12.6	10.6	83.7	57.5	45.6	10.8	17.0	31.0	**128.3**
	69184	28.1	58.5	171.7	359.6	524.7	486.7	340.4	233.3	115.3	50.2	31.4	4251.3	1283.8	1130.9	162.2	131.4	588.5	**9948.0**
	69184 error	6.7	9.6	16.2	23.3	28.1	27.0	22.7	18.9	13.4	8.9	7.1	79.7	58.7	64.4	24.0	14.3	29.4	**138.7**
	69377	46.1	57.7	104.0	261.7	418.7	565.5	476.3	397.3	185.8	83.4	33.8	4798.4	1336.8	401.9	161.2	135.6	744.4	**10208.6**
	69377 error	8.6	9.6	12.8	20.0	25.2	29.2	26.8	24.5	17.0	11.5	7.4	84.6	59.4	34.3	20.1	14.6	33.1	**132.6**
Cooling issues	**69029**	47.7	49.0	140.9	188.3	231.8	250.6	267.7	203.5	139.3	91.8	49.2	3395.5	1077.9	684.2	76.2	226.4	1615.1	**8735.1**
	69029 error	8.7	8.8	14.8	17.0	18.8	19.6	20.2	17.7	14.7	12.0	8.8	71.4	52.5	42.8	12.4	19.3	48.8	**123.1**
	60937	50.6	80.0	152.5	251.0	304.8	423.4	350.1	281.3	187.1	121.8	71.3	3636.6	844.1	557.2	58.2	281.2	1382.8	**9034.0**
	60937 error	8.9	11.2	15.4	19.6	21.5	25.3	23.0	20.7	17.0	13.8	10.6	73.8	49.1	38.9	11.1	21.2	45.1	**124.3**
	69290****	71.0	104.1	182.5	231.6	370.1	467.1	404.0	285.8	220.6	111.6	115.6	5407.2	902.9	493.9	66.6	661.0	1712.0	**11807.6**
	69290 error	10.7	13.0	17.1	19.2	24.2	27.1	25.2	21.3	18.8	13.4	13.6	89.7	53.7	40.4	13.3	32.7	50.2	**142.8**

Table 7.4

Atom loss by various mechanisms during each experimental trial. The top five experimental trials are in the standard flat trap. The middle three trails have a deliberately perturbed magnetic trap configuration for systematic studies. The bottom three trials have improper laser cooling. *69117 measures both the $d-d$ and $c-c$ transition in one experimental trial, and uses a laser kickout, which involves 200 seconds of d-d resonant laser light, kicking out remaining d-states. The remaining runs use resonant microwaves to kick out the c-states. **Ion recapture in parallel, resulting in missing counts. ***Different frequency selection, δ_L = -48, -18, -9, -4.5, -3,-1.5, 1.5, 4.5, 9, 18, 48 kHz. ****100mW laser power during spectroscopy.

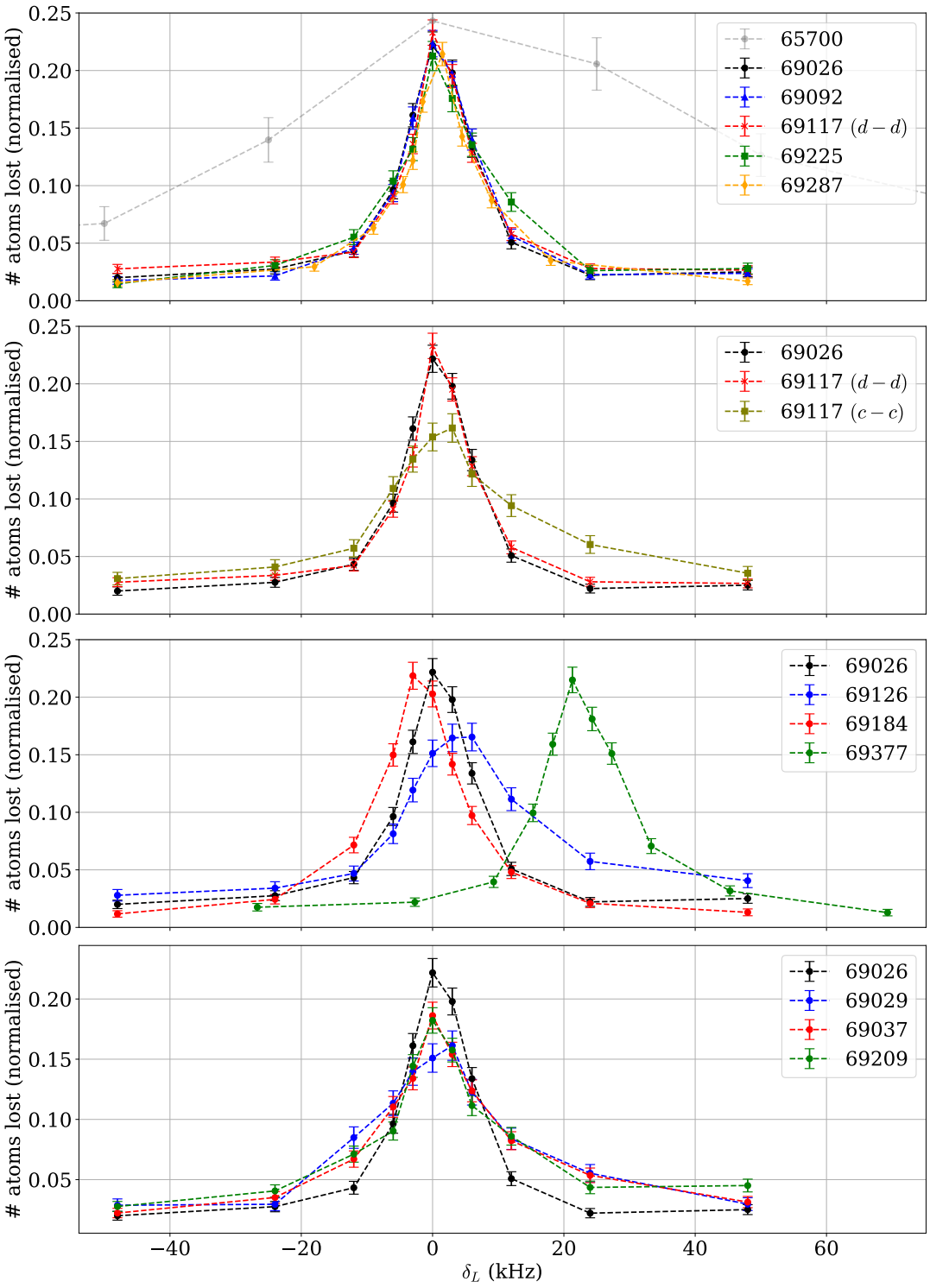

Fig. 7.5. Spectra from the eleven experimental trials. Each spectrum is normalised to the total count from frequencies. The top plot displays the cooled $d-d$ spectra measured in the flat trap. The second plot displays the cooled $c-c$ spectrum taken in the flat trap, alongside the equivalent $d-d$ spectrum. The third plot displays the magnetic field studies, where the detuning of 69377 has is relative to a B_0 of 1.07477 T (rather than the nominal 1.03228 T). The bottom plot displays the trials with improper cooling. Trial 69026 is displayed on all plots for comparative purposes.

CHAPTER 8

Ongoing analysis

> *If you torture the data long enough, it will confess to anything.*
>
> — **Ronald Coase**

The spectra obtained in the 2023 experimental campaign, discussed in the previous chapter, are narrower than any previous 1S-2S measurements taken to date. As a result, they provide an excellent data set to determine the 1S-2S transition frequency and test CPT symmetry with greater precision than before. To extract the 1S-2S transition frequency, we compare the measured spectra to results from simulation, by fitting both with lineshape functions. In addition, we must also determine the magnitude of other systematic sources of uncertainty, such as those originating from the magnetic trap and the laser system. This chapter discusses some of the analysis of the 2023 spectroscopy data. At the time of writing, much of analysis is still ongoing within a working group, consequently, this chapter is more of a discussion of the various method and routes for analysing the data. Where attempts have been made to determine uncertainties, it is important to note that the methods will likely contain differences from the ultimate analysis that determines the 1S-2S transition frequency in a future publication. Furthermore, any analysis which could be used to extract a transition frequency has been blinded.

The chapter first discusses the procedure for fitting line shapes for comparisons with simulations, such that the 1S-2S transition frequency can be extracted from the experimental data sets. We then apply these procedures to an experimentally measured spectrum, examine the sources of uncertainty that stem from the fitting procedures, and make estimates of their magnitude. Following this, I investigate the sources of systematic uncertainty that arise due to the effects of the magnetic trap, and estimate their magnitude. Finally, we examine the uncertainty that occurs due to our laser and metrology system, and estimate its magnitude.

8.1 | Evaluating fitting functions and procedures

In section 3.7, we explored four lineshape functions: P_{asym}, P_{GCADE}, P_{Trap}, and $P_{Trap,\,AC}$. We shall state the expressions again here, highlighting certain features.

$$P_{asym}(f_\epsilon, \chi, \underline{\gamma_R, \gamma_B}) = \begin{cases} \chi \exp\left(\frac{f_L - f_0 - f_\epsilon}{\gamma_R}\right) & f_L \leq f_0 + f_\epsilon \\ \chi \exp\left(\frac{f_0 - f_L}{\gamma_B}\right) & f_0 + f_\epsilon < f_L \end{cases} \tag{8.1}$$

$$\begin{aligned} &P_{GCADE}(f_\epsilon, \chi, \underline{\gamma_R, \gamma_B, \sigma}) = \\ &\chi \frac{\sigma\sqrt{\pi}}{\sqrt{2}} \left[\exp\left(\frac{\sigma^2}{2\gamma_R^2} + \frac{f_L - f_0 - f_\epsilon}{\gamma_R}\right)\left(1 - \operatorname{erf}\left(\frac{\sigma}{\sqrt{2}\gamma_R} + \frac{f_L - f_0 - f_\epsilon}{\sqrt{2}\sigma}\right)\right)\right. \\ &\left. + \exp\left(\frac{\sigma^2}{2\gamma_B^2} - \frac{f_L - f_0 - f_\epsilon}{\gamma_B}\right)\left(1 - \operatorname{erf}\left(\frac{\sigma}{\sqrt{2}\gamma_B} - \frac{f_L - f_0 - f_\epsilon}{\sqrt{2}\sigma}\right)\right)\right], \end{aligned} \tag{8.2}$$

$$\begin{aligned} &P_{trap}(f_\epsilon, \chi, \underline{T_{eff}}) = \\ &\chi N_z \int_{z_{min}}^{z_{max}} \exp\left(\frac{-4\pi w_0 \left|f_L - f_0(z) - f_\epsilon\right|}{\sqrt{2k_B T_{eff}/M}}\right) \exp\left(\frac{-\mu_B (B(z) - B_0)}{k_B T_{eff}}\right) dz. \end{aligned} \tag{8.3}$$

$$\begin{aligned} &P_{trap,\,AC}(f_\epsilon, \chi, \underline{T_{eff}}) = \\ &\chi N_z N_{AC} \int_0^{\sqrt{\frac{2}{3}} f_{AC_+}} \frac{w_0}{2\sqrt{2}} \frac{f_{AC}}{(\sqrt{\frac{2}{3}} f_{AC_+})^2 \sqrt{\log\left(\frac{\sqrt{\frac{2}{3}} f_{AC_+}}{f_{AC}}\right)}} df_{AC} \\ &\int_{z_{min}}^{z_{max}} \exp\left(\frac{-\mu_B \left(B(z) - B_0\right)}{k_B T_{eff}}\right) \exp\left(\frac{-4\pi w_0 \left|f_L - f_0(z) - f_\epsilon - \frac{f_{AC}}{2}\right|}{\sqrt{2k_B T_{eff}/M}}\right) dz. \end{aligned} \tag{8.4}$$

For each lineshape, we have stated in brackets the parameters which will be allowed to vary when fitting the spectra. The underlined parameters define the shape of the function, and they are allowed to vary in some of the fits but not others, detailed in 8.1.2. The value of f_0 is fixed to the transition frequency expected from hydrogen in the magnetic field in the center of the trap, likewise $f_0(z)$ has been fixed to the expected shift in transition frequency in hydrogen (given by equation 3.17). A new fitting parameter has been introduced, f_ϵ, which parameterises a shift in the transition frequency from that expected in hydrogen, due to possible CPT violation. $B(z)$ is fixed to that expected from the field model, w_0 is fixed to 196 μm. In this chaper, when fitting these functions to data, Python's SciPy curve fitting library has been used [142], which applys the trust region reflective algorithm [143], via `scipy.optimize.curve_fit`.

8.1.1 Fitting aggregated spectra from simulations

The simulated spectra discussed in this chapter are produced using the simulations described in section 3.8. The frequency of the 1S–2S transition encoded in the simulations is set to the same value as in hydrogen, with the addition of a random blinding factor, α, ranging from –500 to 500 Hz, the value of which remains unknown at the time of writing. A total of 180 distinct spectra were generated, each with a different permutation of initial temperature T, laser power P, or the frequency array shift S. Specifically, S represents a global shift in the array of eleven laser detuning frequencies used in the spectroscopy. For instance, a shift $S = -2$ Hz would modify the frequency array from $\delta_L(S = 0) =$ [-48, -24, -12, -6, -3, 0, 3, 6, 12, 24, 48] kHz to $\delta_L(S = -2) =$ [-50, -26, -14, -8, -5, -2, 1, 4, 10, 22, 46] kHz. The selection of T, P and S which were simulated were:

$$T = [7, 10, 15, 20, 30, 40] \text{ mK}$$
$$P = [140, 170, 200, 240, 280, 330] \text{ mW}$$
$$S = [-2, -1, 0, 1, 2] \text{ kHz}$$

Every possible perturbation of these parameters results in a grid of 180 simulated spectra. Simulations sharing the same T and P values can be grouped together to form an 'aggregated' spectrum with finer frequency points, illustrated for $T = 10$ mK and $P = 200$ mW in figure 8.1. Lineshape functions can be better constrained when fit to an aggregated spectra spectra, with example fits of all four lineshape functions presented in figure 8.1. By grouping simulations in

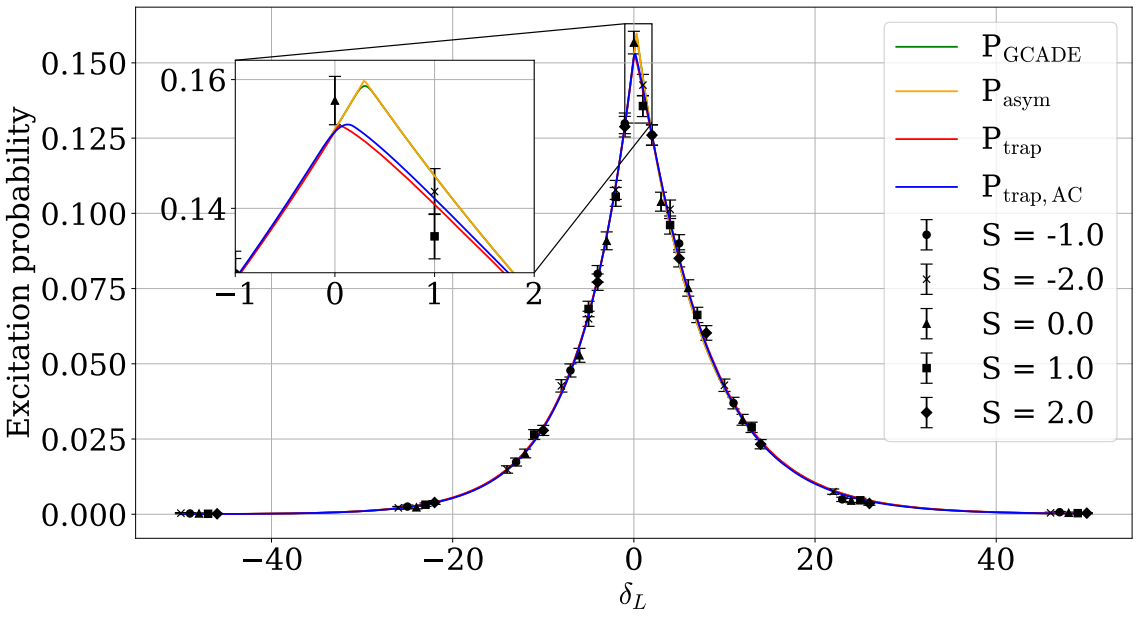

Fig. 8.1. Fits to a combined spectra with simulation parameters $(T, P) = (10\,\text{mK}, 200\,\text{mW})$. Variations in the lineshape functions are most notable at the peak, as shown in the magnified section. The y-axis represents the excitation probability, calculated as the $\bar{H}$ that escape the trap during 50 laser sweeps, divided by the total $\bar{H}$ simulated.

this way, we are able to produce a grid of 36 aggregated spectra which represent every possible permutation of P and T which was simulated. Each of these 36 aggregated spectra can be fitted with each of the four lineshape functions, and the reduced chi-squared statistic, χ^2, is calculated and shown in a histogram in figure 8.2. The average chi-squared value is close to

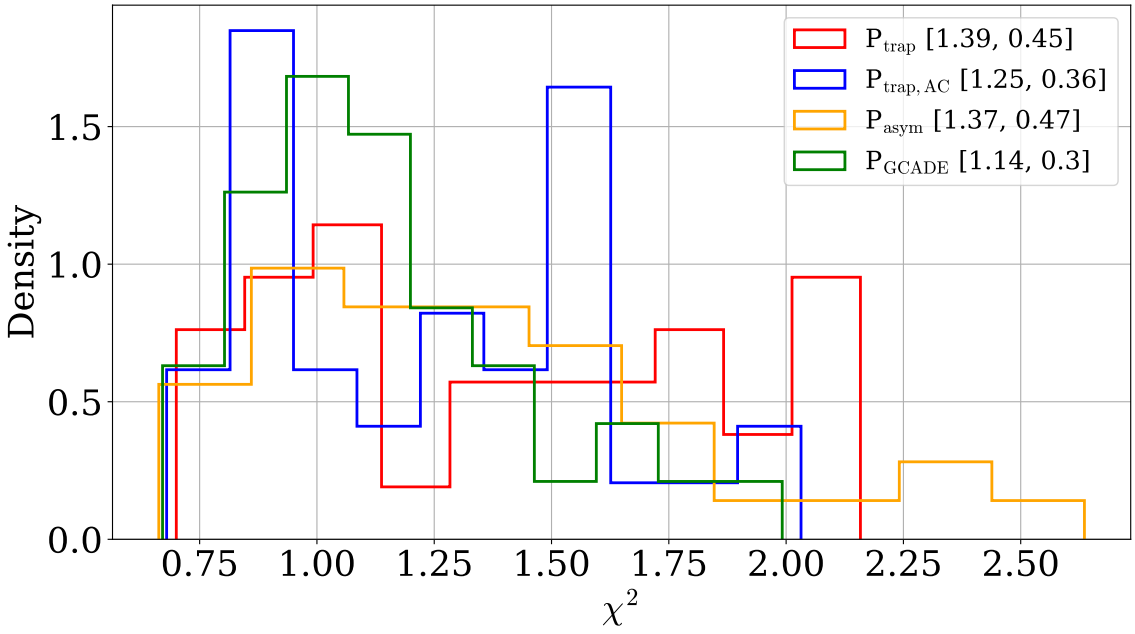

Fig. 8.2. Distribution of χ^2 statistics for the fitting of aggregated spectra. The legend displays the mean χ^2 and standard deviation in the format [mean, standard deviation].

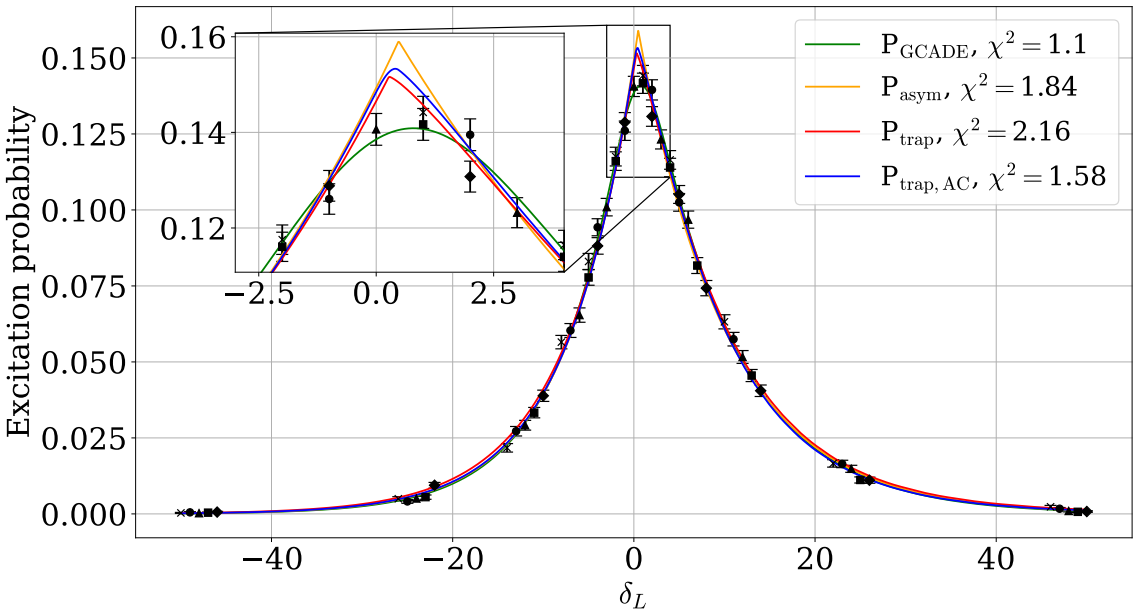

Fig. 8.3. An example aggregated spectrum where fits with all lineshapes, with the exception of P_{GCADE}, inadequately capture the peak's smoothness. The χ^2 value of each fit is displayed in the legend.

unity for all four lineshape functions, however, the spread appears to be smaller for the P_{GCADE}

function, resulting in the lowest average value. This marginally better fitting from P_{GCADE} is due to the behaviour of the fit around the peak. The P_{GCADE} is able to better fit the points around the peak as it contains a fitting parameter σ which controls the smoothness of the peak, which the other functions do not. Although the physics-driven lineshape incorporates some smoothing of the peak due to magnetic trap effects and the AC Stark shift, it is not always sufficient to accurately model the smoothed peak observed in simulations. Figure 8.3 illustrates an example of an aggregated spectrum where the physics-driven lineshapes, and the P_{asym} lineshape, fail to perfectly capture the peak's smoothness, whereas the P_{GCADE} function succeeds.

For each fit, the value of f_ϵ can also be determined. While we are not entirely certain that any of the fitting functions can accurately predict the random blinding factor in the simulation, α, there is reason to believe that the physics-based fits may come close. Therefore, as a precaution, this thesis will only present $f_\epsilon - \beta$ from now on, where β is an additional random blinding factor ranging from –500 to 500 Hz. We can plot f_ϵ against the simulation parameters T and P to examine its dependence on these variables. Figure 8.4 shows the variation of $f_\epsilon - \beta$ with temperature, along with linear fits. The slopes of the linear fits for P_{trap} and $P_{trap,\ AC}$ are consistent with zero (-0.34 ± 1.82 and -1.78 ± 1.8,/Hz/mK respectively), indicating no significant dependence of f_ϵ on T. The slopes for P_{GCADE} and P_{asym} are not consistent with zero (5.48 ± 3.46 and 4.28 ± 2.57 Hz/mK respectively). However, these slopes are still so small that they can be considered negligible over this range. The data has been reorganized in figure 8.5, where $f_\epsilon - \beta$ is plotted against P, with corresponding linear fit for each lineshape function. The linear fits have been extrapolated back to 0 mW to emphasise the effect of the AC Stark shift. This time, it is evident that only $P_{trap,\ AC}$ produces an f_ϵ parameter that remains unaffected by the power. This is because it is the only lineshape function that incorporates the effects of the AC Stark shift. An interesting observable feature is that the extrapolation of the linear fits suggests that P_{trap} and $P_{trap,\ AC}$ would predict the same value of f_ϵ at 0 mW, further supporting that $P_{trap,\ AC}$ accurately accounts for the AC Stark shift. We can also examine the distribution of f_ϵ produced by the different lineshape functions, displayed in a histogram in figure 8.6. There is clearly a significant difference in the f_ϵ values generated by the lineshape functions, except for P_{GCADE} and P_{asym}, which have closely overlapping distributions. The mean f_ϵ for P_{trap} is 385 Hz higher than the mean for $P_{trap,\ AC}$. This discrepancy is due to the AC Stark shift, which P_{trap} does not account for. Furthermore, the mean f_ϵ values for P_{GCADE} and P_{asym} are even more offset from $P_{trap,\ AC}$, by over 700 Hz. This is because, although these functions include the magnetic trap's influence in their shape, they ignore its effect on the f_ϵ parameter. The $P_{trap,\ AC}$ shows the least variation in f_ϵ across fits, indicating it is the most stable against changes in the simulation parameters T and P.

For physics-driven fits it is also of interest to determine how close the effective temperature fitting parameter, T_{eff}, is to the actual temperature, T, used for initialising the $\bar{H}$ in the simulation. T_{eff} is plotted against T for both P_{trap} and $P_{trap,\ AC}$ in figure 8.7, for the different

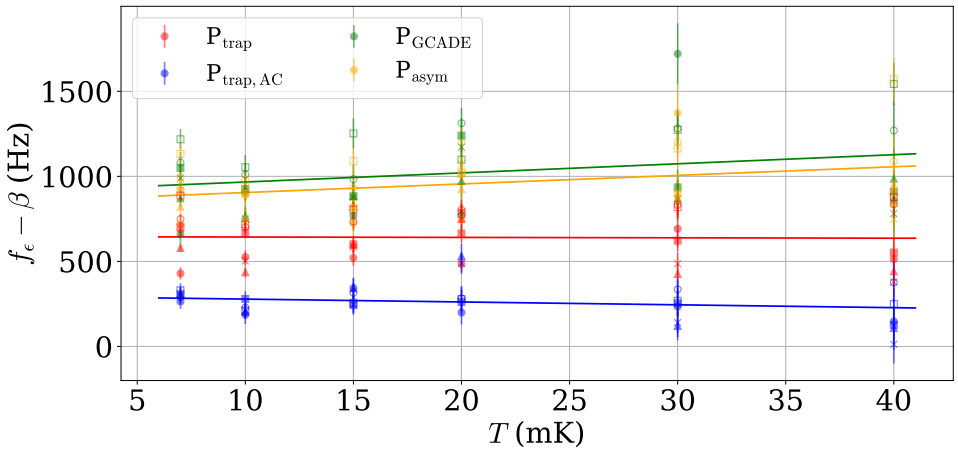

Fig. 8.4. f_ϵ determined through fits with each of the lineshape functions to aggregated spectra plotted as a function of T. Different markers display different values of P, where [•, ▲, ×, ■, ○, □] represent [140, 170, 200, 240, 280, 330] mW respectively. Error bars are derived from the diagonal elements of the covariance matrix of the fit. Solid lines display linear regression of data points.

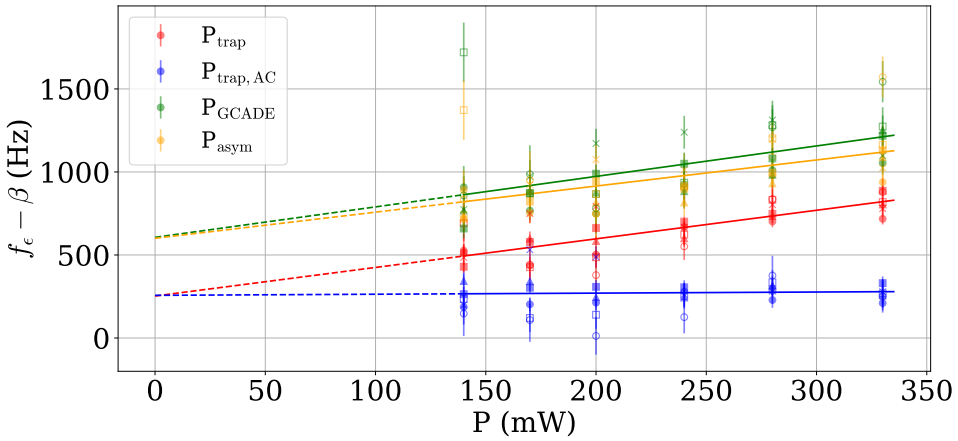

Fig. 8.5. f_ϵ as a function of P. [•, ▲, ×, ■, ○, □] represent [7, 10, 15, 20, 30, 40] mK respectively. Solid lines display linear regression of data points, with dotted line displaying extrapolation to 0 mW.

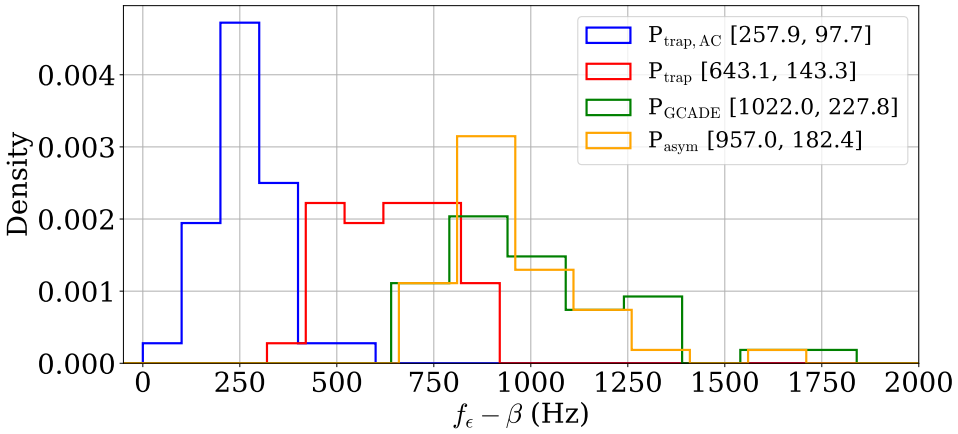

Fig. 8.6. Distribution of f_ϵ from fits to aggregated spectra. The [mean, standard deviation] is displayed in the legend.

values of P. As can be observed, T_{eff} correlates with T but is marginally higher. The disparity between T_{eff} and T also increases with P. Although finite transit time is the primary cause of broadening in our lineshape, it is not the only one, as discussed in section 3.5. T_{eff} is the parameter that characterises the broadness of our lineshape; thus, any additional sources of linewidth broadening in the simulation will manifest as a higher T_{eff} in the fit. A higher rate of photoionisation reduces the lifetime of the 2S state, and therefore broadens the lineshape, as mentioned in 3.6.2. Photoionisation increases with laser power, which results in a larger T_{eff} as P increases.

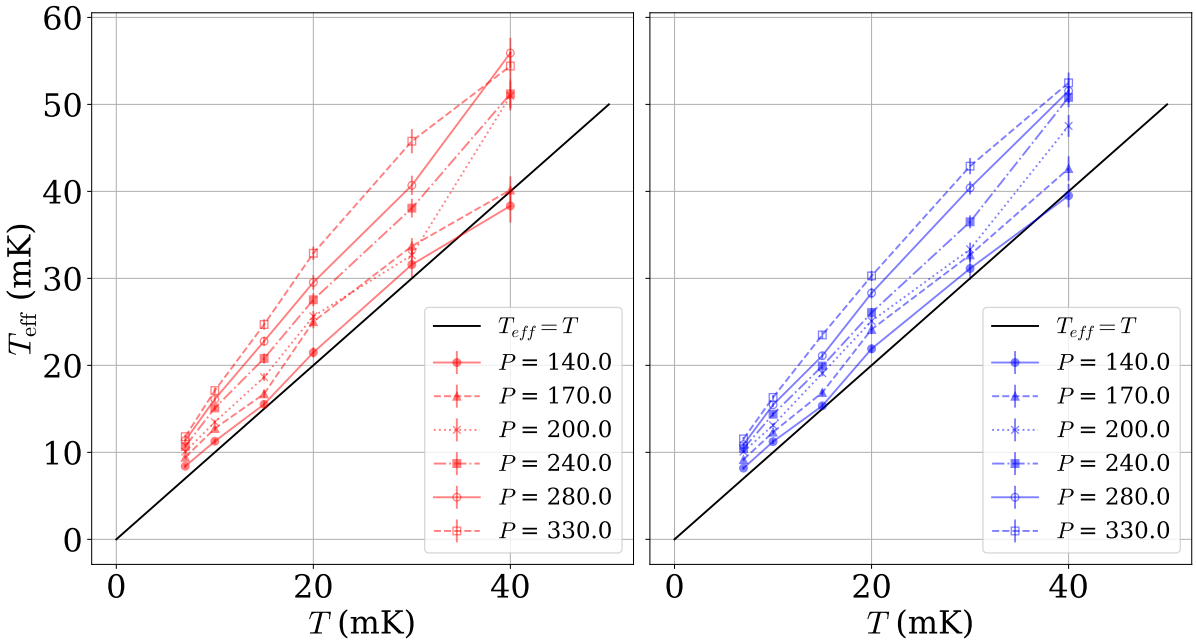

Fig. 8.7. The T_{eff} parameter from fits to aggregated spectra with the physics-driven lineshapes plotted as a function of T. The left hand plot displayed the result of fitting aggregated spectra with P_{trap}, the right displays $P_{trap,\ AC}$. $y = x$ is displayed as a black line on both plots.

8.1.2 Testing fitting procedures on pseudo-experimental spectra

When fitting the experimentally measured spectra, two approaches can be considered. One approach is the 'fixed-shape' fitting procedure, which was used for the spectra measured in 2018 [71]. This method involves determining the shape parameters of a lineshape function (the parameters underlined in equations 8.1 - 8.4) by fitting it to an aggregated spectrum generated through simulations with parameters equivalent to those used in the experiment. The shape parameters are then kept constant, and the line shape function is fit to the experimental spectrum, allowing only f_ϵ and χ to vary as free parameters during the fitting process. The difference between the f_ϵ parameter from the experimental and simulated spectra, Δf_{fixed}, during the fixed shape fit indicates the difference between the expected transition frequency and the measured data, once the unknown blinding parameters have been taken into account. Another approach is the 'free' fitting procedure, where all parameters are allowed to freely

vary when fitting a lineshape function to the experimental spectra. The value of f_ϵ from the free fit is then compared to the value of f_ϵ determined from the fit to an aggregated spectrum produced from simulations with parameters equivalent to those used in the experiment. The difference between the f_ϵ parameter from free fits to experimental and simulated spectra, Δf_{fixed}, indicates the difference between the expected transition frequency and the measured data, once the unknown blinding parameters have been taken into account. Both fitting procedures are illustrated in figure 8.8.

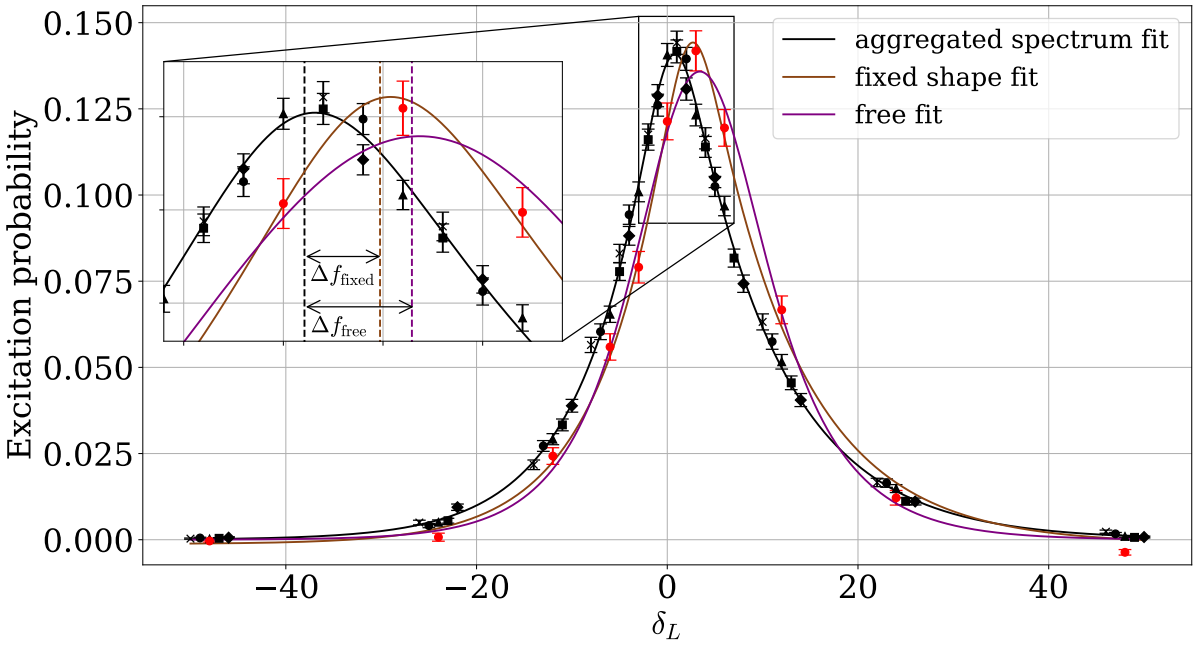

Fig. 8.8. An illustration of fixed shape and free fitting procedures. The black data points display an aggregated spectra formed from simulation with parameters $(T, P) = (15\,\text{mK}, 280\,\text{mK})$, which has been fit with the P_{GCADE} function, displayed by the black line. The red data points display experimental-style data derived from simulation, with an exaggerated difference in center frequency for visualisation purposes. The brown fit displays a fixed shape fit to the red data, with the shape parameters fixed to be equal to those in the black. The purple fit displays a free fit to the red data. Both fits use the P_{GCADE} function. The difference in f_ϵ parameter determined from fixed shape fits and free fits to the red data is displayed visually in the inset by Δf_{fixed} and Δf_{free} respectively.

Both fixed shape and free fitting procedures have their advantages. The advantage of a fixed shape fitting procedure is that the fit to experimental data is less dependent upon the behaviour of the specific lineshape function which is being used, as its shape has been fixed by the simulation. A free fit, on the other hand, requires a lineshape function with minimal interdependence between the shape parameters and the f_ϵ parameter. However, the advantage of the free fitting procedure is that it may result in a better fit to the experimental spectrum, and may depend less upon the simulation parameters matching the condition of the experiment.

To evaluate the suitability of each line-shape function for the fixed shape and free fitting procedure, we use fits to 'pseudo-experimental' spectra. Each of the 180 simulated spectra is

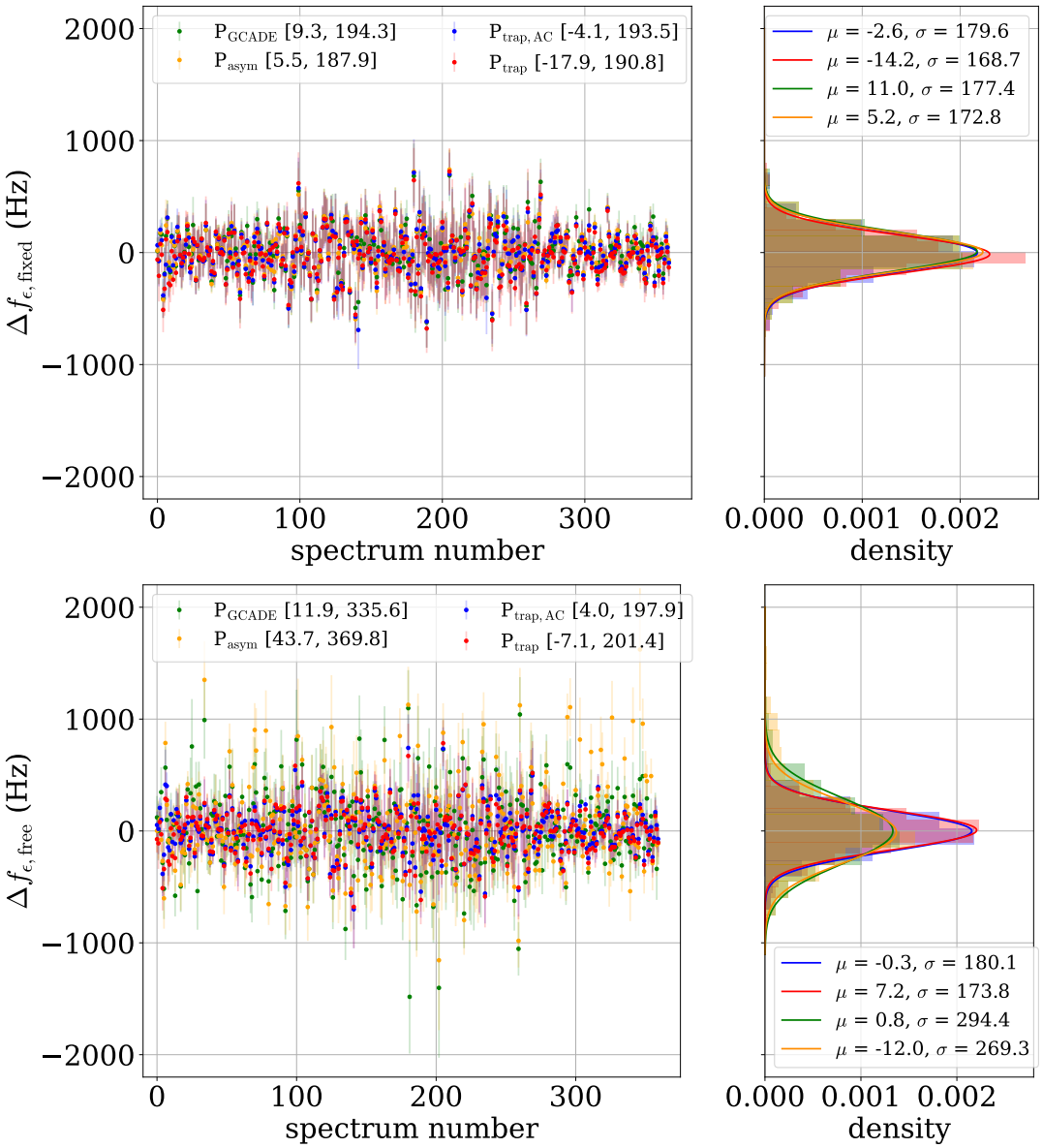

Fig. 8.9. Top plot displays the variation of Δf_{fixed} from fixed shape fits to psuedo-experimental spectra, bottom plot displays the variation of Δf_{free} from free fits to the same spectra. Legend in left plots displays [mean, standard deviation] of the data. Right hand plots display the distribution of Δf_{fixed} and Δf_{free}, which has been fit with a Gaussian distribution, with mean (μ) and standard deviation (σ) for the fit stated within legend.

generated from approximately 10,000 simulated $\bar{\text{H}}$ trajectories, which is approximately three times more than the number of $\bar{\text{H}}$ that are trapped prior to spectroscopy in the experimental runs from 2023. Thus, the trajectories going into each simulation can be randomly split into three, resulting in three simulated pseudo-experimental spectra with statistics more comparable to the experimental runs. Each pseudo-experimental spectrum with temperatures ranging from 7-20 mK (which is the temperature range we expect from the experiment, resulting in 360 pseudo-experimental spectra) are fit with each of the lineshape functions, using both the fixed shape fitting procedure and the free fitting procedure. The difference Δf from the fit to the

aggregated spectrum is plotted for the fixed shape fits in the top figure of figure 8.9 and for the free fits in the bottom figure, along with the distributions of Δf.

Examining the variation of Δf_{fixed} from the fixed shape fits to pseudo-experimental spectra in figure 8.9, we can see that the variation is essentially the same no matter which lineshape function is used. This is not particularly unexpected, as the shape of the function is fixed by the simulation, rendering the choice of lineshape function somewhat arbitrary. The standard deviation of Δf_{fixed} for the fixed shape fits is around 190 Hz, regardless of the choice of the lineshape function. In the case of the free fits, the variation of Δf_{fixed} is smaller for the physics-driven fits P_{trap} and $P_{\text{trap, AC}}$ compared to P_{GCADE} and P_{asym}. This is likely due to the fact that P_{GCADE} and P_{asym} have more fitting parameters to determine, and may be limited by the 11 frequency points. The result is a smaller standard deviation of Δf_{fixed} for the free fits with the physics driven lineshapes compared to P_{GCADE} and P_{asym}. In fact, the variation in Δf is comparable for the fixed shape and free fits when using the physics-driven lineshape functions (190-200 Hz).

8.2 | Fitting experimental spectra

As mentioned at the beginning of this chapter, the 1S-2S analysis is currently ongoing within an ALPHA collaboration working group. At the time of writing, discussions are still underway to decide on the exact lineshape and fitting procedure to apply to the experimental spectra; the contents of some of these discussions is covered in the previous section. However, for the purposes of this thesis, we shall select to fit the experimental spectra using two lineshape functions, P_{GCADE} and $P_{\text{trap, AC}}$. We will apply a fixed-shape fit with both functions and a free fit using only the $P_{\text{trap, AC}}$ function. The aim of using these different functions and procedures is to determine if there is a significant difference in the results they produce and to assess the uncertainty associated with each fit and how it is determined. The result of this analysis will not be to determine a transition frequency, and any frequency parameters will be blinded. In this chapter, we shall only analyse the spectrum resulting from experimental trail 69026. Analysis of the other trails, including those used for systematic studies, will be completed as part of the 1S-2S analysis, but will not be discussed within this thesis.

Figure 8.10 displays all three fits to the spectra resulting from experimental trial 69026. In the case of fixed shape fits, the shape has been fixed by the aggregated spectra generated by the simulations of $T = 10$ mK, $P = 200$ mW. Our focus is the value of Δf derived from these fits, and the associated uncertainty. The values of $\Delta f - \gamma$ resulting from the different fitting procedures are displayed for the round points in figure 8.11. γ is an additional random blinding parameter ranging from -500 to 500 Hz, which is introduced so that this analysis does not potentially reveal the value of the blinding parameter encoded in the simulation, α. The error bars are are determined from the diagonal terms of the covariance matrix of the fitting parameters, and are also used to produce the shaded uncertainty bounds in figure 8.10.

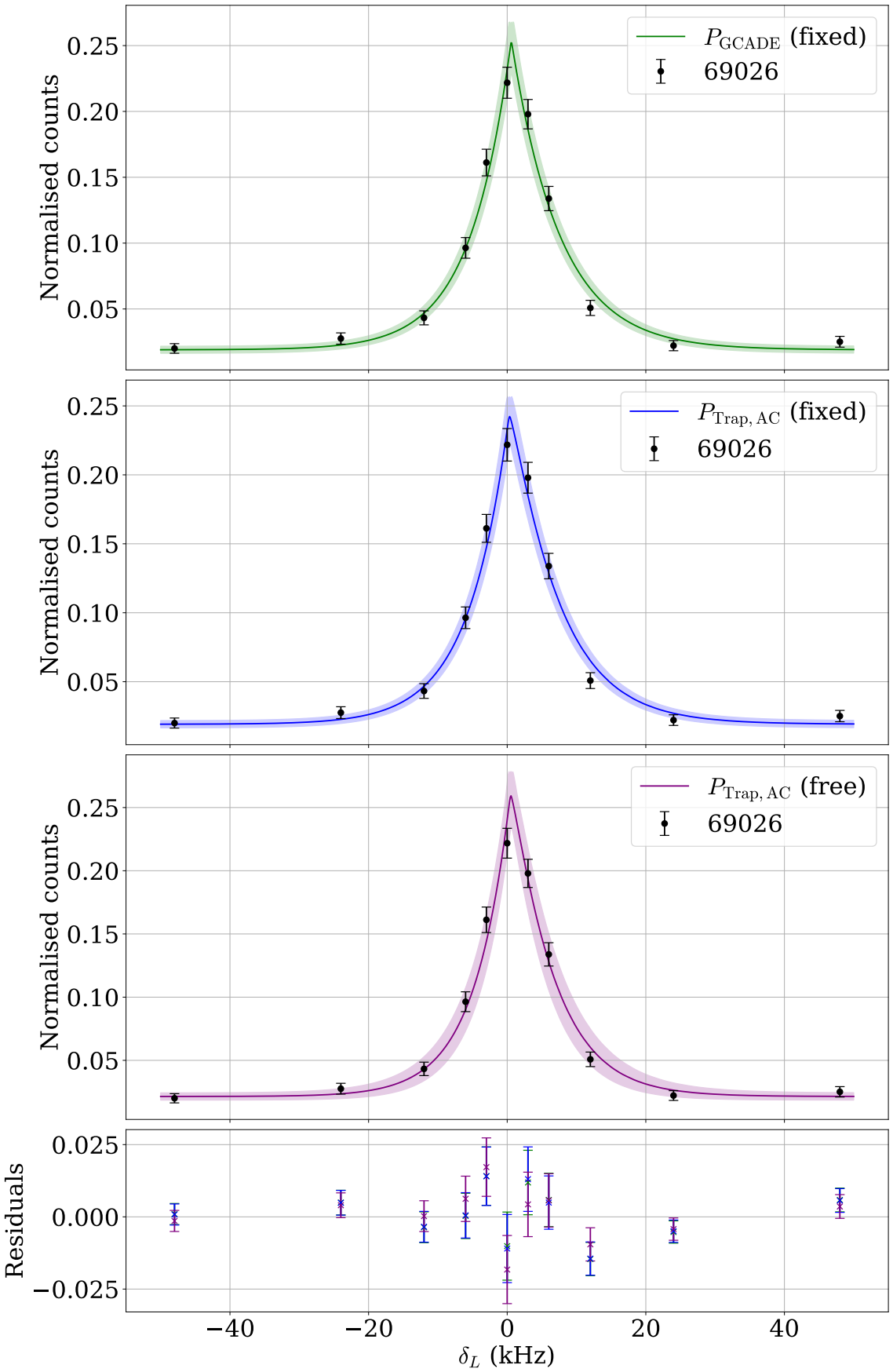

Fig. 8.10. Spectrum from trial 69026 fit with the three procedures described in this section. Shaded regions indicate uncertainty bounds derived from diagonal elements of the covariance matrix. Residuals of the three fits are displayed within the bottom plot, with the corresponding colors.

Deriving the uncertainties from the covariance matrix is based upon a linear approximation to the function around the best fit, and can lead to errors when this approximation becomes invalid. To check the validity of the error bars originating from the covariance, a Monte Carlo test is employed, which follows the following steps:

1. Produce a 'clone' dataset by perturbing normalised count of each datapoint in the spectrum by a small random number drawn from a Gaussian distribution with a standard deviation equal to the error bar.

2. Fit the clone data with the fitting function.

3. Repeat the first two steps 1000 times, recording the value of Δf produced by the fit.

4. The standard deviation of Δf values provides the uncertainty on Δf resulting from the fit.

The mean and standard deviation of Δf resulting from the Monte Carlo test is displayed by the crosses in figure 8.11, and produces similar results to the errors originating from the covariance matrix, within 16% of each other.

All three fitting procedures agree within their uncertainty. The uncertainty originating from fitting the spectrum with any of the three fitting procedures in less than 300 Hz at 243 nm.

8.2.1 Uncertainty in T and P

The temperature T of the trapped $\bar{H}$ prior to spectroscopy and the power P of the 243 nm light circulating within the ALPHA2 enhancement cavity determine the parameters of the simulation which we compare to when determining the deviation Δf. In the case of fixed shape fitting, this also determines the aggregated spectra which fixes the shape of the fitting function used to fit the experimentally measured spectra. As a result, uncertainty in the values of T and P results in uncertainty in Δf due to the fitting of the measured spectra.

There are several methods to estimate the temperature of the antihydrogen sample. In 2023, one of the methods used was the octupole ramp down temperature diagnostic, developed by Danielle Hodgkinson. This technique involves slowly ramping down the octupole current of the magnetic trap, gradually reducing the radial confinement of the $\bar{H}$, eventually leading to their annihilation on the electrode walls. By analysing the distributions of annihilation location and time it is possible to estimate the initial energy distribution of the trapped $\bar{H}$. Further details of the technique can be found in section 4.8 of [39], and in a forthcoming publication. Kinetic energy distributions of $\bar{H}$ parallel to the axis, measured by octupole FRD are displayed in figure 8.12, fit with a one-dimensional Maxwell–Boltzmann distribution.

This method estimates the $\bar{H}$ temperature to be around 10 mK. The measurement of $\bar{H}$ energy via octupole FRD takes place after spectroscopy, so considering that the laser preferentially excites the slowest moving $\bar{H}$ it is likely to be an overestimate of the energy before spectroscopy. Furthermore, a full understanding of this technique is still ongoing, and

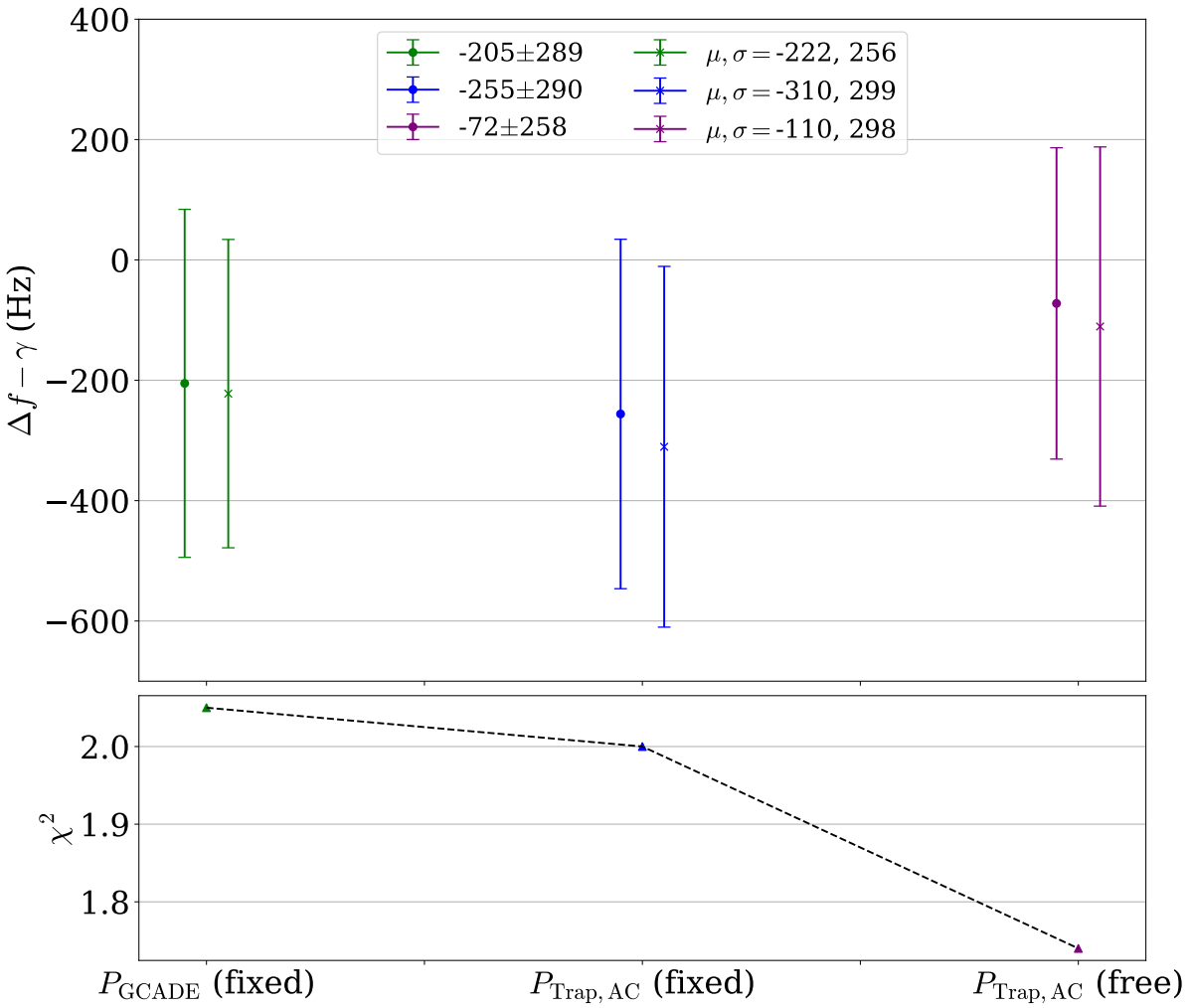

Fig. 8.11. Values of $\Delta f - \gamma$ resulting fits procedures displayed in figure 8.10. Standard fitting with errorbars determined from the coviarance matrix are displayed by the • markers. The Monte Carlo test of the fitting uncertainty, with errorbars representing standard deviation of $\Delta f - \gamma$ from the 1000 clone fits, is displayed by the × markers. Lower plot displays the reduced χ^2 statistic for the fits in figure 8.10.

its accuracy is still to be determined. A second technique to determine the $\bar{\mathrm{H}}$ temperature, discussed earlier in section 2.2.3, involves exciting the $\bar{\mathrm{H}}$ to the 2P level using the pulsed Lyman-α laser, and measuring the time-of-flight (TOF) to determine the kinetic energy. Measurements of the TOF with laser-cooled samples estimate the temperature of the $\bar{\mathrm{H}}$ sample to be between 10 and 15 mK [144]. For the analysis presented here, we assume that the temperature of the trapped $\bar{\mathrm{H}}$ sample is 10 ± 5 mK; however, as the analysis progresses within the working group, a different nominal temperature and uncertainties may be determined.

The power P, circulating in the ALPHA-2 enhancement cavity can be directly inferred from the transmission power through the output coupling mirror, as detailed in section 6.2.4. These measurements indicate that the average circulating power is 200 mW for trial 69026. However, this measurement relies on knowledge of the transmission of the output coupling mirror of the cavity, which was last directly measured in 2017. Since the installation of the cavity mirror in ALPHA-2, the transmission may have changed. An alternative method to estimate the

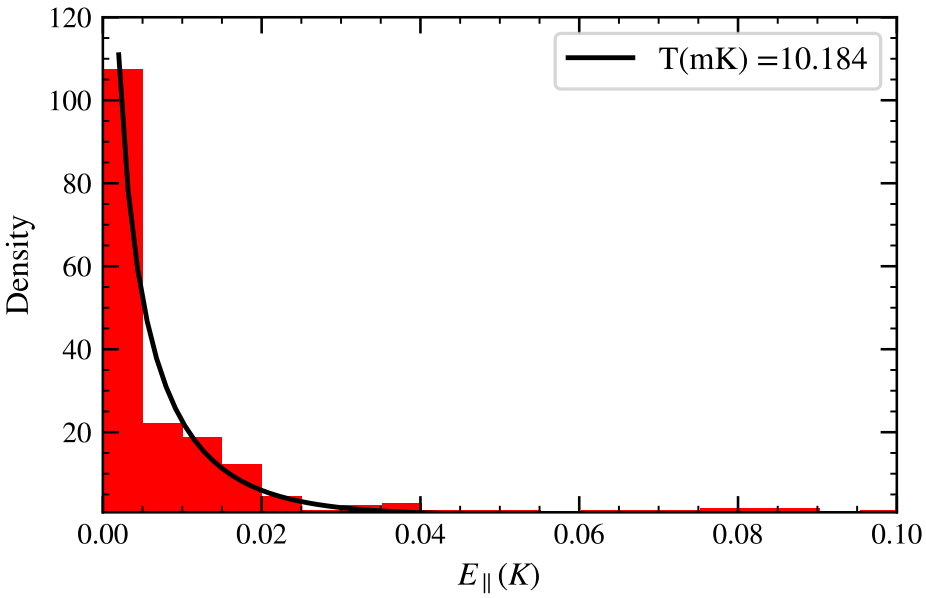

Fig. 8.12. Kinetic energy distributions parallel to the trap axis for $\bar{H}$ remaining surviving after spectroscopy in trial 69026. Energies have been determined by octupole FRD. Distribution has been fit with a one dimensional Maxwell–Boltzmann distribution to estimate the temperature of the sample. Octupole FRD is a method still in development, and this figure may contain differences from the final method.

circulating power within the ALPHA2 cavity involves comparing to simulation the rate at which $\bar{H}$ are excited out of the trap during spectroscopy, which depends on the power, as discussed in section 3.6. Of course, the excitation rate of $\bar{H}$ out of the trap during spectroscopy is also dependent on the temperature of the trapped $\bar{H}$, as colder atoms spend more time and the laser and are therefore more likely to be kicked out. There are also mechanisms other than the 1S-2S excitation which can lead to atoms being removed from the ALPHA2 trap, which are not accounted for in the simulation, a key one of these being annihilations of $\bar{H}$ on background gas. Studies by Levi Oliveira de Araujo Azevedo suggests that the laser light circulating within the ALPHA2 cavity induces the release of background gas from the surfaces of the cavity mirrors [145]. The increased background gas causes an increase in $\bar{H}$ annihilations when there is light circulating in the cavity, referred to as laser induced background gas annihilations (LIBGA). The probability P_{LIBGA}, of an $\bar{H}$ being kicked out of the trap through LIBGA can be modelled as being equal to $P_{\mathrm{LIBGA}} = 1 - \exp(-\lambda t)$, where λ is the LIBGA rate, and t is total laser exposure time. LIBGA can be be inserted into the simulation by randomly selecting $\bar{H}$ trajectories to remove from the trap with a probability P_{LIBGA}. The value of λ can be estimated based on the number of $\bar{H}$ excited when the laser is off resonance, and is estimated to range from 0.00009 and 0.00024 s^{-1} [145]. Comparisons evolution of $\bar{H}$ population in the trap during trial 69026, and the simulated $\bar{H}$ population during spectroscopy with differing amounts of LIBGA are displayed in figure 8.13.

Figure 8.13 shows that excluding LIBGA results in poor agreement between kickout curves from simulation and experiment, indicating that it is necessary. Comparing the experimental

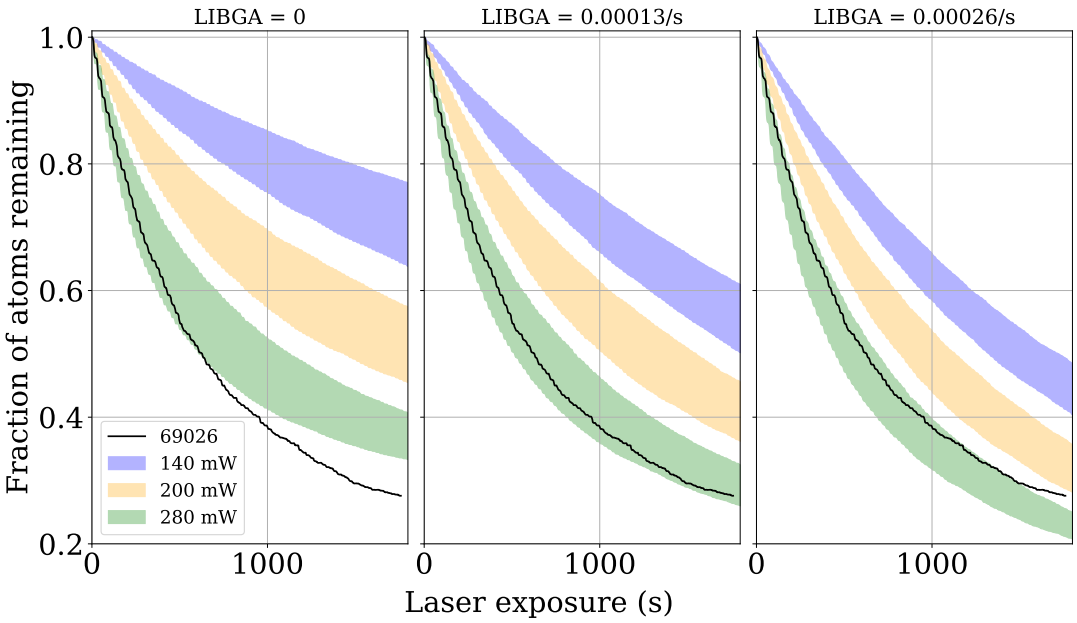

Fig. 8.13. Comparison of $\bar{H}$ kickout during spectroscopy for different laser powers and LIBGA rates. Shaded regions display the kickout for a fixed power, but with temperatures ranging from 7-15 mK. The black line shows the kickout from trial 69026.

kickout to simulations which incorporate LIBGA indicates that the circulating power is around 280 mW, which exceeds the 200 mW value determined by cavity transmission. To account for the difference between these measurements, we assume within this thesis that the power of 243 nm light circulating within the ALPHA2 enhancement cavity is 200 ± 80 mW. As with temperature, the alpha working group may decide upon different nominal power and uncertainties. Figure 8.14 displays how the value of Δf depends on the assumed temperature of the sample $\bar{H}$ for the different fitting procedures, whereas figure 8.15 shows the dependence on assumed power.

The slope from the linear fit to the data in figures 8.14 and 8.15 gives us the dependence of Δf on T and P for each fitting procedure. Firstly, we should note that the free fit of $P_{trap,\,AC}$ has close to no dependence on T, as T_{eff} is a free parameters in the fit; whereas fixing the shape introduces this dependence. The free fit still has a dependence on P, as this is not a free parameter in the fit; however, smaller slope indicates a weaker dependence, which again is due to the non-fixed shape. The slope of each linear fit can be used to convert an uncertainty in T and P into an uncertainty in Δf; these uncertainties are summarised in table 8.1, alongside the statistical error determined earlier in this section. The two fixed shape lineshape functions result in comparable uncertainties originating from the uncertainties in P and T, with P_{GCADE} producing slightly lower uncertainty than $P_{Trap,\,AC}$. The free $P_{Trap,\,AC}$ fit results in a significantly lower frequency uncertainty originating from uncertainties in P and T, as the shape of the function is not fixed and can be adjusted to fit the measured spectrum. However, this does not necessarily mean that the free $P_{Trap,\,AC}$ fit is the 'best – its shape hasn't been directly fixed by the simulation, and there are concerns about whether the

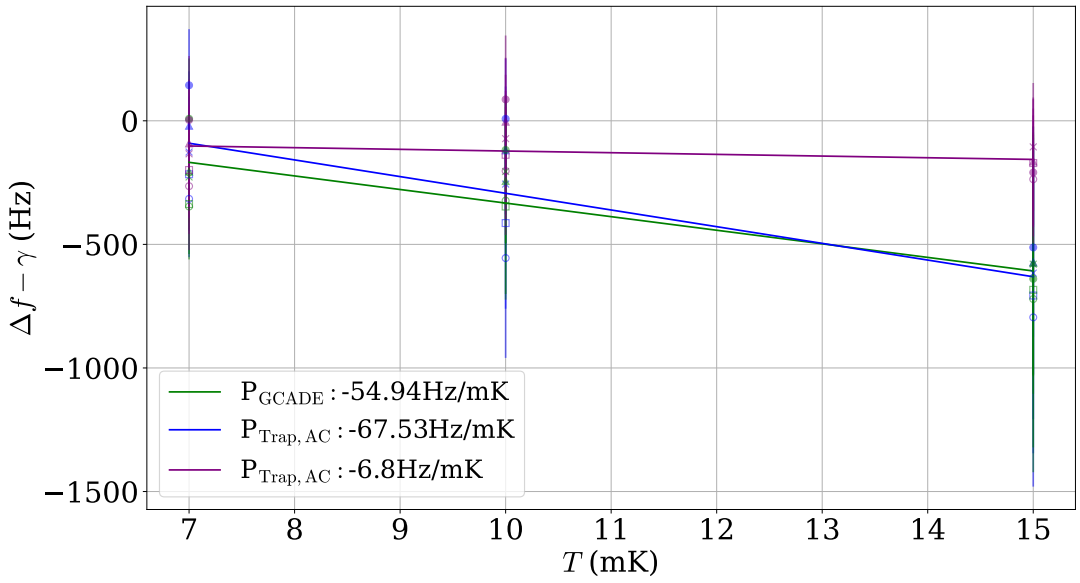

Fig. 8.14. Variation in Δf with assumed temperature T. [•, ▲, ×, ■, ○, □] represent [140, 170, 200, 240, 280] mW respectively. Error bars are derived from the covariance of the fit. Solid lines display linear regression of data points. Slopes are displayed in legend.

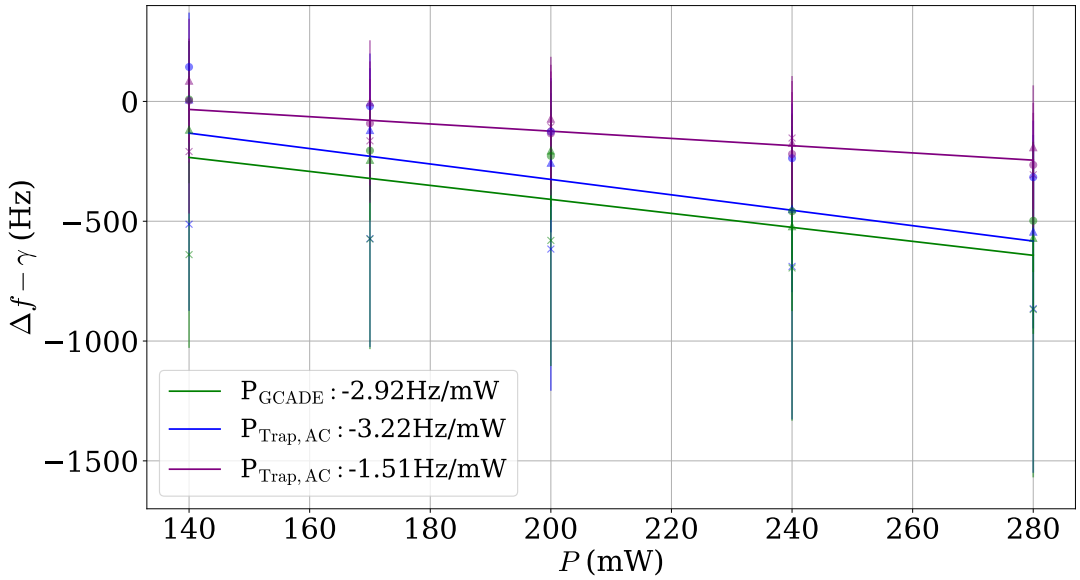

Fig. 8.15. Variation in Δf with assumed power P. [•, ▲, ×] represent [7, 10, 15] mK respectively. Error bars are derived from the covariance of the fit. Solid lines display linear regression of data points. Slopes are displayed in legend.

added degree of freedom in the fit could introduce other unknown uncertainties. The working group continues to investigate the validity of using these free physics-driven fits to extract the centre frequency of the 1S-2S spectra in ALPHA-2. Furthermore, the frequency uncertainties presented in table 8.1 depend on the uncertainties in T and P estimated in this section – as the analysis progresses we may be able to reduce these uncertainties. Another point to note is that because the shape of the spectra depends on T and P, then the spectra themselves could be viewed as an additional method to determine their values by comparison to simulation

Uncertainty	Estimated size (Hz)		
	P_{GCADE} (fixed)	$P_{Trap,\ AC}$ (fixed)	$P_{Trap,\ AC}$ (free)
Statistics	256	299	289
Temperature (10 ± 5 mK)	275	338	34
Power (200 ± 80 mW)	234	258	122

Table 8.1
Frequency uncertainties originating from fit to the spectrum

via the fixed-shape fits. Figure 8.16 displays a grid of the reduced χ^2 values for the fixed shape fits for all permutations of T and P simulated. As can be seen, the uncertainties of $T = 10 \pm 5$ mK and $P = 200 \pm 80$ mK correspond to the lower χ^2 values, indicating that these are good naive estimates for the ranges possible. However, it appears that there is some interplay between value of T and P which correspond to a good fit. The extra information in T and P which can be gleaned from the comparison to simulation could help to reduce their respective uncertainties.

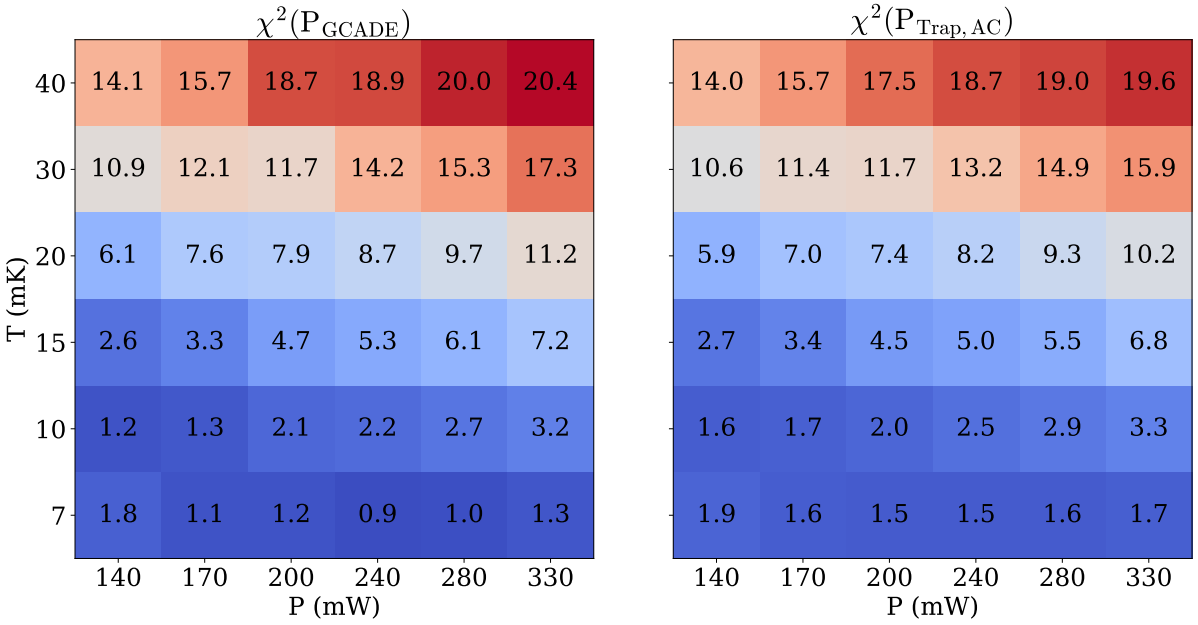

Fig. 8.16. Grid of reduced χ^2 values for the fixed shape fits for all permutations of T and P simulated, using the P_{GCADE} and $P_{Trap,\ AC}$ fixed shape fits. The free $P_{Trap,\ AC}$ fit has a reduced χ^2 of 1.74.

8.3 | Magnetic field uncertainties

The uncertainties originating from the magnetic field can be broadly split into two parts: the uncertainty in the magnetic field at the center of the trap and the uncertainty in the shape of the magnetic trap determined by modelling. The magnetic field at the center of the trap, B_0, is measured both before and after spectroscopy, and its uncertainty is dominated by the

magnetic field drifting in the intermediate time between these measurements. Determining the uncertainty originating from models of magnetic field shape is more complicated, and the exact procedure for doing so is still being discussed within the analysis working group. There are many elements which will likely be used to characterise this uncertainty, such as the magnetic field studies conducted in trails 69126, 69184 and 69290 which use different field configurations. However, analysis which involves these trails has not started and will not be discussed within this thesis, this thesis presents a method for estimating uncertainty due to magnetic field shape using perturbed field models.

8.3.1 Central Field drift

A measurement of the magnetic field in the centre of the trap, B_0, is taken a short time before spectroscopy via ECR, which defines the frequency from which the laser is detuned via equation 3.17. However, during spectroscopy the field of the external solenoid (Carlsberg magnet) drifts linearly; a second measurement is taken after spectroscopy to determine how much the field has drifted by. The two ECR measurements for trail 69026 are displayed in figure 8.17, along with the corresponding drift in $d-d$ transition frequency.

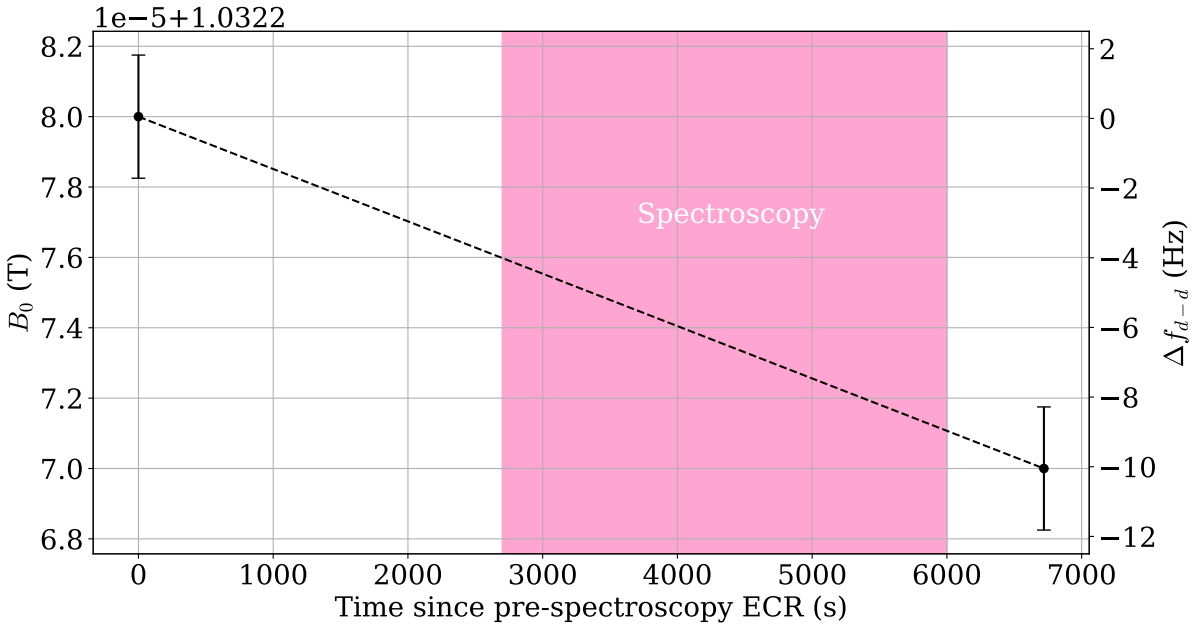

Fig. 8.17. The magnetic field at the center of the trap measured by ECR before and after spectroscopy. The shaded pink region denotes the period during which spectroscopy is taking place. The second axis displays how much the 1S-2S transition frequency changes between the two field measurements, determined using equation 3.17

Between the two ECR measurements taken before and after spectroscopy, B_0 is observed to have decreased by -1×10^{-5} due to linear drift of the Carlsberg field (Carlsberg field is well known to drift linearly with time at first order). This corresponds to a change in the $d-d$ transition frequency, Δf_{d-d}, of –10 Hz (5 Hz at 243 nm), which we take as a conservative estimate of the uncertainty in transition frequency caused by this effect. Less conservative

uncertainties could be taken by interpolating between the ECR measurements for the time that spectroscopy occurs.

8.3.2 Field model uncertainties

The simulation of 1S-2S spectroscopy relies on modelling of the magnetic trap to determine the dynamics of the trapped antihydrogen, and the effects of the magnetic trap on the shape of the spectrum. Errors in the magnetic field model may induce differences in the shape of the simulated spectrum, and those measured in the experiment, as an erroneous magnetic field model in the simulation will deform the shape of the spectra differently, as dicussed in section 3.5.1. To determine the accuracy of the magnetic field model, it can be compared to measurements of the on-axis field measured by ECR, which is displayed in figure 8.18. There is an observable difference between the on-axis magnetic field measured by ECR and the original field model from 2023, displayed by the dashed red line. ALPHA collaborator Francis Robicheaux produced an adapted field model in early 2024, by marginally shifting the location of the solenoids which make up the magnetic trap within the simulation. The adapted model, displayed by the black dashed line in figure 8.18, agrees more closely with the ECR measurements of the on-axis field, although there are still some noticeable discrepancies. How do we translate the uncertainty in the magnetic field model into a frequency uncertainty when comparing the simulated and experimentally determined 1S-2S spectrum? To estimate the size of this uncertainty, we study how small perturbations in the magnetic trap effects the shape of the simulated spectrum, and the value of f_ϵ resulting from the fit of the simulated spectrum. One possible route to do this is to run a large number of simulations, each with a different magnetic field which had been perturbed from the nominal field by roughly the same size as the discrepancies we observe between the model and ECR measurements. The spectra resulting from each of these simulations can then be fit with the lineshape functions (in the case of the physics-driven functions $B(z)$ would be set to the nominal field), the variation in the value of f_ϵ would provide an estimate of the frequency uncertainty originating from the magnetic field error. However, this method requires a large number of simulations to be run, which is computationally expensive; whilst it may be conducted for the full analysis, we present here is a quicker method which makes use of the physics-driven lineshape functions. The physics-driven functions take the on-axis field, $B(z)$, as a fixed parameter, which is usually set to the nominal adapted field model (displayed in black in figure 8.18). However, to account for the uncertainty in the magnetic field model, the value of $B(z)$ can be perturbed slightly. The physics-driven fit with the perturbed field can then be fit to the simulated spectrum, and the value of f_ϵ extracted. Repeating this process for many perturbed fields, the distribution of f_ϵ resulting from the perturbed field, which we will refer to as $f_{\epsilon,pert}$, provides an estimate of the uncertainty originating from magnetic field error. A sample of 1000 perturbed on-axis fields are displayed in amber in figure 8.18. The magnetic field model is used to produce these perturbed fields, by varying the magnet currents input into the field model by a random number drawn

from a Gaussian distribution centered at zero with a standard deviation equal to 0.5% of the nominal current. Figure 8.18 displays the absolute size of these perturbed fields compared to the nominal model, figure 8.19 displays the same on-axis fields, but with the center field, B_0, subtracted to highlight how the shape of the field has been perturbed. The perturbation in shape of the field is the effect we are investigating in this study, as the absolute value of B_0 is accounted for by the ECR pre-spectroscopy as discussed in the previous section 8.3.1.

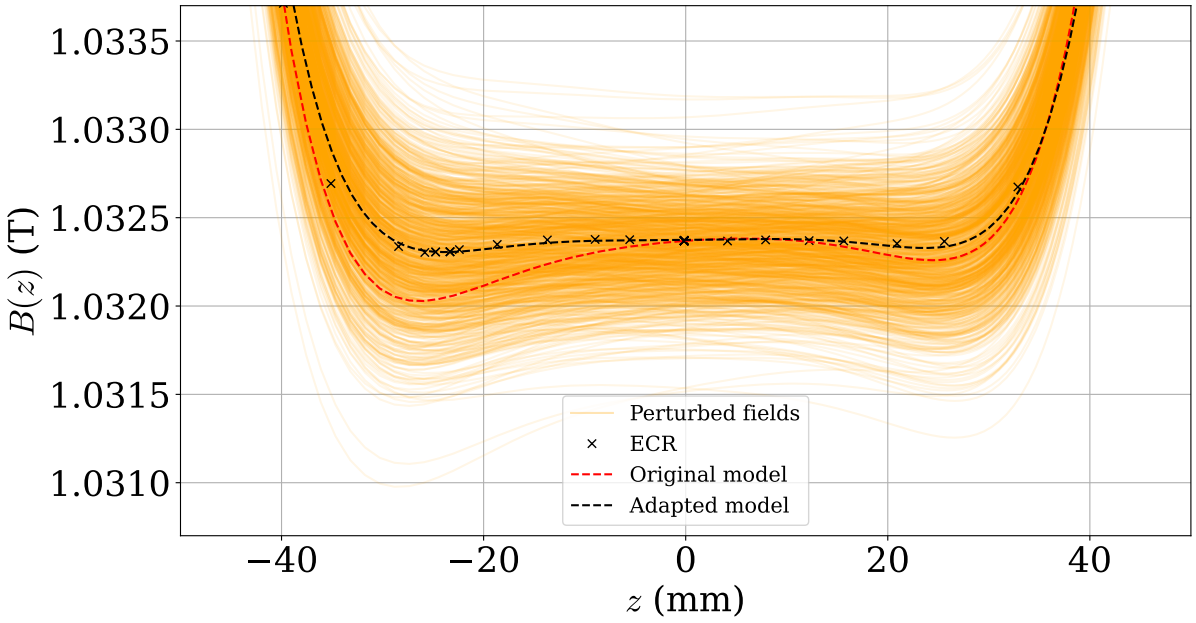

Fig. 8.18. The on-axis magnetic field $B(z)$ predicted by the original (red) and adapted (black) field models in the flat region of the magnetic trap, shown alongside ECR (black crosses) measurements of field. The perturbed fields used for estimating the uncertainty associated with field model error are displayed in semi-transparent amber.

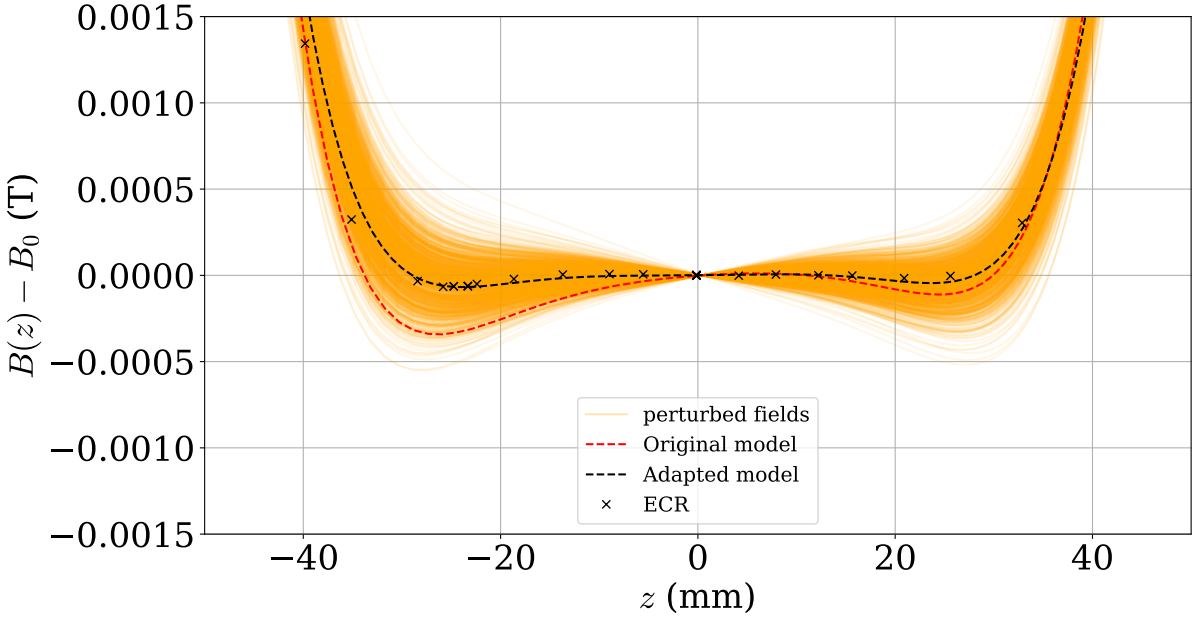

Fig. 8.19. The same field models as in figure 8.18, with the central field $B_0 = B(z = 0)$ subtracted, to highlight the shapes of the field models.

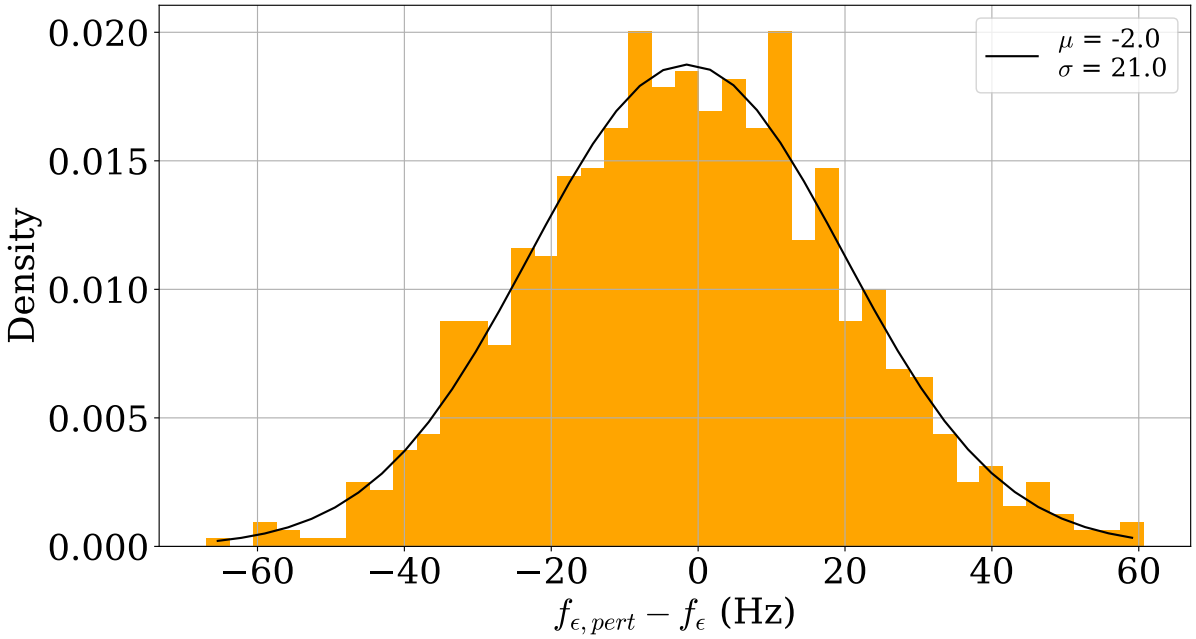

Fig. 8.20. Histogram of $f_{\epsilon,pert}$ generated by fitting the simulated spectrum ($T = 10\,\text{mK}$ and $P = 200\,\text{mW}$) with $\text{P}_{\text{trap, AC}}$, where the perturbed fields displayed in figure 8.18 provide the magnetic field, $B(z)$, encoded into the fitting function. The histogram has been fit with a normal distribution, displayed in black.

The value of 0.5% was chosen for the perturbation of the magnet currents, as it results in a variation of perturbed field shapes which is larger than the discrepancy seen between the adapted field model and the ECR measurements, and roughly the same size as the difference between the original and adapted field models. This choice was made by eye and is probably overestimate of the uncertainty. If a similar method is employed in the final analysis, the size of the perturbation should be determined more rigorously. Each perturbed on-axis field is then used as the value of $B(z)$ in the physics-driven function, which is fit to the simulated spectra to extract many values of $f_{\epsilon,pert}$. The physics driven function used in this study is $\text{P}_{\text{trap, AC}}$, which is fit to the simulated spectra with temperature and laser powers of $T = 10\,\text{mK}$ and $P = 200\,\text{mW}$. The distribution of the 1000 values of $f_{\epsilon,pert}$ produced via this method are displayed in figure 8.20, with the value of f_ϵ resulting from the nominal field model subtracted. The variation in $f_{\epsilon,pert}$ appears to be normally distributed, with a standard deviation of 21 Hz, which we take as the estimate of frequency uncertainty which originates from errors in magnetic field model.

8.4 | Laser-frequency stability

The uncertainty in laser frequency during spectroscopy can be split into two parts: The frequency error of the hydrogen maser and the stability of the laser system during spectroscopy. The maser frequency error is determined using the caesium fountain, and double checked with PPP, as described in chapters 5 and 4. The maser was allowed to freely drift during the 1S-2S

spectroscopy campaign; the fractional frequency error as measured by the fountain and PPP for this period is displayed in the top plot of figure 8.21, binned hourly. The two measurement methods agree, which indicates that the fountain is functioning correctly during spectroscopy. The associated Allan deviation for this period is displayed in the bottom plot of 8.21. The

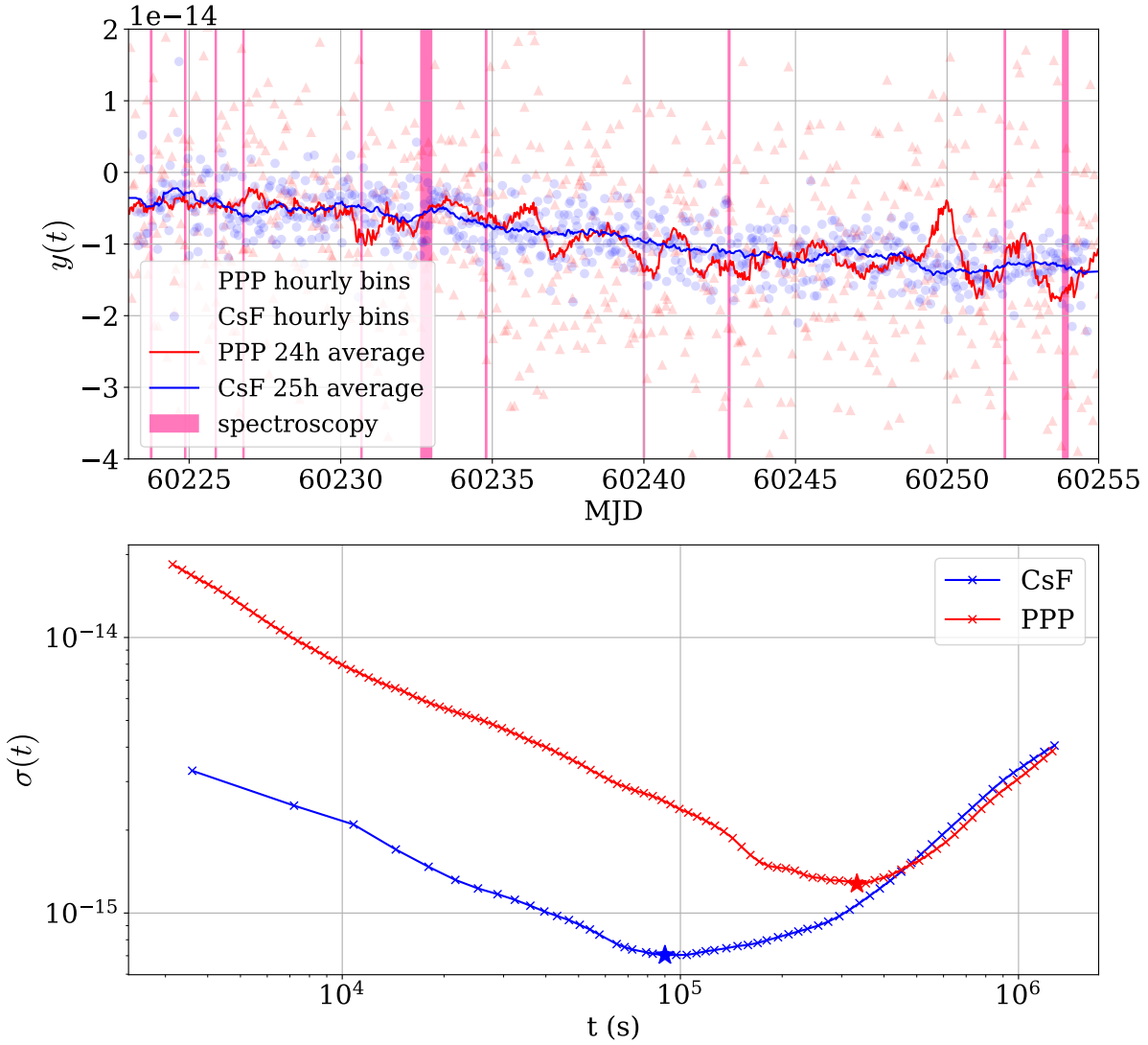

Fig. 8.21. **Top:** Fractional frequency error of the hydrogen maser during the 1S–2S experimental campaign conducted in 2023. Semi-transparent blue dots and red triangles display hourly measurements by the caesium fountain (CsF) and PPP respectively. The blue and red lines display a 25 and 24 hour rolling average of the CsF and PPP hourly bins, which are the minima of the Allan deviations (bottom) and represent the best knowledge of $y(t)$ determined by these two methods. The pink shaded regions denote periods when spectroscopy is occurring, with the cyan shaded region denoting trial 69026 specifically. **Bottom:** Allan deviations of the data in the top plot. Stars indicate the location of the minimum Allan deviation, which determines our best knowledge of the maser frequency error, and the period of the rolling averages used in the top plot.

minimum Allan deviation determines the precision to which we can know the maser frequency; the minimum occurs at 25 hours, and has an value of of $7{\times}10^{-16}$ for the measurement of the caesium fountain. A 25 hour rolling average is displayed on the top plot of Figure 8.21,

which represents our best knowledge of the maser frequency. During experimental trial 69026 the fractional frequency error of the maser is equal to $(-2.8 \pm 0.7) \times 10^{-15}$. This corresponds to a correction of -3.5 Hz at 243 nm with an uncertainty of 3.5 Hz, assuming a conservative estimate that frequency error doubles at each doubling stage.

The stability of our laser system during spectroscopy can be determined by looking at the Allan deviations for the 1S-2S laser system during the 24 hours which include experimental trial 69026, displayed in figure 8.22. During trial 69026, the $\bar{H}$ sample are exposed to 1760 s

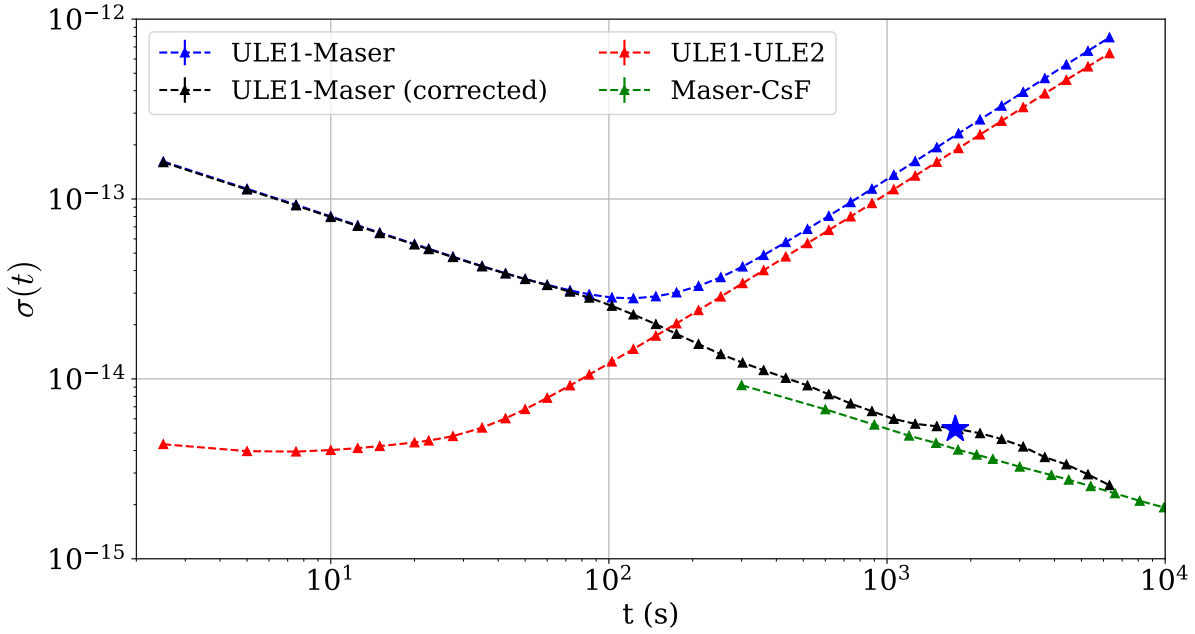

Fig. 8.22. Allan deviations for 1S-2S laser system on the day trail 69026 took place. Red displays the short term stability of our laser, determined via the beatnote between ULE1 and ULE2. Blue displays the measurement of the frequency of ULE1, compared to the maser via the frequency comb. Black displays the corrected comb measurement, which indicates the total stability of our laser system (discussed in section 6.1.3). Green displays the stability of our maser, which indicates the lower limit to which we can know out laser frequency. The blue star displays the stability of the laser system at 1760 s of averaging time (the total laser exposure in trial 69026), which corresponds to $\sigma = 5.4 \times 10^{-15}$. Note, this figure is not the same as figure 6.8, which is the stability of the laser as measured over a prolonged period, whereas this figure is stability of the laser in the day that 69026 took place. This Allan deviation has marginally lower short term stability, resulting from temperature fluctuations in the lab due to the laser cooling laser, which effect the ULE performace.

of laser light, this corresponds the the stability indicated by the blue star in figure 8.22, which is equal to a fractional frequency uncertainty of 5.4×10^{-15} at 972 nm. Using the conservative estimate that the frequency error doubles at each doubling stage, this is equal to 2.16×10^{-14} at 243 nm, which is equal to 27 Hz.

8.5 | Notes on this chapter

In this chapter we have introduced some of the fitting functions and procedures which are currently being discussed within the analysis group. We have applied some of these fitting procedures to experimental trial 69026, and estimated the frequency uncertainty arising from the fitting procedure. We have also highlighted the extra frequency uncertainties which arise from the uncertainty in trapped $\bar{H}$ temperature and circulating laser power during spectroscopy. Taking some conservative estimates of the uncertainty in power and temperature, we have produced estimates of the additional frequency uncertainty from the fit. This thesis has also made estimates of the frequency uncertainties arising from magnetic trap drift and modelling errors, and the stability of the laser. A summary of all of these uncertainties is given in table 8.2, alongside a total where the components are added in quadrature. It is important to note that the items in table 8.2 is not a comprehensive list of all the uncertainties; many more uncertainties will have to be estimated.Also, this chapter has only analysed the results of trail 69026, and the analysis of the other experimental trials may help to reduce statistical uncertainty and better constrain sources of systematic uncertainty.

Uncertainty	**Estimated size (Hz)**		
	P_{GCADE} (fixed)	**$P_{Trap,\ AC}$ (fixed)**	**$P_{Trap,\ AC}$ (free)**
Statistics	256	299	289
Temperature (10 ± 5 mK)	275	338	34
Power (200 ± 80 mW)	234	258	122
Carlsberg drift	5	5	5
Trap modelling	21	21	21
Reference error	3.4	3.4	3.4
Laser stability	27	27	27
Total	444	521	317

Table 8.2
The statistical and systematic errors which have been estimated in this chapter (at 243 nm). Uncertainties in temperature and power mostly represent out current poor knowledge in the value of these parameters, and is likely to reduce as further analysis is conducted to estimate their values.

This chapter was written to expose the reader to the sort of methods which can be used to determine the 1S-2S transition frequency, and how the associated uncertainties could be determined. All of the analysis methods have been applied to spectra determined from the passed cuts (see Section 2.2.4), and the final analysis which will be presented will determine the transition frequency from a spectra produced by a more rigorous multivariate analysis. As this analysis progresses within the working group, some of the methods described here may be applied for this final analysis, whereas others may not. There are many decisions to be made, a central one of these being which lineshape function to use, and whether or not to fix its shape via the simulation. It should also be noted that the functions described

in equations 8.1 - 8.4 are not the full list of lineshape functions being considered. An extra physics-driven lineshape function, developed by Levi Oliveira de Araujo Azevedo and Claudio Cesar, is also being considered as an option. This physics driven lineshape function bares similarity to $P_{Trap,\ AC}$, but with some subtle differences.

CHAPTER 9

Conclusion and outlook

> *That's it, turn the page on the day, walk away*
>
> — **Mike Skinner**
> The Streets

Antihydrogen research is a relatively new field of experimental study – yet, despite the relative infancy, the field has advanced at a remarkable pace. Specifically, there has been significant advancement in measuring the 1S-2S transition of antihydrogen since its first measurement in 2017, depicted in figure 9.1, alongside equivalent measurements made with hydrogen. This thesis summarises the work towards pushing the precision of 1S-2S spectroscopy with antihydrogen even further than any previous measurement.

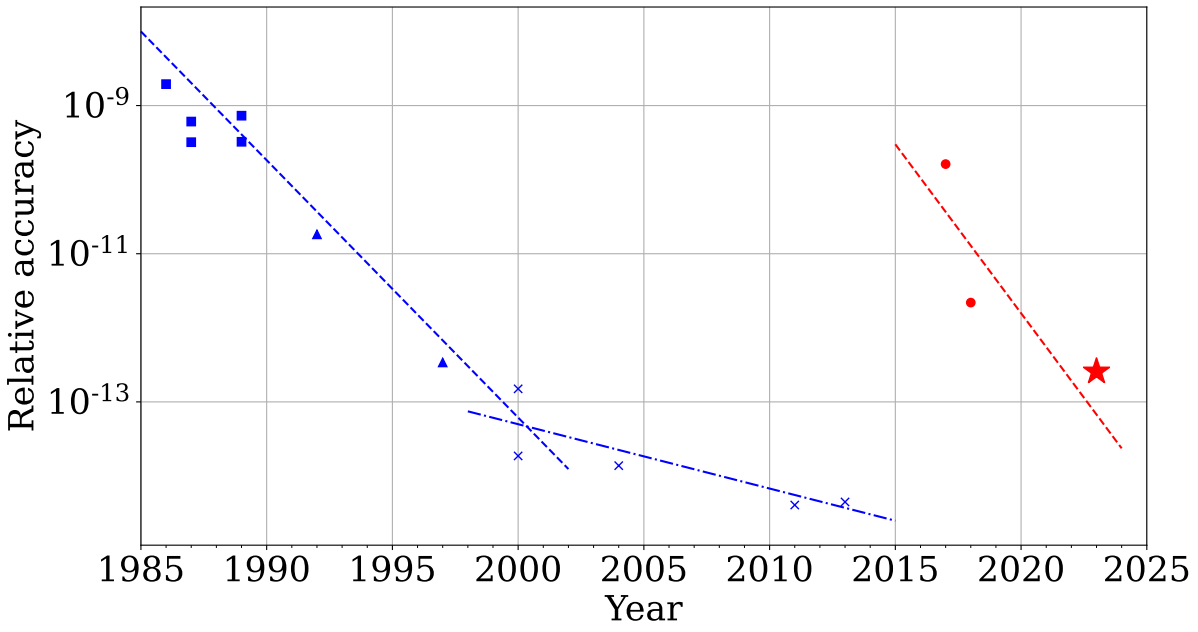

Fig. 9.1. Progression of 1S-2S spectroscopy measurements with hydrogen (blue squares) and antihydrogen (red circles). The red star represents the precision estimated from the analysis with $P_{\text{Trap, AC}}$(free) in chapter 8. Figure was taken and adapted from [146]. Superimposed are (exponential) lines of best fit.

A major focus of this PhD has been upgrading the frequency metrology capabilities at the ALPHA experiment to improve the stability and accuracy of the 243 nm laser system, enabling

high precision 1S-2S spectroscopy of antihydrogen in ALPHA. The metrology upgrades have involved two major developments. Firstly, the integration of an active hydrogen maser and the application of GNSS time-frequency transfer methods to track the evolution of frequency error in the maser, discussed in chapter 4. The GNSS methods contained within this thesis allow the maser frequency error to be determined by comparison to frequency standards maintained by other metrology laboratories with a fractional frequency precision of 1.66×10^{-15} after 3.75 days averaging time. The second major upgrade involved the commissioning of a caesium fountain clock primary standard to serve as a primary reference to the SI second for antihydrogen spectroscopy, discussed in chapter 5. This is the first caesium fountain deployed permanently to serve as a reference for spectroscopy outside of a national metrology institute. The caesium fountain is able to determine the frequency error on the maser with a fractional frequency precision of 1×10^{-15} with less than 3 hours averaging time – far quicker than the GNSS methods. The long term stability of the fountain was determined through GNSS comparisons with other fountains, and has been evaluated to 6.39×10^{-16}, which represents its ultimate precision as an instrument. The ultimate goal of these metrology upgrades, to improve the stability of the 1S-2S laser system, is discussed in Chapter 6. The metrology upgrades have improved the frequency stability of the laser system by around a factor of twenty. Better control of our frequency chain means that, with proper operation and a long enough averaging time, the precision to which we can determine our laser frequency can average down until it reaches the limit set by the fountain.

The latter chapters of this thesis detail the experimental campaigns aimed at improving the precision of the 1S-2S transition measured in antihydrogen. The experimental campaigns, discussed in chapter 7, benefited from the metrology upgrades outlined in this thesis, in addition to other methods that help to improve the precision of the 1S-2S measurement, including laser cooling and beryllium-assisted antihydrogen production. At the time of measurement, the 2023 experimental campaign resulted in the narrowest 1S-2S spectra ever measured in antihydrogen. The analysis to establish the ultimate precision of the 2023 experimental campaign is still ongoing. A preliminary analysis, detailed in chapter 8, suggests a precision on the order of hundreds of Hertz – a more precise measurement of the 1S-2S transition than any of the previous efforts.

However, it is expected that even the measurements from the 2023 experimental campaign will be surpassed in precision in the near future. Work is currently underway to produce even colder samples of antihydrogen through the combination of laser cooling and adiabatic expansion, which will likely result in an even narrower 1S-2S spectrum. Fortunately, the metrology upgrades detailed in this thesis have 'future-proofed' the stability of the laser system. The potential frequency stability of the laser system, dictated by the precision of the fountain, should be able to accommodate for far more precise spectroscopy measurements in the future. Additionally, further work could be undertaken to better evaluate the remaining uncharacterised sources of systematic uncertainty in the fountain, potentially pushing its precision to the low 10^{-16} region, enabling even more precise spectroscopy. While the spectrum of antihydrogen is

an important experimental measurement in its own right, the main motivation for its study is to test CPT symmetry by comparing it with the hydrogen spectrum. As can be seen in figure 9.1, considerable progress has been made with the 1S-2S spectrum of antihydrogen, yet its precision significantly lags behind that of hydrogen. The measurements made in this thesis, and the measurements made in the coming years, will likely close this gap. However, it is also likely that the comparison between the two systems might eventually be constrained by the distinct, hard-to-characterise, systematics inherent in both experiments—-a limit already being reached with hydrogen. One logical pathway to overcome this limit is to push towards direct comparisons between hydrogen and antihydrogen within the same experimental setup. There are many proposals for methods to load cold hydrogen into ALPHA, which are described in [147, 148]. Initial experiments have already demonstrated the principle of detecting 1S-2S transitions via antiproton recapture, mentioned in section 3.6.2; this method could also be applicable to hydrogen spectroscopy. Through direct comparisons of hydrogen and antihydrogen experiments within ALPHA, many of the systematic sources of uncertainty will be common-mode, allowing CPT symmetry tests that nearly systematic free. It is possible that these direct comparisons could surpass the precision of the 1S–2S spectroscopy measurements made with hydrogen.

APPENDIX A

Derivation of two-photon lineshape

A.1 | Transit time limited two photon excitation

The $1S$ state is excited to the $2S$ state through an intermediate virtual nP state. To evaluate such a process, a standard tool to use is second-order time-dependent perturbation theory. The perturbing Hamiltonian due to the laser light in the build-up cavity which induces the transition is $H_I(t) = e\vec{r}\cdot\vec{E}(t)$. Given that $\langle 2S|\, H_I\, |1S\rangle = 0$ due to electric dipole transition selection rules, and assuming that the atom is initially in the $1S$ state ($C_{1S}(0) = 1$) the transition amplitude can be calculated using:

$$C_{2S}^{(2)}(t) = \frac{-1}{\hbar^2}\sum_n \int dt''\, \langle 2S|\, H_I\left(t''\right)|nP\rangle\, e^{i\omega_{2SnP}t''} \underbrace{\int dt'\, \langle nP|\, H_I\left(t'\right)|1S\rangle\, e^{i\omega_{nP1S}t'}}_{I_1} \tag{A.1}$$

Where $\omega_{2SnP} = E_{2S}/\hbar - E_{nP}/\hbar$ and $\omega_{nP1S} = E_{np}/\hbar - E_{1S}/\hbar$. The perturbing hamiltonian comes from the standing wave electirc field produced by the gaussian beam within the build up cavity, which has the form

$$\vec{E}(t) = \hat{\epsilon}E_0\left[w_0/w(z)\right]\exp\left[-r^2/w^2(z)\right]\cos[kz]\cos\left(\omega_{\mathrm{L}}t\right) \tag{A.2}$$

Where $\hat{\epsilon}$ is the polarisation of the lasers, w_0 is the minimum beam waist which occurs at the center of the cavity, $w(z) = \sqrt{w_0^2\left(1 + z^2/Z_{\mathrm{R}}^2\right)}$ is the z dependent beam waist, and ω_L is the angular frequency of the laser ($2\pi f_L$). Substituting this into the interaction Hamiltonian we can evaluate the first integral, I_1, using the rotating wave approximation

$$I_1 = -i\hbar\frac{E_0 w_0 e^{-r^2/w^2}}{2w}\cos(kz)\frac{\langle nP|\,\hat{\epsilon}\cdot\vec{r}\,|1S\rangle}{\hbar\omega_{nP1S} - \hbar\omega_{\mathrm{L}}}\mathrm{e}^{\mathrm{i}(\omega_{nP1S}-\omega_{\mathrm{L}})t''} \tag{A.3}$$

This can be substituted into equation A.1, and rearranged to give

$$\begin{aligned} C_{2S}^{(2)}(t) &= \frac{-iE_0^2 w_0^2}{8\hbar w^2}\sum_n \int dt'' e^{-2r^2/w^2}\frac{\langle 2S|\,\hat{\epsilon}\cdot\vec{r}\,|nP\rangle\,\langle nP|\,\hat{\epsilon}\cdot\vec{r}\,|1S\rangle}{\hbar\omega_{nP1S} - \hbar\omega_{\mathrm{L}}} e^{i(\omega_{2S1S}-2\omega_L)t''}\, dt'' \\ &= \frac{-i\xi E_0^2 w_0^2}{\hbar w}\int e^{-r^2/w^2} e^{i(\omega_{2S1S}-2\omega_L)t''}\, dt'' \end{aligned} \tag{A.4}$$

Where the rotating wave approximation has been used. Furthermore $\cos^2(kz) = 1/4(e^{2ikz} + e^{-2ikz} + 2) \longrightarrow 1/2$ as the $e^{\pm 2ikz}$ terms are set to zero as the Doppler shift pushes them far off resonance. The value of ξ can be calculated from a sum of nP states within a box of radius $30a_0$, which is big enough such that ξ becomes independent of r. This is approximated as [81]

$$\xi = -\frac{e^2}{8} \sum_n \frac{\langle 2S| \hat{\epsilon} \cdot \vec{r} |nP\rangle \langle nP| \hat{\epsilon} \cdot \vec{r} |1S\rangle}{\hbar\omega_{nP1S} - \hbar\omega_{\mathrm{L}}} \simeq 12.3\varepsilon_0 a_0^3. \tag{A.5}$$

To evaluate the integral given in A.4, we should consider how r varies with t. Taking the assumption that the magnetic field is constant over the beam waist, such that the $\bar{H}$ traverse that laser with a constant velocity perpendicular velocity $v_\perp$. In the vicinity of the laser waist the radial coordinate therefore varies as $r^2(t) = \rho^2 + v_\perp^2 t$, which is visually evident from figure A.1, which has been taken from [86]. This can be substituted into equation A.4, and integral

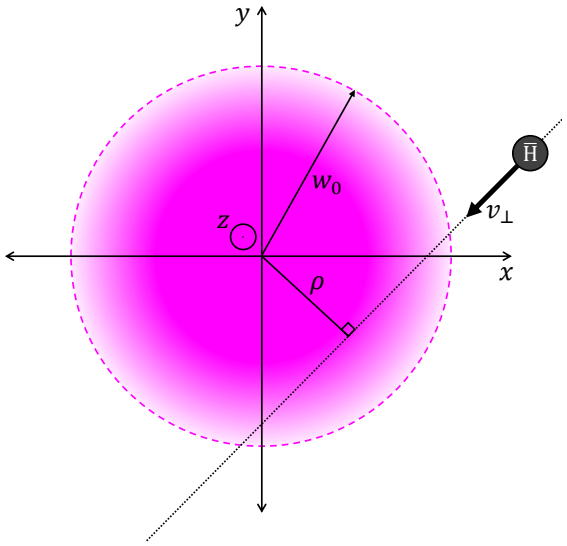

Fig. A.1. Motion of antihydrogen in $x-y$ plane as it traverses the laser beam. The $\bar{H}$ are outside the beam at $t = -\infty$. The light field grows as it moves towards the beam, passing at its distance of closes approach of the beam axis ρ at $t = 0$. Following this the light field diminishes again as the atom moves away.

evaluated between $-\infty$ and $+\infty$, which emulates the change of states during one pass of the laser

$$\begin{aligned} C_{2S} &= \frac{-i\xi w_0^2}{\hbar w^2} E_0^2 \mathrm{e}^{-2\rho^2/w^2} \int_{-\infty}^{\infty} \mathrm{e}^{-2v_\perp^2 t^2/w^2} \mathrm{e}^{-i(\omega_{2S1S} - 2\omega_L)t} dt \\ &= \frac{-i\xi w_0^2}{\hbar w v_\perp} E_0^2 \mathrm{e}^{-2\rho^2/w^2} \sqrt{\frac{\pi}{2}} \mathrm{e}^{-\frac{(\omega_{2S1S} - 2\omega_L)^2 w^2}{8v_\perp}} \end{aligned} \tag{A.6}$$

Given that $E_0^2 = 8I_0/(\varepsilon_0 c)$, this can be squared to find the probability of excitation of exciting the $1S-2S$ transition with two counter propagating photons during one pass of the laser.

This is given by

$$P_{2S}(f_0|v_\perp,\rho,z) = |C_{2S}|^2 = 32\pi\frac{\xi^2 I_0^2}{\hbar^2\varepsilon_0^2 c^2}\frac{w_0^4}{w(z)^2 v_\perp^2}e^{-4\rho^2/w^2}e^{-\left[2\pi w(f_L-f_0)/v_\perp\right]^2} \tag{A.7}$$

where $f_0 = \omega_{2S1S}/4\pi = (E_{2S}-E_{1S})/2h$. The assumptions so far have been that the laser is monochromatic, which is a valid assumption is that linewidth of the laser is much narrower than the transit time broadened linewidth. In the case that the laser has a substantial linewidth, then we must convolve equation A.7 with the spectrum of the laser.

The expression given in equation A.7 is for one $\bar{H}$ with perpendicular velocity $v_\perp$, during a single pass of the laser. To determine excitation rate of the entire ensemble of trapped atoms, $\bar{P}_{2S}$ we must multiply by the flux of atoms of a specific $v_\perp$ passing through the laser and integrate over position and perpendicular velocity [36].

$$\bar{P}_{2S} = \int_{z_{min}}^{z_{max}} dz \int_0^\infty d\rho \int_0^\infty dv_\perp 2v_\perp n_{2D}(z) f(v_\perp) P_{2S}(f_0|v_\perp,\rho,z) \tag{A.8}$$

Where the flux of a $\bar{H}$ with velocity is given by $v_\perp$ is $2f(v_\perp)v_\perp n_{2D}(z)$ - where $f(v_\perp)$ is the probability distribution of $v_\perp$, and $n_{2D}(z)$ is the 2D cross-sectional density, which varies along z. The factor of 2 arises because the $\bar{H}$ can pass through either side of the beam.

$$\begin{aligned}
&= 64\pi\frac{\xi^2 I_0^2}{\hbar^2\varepsilon_0^2 c^2}\int_{z_{min}}^{z_{max}} dz \int_0^\infty d\rho \frac{w_0^4}{w(z)^2}e^{-4\rho^2/w^2}\int_0^\infty dv_\perp \frac{2n_{2D}(z)f(v_\perp)}{v_\perp}e^{-\left[2\pi w(f_L-f_0)/v_\perp\right]^2}\\
&= 64\pi\frac{\xi^2 I_0^2}{\hbar^2\varepsilon_0^2 c^2}\int_{z_{min}}^{z_{max}} dz \frac{w_0^4\sqrt{\pi}}{2w(z)}n_{2D}(z)\int_0^\infty dv_\perp \frac{f(v_\perp)}{v_\perp}e^{-\left[2\pi w(f_L-f_0)/v_\perp\right]^2}
\end{aligned} \tag{A.9}$$

For the axial length that the $\bar{H}$ are confined, from z_{min} to z_{max} we can assume that the laser waist does not vary significantly; $w(z_{min} < z < z_{max}) \approx w_0$. As a result we write

$$\bar{P}_{2S} = 32w_0^3\pi\sqrt{\pi}\frac{\xi^2 I_0^2}{\hbar^2\varepsilon_0^2 c^2}\bar{n}_{2D}\int_0^\infty dv_\perp \frac{f(v_\perp)}{v_\perp}e^{-\left[2\pi w_0(f_L-f_0)/v_\perp\right]^2} \tag{A.10}$$

Where $\bar{n}_{2D}$ is the average cross sectional density of atoms in the trap. If we consider a 2D Maxwell-Boltzman velocity distribution $f(v_\perp) = 2v_\perp/u^2\exp\left(-v_\perp^2/u^2\right)$ where $u^2 = 2k_B T/m$ for the $\bar{H}$ when we can evaluate the velocity integral

$$\bar{P}_{2S} = \sqrt{\pi}\frac{32\pi w_0^3}{u^2}\frac{\xi^2 I_0^2}{\hbar^2\varepsilon_0^2 c^2}\bar{n}_{2D}\int_0^\infty dv_\perp \exp\left(-\left[\frac{2\pi w(f_L-f_0)}{v_\perp}\right]^2 - \frac{v_\perp^2}{u^2}\right) \tag{A.11}$$

$$\bar{P}_{2S} = \chi\exp\left(\frac{-4\pi w_0|f_L-f_0|}{u}\right) \tag{A.12}$$

where

$$\chi = \frac{16\pi^2 w_0^3}{u}\frac{\xi^2 I_0^2}{\hbar^2\varepsilon_0^2 c^2}\bar{n}_{2D} \tag{A.13}$$

A.2 | AC stark shift approximation

If we start with equation A.9

$$\bar{P}_{2S} = 64\pi \frac{\xi^2 I_0^2}{\hbar^2 \varepsilon_0^2 c^2} \int_{z_{min}}^{z_{max}} dz \int_0^\infty d\rho \frac{w_0^4}{w(z)^2} e^{-4\rho^2/w^2} \int_0^\infty dv_\perp \frac{2n_{2D}(z) f(v_\perp)}{v_\perp} e^{-\left[2\pi w (f_L - f_0)/v_\perp\right]^2} \tag{A.14}$$

Evaluate the z integral, as done in equations A.9, but leave the ρ integral unevaluated.

$$\bar{P}_{2S} = 32 w_0^3 \pi \frac{\xi^2 I_0^2}{\hbar^2 \varepsilon_0^2 c^2} \bar{n}_{2D} \int_0^\infty d\rho e^{-4\rho^2/w^2} \int_0^\infty dv_\perp \frac{f(v_\perp)}{v_\perp} e^{-\left[2\pi w_0 (f_L - f_0)/v_\perp\right]^2} \tag{A.15}$$

Now, we know from equation 3.25, that the AC stark shift of the 1S-2S frequency is given by

$$f_{AC}(\rho, v_\perp, t) = 1.667 \times 10^{-4} \frac{4P\beta_{AC}}{\pi w_0^2} e^{-2r^2/w_0^2} = f_{AC_+} \exp\left(\frac{-2v_\perp^2 t^2 - 2\rho^2}{w_0^2}\right) \tag{A.16}$$

To simplify the situation, we integrate out the t variable and approximate the AC stark shift as the mean AC stark shift over one pass of the laser. Since we are only interested in AC stark shift of antihydrogen that gets excited to the 2S state, we determine the mean AC stark shift by integrating f_{AC} over the t dependent probability density function for excitation, $p_{2S}(t)$ during one pass over the laser. This gives

$$f_{AC_+} = 1.667 \times 10^{-4} \frac{4P}{\pi w_0^2} \tag{A.17}$$

$$f_{AC}(\rho, v_\perp) \approx f_{AC_+} \exp\left(\frac{-2\rho^2}{w_0^2}\right) \int_{-\infty}^{\infty} \exp\left(\frac{-2v_\perp^2 t^2}{w_0^2}\right) p(t) dt \tag{A.18}$$

Considering that excitation is proportional to power squared, and the power exposed to the antihydrogen is proportional to $\exp\left(-2v_\perp^2 t^2/w_0^2\right)$, the normalised t dependent probability density function for excitation during one pass of the laser is given by

$$p(t) = \frac{2v_\perp}{\sqrt{\pi} w_0} \exp\left(\frac{-4v_\perp^2 t^2}{w_0^2}\right) \tag{A.19}$$

Substituting this into equation A.18, and evaluating the integral gives

$$f_{AC}(\rho) \approx \sqrt{\frac{2}{3}} f_{AC_+} \exp\left(\frac{-2\rho^2}{w_0^2}\right) \tag{A.20}$$

This has the added benefit of cancelling out $v_\perp$, which means the only remaining varibale which f_{AC} depends on is ρ. Equation A.20 can then be rearranged to find

$$\rho = \frac{w_0}{\sqrt{2}}\sqrt{\log\left(\frac{\sqrt{\frac{2}{3}}f_{AC_+}}{f_{AC}}\right)} \rightarrow \frac{d\rho}{df_{AC}} = -\frac{w_0}{2\sqrt{2}}\frac{1}{f_{AC}}\sqrt{\log\left(\frac{\sqrt{\frac{2}{3}}f_{AC_+}}{f_{AC}}\right)} \tag{A.21}$$

We can then insert f_{AC} by hand into equation A.15 as a shift on f_0. f_0 is the frequency of the 243 nm light, whereas f_{AC} is in units of 121 nm, so the shift to f_0 is $f_{AC}/2$ at 243 nm. This is gives

$$P_{AC} = 32w_0^3\pi\frac{\xi^2 I_0^2}{\hbar^2\varepsilon_0^2c^2}\bar{n}_{2D}\int_0^\infty d\rho e^{-4\rho^2/w^2}\int_0^\infty dv_\perp\frac{f(v_\perp)}{v_\perp}e^{-\left[2\pi w_0(f_L-f_0-f_{AC}/2)/v_\perp\right]^2} \tag{A.22}$$

The rho integral can then be written in terms of f_{AC} by substituting in equations A.20 and A.21, giving

$$\int_0^\infty d\rho e^{-4\rho^2/w^2} = \int_0^{\sqrt{\frac{2}{3}}f_{\mathrm{AC}_+}} df_{AC}\frac{w_0}{2\sqrt{2}}\frac{f_{AC}}{(\sqrt{\frac{2}{3}}f_{\mathrm{AC}_+})^2\sqrt{\log\left(\frac{\sqrt{\frac{2}{3}}f_{AC_+}}{f_{AC}}\right)}} \tag{A.23}$$

which can be substituted into equation A.22 to give

$$P_{AC} = 32w_0^3\pi\frac{\xi^2 I_0^2}{\hbar^2\varepsilon_0^2c^2}\bar{n}_{2D}\int_0^{\sqrt{\frac{2}{3}}f_{\mathrm{AC}_+}} df_{AC}\frac{w_0}{2\sqrt{2}}\frac{f_{AC}}{(\sqrt{\frac{2}{3}}f_{\mathrm{AC}_+})^2\sqrt{\log\left(\frac{\sqrt{\frac{2}{3}}f_{AC_+}}{f_{AC}}\right)}}\int_0^\infty dv_\perp\frac{f(v_\perp)}{v_\perp}e^{-\left[2\pi w_0(f_L-f_0-f_{AC}/2)/v_\perp\right]^2} \tag{A.24}$$

Evaluating the $v_\perp$ integral as previously gives

$$P_{AC} = \frac{\chi}{\sqrt{\pi}}\int_0^{\sqrt{\frac{2}{3}}f_{\mathrm{AC}_+}} df_{AC}\frac{w_0}{2\sqrt{2}}\frac{f_{AC}}{(\sqrt{\frac{2}{3}}f_{\mathrm{AC}_+})^2\sqrt{\log\left(\frac{\sqrt{\frac{2}{3}}f_{AC_+}}{f_{AC}}\right)}}\exp\left(\frac{-4\pi w_0\left|f_L-f_0-f_{AC}/2\right|}{u}\right) \tag{A.25}$$

The f_{AC} integral cannot be evaluated analytically, but it can be numerically. This lineshape function can be combined with the a further magnetic field integral, to produce the physics-driven lineshape function discussed in section 3.7.

$$P_{\text{trap, AC}} = \chi'' \int_0^{\sqrt{\frac{2}{3}} f_{\mathrm{AC_+}}} \frac{w_0}{2\sqrt{2}} \frac{f_{AC}}{(\sqrt{\frac{2}{3}} f_{\mathrm{AC_+}})^2 \sqrt{\log\left(\frac{\sqrt{\frac{2}{3}} f_{AC_+}}{f_{AC}}\right)}} df_{AC} \tag{A.26}$$
$$\int_{z_{\min}}^{z_{\max}} \exp\left(\frac{-\mu_B \left(B(z) - B_0\right)}{k_B T}\right) \exp\left(\frac{-4\pi w_0 \left|f_L - f_0(z) - f_{AC}/2\right|}{u}\right) dz$$

APPENDIX B

PPP

The pseudorange and carrier-phase observable equations for satellite S are given by:

$$P_R^S = \underbrace{\sqrt{\left(x - x^S\right)^2 + \left(y - y^S\right)^2 + \left(z - z^S\right)^2} + c\left(dt - dt^S\right) + Mzpd}_{P_C^R(x,y,z,dt,zpd)} + \varepsilon_P \tag{B.1}$$

$$L_R^S = \underbrace{\sqrt{\left(x - x^S\right)^2 + \left(y - y^S\right)^2 + \left(z - z^S\right)^2} + c\left(dt - dt^S\right) + Mzpd + \lambda N^S}_{L_C^R(x,y,z,dt,zpd,N^S)} + \varepsilon_L \tag{B.2}$$

Where P_R^S and L_R^S are the pseudorange and carrier-phase observables measured by the receiver, and $P_C^R(x, y, z, dt, zpd)$ and $L_C^R(x, y, z, dt, zpd)$ are the observable calculated from parameters (x, y, z, dt, zpd). The equations can be linearity around parameters $\mathbf{x_0} = (x_0, y_0, z_0, dt_0, zpd_0, N_0)$ via first-order Taylor series expansion

$$P_R^S = P_C^S(\mathbf{x_0}) + \frac{\partial P_C^S}{\partial x}\Delta x + \frac{\partial P_C^S}{\partial y}\Delta y + \frac{\partial P_C^S}{\partial z}\Delta z + \frac{\partial P_C^S}{\partial dt}\Delta dt + \frac{\partial P_C^S}{\partial zpd}\Delta zpd + \varepsilon_P \tag{B.3}$$

$$L_R^S = L_C^S(\mathbf{x_0}) + \frac{\partial L_C^S}{\partial x}\Delta x + \frac{\partial L_C^S}{\partial y}\Delta y + \frac{\partial L_C^S}{\partial z}\Delta z + \frac{\partial L_C^S}{\partial dt}\Delta dt + \frac{\partial L_C^S}{\partial zpd}\Delta zpd + \frac{\partial L_C^S}{\partial N^S}\Delta N^S + \varepsilon_P \tag{B.4}$$

We can rearrange and rewrite the linearised equations in matrix form

$$\begin{bmatrix} \Delta P_R^S \\ \Delta L_R^S \end{bmatrix} = \begin{bmatrix} \frac{\partial P_C^S}{\partial x} & \frac{\partial P_C^S}{\partial y} & \frac{\partial P_C^S}{\partial z} & \frac{\partial P_C^S}{\partial dt} & \frac{\partial P_C^S}{\partial zpd} & \frac{\partial P_C^S}{\partial N^S} \\ \frac{\partial L_C^S}{\partial x} & \frac{\partial L_C^S}{\partial y} & \frac{\partial L_C^S}{\partial z} & \frac{\partial L_C^S}{\partial dt} & \frac{\partial L_C^S}{\partial zpd} & \frac{\partial L_C^S}{\partial N^S} \end{bmatrix} \begin{bmatrix} \Delta x \\ \Delta y \\ \Delta z \\ \Delta dt \\ \Delta zpd \\ \Delta N^S \end{bmatrix} + \begin{bmatrix} \varepsilon_P^S \\ \varepsilon_L^S \end{bmatrix} \tag{B.5}$$

Where $\Delta P_R^S = P_R^S - P_C^R(\mathbf{x_0})$ and $\Delta L_R^S = L_R^S - L_C^R(\mathbf{x_0})$. This are the observable equations for satellite S, but the receiver R is receiving signals from n_{Sat} satellites (around 30). We can therefore write a matrix equation for all satellite observables reaching the receiver.

$$\begin{bmatrix} \Delta P_R^0 \\ \Delta L_R^0 \\ \vdots \\ \Delta P_R^{n_{Sat}} \\ \Delta L_R^{n_{Sat}} \end{bmatrix} = \begin{bmatrix} \frac{\partial P_C^0}{\partial x} & \frac{\partial P_C^0}{\partial y} & \frac{\partial P_C^0}{\partial z} & \frac{\partial P_C^0}{\partial dt} & \frac{\partial P_C^0}{\partial zpd} & \frac{\partial P_C^0}{\partial N^S_{(S=0,n_{Sat})}} \\ \frac{\partial L_C^0}{\partial x} & \frac{\partial L_C^0}{\partial y} & \frac{\partial L_C^0}{\partial z} & \frac{\partial L_C^0}{\partial dt} & \frac{\partial L_C^0}{\partial zpd} & \frac{\partial L_C^0}{\partial N^S_{(S=0,n_{Sat})}} \\ \vdots & \vdots & \vdots & \vdots & \vdots & \vdots \\ \frac{\partial P_C^{n_{Sat}}}{\partial x} & \frac{\partial P_C^{n_{Sat}}}{\partial y} & \frac{\partial P_C^{n_{Sat}}}{\partial z} & \frac{\partial P_C^{n_{Sat}}}{\partial dt} & \frac{\partial P_C^{n_{Sat}}}{\partial zpd} & \frac{\partial P_C^{n_{Sat}}}{\partial N^S_{(S=0,n_{Sat})}} \\ \frac{\partial L_C^{n_{Sat}}}{\partial x} & \frac{\partial L_C^{n_{Sat}}}{\partial y} & \frac{\partial L_C^{n_{Sat}}}{\partial z} & \frac{\partial L_C^{n_{Sat}}}{\partial dt} & \frac{\partial L_C^{n_{Sat}}}{\partial zpd} & \frac{\partial L_C^{n_{Sat}}}{\partial N^S_{(S=0,n_{Sat})}} \end{bmatrix} \begin{bmatrix} \Delta x \\ \Delta y \\ \Delta z \\ \Delta dt \\ \Delta zpd \\ \Delta N^S_{(S=0,n_{Sat})} \end{bmatrix} + \begin{bmatrix} \varepsilon_P^0 \\ \varepsilon_L^0 \\ \vdots \\ \varepsilon_P^{n_{Sat}} \\ \varepsilon_L^{n_{Sat}} \end{bmatrix} \tag{B.6}$$

$$\mathbf{b} = \mathbf{A}\mathbf{x} + \varepsilon \tag{B.7}$$

The $2 \cdot N_{sat}$ sets of equations will not be linearly dependent, and so no exact solution to the system can be obtained via linear algebra. Instead this takes the form of an ordinary least squares problem, where we wish to find a value of $\mathbf{x}$ that minimises the sum of squared residuals $\varepsilon^T \varepsilon$, which satisfied when $\frac{d}{d\mathbf{x}}(\varepsilon^{\mathbf{T}}\varepsilon) = 0$. The value $\hat{\mathbf{x}}$ which satisfies this is found through

$$\begin{aligned} \frac{d}{d\mathbf{x}}(\varepsilon^{\mathbf{T}}\varepsilon) = \frac{d}{d\mathbf{x}}\left\{(\mathbf{b}-\mathbf{A}\hat{\mathbf{x}})^{\mathrm{T}}(\mathbf{b}-\mathbf{A}\hat{\mathbf{x}})\right\} &= 0 \\ \frac{d}{d\mathbf{x}}(\mathbf{b}-\mathbf{A}\hat{\mathbf{x}})^{\mathrm{T}}(\mathbf{b}-\mathbf{A}\hat{\mathbf{x}}) + (\mathbf{b}-\mathbf{A}\hat{\mathbf{x}})^{\mathrm{T}}\frac{d}{d\mathbf{x}}(\mathbf{b}-\mathbf{A}\hat{\mathbf{x}}) &= 0 \\ (-\mathbf{A}\frac{d\mathbf{x}}{d\mathbf{x}})^{\mathrm{T}}(\mathbf{b}-\mathbf{A}\hat{\mathbf{x}}) + (\mathbf{b}-\mathbf{A}\hat{\mathbf{x}})^{\mathrm{T}}(-\mathbf{A}\frac{d\mathbf{x}}{d\mathbf{x}}\hat{\mathbf{x}}) &= 0 \\ (-2\mathbf{A}\frac{d\mathbf{x}}{d\mathbf{x}})^{\mathrm{T}}(\mathbf{b}-\mathbf{A}\hat{\mathbf{x}}) &= 0 \\ \left(\frac{d\mathbf{x}}{d\mathbf{x}}^{\mathrm{T}}\mathbf{A}^{\mathrm{T}}\right)(\mathbf{b}-\mathbf{A}\hat{\mathbf{x}}) &= 0 \\ \frac{d\mathbf{x}}{d\mathbf{x}}^{\mathrm{T}}\left(\mathbf{A}^{\mathrm{T}}\mathbf{b}-\mathbf{A}^{\mathrm{T}}\mathbf{A}\hat{\mathbf{x}}\right) &= 0 \\ \mathbf{A}^{\mathrm{T}}\mathbf{A}\hat{\mathbf{x}} &= \mathbf{A}^{\mathrm{T}}\mathbf{b} \end{aligned} \tag{B.8}$$

Bibliography

1. Dirac, P. A. M., "The quantum theory of the electron". *Proc. Roy. Soc. Lond. A* 117, 610–624 1928.
2. Dirac, P. A. M., "Quantised singularities in the electromagnetic field". *Proc. Roy. Soc. Lond. A* 133, 60–72 1931.
3. Anderson, C. D., "The Positive Electron". *Phys. Rev.* 43, 491–494 6 Mar. 1933.
4. Dirac, P. A. M. Theory of electrons and positrons. *Nobel Lecture* 1933.
5. Chamberlain, O., *et al.*, "Observation of Antiprotons". *Phys. Rev.* 100, 947–950 3 Nov. 1955.
6. Cork, B., *et al.*, "Antineutrons Produced from Antiprotons in Charge-Exchange Collisions". *Phys. Rev.* 104, 1193–1197 4 Nov. 1956.
7. Baur, G., *et al.*, "Production of antihydrogen". *Physics Letters B* 368, 251–258 1996.
8. Blanford, G., *et al.*, "Observation of Atomic Antihydrogen". *Phys. Rev. Lett.* 80, 3037–3040 14 Apr. 1998.
9. Amoretti, M., *et al.*, "Production and detection of cold antihydrogen atoms". *Nature* 419, 456–9 Nov. 2002.
10. Gabrielse, G., *et al.*, "Driven Production of Cold Antihydrogen and the First Measured Distribution of Antihydrogen States". *Phys. Rev. Lett.* 89, 233401 23 Nov. 2002.
11. Lee, T. D., & C. N. Yang, "Question of Parity Conservation in Weak Interactions". *Phys. Rev.* 104, 254–258 1 Oct. 1956.
12. Wu, C. S., *et al.*, "Experimental Test of Parity Conservation in Beta Decay". *Phys. Rev.* 105, 1413–1415 4 Feb. 1957.
13. Christenson, J. H., *et al.*, "Evidence for the 2π Decay of the K_2^0 Meson". *Phys. Rev. Lett.* 13, 138–140 4 July 1964.
14. Canetti, L., M. Drewes & M. Shaposhnikov, "Matter and Antimatter in the Universe". *New Journal of Physics* 14 Sept. 2012.
15. Sakharov, A. D., "Violation of CP Invariance, C asymmetry, and baryon asymmetry of the universe". *Pisma Zh. Eksp. Teor. Fiz.* 5, 32–35 1967.
16. Charlton, M., S. Eriksson & G. M. Shore, *Antihydrogen and Fundamental Physics*. Springer, July 2020.
17. Lehnert, R., "CPT Symmetry and Its Violation". *Symmetry* 8, 114 2016.

18. Carli, C., *et al.*, "ELENA: Bright Perspectives for Low Energy Antiproton Physics". *Nuclear Physics News* 32, 21–27 Sept. 2022.

19. Baird, S. A., *et al.*, "Design study of the antiproton decelerator: AD". *CERN Document Server* Nov. 1996.

20. Alanzeau, C., *et al.*, "Extra Low ENergy Antiproton (ELENA) ring and its Transfer Lines: Design Report". *CERN Document Server* Apr. 2014.

21. Smorra, C., *et al.*, "BASE – The Baryon Antibaryon Symmetry Experiment". *Eur. Phys. J. ST* 224, 3055–3108. arXiv: 1604.08820 [physics.atom-ph] 2015.

22. Smorra, C., *et al.*, "BASE-STEP: A transportable antiproton reservoir for fundamental interaction studies". *Review of Scientific Instruments* 94 Nov. 2023.

23. Aumann, T., W. Bartmann & O. Boine-Frankenheim, "PUMA, antiProton unstable matter annihilation". *European Physical Journal A* May 2022.

24. Malbrunot, C., *et al.*, "The ASACUSA antihydrogen and hydrogen program : results and prospects". *Philosophical Transactions of The Royal Society A Mathematical Physical and Engineering Sciences* 376 Feb. 2018.

25. Perez, P., *et al.*, "The GBAR antimatter gravity experiment". *Hyperfine Interactions* 233, 21–27 Apr. 2015.

26. Andresen, G. B., *et al.*, "Trapped antihydrogen". *Nature* 468, 673–676 2010.

27. Gabrielse, G., *et al.*, "Trapped Antihydrogen in Its Ground State". *Phys. Rev. Lett.* 108, 113002 11 Mar. 2012.

28. "Confinement of antihydrogen for 1,000 seconds". *Nature Physics* 7, 558–564 June 2011.

29. Ahmadi, M., *et al.*, "Observation of the 1S-2S transition in trapped antihydrogen". *Nature* 541 Jan. 2017.

30. Ahmadi, M., *et al.*, "Observation of the 1S–2P Lyman- transition in antihydrogen". *Nature* 561, 1 Sept. 2018.

31. Amole, C., *et al.*, "Resonant quantum transitions in trapped antihydrogen atoms". *Nature* 483, 439–43 Mar. 2012.

32. Baker, C., *et al.*, "Laser cooling of antihydrogen atoms". *Nature* 592, 35–42 Apr. 2021.

33. Anderson, E., *et al.*, "Observation of the effect of gravity on the motion of antimatter". *Nature* 621, 716–722 Sept. 2023.

34. Parthey, C. G., *et al.*, "Improved Measurement of the Hydrogen $1S - -2S$ Transition Frequency". *Phys. Rev. Lett.* 107, 203001 20 Nov. 2011.

35. Ahmadi, M., *et al.*, "Characterization of the 1S–2S transition in antihydrogen". *Nature* 557 May 2018.

36. Gustafson, R. A., & F. Robicheaux, "Theory of the line shape of the 1S–2S transition for magnetically trapped antihydrogen". *Journal of Physics B: Atomic, Molecular and Optical Physics* 54, 185001 Oct. 2021.

37. Enomoto, Y., *et al.*, "Synthesis of Cold Antihydrogen in a Cusp Trap". *Phys. Rev. Lett.* 105, 243401 24 Dec. 2010.

38. Dehmelt, H. G., "Radiofrequency Spectroscopy of Stored Ions I: Storage". *Advances in Atomic and Molecular Physics* 3, 53–72 Jan. 1968.

39. Hodgkinson, D. *On the Dynamics of Adiabatically Cooled Antihydrogen in an Octupole-Based Ioffe-Pritchard Magnetic Trap* PhD thesis Manchester U., Manchester U., 2022.

40. Malmberg, J. H., & J. S. Degrassie, "Properties of nonneutral plasma". *Physical Review Letters* 35, 577–580 1975.

41. Fabbri, S. *Optimization of Antiproton Capture and Delivery for the ALPHA Antihydrogen Experiment* PhD thesis University of Manchester, 2021.

42. Paul, W., & H. Steinwedel, "Notizen: Ein neues Massenspektrometer ohne Magnetfeld". *Zeitschrift Naturforschung Teil A* 8, 448–450 July 1953.

43. Tjoelker, R. L. *Antiprotons in a Penning Trap: A New Measurement of the Inertial Mass* PhD thesis Harvard University, 1990.

44. Brown, L. S., & G. Gabrielse, "Geonium theory: Physics of a single electron or ion in a Penning trap". *Rev. Mod. Phys.* 58, 233–311 1 Jan. 1986.

45. Davidson, R. C., *Physics of Nonneutral Plasmas*. Allied, 1990.

46. Knoop, M., Madsen, N. & Thompson, R. *Physics with Trapped Charged Particles: Lectures from the Les Houches Winter School* 1–364 Jan. 2014.

47. Danielson, J. R., & C. M. Surko, "Torque-Balanced High-Density Steady States of Single-Component Plasmas". *Phys. Rev. Lett.* 94, 035001 3 Jan. 2005.

48. Ahmadi, M., *et al.*, "Enhanced Control and Reproducibility of Non-Neutral Plasmas". *Phys. Rev. Lett.* 120, 025001 2 Jan. 2018.

49. Amole, C., *et al.*, "The ALPHA antihydrogen trapping apparatus". *Nuclear Instruments and Methods in Physics Research Section A: Accelerators, Spectrometers, Detectors and Associated Equipment* 735, 319–340 2014.

50. van der Werf, D., *et al.*, "The ATHENA positron accumulator". *Applied Surface Science* 194. 9th International Workshop on Slow Positron Beam Techniques for Solids and Surfaces, 312–316 2002.

51. Murphy, T. J., & C. M. Surko, "Positron trapping in an electrostatic well by inelastic collisions with nitrogen molecules". *Phys. Rev. A* 46, 5696–5705 9 Nov. 1992.

52. Pritchard, D. E., "Cooling Neutral Atoms in a Magnetic Trap for Precision Spectroscopy". *Phys. Rev. Lett.* 51, 1336–1339 15 Oct. 1983.

53. Hunter, E., *et al.*, "Electron cyclotron resonance (ECR) magnetometry with a plasma reservoir". *Physics of Plasmas* 27, 032106 Mar. 2020.

54. Granum, P., *Measuring the Properties of Antihydrogen*. Presented 19 Sep 2022. PhD thesis. Aarhus University, 2022.

55. Eggleston, D. L., *et al.*, "Parallel energy analyzer for pure electron plasma devices". *Physics of Fluids B: Plasma Physics* 4, 3432–3439 Oct. 1992.

56. Baker, C., *et al.*, "Sympathetic cooling of positrons to cryogenic temperatures for antihydrogen production". *Nature Communications* 12 Oct. 2021.

57. Sameed, M., D. Maxwell & N. Madsen, "Ion generation and loading of a Penning trap using pulsed laser ablation". *New Journal of Physics* 22 Jan. 2020.

58. Klempt, E., C. Batty & J.-M. Richard, "The antinucleon–nucleon interaction at low energy: Annihilation dynamics". *Physics Reports* 413, 197–317 July 2005.

59. Ahmadi, M., *et al.*, "Antihydrogen accumulation for fundamental symmetry tests". *Nature Communications* 8 Sept. 2017.

60. Glinsky, M. E., & T. M. O'Neil, "Guiding center atoms: Three-body recombination in a strongly magnetized plasma". *Physics of fluids. B, Plasma physics* 3, 1279–1293 1991.

61. Taylor, C., J. Zhang & F. Robicheaux, "Cooling of Rydberg H during radiative cascade". *Journal of Physics B: Atomic, Molecular and Optical Physics* 39, 4945 Nov. 2006.

62. Zhong, M., J. Fajans & A. Zukor, "Axial to transverse energy mixing dynamics in octupole-based magnetostatic antihydrogen traps". *New Journal of Physics* 20 May 2018.

63. Andresen, G., *et al.*, "Antihydrogen annihilation reconstruction with the ALPHA silicon detector". *Nuclear Instruments and Methods in Physics Research Section A: Accelerators, Spectrometers, Detectors and Associated Equipment* 684, 73–81 2012.

64. Capra, A., *et al.*, *Design of a Radial TPC for Antihydrogen Gravity Measurement with ALPHA-g*. Nov. 2017.

65. Stracka, S., "Real-time Detection of Antihydrogen Annihilations and Applications to Spectroscopy". *EPJ Web Conf.* 71. eds Bravina, L., Foka, Y. & Kabana, S. , 00126 2014.

66. Capra, A., & for the ALPHA Collaboration, "Machine learning for antihydrogen detection at ALPHA". *Journal of Physics: Conference Series* 1085, 042007 Sept. 2018.

67. Amole, C., *et al.*, "An experimental limit on the charge of antihydrogen". *Nature Communications* 5 June 2014.

68. Ahmadi, M., *et al.*, "An improved limit on the charge of antihydrogen from stochastic acceleration". *Nature* 529, 373–376 Jan. 2016.

69. Ahmadi, M., *et al.*, "Observation of the hyperfine spectrum of antihydrogen". *Nature* 548, 66–69 Aug. 2017.

70. Michan, J., *et al.*, "Narrowband solid state vuv coherent source for laser cooling of antihydrogen". *Hyperfine Interactions* 235 May 2015.

71. Baker, C. *et al. Precision spectroscopy of the 1S-2S transition in antihydrogen: hyperfine structure and CPT invariance* Nature Physics (Accepted for Publication).

72. Branson, J., *Solution of the Dirac Equation for Hydrogen*. UCSD Lecture Notes on Quantum Physics, 2013.

73. Lamb, W. E., & R. C. Retherford, "Fine Structure of the Hydrogen Atom by a Microwave Method". *Phys. Rev.* 72, 241–243 3 Aug. 1947.

74. Tiesinga, E., *et al.*, "CODATA Recommended Values of the Fundamental Physical Constants: 2018". en 2021-06-30 04:06:00 2021.

75. *Nuclear magneton. CODATA recommended value. 2018* `https://physics.nist.gov/cgi-bin/cuu/Value?mun`. Accessed: 2023-11-16.

76. Ramsey, N. F., "Experiments with trapped hydrogen atoms and neutrons". *Physica Scripta* 1995, 323 Jan. 1995.

77. Kolachevsky, N., *et al.*, "Measurement of the 2S Hyperfine Interval in Atomic Hydrogen". *Phys. Rev. Lett.* 102, 213002 21 May 2009.

78. I. Eides, M., H. Grotch & V. A. Shelyuto, "Theory of light hydrogenlike atoms". *Physics Reports* 342, 63–261 2001.

79. Bethe, H. A. & Salpeter, E. E. *Quantum Mechanics of one- and two-electron atoms* 110 SPRINGER-VERLAG, 1957.

80. Mockler, R. C., *Atomic Beam Frequency Standards*. ed Marton, L. , 1–71. Academic Press, 1961.

81. Rasmussen, C. Ø., N. Madsen & F. Robicheaux, "Aspects of 1S-2S spectroscopy of trapped antihydrogen atoms". *Journal of Physics B: Atomic, Molecular and Optical Physics* 50, 184002 Sept. 2017.

82. Mohr, P. J., & B. N. Taylor, "CODATA recommended values of the fundamental physical constants: 1998". *Rev. Mod. Phys.* 72, 351–495 2 Apr. 2000.

83. Jentschura, U., *et al.*, "Mass measurements and the bound-electron g factor". *International Journal of Mass Spectrometry* 251, 102–108 2006.

84. Breit, G., & I. I. Rabi, "Measurement of Nuclear Spin". *Phys. Rev.* 38, 2082–2083 11 Dec. 1931.

85. Göppert-Mayer, M., "Über Elementarakte mit zwei Quantensprüngen". *Annalen der Physik* 401 2006.

86. Biraben, F., M. Bassini & B. Cagnac, "Line-shapes in Doppler-free two-photon spectroscopy. The effect of finite transit time". *Journal de Physique* 40 May 1979.

87. Killian, T. C. *1S-2S spectroscopy of trapped hydrogen: The cold- collision frequency shift and studies of BEC* PhD thesis Massachusetts Institute of Technology, Jan. 1999.

88. Branson, J., *General Time Dependent Perturbations*. UCSD Lecture Notes on Quantum Physics, 2013.

89. Haas, M., *et al.*, "Two-photon excitation dynamics in bound two-body Coulomb systems including ac Stark shift and ionization". *Phys. Rev. A* 73, 052501 5 May 2006.

90. Walraven, J., *Quantum gases*. University of Amsterdam Lecture notes, 2019.

91. Forest, E., & R. D. Ruth, "Fourth-order symplectic integration". *Physica D: Nonlinear Phenomena* 43, 105–117 1990.

92. Donnan, P. H., M. C. Fujiwara & F. Robicheaux, "A proposal for laser cooling antihydrogen atoms". *Journal of Physics B: Atomic, Molecular and Optical Physics* 46, 025302 Jan. 2013.

93. Riehle, F., *Frequency Standards: Basics and Applications*. Wiley-VCH, 2004.

94. Barrell, H., "Thirteenth General Conference of Weights and Measures". *Physics Bulletin* 20, 61–62 Feb. 1969.

95. Mattison, E., "Physics of systematic frequency variations in hydrogen masers". *IEEE Transactions on Ultrasonics, Ferroelectrics, and Frequency Control* 39, 250–255 1992.

96. Griffin, S. J., *et al.*, *Drift Correction for Active Hydrogen MASERs*. 2021 Joint Conference of the European Frequency and Time Forum and IEEE International Frequency Control Symposium (EFTF/IFCS). 2021, 1–6.

97. Blewitt, G., "Basics of the GPS Technique : Observation Equations". *Geodetic applications of GPS* 1 1997.

98. Rodríguezs, J. Á., "GPS Signal Plan". en. *European Space Agency GNSS Science Support Centre* 2011.

99. J. Sanz Subirana, J. J. Z., & M. Hernández-Pajares, "Ionospheric Delay". en. *European Space Agency GNSS Science Support Centre* 2011.

100. J. Sanz Subirana, J. J. Z., & M. Hernández-Pajares, "Ionosphere-free Combination for Dual Frequency Receivers". en. *European Space Agency GNSS Science Support Centre* 2011.

101. Larson, K., & J. Levine, "Carrier-phase time transfer". *IEEE Transactions on Ultrasonics, Ferroelectrics, and Frequency Control* 46, 1001–1012 1999.

102. Altamimi, Z., *et al.*, "ITRF2014: A new release of the International Terrestrial Reference Frame modeling non-linear station motions: ITRF2014". *Journal of Geophysical Research: Solid Earth* 121 July 2016.

103. Hilla, S., "The Extended Standard Product 3 Orbit Format (SP3-c)". *National Geodetic Survey* Aug. 2010.

104. Defraigne, P., & G. Petit, "CGGTTS-Version 2E : an extended standard for GNSS Time Transfer". *Metrologia* 52 Oct. 2015.

105. Kouba, J., & P. Héroux, "Precise Point Positioning Using IGS Orbit and Clock Products". *GPS Solutions* 5, 12–28 Oct. 2001.

106. Survey, C. G. *GPSPACE* `https://github.com/CGS-GIS/GPSPACE`. Accessed: 2010-09-30.

107. Pavlis, N., *et al.*, "The Development and Evaluation of the Earth Gravitational Model 2008 (EGM2008) (vol 117, B04406, 2012)". *Journal of Geophysical Research* 118 Apr. 2012.

108. Hendricks, R. *Personal communication* 2023.

109. Cohen, V. W., "The Nuclear Spin of Caesium". *Phys. Rev.* 46, 713–717 8 Oct. 1934.

110. Steck, D., *Cesium D line data*. Jan. 2010.

111. Chu, S., *et al.*, "Three-dimensional viscous confinement and cooling of atoms by resonance radiation pressure". *Phys. Rev. Lett.* 55, 48–51 1 July 1985.

112. Berthoud, P., E. Fretel & P. Thomann, "Bright, slow, and continuous beam of laser-cooled cesium atoms". *Phys. Rev. A* 60, R4241–R4244 6 Dec. 1999.

113. Raab, E. L., *et al.*, "Trapping of Neutral Sodium Atoms with Radiation Pressure". *Phys. Rev. Lett.* 59, 2631–2634 23 Dec. 1987.

114. Foot, C. J. *Atomic physics* Oxford University Press, Oxford, 2007.

115. Ramsey, N. F., "A Molecular Beam Resonance Method with Separated Oscillating Fields". *Phys. Rev.* 78, 695–699 6 June 1950.

116. Frimmer, M., & L. Novotny, "The Classical Bloch Equations". *American Journal of Physics* 82 Sept. 2014.

117. Paschotta, R., *Rabi oscillations*. RP Photonics Encyclopedia, Dec. 2022.

118. Hendricks, R., *et al.*, "Cs Fountain Clocks for Commercial Realizations—An Improved and Robust Design". *IEEE Transactions on Ultrasonics, Ferroelectrics, and Frequency Control* PP, 1–1 Oct. 2018.

119. Szymaniec, K., *et al.*, "Evaluation of the primary frequency standard NPL-CsF1". *Metrologia* 42, 49 Feb. 2005.

120. Szymaniec, K., *et al.*, *Cancellation of the collisional frequency shift in caesium fountain clocks*. Conference on Coherence and Quantum Optics. Optica Publishing Group, 2007, CSuA13.

121. Szymaniec, K., & S. E. Park, "Primary frequency standard NPL-CsF2: optimized operation near the collisional shift cancellation point". *IEEE Transactions on Instrumentation and Measurement* 60, 2475–2481 July 2011.

122. Itano, W. M., L. L. Lewis & D. J. Wineland, "Shift of $^2S_{\frac{1}{2}}$ hyperfine splittings due to blackbody radiation". *Phys. Rev. A* 25, 1233–1235 2 Feb. 1982.

123. Rosenbusch, P., S. Zhang & A. Clairon, *Blackbody radiation shift in primary frequency standards*. 2007 IEEE International Frequency Control Symposium Joint with the 21st European Frequency and Time Forum. 2007, 1060–1063.

124. Angstmann, E. J., V. A. Dzuba & V. V. Flambaum, "Frequency shift of hyperfine transitions due to blackbody radiation". *Phys. Rev. A* 74, 023405 2 Aug. 2006.

125. Shirley, J. H., *et al.*, "Microwave leakage-induced frequency shifts in the primary frequency Standards NIST-F1 and IEN-CSF1". *IEEE Transactions on Ultrasonics, Ferroelectrics, and Frequency Control* 53, 2376–2385 Dec. 2006.

126. Pavlis, N. K., & M. A. Weiss, "A re-evaluation of the relativistic redshift on frequency standards at NIST, Boulder, Colorado, USA*". *Metrologia* 54, 535 July 2017.

127. Gibble, K., "Difference between a Photon's Momentum and an Atom's Recoil". *Phys. Rev. Lett.* 97, 073002 7 Aug. 2006.

128. Szymaniec, K., *et al.*, "NPL Cs fountain frequency standards and the quest for the ultimate accuracy". *Journal of Physics: Conference Series* 723, 012003 June 2016.

129. Weyers, S., *et al.*, "Advances in the accuracy, stability, and reliability of the PTB primary fountain clocks". *Metrologia* 55, 789 Oct. 2018.

130. Guéna, J., *et al.*, "Evaluation of Doppler Shifts to Improve the Accuracy of Primary Atomic Fountain Clocks". *Physical Review Letters* 106, 130801 Apr. 2011.

131. Burrows, K., *et al.*, "Measuring atom positions in a microwave cavity to evaluate distributed cavity phase shifts". en. *Metrologia* 57. Publisher: IOP Publishing, 065003 Oct. 2020.

132. Audoin C., J. V., *The Quantum Physics of Atomic Frequency Standards*. Boca Raton, CRC Press, Jan. 1989.

133. Sweeny, E. Drift Correction of the Hydrogen MASER. *CERN Summer student report* 2024.

134. *Toptica TA-FHG pro* `https://www.toptica.com/products/tunable-diode-lasers/frequency-converted-lasers/ta-fhg-pro/`. Accessed: 2023-04-12.

135. Drever, R., *et al.*, "Laser Phase and Frequency Stabilization Using an Optical Resonator". *Appl. Phys. B* 31, 97–105 June 1983.

136. *Optical Reference System (ORS): Design and Performance* Menlo Sytems, 2016.

137. Jones, S. *Observation of the 1S-2S Transition in Trapped Antihydrogen* PhD thesis Swansea University, 2017.

138. Franken, P. A., *et al.*, "Generation of Optical Harmonics". *Phys. Rev. Lett.* 7, 118–119 4 Aug. 1961.

139. Oliveira, A., *et al.*, "Cryogenic mount for mirror and piezoelectric actuator for an optical cavity". *Review of Scientific Instruments* 88, 063104 June 2017.

140. Dominec, F. *Stability diagram for a two-mirror cavity* https://en.wikipedia.org/wiki/Optical_cavity#/media/File:Laser_resonator_stability.svg. Accessed: 2024-07-23.

141. Yariv, A. *Quantum Electronics* **3** Wiley, 1989.

142. Virtanen, P., *et al.*, "SciPy 1.0: Fundamental Algorithms for Scientific Computing in Python". *Nature Methods* 17, 261–272 2020.

143. Branch, M., T. Coleman & Y. li, "A Subspace, Interior, and Conjugate Gradient Method for Large-Scale Bound-Constrained Minimization Problems". *SIAM Journal on Scientific Computing* 21 Dec. 1999.

144. De Araujo Azevedo, L. O. *Personal communication* 2024.

145. De Araujo Azevedo, L. O. Laser Induced Background Gas Annihilation during 1s-2s spectroscopy. en. *Internal ALPHA note* 2024.

146. Schmid, F. *Towards high resolution spectroscopy on trapped helium ions* PhD thesis Ludwig-Maximilians Universität, 2022.

147. Jones, S., "An ion trap source of cold atomic hydrogen via photodissociation of the BaH + molecular ion". *New Journal of Physics* 24 Feb. 2022.

148. Azevedo, L., *et al.*, "Adaptable platform for trapped cold electrons, hydrogen and lithium anions and cations". *Communications Physics* 6 May 2023.

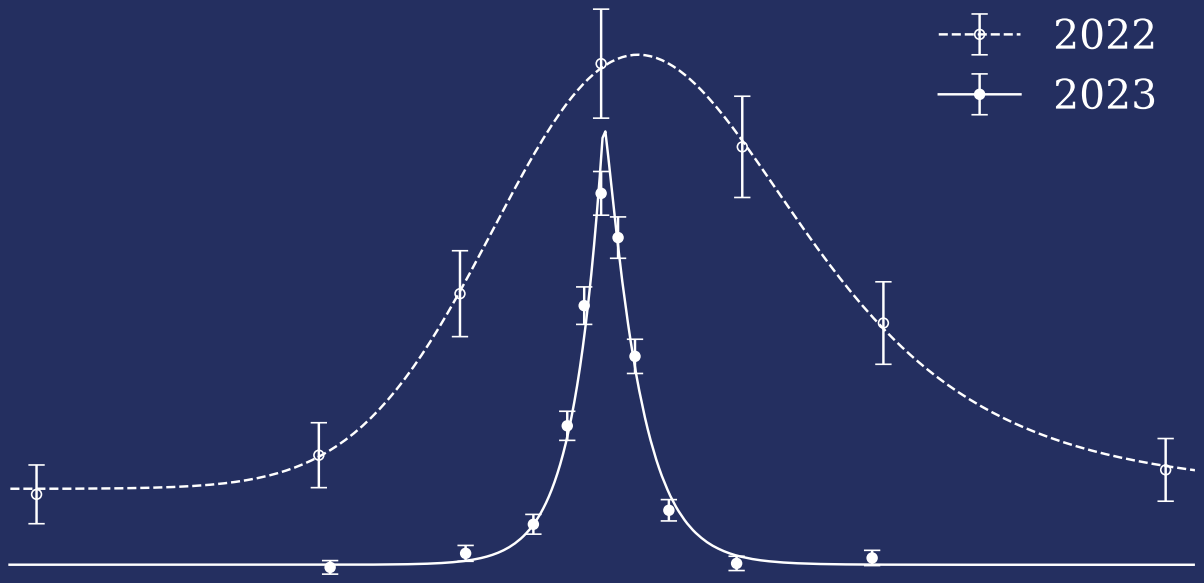

Antihydrogen, the simplest pure antimatter atom, can be synthesised and confined for extended periods in the ALPHA experiment at CERN. According to the CPT invariance, antihydrogen is predicted to exhibit an energy spectrum identical to that of hydrogen. Consequently, a precise comparison of the spectra of both antihydrogen and hydrogen constitutes a direct test of CPT invariance. The narrow 1S-2S two-photon transition serves as the gold standard for precision measurements of hydrogen, where it has been measured with an exceptional 15 digits of precision. Equivalent measurements conducted with antihydrogen have so far been limited to 12 digits of precision – this thesis presents work which took place to improve this precision, through updated instrumentation and new methodologies.

The stability of the laser frequency was a key limitation in the precision of the previous 1S-2S measurements in antihydrogen. A major focus of this thesis is the development of a new frequency metrology suite to improve laser frequency stability, integrating a caesium fountain clock and a hydrogen maser. Preliminary measurements indicate that the upgraded metrology yields a significantly more stable laser system which can be used for extremely precise spectroscopy. This thesis also presents preliminary results of the 2023 experimental campaign to improve the precision of the 1S-2S transition in antihydrogen. This effort made use of the significantly improved laser frequency stability, and is also aided by other new techniques such as laser-cooling of antihydrogen and improved antihydrogen production. Although a full analysis of the experimental data is still ongoing, some preliminary approaches presented in this thesis suggest results that may substantially improve the precision of the 1S-2S antihydrogen transition frequency.